

Magnetic manipulation of membrane molecule motion

Inaugural-Dissertation

to obtain the academic degree

Doctor rerum naturalium (Dr. rer. nat.)

submitted to the Department of Biology, Chemistry, Pharmacy

of Freie Universität Berlin

by

Jia Hui Li

2021

This doctorate study was conducted from October 2015 to December 2020 under the supervision of Prof. Dr. Helge Ewers in the Department of Biology, Chemistry and Pharmacy of the Freie Universität Berlin.

1st Reviewer: Prof. Dr. Helge Ewers, Freie Universität Berlin

2nd Reviewer: Dr. Stephan Block, Freie Universität Berlin

Date of defense: 27th May 2021

Declaration of independent work

This is to confirm that this thesis was independently composed and authored by myself, using solely the referred sources and support.

Abstract

The plasma membrane is the organelle that encompasses the cell and represents the interface through which the cell interacts with its environment. As the membrane is fluid, membrane components can diffuse laterally in the plane of the membrane and their function often depends on their location and dynamics in the membrane. In polarized cells, where the plasma membrane is segregated into functional domains, the lateral diffusion must be restricted to ensure the distinct composition of the membrane domains. This is facilitated by diffusion barriers which impede the movement of molecules in the membrane but in many cases, it is unclear how the barriers are established, and which molecules are involved. At nanoscopic scales, the plasma membrane is thought to be compartmentalized by the underlying cytoskeleton and anchored transmembrane proteins (Picket and Fence model). To study these nanoscopic barriers, the random movements of membrane molecules are usually observed by microscopy, e.g. by single-particle tracking (SPT), and the movement pattern correlated with cellular structures such as the cortical cytoskeleton. However, to directly detect the presence of a physical barrier, a membrane probe could be steered against it to observe its interaction with the barrier. To do so, we developed a method using fluorescent magnetic nanoparticles (FMNPs) and magnetic tweezers. By coupling FMNPs to membrane molecules, we can follow their diffusion by SPT and direct their movement with magnetic tweezers. This way, we moved lipids through artificial lipid bilayers, and membrane proteins through the plasma membrane of living cells. We achieved SPT with ~10 nm localization precision and 5 ms time resolution, while dragging the molecules with magnetic forces of 1-10 fN. Pulling single membrane proteins over the cell surface, we were indeed able to detect obstacles to the protein motion and, with correlative super-resolution imaging, localized them to the site of actin filaments underneath the plasma membrane. Our method hence enables the remote control of single molecule motion and the detection of diffusion barriers with high spatiotemporal resolution. On a broader perspective, the method can also be used to observe and perturb other coordinated activities of membrane molecules such as receptor signaling. We thus contribute a straightforward and versatile tool to investigate the dynamic organization of the plasma membrane at nanoscopic scales.

Zusammenfassung

Die Plasmamembrane ist das Organell, das die Zelle umhüllt, und die Kontaktfläche, über die die Zelle mit ihrer Umwelt interagiert. Da die Membran flüssig ist, können Membranmoleküle lateral in der Ebene der Membran diffundieren und ihre Funktion hängt häufig von dem Aufenthaltsort und der Dynamik in der Membrane ab. In polarisierten Zellen, in denen die Plasmamembran in funktionale Bereiche aufgeteilt ist, muss die laterale Diffusion begrenzt werden, um die unterschiedliche Zusammensetzung der Bereiche aufrechtzuerhalten. Das wird ermöglicht durch Diffusionsbarrieren, die die Bewegung der Moleküle in der Membran behindern, aber in vielen Fällen ist es unklar, wie die Barrieren aufgebaut sind und welche Moleküle beteiligt sind. Es wird angenommen, dass die Plasmamembran in nanoskopische Bereiche aufgeteilt ist durch das darunterliegende Zytoskelett und daran verankerten Transmembranproteinen (Picket-Fence-Model). Um diese nanoskopischen Barrieren zu untersuchen, werden meist die zufälligen Bewegungen von Membranmolekülen im Mikroskop beobachtet, z.B. durch Einzelpartikelverfolgung, und die Bewegungsmuster mit zellulären Strukturen wie dem kortikalen Zytoskelett korreliert. Doch um eine physische Barriere direkt nachzuweisen, könnte man ein Membranmolekül gegen die Barriere steuern und die Interaktion damit beobachten. Dafür haben wir eine Methode entwickelt, die sich fluoreszente magnetische Nanopartikel und magnetische Pinzetten zunutze macht. Indem wir die Magnetpartikel an Membranmoleküle binden, können wir ihre Diffusion mit Einzelpartikelverfolgung beobachten und ihre Bewegung durch die magnetische Pinzette gerichtet steuern. Auf diese Weise haben wir Lipide durch künstliche Membranen bewegt und Membranproteine durch die Plasmamembran von lebenden Zellen. Wir erzielen bei der Einzelpartikelverfolgung eine Lokalisationsgenauigkeit von ~ 10 nm und eine zeitliche Auflösung von 5 ms und erzeugen magnetische Zugkräfte von 1-10 fN. Indem wir einzelne Membranproteine über die Zelloberfläche zogen, konnten wir Hindernisse für die Proteinbewegung detektieren und mithilfe super-hochauflösender Mikroskopie den Ort der Behinderung mit Aktinfilamenten unterhalb der Plasmamembran korrelieren. Unsere Methode ermöglicht daher einzelne Membranmoleküle fernzusteuern und Diffusionsbarrieren mit hoher räumlich-zeitlicher Auflösung auffindig zu machen. Das Verfahren kann auch auf eine breitere Verwendung übertragen werden, um in andere koordinierte Vorgänge in der Membran wie z.B. die Rezeptorsignalübertragung einzugreifen. Wir stellen daher ein einfaches und vielseitiges Werkzeug zu Verfügung, das es ermöglicht, die dynamische Organisation der Plasmamembran in nanoskopischer Größenordnung zu untersuchen.

Table of contents

Abstract.....	3
Zusammenfassung	4
Table of contents.....	5
Abbreviations.....	7
Figures and Tables.....	9
Introduction.....	10
1. The plasma membrane	10
1.1. The Fluid Mosaic model	10
1.2. Membrane molecule diffusion.....	11
1.3. Restricted movement	12
1.3.1. Barriers	15
1.3.2. Specific interactions.....	19
2. Methods to study membrane molecule location and dynamics.....	21
2.1. Fluorescence microscopy.....	21
2.2. Ensemble methods	23
2.3. Single-molecule or -particle tracking.....	24
2.3.1. Principle and general considerations.....	24
2.3.2. Labels.....	26
2.3.3. Diffusion coefficient and other analyses	29
2.4. Super-resolution microscopy	31
2.4.1. Single-molecule localization microscopy	31
3. Methods to manipulate membrane molecules and their motion	34
3.1. (Opto-)Genetic and pharmacologic means	34
3.2. Optical tweezers	35
4. Magnetic particles	38
4.1. Physical and technical background	38
4.1.1. Magnetism	38
4.1.2. Structure and composition of magnetic particles for biological applications	40
4.1.3. Magnetic tweezers	41
4.2. Applications in life sciences	45
4.2.1. Overview of applications.....	45
4.2.2. Advantages and limitations	47
4.2.3. Magnetogenetics	48
5. Aims of the study	51
Results and Discussion	53
6. Selection of suitable FMNPs	53
6.1. Requirements in particle properties	53
6.2. Characterization of FMNP properties	55
6.3. Discussion.....	57
6.3.1. Limitations of the FMNPs	58
6.3.2. Alternative fluorescent magnetic particles.....	59
7. Magnetic manipulation of membrane molecules	61
7.1. Lateral magnetic tweezer setup.....	61
7.2. Manipulation of lipids in an artificial membrane	62
7.2.1. Tracking of lipids by FMNPs	62

Table of contents

7.2.2.	Directional manipulation of lipid movement.....	63
7.3.	Discussion	64
7.3.1.	Diffusion coefficient of FMNP-tracked lipids	64
7.3.2.	Potential causes of reduced lipid diffusion on SLBs	64
7.3.3.	Alternative applications of magnetic SPT	67
7.4.	Magnetic forces.....	67
7.5.	Discussion	70
7.5.1.	Physiological relevance of exerted magnetic forces	70
7.6.	Manipulation of membrane proteins in living cells	72
7.6.1.	Targeting and tracking of membrane proteins by FMNPs.....	72
7.6.2.	Directional manipulation of membrane proteins.....	74
7.7.	Discussion	77
7.7.1.	Diffusion coefficient of membrane probes tracked with FMNPs	78
7.7.1.	FMNP tracking on other cells	79
7.7.1.	Movement behavior under magnetic drag	80
8.	Detection of barriers to the diffusion of membrane molecules	84
8.1.	Correlation with absolute barriers.....	84
8.2.	Correlation with cellular structures.....	88
8.3.	Discussion	92
8.3.1.	Relevance of membrane topography for magnetic pulling.....	93
8.3.1.	Effect of actin on magnetically dragged GFP-GPI.....	93
8.3.2.	Further correlative approaches with magnetic SPT.....	96
	Conclusion.....	98
	Materials and Methods.....	100
9.	Procedures	100
9.1.	Nanoparticle characterization	100
9.1.1.	Dynamic light scattering	100
9.1.2.	Electron microscopy.....	101
9.2.	Magnetic tweezer setup	101
9.3.	Supported lipid bilayer experiments.....	101
9.3.1.	SUV preparation and SLB formation	101
9.3.2.	Force calibration experiments.....	102
9.3.3.	Force calibration data analysis	102
9.4.	Cell culture and transfection	103
9.5.	Live cell experiments	103
9.5.1.	Particle functionalization.....	103
9.5.2.	Membrane sheet generation.....	104
9.5.3.	Live imaging	104
9.5.4.	Data analysis	104
9.6.	Super-resolution imaging	105
9.6.1.	Fixation and staining	105
9.6.2.	dSTORM imaging	105
9.6.3.	Data analysis	105
9.7.	Materials.....	105
	References.....	108
	Curriculum Vitae.....	124
	Appendix.....	126
	Acknowledgments	129

Abbreviations

ABBREVIATION	FULL FORM
AF	Alexa Fluor
AFM	Atomic force microscopy
AIS	Axon initial segment
BFP	Barrier-free path
BME	β -mercaptoethanol
BSA	Bovine serum albumin
<i>cf.</i>	Confer
CytoD	Cytochalasin D
DMEM	Dulbecco's Modified Eagle Medium
DNA	Deoxyribonucleic acid
DOPE-CF	1,2-dioleoyl-sn-glycero-3-phosphoethanolamine-N-carboxyfluorescein
DSPE	1,2-distearoyl-sn-glycero-3-phosphoethanolamine
<i>d</i> STORM/ <i>(d)</i> STORM	(direct) stochastic optical reconstruction microscopy
e.g.	Exemplum gratia
ECM	Extracellular matrix
eGFP/GFP	Enhanced green fluorescent protein
em	Emission
EM	Electron microscopy
EMCCD	Electron Multiplying Charge-Coupled Device
Eq./Eqs.	Equation(s)
ER	Endoplasmic reticulum
<i>et al.</i>	Et alii
ex	Excitation
eYFP/YFP	Enhanced yellow fluorescent protein
F _{ab}	Antigen-binding fragment
FBS	Fetal bovine serum
FCS	Fluorescence correlation spectroscopy
FMNP	Fluorescent magnetic nanoparticle
FWHM	Full width half maximum
GFP	Green fluorescent protein
GPI	Glycosylphosphatidylinositol
HILO	Highly inclined and laminated optical sheet
i.e.	Id est
IRIS	Image reconstruction by integrating exchangeable single-molecule localization
iSCAT	Interferometric scattering
LDL	Low-density lipoprotein
LUT	Look-up table
MEA	β -mercaptoethylamine
MNP	Magnetic nanoparticle
MP-YFP/MyrPalm-YFP	Myristoylated and palmitoylated eYFP
MSD	Mean square displacement
MSS	Moment scaling spectrum
PAINT	Point accumulation for imaging in nanoscale topography
PALM	Photoactivated localization microscopy
PBS	Phosphate buffered saline
PEG	Polyethylene glycol
PSF	Point spread function
QD	Quantum Dot
RFP	Red fluorescent protein
RT	Room temperature
s.d.	Standard deviation
sCMOS	Scientific Complementary Metal-Oxide-Semiconductor
SEM	Scanning electron microscopy

Abbreviations

ABBREVIATION	FULL FORM
si/shRNA	Small interfering or short hairpin ribonucleic acid
SIM	Structured illumination microscopy
SLB	Supported lipid bilayer
SMLM	Single-molecule localization microscopy
SMT	Single-molecule tracking
SPT	Single-particle tracking
STED	Stimulated emission depletion
TEM	Transmission electron microscopy
TfR	Transferrin receptor
TIRF	Total internal reflection fluorescence
uPAINT	Universal PAINT
UV	Ultraviolet
vs.	Versus
NA	Numerical aperture
DIC	Differential interference contrast
PA-GFP	Photoactivatable GFP
nb	Nanobodies
n.s.	not significant
ER	Endoplasmic reticulum

Figures and Tables

Figure 1: The Fluid Mosaic model of the cell membrane	11
Figure 2: Current view of the plasma membrane	14
Figure 3: Picket and Fence models	16
Figure 4: Examples of macroscopic barriers in the plasma membrane	18
Figure 5: Basics of fluorescence microscopy	22
Figure 6: Principle of single-particle tracking	25
Figure 7: Overview of common probes for single-particle tracking	27
Figure 8: Concept of single-molecule localization microscopy	32
Figure 9: Magnetic properties of (bulk) ferromagnetic materials and magnetic particles	40
Figure 10: Types of fluorescent magnetic composite particles	41
Figure 11: Typical magnetic tweezer configurations	43
Figure 12: Magnetogenetic control of plasma membrane proteins.	49
Figure 13: FMNPs and magnetic tweezers as a tool to manipulate membrane molecule motion and to detect diffusion barriers in the plasma membrane.....	52
Figure 14: Screening of different FMNPs for desired properties	55
Figure 15: Characterization of “BNF-Starch-redF Streptavidin” particles (Micromod)	56
Figure 16: Relationship of desired particle properties for FMNPs	58
Figure 17: Lateral magnetic tweezer setup	61
Figure 18: SPT of lipids in an SLB by FMNPs.....	62
Figure 19: Magnetic manipulation of lipid motion in an SLB by the magnetic needle.....	63
Figure 20: Magnetic force calibration on SLBs.....	69
Figure 21: SPT of GFP-GPI via GFP nanobody-coated FMNPs	73
Figure 22: SPT and magnetic manipulation of GFP-GPI via GFP nanobody-coated FMNPs.....	75
Figure 23: SPT and magnetic pulling of different membrane probes via GFP nanobody-coated FMNPs	77
Figure 24: Correlation of FMNP-pulled lipid trajectories with the SLB topography	85
Figure 25: Correlation of FMNP-pulled MP-YFP trajectories with the cortical actin on membrane sheets	87
Figure 26: Correlation of FMNP-pulled GFP-GPI trajectories with membrane ruffles	89
Figure 27: Correlation of FMNP-pulled GFP-GPI trajectories with the subplasmalemmal actin cytoskeleton	91
Figure S28: DLS measurement of FMNPs	126
Figure S29: Histogram of diffusion coefficients for FMNPs in solution	126
Figure S30: FEMM simulation of the magnetic needle setup	127
Figure S31: Variability of apparent magnetic forces with tip position.....	127
Figure S32: Examples of FMNP-pulled GFP-GPI trajectories correlated with the cortical actin cytoskeleton	128
Table 1: Criteria for the suitability of FMNPs for SPT and magnetic manipulation	54
Table 2: Experiments to check the suitability of FMNPs for SPT and magnetic manipulation	57
Table 3: Quality assessment of FMNPs	100
Table 4: FMNPs tested in this study	105
Table 5: Reagents used in this work.....	106
Table 6: Other materials and equipment used in this work	106
Table 7: Buffer compositions.....	107
Table 8: Plasmid constructs used for transfection.....	107

Introduction

I. The plasma membrane

All cellular life is encapsulated by biological membranes which separate the cell interior from the exterior. However, the plasma membrane is not merely a passive barrier as the cell interacts through it with the outside environment. This interface must therefore enable the selective flow of both information and material (nutrients or waste). Biological membranes represent a hydrophobic barrier for inorganic ions, charged or polar molecules and larger macromolecules which can only pass through specific transport proteins. Additionally, the plasma membrane is involved in many metabolic pathways through membrane enzymes. Continuous turnover of membrane constituents is sustained through *de novo* synthesis and insertion, internalization and degradation. On a larger scale, the cell membrane gives the cell its size and shape, and membrane remodeling allows cellular movement. The plasma membrane is thus a highly dynamic organelle which allows a variety of cellular processes such as cell division or migration while maintaining its integrity. Although the basic principles of the organization of the plasma membrane have already been uncovered in the early 1970's (Figure 1; see 1.1), research accumulated in the last decades have led to an ever finer picture of the plasma membrane and its functions (Figure 2; see 1.3), but have also raised new questions and controversies.

I.1. The Fluid Mosaic model

The Fluid Mosaic Model laid the foundation for our understanding of biological membranes to date (Singer and Nicolson, 1972). The model describes cellular membranes as a fluid bilayer of lipids traversed by proteins (Figure 1a). Lipids are amphiphilic molecules that assemble through hydrophobic interactions between their hydrophobic parts into a quasi-two-dimensional structure. The fatty acid chains of phospholipids, the main class of lipids constituting biological membranes, are laterally packed together, and two leaflets are stacked to form a bilayer such that only the hydrophilic headgroups are exposed to the aqueous environment. Proteins can be either incorporated in the membrane (integral proteins) or be only attached by transient interactions (peripheral). The former type can have transmembrane domains which pass the bilayer once or multiple times, embedded domains which are inserted into the bilayer but do not cross it, or lipid-modifications which anchor the protein in one leaflet of the membrane bilayer (Figure 1b). Additionally, both lipids and proteins can be modified with oligosaccharides on the extracellular side, forming glycolipids and glycoproteins or proteoglycans. Of these three chemical classes – lipids, proteins, and carbohydrates – the proteins constitute the largest fraction in terms of mass (Korn, 1969; Mitra *et al.*, 2004; Milo *et al.*, 2009). The membrane proteins therefore represent the mosaic pieces in the model and the

phospholipids the mortar. Importantly, because of the non-covalent nature of most interactions between lipids and membrane proteins, they are free to move laterally in the plane of the membrane. Several studies preceding the Fluid Mosaic Model demonstrated that membrane proteins exhibit a disordered distribution within a liquid-like environment (Blasie and Worthington, 1969). Notably, when two cells with fluorescently labeled surface antigens were fused, the two colors would quickly mix (Frye and Edidin, 1970). The membrane is thus *fluid*, rendering it a highly dynamic structure in which the principles of thermo- and hydrodynamics apply.

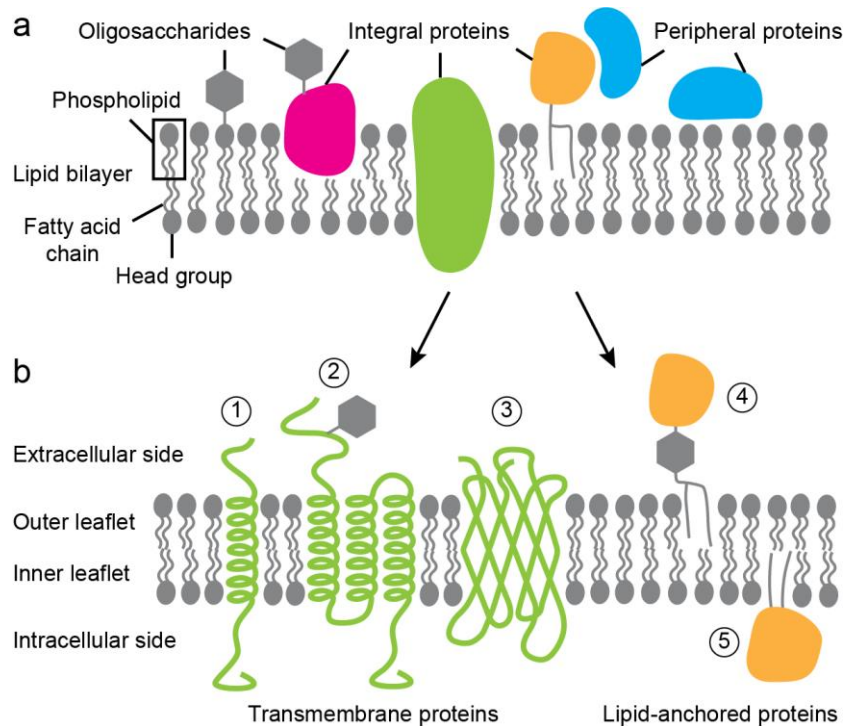


Figure 1: The Fluid Mosaic model of the cell membrane

a) General Fluid Mosaic model of biological membranes. Phospholipids form a two-dimensional bilayer in which proteins are incorporated. Additionally, peripheral proteins associate non-covalently to the membrane. Carbohydrates can be covalently linked to both lipids and proteins and associate non-covalently which constitute the glycocalyx. The lipid bilayer alone is only 3-4 nm thick (Rawicz *et al.*, 2000; Mitra *et al.*, 2004) but can be much thicker (5-30 nm) with the extruding protein and glycosyl moieties (Bayer, 1991; Schneiter *et al.*, 1999; Yamaguchi *et al.*, 2011; Son *et al.*, 2020) **b)** Types of membrane proteins: Transmembrane proteins (1-3) can span the lipid bilayer once (1) or several times (2, 3), with α -helices (1, 2) or as a β -barrel (3). Proteins can also be covalently linked to lipids (4, 5). Proteins with glycosylphosphatidylinositol (GPI; a group of C-terminal lipid anchors consisting of a short oligosaccharide, inositol, and 2-3 varying fatty acid chains) are found in the outer leaflet of the plasma membrane (4). On the other side of the membrane reside proteins with palmitoyl, N-myristoyl, farnesyl and/or geranylgeranyl modifications (5). **a, b)** Not drawn to scale. Oligosaccharides are simplified as a single hexagon.

1.2. Membrane molecule diffusion

The membrane can be taken as a two-dimensional viscous fluid in which the integral proteins and lipids undergo Brownian motion (Singer and Nicolson, 1972; Saffman and Delbrück, 1975). In solution, Brownian motion can be described by the diffusion coefficient D which relates to the translational mobility b_T of the molecules by the Einstein relation

$$D = k_B T b_T, \quad (1)$$

where k_B is the Boltzmann constant and T the absolute temperature. For a particle of hydrodynamic radius r in a fluid of viscosity η , the diffusion coefficient is specified by the Stokes-Einstein relation

$$D = \frac{k_B T}{6\pi \eta r}. \quad (2)$$

However, the diffusion of membrane proteins and lipids is different as they are limited to the plane of the membrane, a viscous fluid suspended in a less viscous fluid, i.e. the aqueous medium (Saffman and Delbrück, 1975). According to the Saffman-Delbrück approximation,

$$b_T = \frac{1}{4\pi \eta h} \left(\log \frac{\eta h}{\eta' r} - e \right), \quad (3)$$

where r is the radius of a cylindrical membrane-embedded moiety and e is Euler's number, the lateral mobility b_T of a membrane molecule mainly depends on the thickness h and viscosity of the membrane η , and to a lesser extent on the size of the molecule within the membrane or the viscosity of the surrounding aqueous phase η' . Because the viscosity of the exterior aqueous phase is lower by two orders of magnitude than the viscosity of the membrane, the translational drag exerted by the aqueous medium on the lipid headgroups, protein or oligosaccharide moieties extruding the membrane bilayer can be mostly neglected. Although other hydrodynamic theories that take length-scale dependent effects into account have been developed later (Gambin *et al.*, 2006; Petrov and Schwille, 2008), the model generally predicts the diffusion coefficient correctly for a given membrane protein size (Weiß *et al.*, 2013). Since the proposal of the Fluid Mosaic model and the theory of membrane molecule diffusion (Singer and Nicolson, 1972; Saffman and Delbrück, 1975), the diffusion of numerous membrane components have been experimentally observed both *in vitro* (in artificial lipid bilayers) and *in vivo* using different techniques (reviewed in 2.2 and 2.3) such as single-particle tracking (SPT), fluorescence recovery after photobleaching (FRAP) or fluorescence correlation spectroscopy (FCS). These measurements uncovered movement behaviors of membrane lipids and proteins that could not be explained by the Fluid Mosaic model and Saffman-Delbrück diffusion model alone.

1.3. Restricted movement

Early on, it was recognized that membrane components are not free in their movement despite the general property of membrane fluidity and diffusion of its constituents (Nicolson, 1976). Consistently, a 5 to 50-fold slower diffusion for both lipids and proteins was observed in the plasma membrane of living cells compared to artificial membranes and liposomes (Kusumi *et al.*, 2012). Also, membrane molecules such as signaling receptors change in diffusion coefficient drastically upon

oligomerization whereas the Saffman-Delbrück model predicts only a relatively small change with the increase in diameter of the membrane-inserted portion (Iino, Koyama and Kusumi, 2001; Andrews *et al.*, 2008; Suzuki *et al.*, 2012). Furthermore, membrane constituents are highly unevenly distributed in the plasma membrane although lateral randomization of locations would be expected over time according to the Fluid Mosaic model (Garcia-Parajo *et al.*, 2014; Saka *et al.*, 2014; Paparelli *et al.*, 2016; Sezgin *et al.*, 2017). Localized insertion by exocytosis or synthesis and endocytosis contribute to the distribution of a certain compound in the plasma membrane but seem insufficient to generally explain the inhomogeneity (Trimble and Grinstein, 2015; Goiko, de Bruyn and Heit, 2018). These observations can be explained by different mechanisms including homo- and hetero-oligomerization of proteins and lipids, formation of micro- or nanodomains, interactions with the intracellular contractile cytoskeleton as well as with extracellular matrix (ECM) components (Figure 2) (Nicolson, 1976). These possible mechanisms can be categorized as either physical barriers (see 1.3.1) or specific interactions (see 1.3.2). Physical obstacles are *per se* unspecific and universally affect the movement of all membrane constituents in the plane of the membrane. On the other hand, interactions that limit the movement of membrane molecules can be highly specific between certain molecular species or can be based on more general physico-chemical properties such as hydrophobicity. It should be noted that these mechanisms are not mutually exclusive as they can act together in the same process. A massive body of literature dealing with these different organizing principles of the plasma membrane has been collected since the 1970's. Altogether, these studies paint a complex and multilayered picture of this dynamic organelle (Figure 2) (Jacobson, Liu and Lagerholm, 2019).

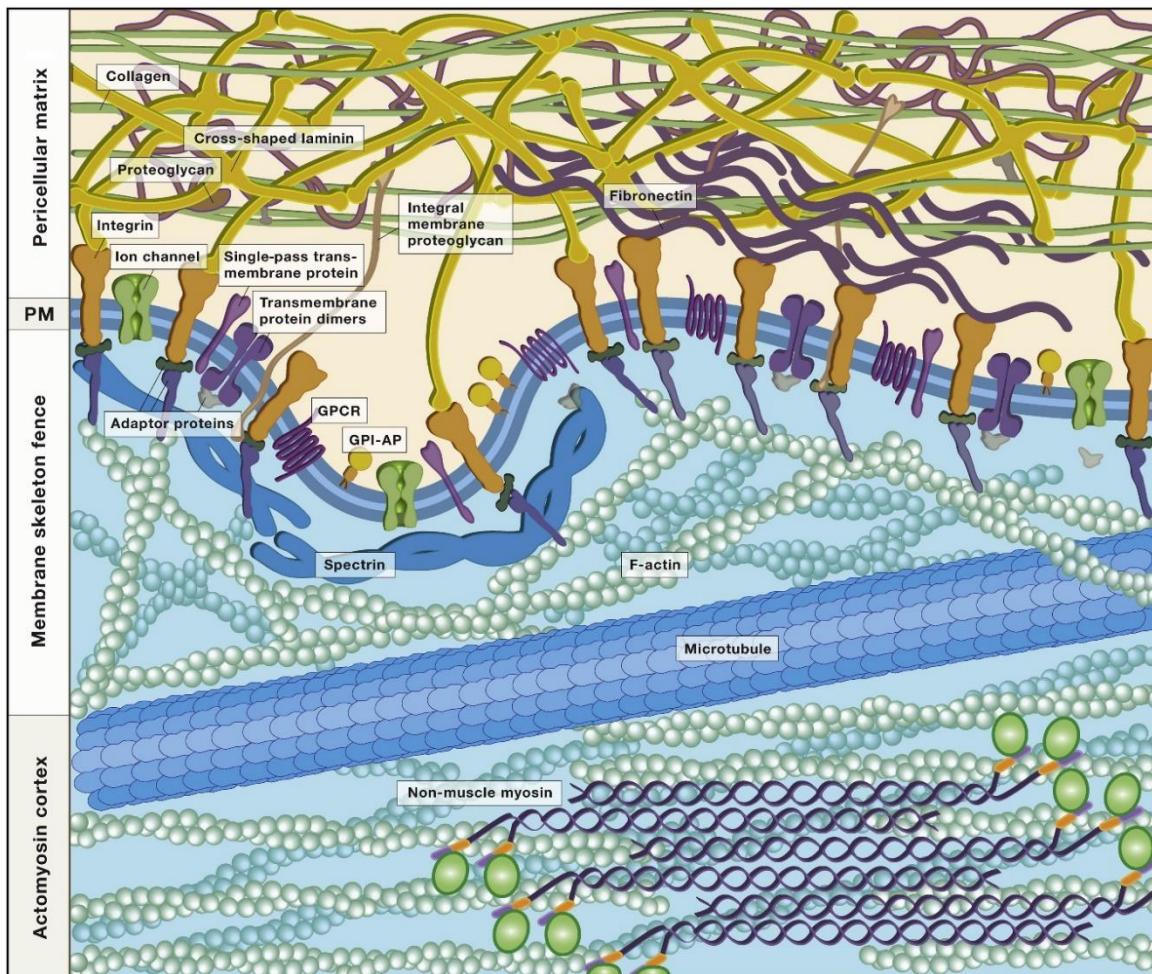


Figure 2: Current view of the plasma membrane

The plasma membrane consists of the lipid bilayer and embedded proteins as described in the Fluid Mosaic model. However, this model can only predict the dynamic behavior of membrane molecules at nanometer scales. At larger scales, the mobility and activity of membrane constituents is regulated by adjacent structures which are the cortical cytoskeleton on the intracellular face of the plasma membrane and the pericellular matrix on the extracellular side. From (Jacobson, Liu and Lagerholm, 2019) with permission.

Irrespective of the exact mechanism, one might wonder why cells would have evolved to restrict the movement of membrane constituents. Compared to the cytosol, the diffusion in the membrane is already much slower (Saffman and Delbrück, 1975), and particularly in large mammalian cells, the length scales that can be covered by diffusion is small relative to the size of the plasma membrane. There are mainly two purposes that can be achieved by restricting the movement of membrane molecules: 1. to separate the membrane into distinct functional domains, and 2. to generate locally high concentrations of certain molecules. The former aspect applies mainly at larger, micron-to-submicron scales, where cells form subcellular domains of the plasma membrane which perform different physiological functions (Figure 4; see 1.3.1) (Caudron and Barral, 2009; Kusumi *et al.*, 2012). The latter aspect relates to the nano- to mesoscale (submicron) organization of the plasma membrane, where molecules such as receptors or enzymes are locally concentrated to enhance signaling or catalysis (Choquet and Triller, 2003; Bethani *et al.*, 2010; Kalay, Fujiwara and Kusumi, 2012; Weinberg

and Puthenveedu, 2019). Spatial compartmentalization of distinct activities is a universal strategy found in all complex systems across scales to increase the efficiency and to avoid interference with other activities.

1.3.1. Barriers

All molecular assemblies in and close to the plasma membrane could potentially pose obstacles to the diffusion of membrane molecules, especially if they are relatively static. These include the pericellular matrix of proteoglycans and glycolipids, the intracellular cytoskeletal cortex which dominantly consists of actin, and integral protein complexes attached to either of them. Specifically the partitioning of the plasma membrane by the membrane-associated cytoskeleton (1.3.1) has been studied extensively (Kusumi *et al.*, 2005, 2012). One of the first studies which attributed the reduced lateral mobility of integral membrane proteins to the membrane skeleton was conducted in erythrocytes, from which the major components of the membrane cytoskeleton were stripped (erythrocyte ghosts) (Sheetz, Schindler and Koppel, 1980). The diffusion coefficient of the erythrocyte transmembrane protein Band 3 measured by FRAP was 50 times faster in these ghosts than in untreated erythrocytes membranes. Based on a series of studies using SPT (see 2.3) and optical tweezers (see 3.2), Kusumi *et al.* proposed the Fence model (Figure 3, left) (Tsuji *et al.*, 1988; Kusumi, Sako and Yamamoto, 1993; Sako *et al.*, 1998; Tomishige, Sako and Kusumi, 1998). This model explains the restricted mobility of transmembrane proteins by steric interactions of the cytosolic domains protruding from the plasma membrane with the cortical cytoskeleton. Within the compartments formed by the cytoskeleton, the transmembrane proteins diffuse as fast as in artificial membranes such as supported lipid bilayers (SLBs) or in membrane blebs, where the cortical cytoskeleton is detached from the plasma membrane. The proteins can stochastically pass the barriers to the next compartment, leading to so-called hop diffusion, and the residence time within compartments depends on the size of the cytoplasmic tails. Several studies of other groups using complementary methods have confirmed an influence of the submembrane cytoskeleton in the movement of membrane components (Lenne *et al.*, 2006; Andrews *et al.*, 2008; Treanor *et al.*, 2010; Di Rienzo *et al.*, 2013; Sungkaworn *et al.*, 2017). However, this model could not explain the reduced mobility of lipids or GPI-anchored proteins which lack a cytoplasmic domain. By increasing the time resolution of SPT to 25 μ s (40,000 Hz), Fujiwara *et al.* discovered that also phospholipids undergo hop diffusion but reside shorter within one compartment than transmembrane proteins. In this case, the impedance is explained by so-called pickets, transmembrane proteins which are anchored to the underlying cytoskeleton (Figure 3, right) (Fujiwara *et al.*, 2002; Murase *et al.*, 2004). The pickets compartmentalize the diffusion of both lipids and proteins by steric hindrance in the membrane and additionally by the hydrodynamic friction-like effect which slows the lateral diffusion in the vicinity of the pickets (Bussell, Koch and Hammer, 1995). Other studies support the Picket model and found that other

lipids as well as GPI-anchored proteins also exhibit hop diffusion (Umemura *et al.*, 2008; Day and Kenworthy, 2012; Clausen and Lagerholm, 2013; Hiramoto-Yamaki *et al.*, 2014; Andrade *et al.*, 2015; Albrecht *et al.*, 2016). Electron tomography of the plasma membrane showed that the actin meshwork close to the plasma membrane (≤ 0.8 nm) matches in size with the confinement sizes detected by SPT for one cell type while the sizes differ between different cell types (Morone *et al.*, 2006; Fujiwara *et al.*, 2016). Anchorage of picket proteins to the cortical cytoskeleton is even thought to resist large-scale lipid flow and propagation of membrane tension (Shi *et al.*, 2018; Cohen and Shi, 2020).

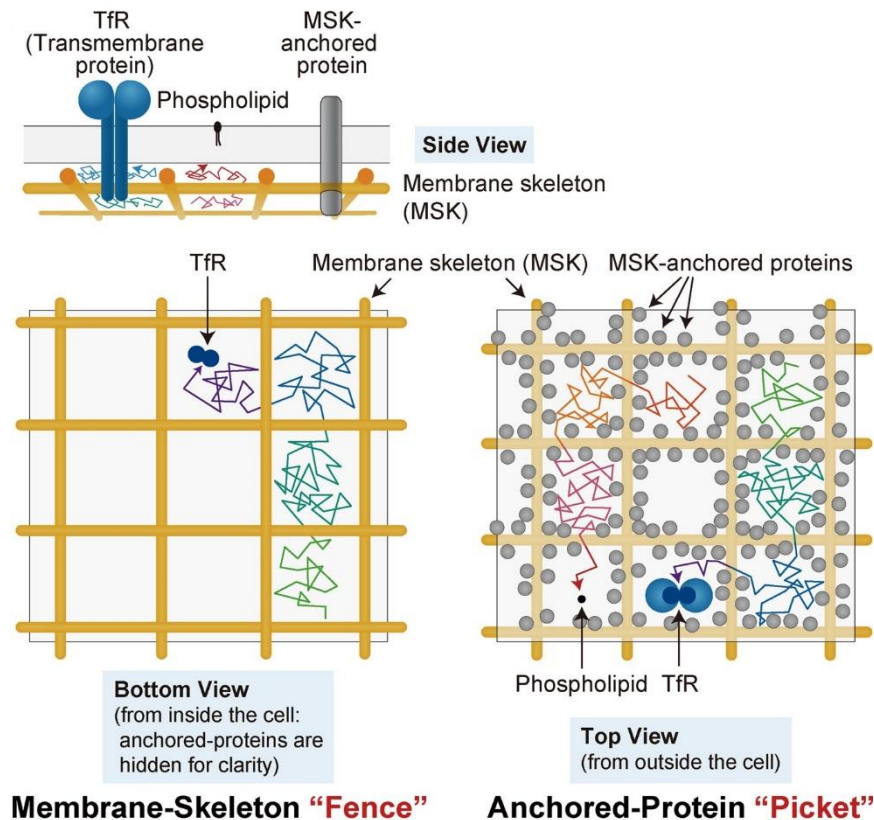


Figure 3: Picket and Fence models

In the Fence model (left), the movement of transmembrane proteins such as the transferrin receptor (Tfr) is restricted due to collisions of the cytoplasmic tail with the membrane-apposed cytoskeleton. The protein occasionally hops to the neighboring compartment if the distance between the cytoskeletal mesh and the membrane permits or through gaps created by dynamic rearrangement of the cortex. The Picket model (right) extends the concept of cytoskeletal compartmentalization to both phospholipids and transmembrane proteins through the action of other transmembrane proteins that associate with their cytoplasmic domains to the cytoskeleton. The immobilized pickets present a barrier in the lipid plane of the membrane. The effect of the pickets is possibly enhanced by the hydrodynamic friction-like effect (Kusumi *et al.*, 2012). Figure reproduced from (Fujiwara *et al.*, 2016) under CC BY-NC-SA 3.0 license.

Although the Picket and Fence models are widely accepted, the methodology has been criticized. Major evidence was collected by tracking single nanoparticles (SPT) which have been attached to the molecule of interest by antibodies. These 20-40 nm sized gold nanoparticles or Quantum Dots (QDs) enable extremely fast tracking with 25 μ s frame rate, and only at this speed the hop diffusion of lipids becomes visible (see also 2.3) (Fujiwara *et al.*, 2002; Clausen and Lagerholm, 2013; Hiramoto-Yamaki

et al., 2014). But since the stoichiometry between nanoparticles and antibodies cannot be precisely controlled, they could introduce crosslinking and thus unintended oligomerization of the target molecule as well as other sized-related effects (see 2.3.2). This argument could be partially resolved with the development of Stimulated Emission Depletion (STED)-FCS, which allows the detection of compartmentalization at similar size scales using small organic dyes (Honigmann *et al.*, 2014; Andrade *et al.*, 2015; Schneider *et al.*, 2017). Another discussion revolves around the analysis of the SPT data, for example whether the localization error has been addressed adequately (see 2.3.3) (Martin, Forstner and Käs, 2002; Berglund, 2010; Michalet, 2010; Michalet and Berglund, 2012). Although not contradicting the Picket and Fence models, it has been criticized that apart from the target molecule, the other components appear to be static in the model, and that the dynamic remodeling of the membrane, cytoskeleton, and pickets is neglected. Others view the cytoskeleton as active regulators rather than as passive barriers which organize the location and movements of membrane molecule under energy consumption (Goswami *et al.*, 2008; Gowrishankar *et al.*, 2012; Rao and Mayor, 2014; Liu *et al.*, 2017). Additionally, irregularities in membrane topography can compromise conclusions from SPT (Adler *et al.*, 2010). Lastly, the molecular identity of the putative pickets was completely unknown until recently when the transmembrane protein CD44 was proposed to act as pickets (Freeman *et al.*, 2018; Sil *et al.*, 2020). However, in most instances, the molecular species of pickets as well as those proteins that anchor them to the cytoskeleton and thus regulate their barrier function remain enigmatic (see also below).

Similar to the intracellular cortical cytoskeleton, the pericellular matrix (the membrane-proximal part of the ECM) could contribute to the compartmentalization of membrane molecule movement. Although this was considered early on (Nicolson, 1976), the effects of the pericellular matrix on lateral diffusion was less investigated, possibly because the Kusumi group found that removal of ECM and of the extracellular domains of transmembrane proteins hardly affected hop diffusion (Fujiwara *et al.*, 2002). Other groups however came to different conclusions and suggested a viscous drag effect of the pericellular matrix (Lee *et al.*, 1993). Recent studies support the idea that the picket protein CD44 could interact with both the ECM and the cytoskeleton (Freeman *et al.*, 2018; Sil *et al.*, 2020). These studies also consider the lateral diffusion of the picket itself as it binds and unbinds from the cytoskeleton or ECM. The pericellular matrix can also organize the distribution of glycosylated proteins via specific interactions (see 1.3.2) (Liu *et al.*, 2012). The ECM is generally less well characterized than the cytoskeleton, owing to its highly amorphous structure and substantial heterogeneity between different cell and tissue types, although advances have been made recently (Letschert *et al.*, 2014; Möckl *et al.*, 2019; Son *et al.*, 2020).

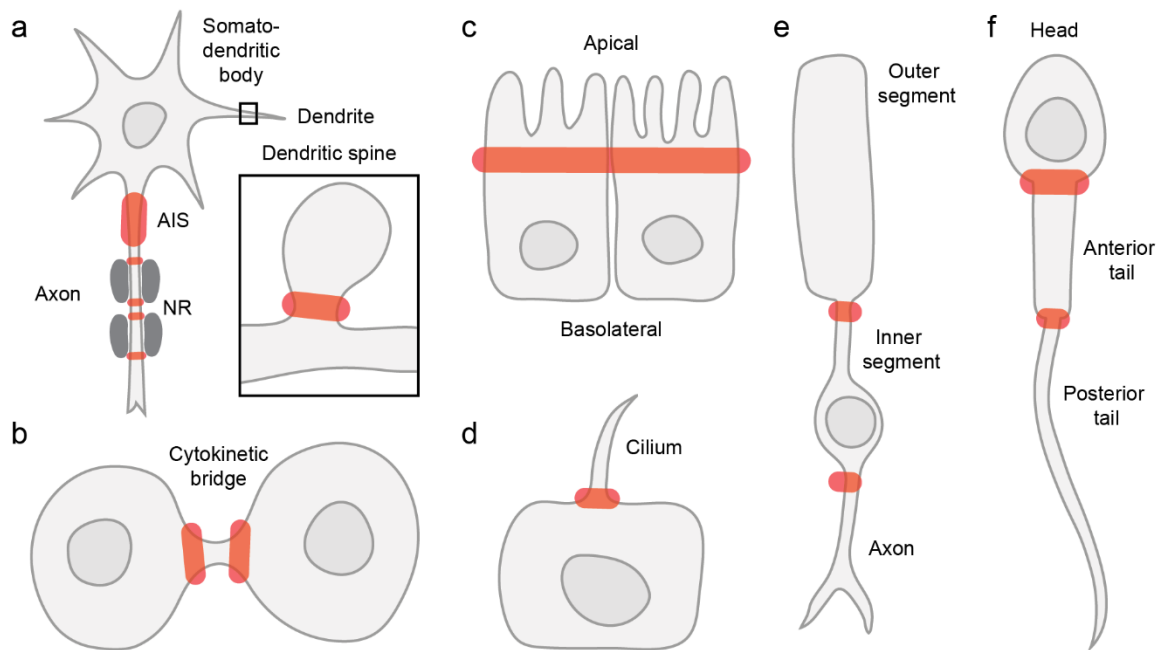


Figure 4: Examples of macroscopic barriers in the plasma membrane

a) Neurons are highly polarized cells with several specialized domains in the plasma membrane. A diffusion barrier in the axon initial segment (AIS), the first 50-150 μm of the axon, separates the axon from the somatodendritic body to maintain the composition and function these domains. (Winckler, Forscher and Mellman, 1999; Nakada *et al.*, 2003; Albrecht *et al.*, 2016). At the nodes of Ranvier (NR) in myelinated axons, the movement of proteins between neighboring myelin segments is restricted by diffusion barriers at the paranodal junctions, which ensures saltatory conduction (Rios *et al.*, 2003; Bekku *et al.*, 2010). Inset: A diffusion barrier at the neck of dendritic spines maintains specific receptors in the spine (Ashby *et al.*, 2006). **b)** During cytokinesis, a diffusion barrier is formed separating the membranes of the resulting cells (Schmidt and Nichols, 2004). This is particularly important for asymmetrically dividing cells such as budding yeast where specific membrane components are differentially sorted to the mother vs. daughter cell (Dobbelaere and Barral, 2004), but the diffusion barrier is conserved throughout the animal and fungi kingdoms. **c)** Tight and adherens junctions form a diffusion barrier in epithelial, thereby segregating the functionally distinct basolateral and apical plasma membranes (Matter and Balda, 2003; Zihni *et al.*, 2016). **d)** The primary cilium contains a diffusion barrier at its base to enrich certain signaling proteins (Vieira *et al.*, 2006; Hu *et al.*, 2010; Lee *et al.*, 2018). **e)** A special case of the cilium is the outer segment of photoreceptor cells which facilitates photoreception. Additionally, there is a barrier separating the inner segment with the soma from the axon, similar to a). **f)** Spermatozoa are segmented in several zones between the head and the tail, and at the annulus between anterior and posterior tail (Ihara *et al.*, 2005; Kwitny, Klaus and Hunnicutt, 2010). The annulus, a septin-based structure, develops dynamically over the course of spermiogenesis and establishment of this diffusion barrier is required for the motility of spermatozoa. **a-f)** The barriers are highlighted in red. Not drawn to scale. (Caudron and Barral, 2009; Kusumi *et al.*, 2012)

The Picket and Fence models provide a hierarchical view of the organization of the plasma membrane. At nanoscopic scales of 2-40 nm, the membrane molecules diffuse much like originally proposed in the Fluid Mosaic model (see 1.2) (Singer and Nicolson, 1972; Saffman and Delbrück, 1975). At 40-250 nm (depending on the cell type), the movement is dominated by confinement within compartments, and at larger scales, the motion is characterized by the long-term hop-diffusion between compartments. This nanoscopic compartmentalization is hypothesized to give rise to large-scale diffusion barriers that segregate functional membrane domains (Figure 4) (Caudron and Barral, 2009; Kusumi *et al.*, 2012). Polarized cells such as neurons or epithelial cells require diffusion barriers to maintain the physiological composition of their plasma membrane in different parts of the cell

(Figure 4a, c). Also, in (asymmetric) cell division, a diffusion barrier has to be established to sort the membrane components accordingly to the daughter cells (Figure 4b). However, how exactly these diffusion barriers are organized, and which molecular species constitute these barriers remain understudied questions. In several of the examples shown in Figure 4 (a, b, d, f), septins, a family of cytoskeletal proteins, are involved in the formation of the barrier, but the supramolecular assembly and the interactions with the membrane and other adaptor proteins is poorly understood. Even in cases where the organization of the cytoskeletal component seems resolved, many questions remain. This is the case for the diffusion barrier found in the axon initial segment (AIS) of neurons. It is required to maintain the distinct composition of the somatodendritic membrane domain *vs.* the axonal domain (Figure 4a) (Kobayashi *et al.*, 1992; Winckler, Forscher and Mellman, 1999; Nakada *et al.*, 2003; Albrecht *et al.*, 2016). The neural cytoskeleton has a special periodic arrangement of actin filaments (“rings”) in a regular spacing of ~190 nm with spectrin interlaced between the actin rings (Xu, Zhong and Zhuang, 2013; Hauser *et al.*, 2018; Vassilopoulos *et al.*, 2019). In the AIS, large transmembrane channels are anchored to spectrin by the AIS-specific protein AnkyrinG. In a previous study conducted in our laboratory, Albrecht *et al.* demonstrated that the trajectories of GPI-anchored GFP (GFP-GPI) tracked with QDs correlate with spectrin but anticorrelate with actin (Albrecht, 2016; Albrecht *et al.*, 2016). Although these findings support the Picket and Fence model, it remained unclear whether the GFP-GPI experienced a barrier through the actin (possibly via an unknown associated picket) or whether it was trapped between the anchored channels which potentially acted as pickets. Therefore, additional studies with other methods that are capable of distinguishing between these possibilities are required.

1.3.2. Specific interactions

If not by physical barriers, the movement of membrane molecules could be limited by different molecular interactions. Lipid-lipid and lipid-protein interactions may contribute to their mobility. Lipids are distributed asymmetrically between the two leaflets of the plasma membrane and also laterally (Sezgin *et al.*, 2017; Lorent *et al.*, 2020). Depending on temperature and lipid composition, lipid bilayers can adopt a liquid-ordered or a liquid-disordered or even gel phase. Since biological membranes have a mixed composition of thousands of lipid and protein species, no sharp phase transitions are observed (Cox and Nelson, 2008; Schuhmacher *et al.*, 2020). However, in the lipid raft theory, it is thought that certain lipid species partition into nanodomains in the membrane according to their preference to reside in the liquid-ordered or -disordered phase at physiological temperatures (Lingwood and Simons, 2010). Cholesterol, which is enriched in these nanodomains, plays a major role in this context, as the distribution and mobility of many membrane molecules has been shown to be cholesterol-dependent (Nishimura *et al.*, 2006; Ma *et al.*, 2007; Saka *et al.*, 2014). Enrichment of certain lipid species in nanodomains may also be enhanced by interactions with the cytoskeleton

(Mueller *et al.*, 2011; Raghupathy *et al.*, 2015). Integral membrane proteins can also sort into these nanodomains or are excluded depending on the physico-chemical properties of their membrane-inserted moiety (Lingwood and Simons, 2010; Sezgin *et al.*, 2017). Due to technical advances in the recent years, it has become clear that lipid nanodomains are only relatively short lived and act only over a few nanometers but may still contribute to the lateral mobility of membrane lipids and proteins and thus regulate signal transduction (Pike, 2006; Eggeling *et al.*, 2009).

Highly specific interactions between certain species of membrane constituents can also affect the lateral mobility. Oligomerization-dependent trapping has been shown to reduce diffusion of the GPI-anchored CD59 and transmembrane proteins E-cadherin and Fc ϵ RI receptor (Iino, Koyama and Kusumi, 2001; Andrews *et al.*, 2008; Suzuki *et al.*, 2012). The slowed diffusion is less due to the increased diameter in the membrane-spanning part (see 1.2) (Saffman and Delbrück, 1975) but because the oligomers are more prone to interact with the cytoskeleton or other cellular assemblies. Many proteins oligomerize or form clusters on the surface of the membrane, which is particularly relevant for receptor signaling (Kamboj and Haganir, 1998; Garcia-Parajo *et al.*, 2014; Saka *et al.*, 2014; Magenau *et al.*, 2015; Zhou and Hancock, 2015; Dustin and Choudhuri, 2016). Furthermore, specific interactions with the cytoskeleton, ECM components, focal adhesions, recruitment by endocytic machineries (clathrin- or caveolin-mediated or other mechanisms like macropinocytosis) or internal organelles such as mitochondria or the endoplasmic reticulum (ER) can modulate the movement of membrane molecules (Lebiedzinska *et al.*, 2009; Liu *et al.*, 2012; Rossier *et al.*, 2012; Poteser *et al.*, 2016; Hsieh *et al.*, 2017; Szymański *et al.*, 2017; Sil *et al.*, 2020). For example, the transmembrane receptor CD36 exhibits diffusion along microtubules in macrophages and the confinement is thought to enhance the clustering-dependent signaling activity (Jaqaman *et al.*, 2011). The C-type lectin transmembrane receptor DC-SIGN is even actively transported through transmembrane interaction with the microtubule cytoskeleton (Liu *et al.*, 2017).

Taken together, both strong and weak interactions between all membrane constituents and with structures peripheral to the membrane contribute to the organization of the plasma membrane. The impact on diffusion ranges from transient immobilization to clustering, confined diffusion and directed transport. The importance of each of those interactions has to be reviewed in the light of their specific biological context using appropriate methods to map their location and mobility, and to perturb them in order to understand their working principles.

2. Methods to study membrane molecule location and dynamics

The structure and composition of the plasma membrane can be studied by a plethora of methods including mass spectroscopy, electron microscopy, atomic force microscopy (AFM), nuclear magnetic resonance and many others. To investigate the dynamic location and distribution of molecules in the plasma membrane, the most versatile and commonly used method is fluorescence microscopy (see 2.1). Optical microscopy allows spatial detection across different size scales under conditions compatible with living cells. Fluorescence labeling or tagging confers specificity in molecular identity within complex and crowded environments and enables visualization of the structure of interest with bright signals against a dark background. There is a wealth of optical fluorescence-based microscopy techniques for an experimentalist to choose from. To assess dynamic processes and measure diffusion in the plasma membrane, the microscopy technique must be sufficiently time-resolved. Three methods have been particularly useful to study the plasma membrane and its compartmentalization (see 1.3): fluorescence after photobleaching (FRAP), fluorescence correlation spectroscopy (FCS), and single-particle tracking (SPT). These methods measure the molecule diffusion and thus allow the calculation of descriptive parameters such as diffusion coefficients and immobilized fractions. An important distinction must be made in this regard between ensemble measurements (see 2.2), in which the behavior of a population of molecules is averaged, and single-molecule approaches such as SPT (see 2.3). To map the distribution of membrane molecules and the organization of associated assemblies such as the cytoskeletal cortex, super-resolution imaging can be applied (see 2.4). This relatively new class of optical microscopy methods provide spatial resolution well below the physical limit imposed by the diffraction of light.

2.1. Fluorescence microscopy

Fluorescent materials such as organic dyes, fluorescent proteins or semiconductor nanoparticles (QDs) absorb light in a certain wavelength spectrum (Figure 5b) which excites the electrons in the material to a higher energy state. When the excited electron returns to the ground state, energy is emitted as a photon. Because the irradiated light has less energy than the absorbed light, it is red shifted (longer wavelength; Figure 5b) and can thus be separated from the excitation light through suitable dichroic mirrors and filters in the microscope (Figure 5a). The simplest fluorescence microscope is a widefield setup as shown in Figure 5a. However, because a large volume of the sample is illuminated by the excitation light path, out-of-focus emission light is also collected by the detector, deteriorating the signal-to-noise ratio, and leading to blurred images. The most common methods to spatially limit the illumination (optical sectioning) are confocal and Total Internal Reflection Fluorescence (TIRF) microscopy. In confocal microscopy, the excitation and emission volume is reduced to a spot in the focal plane by placing pinholes in optically conjugate planes in

front of the sample and the detector (Minsky, 1957). The confocal spot is either scanned over the sample (laser scanning confocal microscopy), or an array of pinholes on a spinning disk is used to detect several spots simultaneously (spinning disk confocal microscopy). TIRF relies on the reflection of light at the interface between media with different refractive indices (i.e. between the glass coverslip and the aqueous sample) at high incidence angles, which creates an evanescent wave (Ambrose, 1956; Axelrod, 1981). As the evanescent field decays exponentially from the interface, only ~200 nm into the sample medium is excited, which is ideal to visualize the ventral cell surface with high signal-to-noise ratio. Similarly, a highly inclined and laminated optical sheet (HILO) can be generated at high incidence angle slightly below the TIRF angle to selectively illuminate an optical section of the sample (Tokunaga, Imamoto and Sakata-Sogawa, 2008).

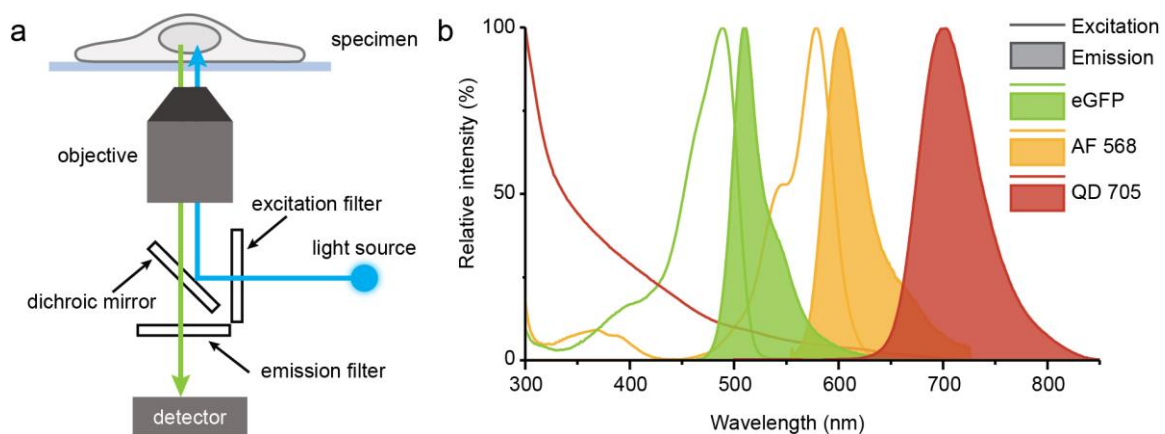


Figure 5: Basics of fluorescence microscopy

a) Setup of a simple inverted fluorescence microscope. The excitation light (blue) is focused on the sample through the objective. The fluorescence light emitted from the sample (green) is collected by the same objective and sent onto the detector (a camera in widefield microscopes). The dichroic mirror reflects the shorter excitation wavelength while transmitting the longer-wavelength emission light, which is further cleaned up through the emission filter for a certain color. The light source is usually provided by several lasers of different colors or an arc lamp, in which case the white light is filtered for the desired color through the excitation filter. **b)** Spectra of three exemplary fluorescent materials of different types. The excitation spectra (solid line) and emission spectra (filled under the curve) of the fluorescent protein enhanced Green Fluorescent Protein (eGFP), the organic dye Alexa Fluor 568 and the Quantum Dot 705. The excitation and emission peaks are well separated which would allow multicolor imaging using (multi) bandpass filters.

Different strategies are employed to label the molecule of interest depending on the type of fluorophore (see also 2.3.2). Organic dyes are available in a wide range of colors and provide bright, relatively photostable fluorescence signal. To deliver them to the molecule of interest, they can be covalently conjugated to lipids, proteins, DNA, ligands, and other organic substrates. Dyes are often conjugated to antibodies, nanobodies or antigen binding fragments (F_{ab}) which bind the target molecules with high specificity. Fluorescent proteins have the major advantage that they can be genetically encoded as fusion proteins to the protein of interest. Live-cell imaging is straightforward in this case and if stably expressed, no additional labeling is required prior to imaging. The fluorescent fusion protein can be overexpressed or expressed at endogenous level using genome

editing (e.g. CRISPR/Cas9). Plasmid libraries of fluorescent protein fusion constructs and clone libraries of some species like *Saccharomyces cerevisiae* make the use of fluorescent proteins even more convenient. GFP was the first fluorescent protein to be discovered in the jellyfish *Aequorea victoria* and is by far the most used one to date. The Nobel prize in Chemistry in 2008 was awarded to Osamu Shimomura, Martin Chalfie and Roger Y. Tsien for its discovery and development. Fluorescent proteins of other colors were engineered from GFP, e.g. the yellow fluorescent protein (YFP), or discovered later in other organisms, e.g. the red fluorescent protein (RFP).

2.2. Ensemble methods

FRAP and FCS have been extensively used to observe dynamic processes in biological systems. Developed in the 1970s, FRAP has mainly been used to study the mobility of lipids and proteins in artificial and cellular membranes (Axelrod *et al.*, 1976; Edidin, Zagyansky and Lardner, 1976; Reits and Neefjes, 2001). Practically, an area on a membrane containing the fluorescently labeled target molecule is photobleached. The fluorescence is recovered due to diffusion of bleached molecules out of the bleached area and of surrounding fluorescent molecules into the area. The curve of the fluorescence intensity over time in the bleached area, corrected for overall bleaching and background, can then be fitted with diffusion models to obtain the mobility of the target molecule and the fractions of mobile and immobile molecules.

FCS is based on the spatially limited illumination volume of the sample by a confocal or two-photon microscope (Fahey *et al.*, 1977; Schwille, Korlach and Webb, 1999; Diaspro *et al.*, 2001). If the density of fluorescently labeled molecules is sparse enough, the passage of single fluorophores through the confocal spot can be detected as fluctuations in the fluorescence intensity. Autocorrelation analysis of the intensity time traces yields the average concentration of molecules and the diffusion time in the confocal spot, from which the diffusion coefficient or the oligomeric state can be calculated. Furthermore, by cross-correlation between two fluorescently labeled species in two different colors, co-localization/co-locomotion can be demonstrated. Another related method is image correlation spectroscopy which uses the individual pixels of the image over time instead of a confocal spot (Petersen *et al.*, 1993; Hebert, Costantino and Wiseman, 2005; Di Rienzo *et al.*, 2013).

Both FRAP and FCS are ensemble methods, as they measure statistical parameters of a population of molecules. Although FCS detects single molecules, meaningful values can only be derived through autocorrelation analysis of a large number of single-molecule detections. Additionally, the spatial resolution is limited by the diffraction of light (for FRAP, usually much larger regions are selected for bleaching), therefore, nanoscale heterogeneities in the mobility of membrane molecules and very fast interactions cannot be resolved. An exception here is the combination of FCS with stimulated

emission depletion (STED) (Eggeling *et al.*, 2009) or optical nano-antennas (Winkler *et al.*, 2018), which allow significantly smaller illumination volumes.

2.3. Single-molecule or -particle tracking

In contrast to ensemble methods, SPT follows the movement of individual molecules or particles over time (Figure 6). Therefore, information on subpopulations can be obtained and rare but statistically and functionally relevant events can be observed. In principle, the tracked objects can be of any size, from single molecules, nano- or microparticles, to even whole cells. Here, I will focus on the subcellular tracking of membrane molecules using optical microscopy.

2.3.1. Principle and general considerations

The biomolecule to be tracked is labeled with a fluorescent or non-fluorescent (scattering-based) reporter (see 2.3.2) and a time stack of microscopy images is recorded (Figure 6a). The optical instrumentation for SPT requires a high numerical aperture (NA) objective and a sensitive camera with low noise (modern Electron Multiplying Charge-Coupled Device (EMCCD) or scientific Complementary Metal-Oxide-Semiconductor (sCMOS) cameras). From the recorded time stack, the localizations of the particles are determined in every single image and then connected between frames to reconstruct the trajectory of the particle (Figure 6a). In each frame of the time stack, the particles appear as diffraction-limited spots. A principal limit in spatial resolution is given by the Abbe formula

$$d = \frac{\lambda}{2n \sin \theta} = \frac{\lambda}{2NA}, \quad (4)$$

where d is the distance between two objects that can still be resolved, λ is the wavelength of the light, n is the refractive index, and θ the opening angle of the objective. The image of a point-like emitter formed by an optical microscope, the point spread function (PSF), thus depends on the fluorescence emission wavelength and numerical aperture of the objective, and its full width at half maximum (FWHM) is approximately d . If the fluorescent particles are sufficiently spaced apart, the center position of the particle in each frame can be localized with sub-diffraction precision by fitting the intensity profile of the spots with a Gaussian or an experimentally measured PSF. The intensity of the spot, however, is given by the number of collected photons and the localization error is inversely proportional to the square root of the number of photons (in the photon noise-limited case; in the background-limited case, it is inversely proportional to the number of photons) (Thompson, Larson and Webb, 2002; Ober, Ram and Ward, 2004). If 3D SPT is performed by astigmatism or biplane imaging (z-stacking is unsuitable as it is too slow), a 3D PSF is used for localization.

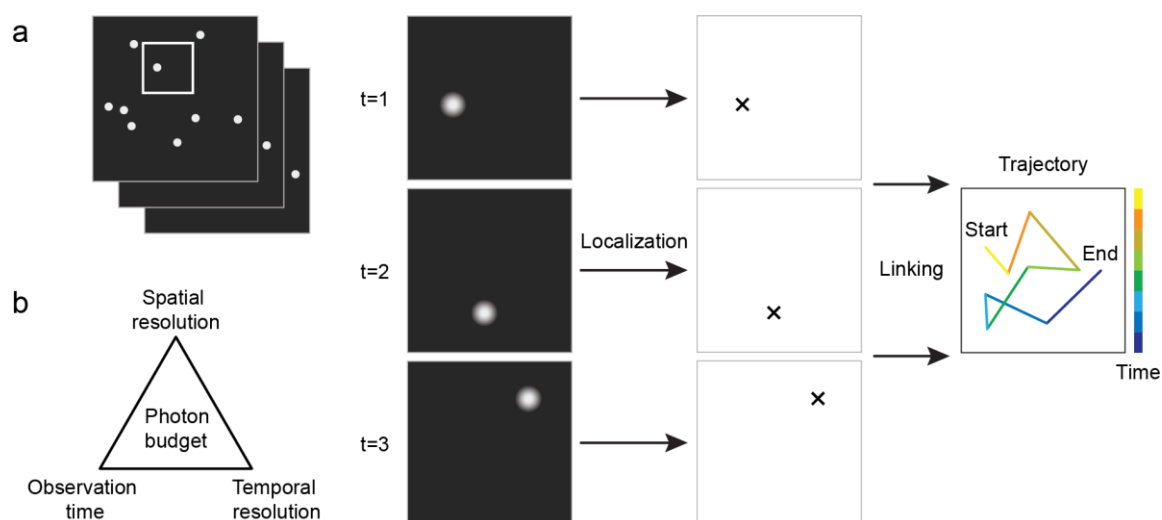


Figure 6: Principle of single-particle tracking

a) A time sequence of images of sparse, fluorescent particles is recorded. In each frame, the centroid position of the fluorescent spots is determined (localization). The localized particles are then connected frame by frame (linking) to obtain the trajectory. **b)** The spatial localization precision, the temporal resolution and the observation time (average track length) are coupled to the number of photons emitted by the fluorophore.

In the second step, the localizations are linked from frame to frame based on the nearest neighbor or another distance-related criterion (within a certain search radius) (Figure 6a). Although most tracking algorithms follow this order (first localization, then particle linking), it is also possible to perform both steps iteratively or simultaneously (e.g. the spots are first detected with pixel-size resolution, then linked, and lastly, the localizations are refined to sub-pixel resolution). The principle of SPT inherently imposes the requirement of a low density of particles to be tracked, which is given if the target is a very low-abundant molecule (Richter *et al.*, 2017; Wilmes *et al.*, 2020), but in the majority of cases, a sparse labelling is used such that only a subpopulation is observed at a time. Too dense labeling affects both localization and linking. At very high densities, the PSFs can overlap such that two particles are wrongly detected as one or multi-emitter localization algorithms are required to distinguish them. At only slightly lower densities, the linking process can still be ambiguous due to particles crossing each other's path. In addition to technical challenges such as background noise, blinking or missed localizations, density issues can lead to fragmentation of longer trajectories or mis-linking trajectories of different particles.

There is a fundamental trade-off between spatial and temporal resolution (Figure 6b) because the number of photons emitted by the fluorescent label per unit time and before photobleaching is limited (non-fluorescent methods do not suffer from this but have other limitations, see 2.3.2) (Ortega-Arroyo and Kukura, 2012). The number of photons depends on the photophysical properties of the fluorophore and the intensity of excitation. The length of trajectories is immediately limited by bleaching. To prolong the observation time of a single fluorophore before bleaching, the intensity of

the excitation light can be reduced. However, if the number of photons collected per frame is reduced, the spatial precision is compromised due to the inversely proportional relationship with the localization error. The number of photons collected for one image depends also on the frame rate (camera integration time), therefore, the localization precision is better with longer integration times per frame (i.e. low sampling rate). But long exposure times suffer from motion blur, as the particles continuously move during the camera integration time (Berglund, 2010; Frost *et al.*, 2012; Izeddin *et al.*, 2014). Therefore, the optimal sampling rate depends also on the mobility of the diffusing particle. To reduce motion blur, stroboscopic (pulsed) illumination can be implemented such that the molecules are excited in a shorter time than the time interval between consecutive frames (Wieser and Schütz, 2008; Frost *et al.*, 2012; Albrecht, Winterflood and Ewers, 2015; Hansen *et al.*, 2018; Yan, Chen and Xu, 2020).

2.3.2. Labels

The choice of the label used for SPT is crucial as it determines the accessible temporal and spatial regimes (Cognet, Leduc and Lounis, 2014; Manzo and Garcia-Parajo, 2015). A basic distinction must be made between fluorescence- and scattering-based methods. The latter was used when SPT was first invented by De Brabander *et al.* in the 1980s, and the method was then called “Nanovid Microscopy” (Geerts *et al.*, 1987; De Brabander *et al.*, 1988). In these original works, colloidal gold particles of 40 nm diameter (Figure 7) were visualized with differential interference contrast (DIC) microscopy and allowed for the first time to track cellular components with nanometer precision. Larger latex, silica or polystyrene beads can also be used, and dark-field microscopy have been employed to reduce background scattering. Later bright-field implementations achieved time resolutions of down to 25 μ s (40,000 Hz) with \sim 20 nm spatial precision (Fujiwara *et al.*, 2002, 2016). A relatively new variation is interferometric scattering (iSCAT) microscopy, which uses the reflected signal at the glass/water interface and thereby enables detection of smaller nanoparticles down to 5 nm. With 20-40 nm sized gold particles, 2-6 nm localization precisions at temporal resolutions of \sim 20 μ s were accomplished for the tracking of lipids in SLBs and of EGF receptors on the cell surface (Spillane *et al.*, 2014; Taylor *et al.*, 2019). The main advantage of these scattering-based approaches is that the observation time is in principle unlimited since the particles do not bleach. The spatiotemporal resolution is only limited by background scattering and phototoxicity at high illumination powers. However, the gold particles impose the problem of cross-linking since the valency of the bio-functionalization is difficult to control, potentially leading to unintended signaling activation or recruitment of cytoskeleton and endocytic activity (Saxton and Jacobson, 1997; Clausen and Lagerholm, 2011). Additionally, the mobility and the activity of the target molecules could be affected by the large size of the probe (Abraham *et al.*, 2017).

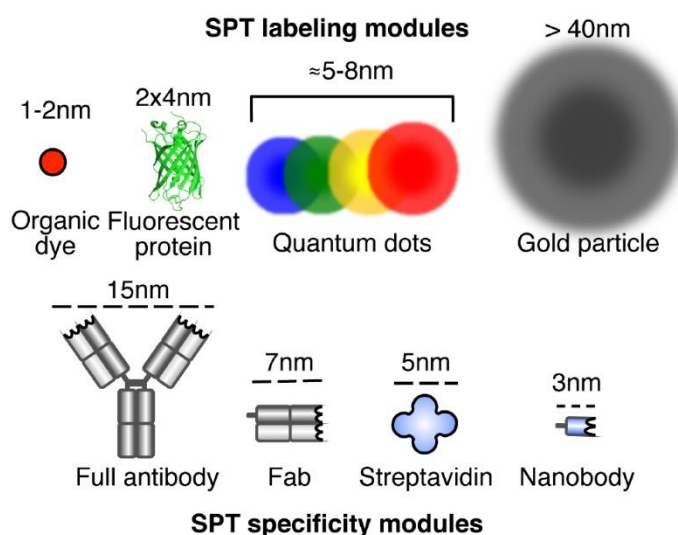


Figure 7: Overview of common probes for single-particle tracking

The labeling modules which are detected by fluorescence- or scattering-based microscopy can be delivered to the molecule of interest through different specificity modules (Clausen and Lagerholm, 2011). Of the fluorescent labels, organic dyes are the smallest followed by fluorescent proteins. QDs have a core diameter of <10 nm, however, for colloidal stability and bio-functionalization, they are coated such that the effective size is 10-30 nm. For scattering based SPT, gold nanoparticles are used. The standard size is 40 nm in diameter, although studies in the recent years have used 20 nm. The specificity modules can be IgG antibodies, including monovalent variations hereof (F_{ab} fragments and nanobodies) as well as other specific binding systems such as biotin/streptavidin or Halo/HaloTag or SNAP/benzylguanine (not shown). Not drawn to scale. Adapted from (Manzo and Garcia-Parajo, 2015) with permission.

With the advent of fluorescence microscopy, fluorescent dyes or proteins could be used for tracking instead of colloidal particles (single-molecule tracking; SMT) (Figure 7). Single organic dyes are the smallest among the SPT probes and potentially suffer least from size-related effects. However, especially for SPT on membranes, the dye should be selected with care as some dyes are prone to unspecific binding (Zanetti-Domingues *et al.*, 2013). The track length is usually only a few seconds long at best, with 20-50 nm localization precisions at tens of milliseconds camera integration time (Alcor, Gouzer and Triller, 2009; Cognet, Leduc and Lounis, 2014; Manzo and Garcia-Parajo, 2015). Under reduced oxygen conditions and addition of reducing-plus-oxidizing system (ROXS) reagents, fluorescent dye-based SMT can be optimized such that single dyes can be tracked for minutes (at video rate and ~20 nm localization precision) (Aitken, Marshall and Puglisi, 2008; Tsunoyama *et al.*, 2018). Like nanoparticles, organic dyes also require a specificity module to bind the molecule of interest (Figure 7). Multivalent specificity modules such as IgG antibodies or streptavidin may induce unwanted dimerization or oligomerization of the target molecules and therefore, monovalent specificity modules are more desirable (e.g. F_{ab} fragments, nanobodies, or monovalent streptavidin; Figure 7) (Howarth *et al.*, 2006; Helppolainen *et al.*, 2007; Clausen and Lagerholm, 2011; Ries *et al.*, 2012).

Fluorescent proteins have the advantage that they can be genetically encoded as fusion to the protein of interest (see also 2.1). The stoichiometry of the label and the target is then fixed. The major

disadvantages of fluorescent proteins are the low quantum yield and photostability, which usually only allow tracking of relatively slow-moving particles with poor localization accuracies and short track lengths (Alcor, Gouzer and Triller, 2009; Cognet, Leduc and Lounis, 2014; Manzo and Garcia-Parajo, 2015). Additionally, sparse labeling is difficult to achieve with standard protein expression strategies (unless tagging an endogenously low-expressing target by genomic editing). The fluorescent protein itself can also be targeted with an organic dye, e.g. by a dye-labeled anti-GFP nanobody (Albrecht, Winterflood and Ewers, 2015) which is then used for SPT instead of the dim fluorescent protein. Another alternative offers sptPALM (Manley *et al.*, 2008), the SPT adaptation of the super-resolution technique Photoactivated Localization Microscopy (PALM; see also 2.4). Here, only a subset of photo-activatable proteins fused to the target protein is activated at a time and tracked until bleaching. This can be repeated in principle until all photoactivatable proteins have been bleached and therefore affords large statistics, albeit still with the short individual track length and poor localization precision fluorescent proteins afford. Similarly, the principle of point accumulation for imaging in nanoscale topography (PAINT) can be used for SPT (universal PAINT, uPAINT) (Giannone *et al.*, 2010). It is based on the continuous and stochastic binding of the fluorescent label to the target molecules in the plasma membrane from the surrounding medium. The movement of the unbound probes in solution is blurred out with 50 ms integration time and hence not detected by the tracking algorithm which inherently requires a small, quickly diffusing fluorescent probe. To reduce background fluorescence from the fluorescent probes in solution, optical sectioning is required by TIRF or HILO illumination. The labeling density can be conveniently tuned with the concentration of the fluorescent binder in solution and the track length and localization precision benefits from the use of organic dyes compared to fluorescent proteins. Generally, methods that yield short track lengths are less suited for low-abundance targets because the bleached molecules are lost, and individual molecules cannot be followed long enough to observe transient changes in their behavior.

Relatively long trajectories (tens of minutes) can be recorded with QDs due to their excellent optical properties which allow SPT at a localization precision of 10-15 nm (Dahan *et al.*, 2003; Pinaud *et al.*, 2010; Albrecht *et al.*, 2016). One drawback of QDs in terms of optical properties is the random intermittency of emission (blinking) (Nirmal *et al.*, 1996; Kuno *et al.*, 2000), which requires the tracking algorithm to close localization gaps (i.e. to link over several frames). It should be mentioned here that the issue of blinking is also common for fluorescent dyes and proteins but can be tuned by the choice of the fluorophore and imaging conditions such as the laser intensity (*cf.* 2.4.1) (Garcia-Parajo *et al.*, 2000; Aitken, Marshall and Puglisi, 2008). Furthermore, the concerns about valency and size for the gold nanoparticles apply to QDs as well (see above) and persist despite of technical improvements in this respect (Howarth *et al.*, 2008; Pinaud *et al.*, 2010; Abraham *et al.*, 2017; Zahid *et al.*, 2018).

2.3.3. Diffusion coefficient and other analyses

The outputs of the tracking algorithm are trajectories with xy positions of each particle at each time point (or xyz, if 3D SPT). These trajectories are further analyzed to retrieve dynamic information on the molecule of interest. Usually, the aim is to determine the type of motion and the diffusion coefficient. The most common way to calculate the diffusion coefficient is the mean square displacement (MSD) analysis (Qian, Sheetz and Elson, 1991). The MSD is a measure of the area that is explored by the particle for a certain time lag $t_{lag}=n\Delta t$, where the Δt is the time interval between frames $n = (1, 2, 3, \dots, N)$ for a trajectory of length N . The squared displacements r^2 between localizations of a given time lag $n\Delta t$ are averaged and plotted as a function of the time lag.

$$MSD = \langle (r(n\Delta t))^2 \rangle = \frac{1}{N-n} \sum_{i=1}^{N-n} (r_{i,i+n}(n\Delta t))^2. \quad (5)$$

For simple Brownian diffusion in which the particle undergoes a random walk, the MSD *vs.* time lag plot yields a linear curve and the slope of the curve relates to the diffusion coefficient D (derived from the Einstein relation in Eq. (1)).

$$MSD(t_{lag}) = 4Dt_{lag}. \quad (6)$$

The factor 4 is given by the dimensionality (e.g. 6 for 3D SPT). At large t_{lag} approaching $N\Delta t$, there are only few datapoints to average and hence the curve becomes noisy. Therefore, only a portion of the whole MSD curve is usually taken for linear fitting. The diffusion of many biological molecules has been found to be anomalous, i.e. showing a non-linear MSD with time lag (Saxton and Jacobson, 1997; Schütz, Schindler and Schmidt, 1997; Ferrari, Manfroi and Young, 2001; Metzler *et al.*, 2014). The type of anomalous diffusion can be described by a power law:

$$MSD(t_{lag}) = 4Dt_{lag}^\alpha, \quad (7)$$

where α is the so-called anomalous exponent. If $\alpha > 1$, the diffusion is in the super-diffusive regime, and for $\alpha < 1$ it is in the sub-diffusive regime. A type of motion in the super-diffusive regime is observed for particles that are actively transported (Saxton and Jacobson, 1997):

$$MSD(t_{lag}) = 4Dt_{lag} + (vt_{lag})^2. \quad (8)$$

This directed motion consists of a term for random diffusion and a term for ballistic movement characterized by the velocity v . Another important type of motion in the sub-diffusive regime is confined diffusion such as for membrane molecules in the Picket and Fence model (see 1.3.1) (Kusumi *et al.*, 2005, 2012). In this case, the MSD initially increases linearly with small lag times when the

particle is moving well within the compartment but reaches a plateau at larger lag times due to the restrictions imposed by the boundaries of the compartment. From the MSD value at which the plateau is reached, the characteristic linear length L of the compartment can be calculated (Kusumi, Sako and Yamamoto, 1993; Destainville and Salomé, 2006). However, a steady plateau is only reached if the barrier at the sides of the compartments is impermeable. Instead, if the particle can stochastically cross the compartment boundary to the next one, i.e. when undergoing hop diffusion, the MSD increases linearly again for larger t_{lag} . Therefore, a microscopic and macroscopic diffusion coefficient can be calculated (Sako and Kusumi, 1994). The short-range (also called instantaneous) diffusion coefficient D_{micro} describes the unhindered diffusion within a compartment, while the long-range diffusion coefficient D_{MACRO} describes the movement at much larger time scales than the average residency time in one compartment and thus reflects the diffusion across compartments or other heterogeneities in the membrane. D_{micro} is often calculated as D_{2-4} for which only the MSD at the time lags $n\Delta t$, $n = (2, 3, 4)$ is considered. This is only possible if the sampling rate is high enough such that the time interval Δt is significantly smaller than the residence time (depending on the size of the compartments and the free diffusion coefficient of the membrane molecule) which is often not accessible through fluorescence-based microscopy (Fujiwara *et al.*, 2016).

A difficulty in SPT analysis is the finite localization precision, which biases the MSD analysis and causes an offset in the MSD curve (Saxton and Jacobson, 1997; Martin, Forstner and Käs, 2002; Berglund, 2010; Michalet, 2010; Michalet and Berglund, 2012). This uncertainty can be overcome by improving the statistics, either through longer trajectories (e.g. by using QD or scattering particles) such that the MSD can be averaged over more steps, or by averaging over the ensemble. In the latter case, information on individual molecules becomes inaccessible but subpopulations with distinct diffusion modes can still be extracted by globally fitting the distribution of step sizes with a mixed model (Schütz, Schindler and Schmidt, 1997; Hansen *et al.*, 2018).

The anomalous exponent α is determined from the MSD $\langle r^2 \rangle$ which is the second moment of the particle displacements r (Eq. (6)). However, it is possible to generalize this to other orders p of the displacement moments (Ferrari, Manfroi and Young, 2001):

$$\langle r^p \rangle \sim t^{\gamma_p}. \quad (9)$$

The MSD is then the special case of $p = 2$ and $\gamma_p = \alpha$. The plot of γ_p vs. p is called the moment scaling spectrum (MSS) (Ewers *et al.*, 2005) and shows a straight line through the origin because $\gamma_0 = 0$. The slope of the MSS curve can be fitted with smaller errors than the MSD and is thus better suited for the classification of different diffusion modes. The MSS slope is 0.5 for random Brownian motion, >0.5 for super-diffusive motion, <0.5 for sub-diffusive motion and 0 for immobility.

The methods for diffusion mode classification can also be applied to segments of a single long trajectory in order to detect changes in diffusive behavior for a single molecule of interest (Vega *et al.*, 2018; Yin, Song and Yang, 2018). For example, Vega *et al.* uses rolling windows over the trajectories to calculate the MSS slope and to thus classify the movement mode of sub-tracks. Furthermore, there is a wealth of alternative methods to calculate the diffusion coefficient and to detect different modes of motion or spatiotemporal changes hereof using various concepts of statistical physics such as Bayesian inference or Hidden Markov Models (Manzo and Garcia-Parajo, 2015; Slator, Cairo and Burroughs, 2015; Karlake *et al.*, 2020).

2.4. Super-resolution microscopy

Super-resolution microscopy allows to visualize the organization of biological systems at nanoscopic scales using optical microscopy. Before its invention in the mid 2000's, size scales below the diffraction limit of light (Eq. (4), see 2.3.1) were only accessible by electron microscopy. By combining the molecular specificity of fluorescence microscopy with the unprecedented spatial resolution, super-resolution microscopy enabled spectacular discoveries within a short time which has been recognized with the Nobel prize in Chemistry awarded to Eric Betzig, Stefan W. Hell, and William E. Moerner in 2014. In principle, these types of microscopy techniques surpass the diffraction limit by separating the fluorescence signals either in time or in space. The latter case includes stimulated emission depletion (STED) microscopy and structured illumination microscopy (SIM) (Klar and Hell, 1999; Gustafsson, 2000). The former case applies to single-molecule localization techniques such as (direct) stochastic optical reconstruction microscopy ((*d*)STORM), photoactivated localization microscopy (PALM) or different variations of PAINT e.g. DNA-PAINT or image reconstruction by integrating exchangeable single-molecule localization (IRIS) (Betzig *et al.*, 2006; Rust, Bates and Zhuang, 2006; Heilemann *et al.*, 2008; Jungmann *et al.*, 2010; Kiuchi *et al.*, 2015). This group of techniques is also termed single-molecule localization microscopy (SMLM) or single-molecule nanoscopy.

2.4.1. Single-molecule localization microscopy

The principle of SMLM is closely related to SPT. As introduced in 2.3.1, two fluorescently labeled molecules spaced apart at a distance closer than the FWHM of their PSF cannot be distinguished through the microscope. In the visible light spectrum commonly used in fluorescence microscopy, this distance is ~250 nm, which is huge compared to single biomolecules (~1-10 nm) or even macromolecular assemblies (tens of nanometers). But as we have seen for SPT, if the single emitters are sparsely spread out in space, the centroid position of the molecule can be determined with much greater spatial precision. In SMLM, the single emitters are spaced out in time by exploiting the photophysical properties of fluorescent dyes and proteins or binding kinetics (Figure 8). The position

of the single fluorophores in each image is localized with nanometer precision as in SPT (Figure 8b, c). A large number of images (10^4 - 10^6) is recorded such that a super-resolved image can be reconstructed (Figure 8d). Instead of being limited by diffraction, the image resolution now depends on the spatial precision and accuracy of each fluorophore localization (which depends on the number of photons, see 2.3.1), the density of labels and localizations on the target structure, and background through noise or autofluorescence. The precision of position determination can be encoded in the reconstructed image by representing each localization with a Gaussian relative to the intensity of the emitter.

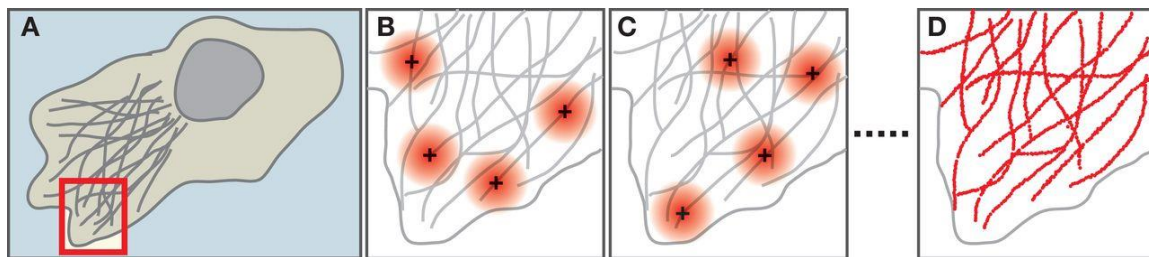


Figure 8: Concept of single-molecule localization microscopy

a) A cell with the structure of interest, e.g. microtubules, shown as grey filaments here. The structure is labeled with photo-switchable fluorophores (*d*STORM or PALM), a DNA binder (DNA-PAINT) or not at all (IRIS). **b)** A subset of fluorophores at a time is activated to the fluorescent state or becomes visible by binding of a fluorescent probe to the DNA binder (DNA-PAINT) or directly to the structure of interest (IRIS). The activated or bound fluorophores must be sparse (large red circles) so that the diffraction-limited spots do not overlap. The position of each fluorophore is determined by fitting to find the centroid of the PSF (black crosses). **c)** In the next image, a different subset of fluorophores is activated or bound, and their positions are localized. **d)** After acquisition of 10^4 - 10^6 images and localization of the single fluorophores, the image is reconstructed from the collected localizations (red dots). Adapted from (Bates, Huang and Zhuang, 2008) with permission.

The super-resolution technique used in this work, *d*STORM, employs photo-switchable organic dyes (Rust, Bates and Zhuang, 2006; Heilemann *et al.*, 2008, 2009). These fluorophores can reversibly transition to a meta-stable triplet state in which they do not fluoresce. By adding thiol-containing reducing agents such as β -mercaptoethanol (BME) or β -mercaptoethylamine (MEA) and an enzymatic oxygen scavenging system (glucose, glucose oxidase and catalase) and by illuminating with high laser intensities, the cycling of the fluorophore through the fluorescent and the non-fluorescent state can be optimized for SMLM (Aitken, Marshall and Puglisi, 2008; Heilemann *et al.*, 2009). Additionally, ultraviolet (UV) light (405 nm) can activate the transition from the dark to the fluorescent state such that the density of fluorescent spots per frame can be tuned by low UV-light exposure. The image resolution, which is different than the localization precision, is usually ~20-40 nm in lateral direction (Heilemann *et al.*, 2009). For 3D imaging, biplane imaging can be used (Jüette *et al.*, 2008), where the image at two slightly different focuses is projected onto the halves of a camera chip or onto two separate cameras. Due to the characteristic shape of the defocused PSF, the z-position can be determined (although the absolute z-position can be ambiguous, either above or

below the focal plane). Alternatively, the shape of the PSF can be altered through a cylindrical lens to generate axial astigmatism or through a phase mask to engineer the shape of a double helix to enable 3D imaging with 50-75 nm axial precision (Kao and Verkman, 1994; Holtzer, Meckel and Schmidt, 2007; Pavani *et al.*, 2009).

The imaging conditions of (*d*)STORM are clearly not suitable for live-cell imaging. In these cases, PALM can be used (Betzig *et al.*, 2006; Hess, Girirajan and Mason, 2006), which is based on photo-activatable fluorescent proteins such as mEos or photoactivatable GFP (PA-GFP) which are initially dark but can be activated by low intensities of UV light. The general advantages and limitations of fluorescent protein (e.g. genetic encoding or low photon yield) apply also to these photo-activatable proteins (*cf.* 2.1 and 2.3.2). While the total number of localizations collected in PALM and (*d*)STORM is ultimately limited by photobleaching, PAINT-based approaches can in principle be performed for an infinite time on a fixed sample (see 2.3.2). While DNA-PAINT relies on the on-/off-binding of complementary short DNA oligos (Jungmann *et al.*, 2010, 2014), other methods generalize the concept of PAINT (Sharonov and Hochstrasser, 2006) to different specific binders with low affinity (high dissociation rate k_{off}) (Giannone *et al.*, 2010; Schoen *et al.*, 2011; Kiuchi *et al.*, 2015). These methods, however, require relatively long exposure times (~100 ms) to localize only the bound fluorophores (while the unbound ones are blurred out due to fast diffusion in the medium) and optical sectioning by TIRF, HILO, or confocal illumination to reduce out-of-focus background (Schueder *et al.*, 2017; Strauss and Jungmann, 2020).

3. Methods to manipulate membrane molecules and their motion

Observation alone already allows the researcher to learn a great deal about living systems. By correlating the observations, hypotheses can be formed, and behaviors predicted. However, only through controlled perturbation of the system is it possible to demonstrate causality. The toolbox to perturb molecular and cellular processes is plentiful. In the plasma membrane, the activity of membrane components and apposed assemblies can be tested in different ways. The molecule of interest could be reduced in abundance or removed entirely, its activity or kinetics could be changed or its subcellular localization and higher order organization.

3.1. (Opto-)Genetic and pharmacologic means

Genetic perturbation by knockdown or knockout is one of the most common approaches to study the function of a given protein. Knockdown by RNA interference (small interfering or short hairpin RNA; si/shRNA) reduces the protein of interest in the cell while knockout by gene editing (e.g. by CRISPR/Cas9) eliminates it completely (Pratt and MacRae, 2009; White *et al.*, 2017). Other than the abundance of a protein, its activity can be modulated by targeted mutagenesis using knock-in or transient (over-)expression approaches. The enzymatic or binding kinetics can be changed, for example by point mutation of the active center or the binding motif. Alteration of posttranslational modifications can affect both the function and localization of the molecule of interest (Cox and Nelson, 2008). For example, a constitutively active version of ezrin, a protein that crosslinks the plasma membrane and the underlying actin cytoskeleton, was generated by targeted mutation of a conserved phosphorylation site and expression of it induces membrane protrusions (Gautreau, Louvard and Arpin, 2000). Protein engineering approaches that remove functional domains from the protein of interest (e.g. truncations) or swap domains between different proteins (fusions) have been employed to understand their function (Edidin, Zúñiga and Sheetz, 1994; Feder *et al.*, 1996; Sako *et al.*, 1998; Gowrishankar *et al.*, 2012; Freeman *et al.*, 2018). For example, truncated versions of transmembrane proteins were engineered to investigate the contribution of the size of the cytoplasmic tail to the lateral mobility. Furthermore, the subcellular location and distribution can be modified by removing or adding signal peptides or binding motifs (Keller *et al.*, 2001).

On the other hand, drugs can also be applied to perturb cellular processes. These small organic molecules usually diffuse through the plasma membrane and can inhibit or modify the activity of a given molecule by binding to them or an upstream effector. To study the influence of the cytoskeleton on the diffusion of membrane molecules, a variety of drugs is available to modify the dynamics of actin or microtubules (Sako and Kusumi, 1995; Lenne *et al.*, 2006; Treanor *et al.*, 2010). For example, Cytochalasin D (CytoD), a fungal toxin, binds the barbed ends of actin filaments and inhibits both polymerization and depolymerization, making it a potent modifier of actin dynamics (Shoji *et al.*,

2012). Fewer drugs are available to affect lipid or glycan function which mostly target their synthetases (Sezgin *et al.*, 2017). Notably, cyclodextrins, a class of cyclic oligosaccharides, is used to remove cholesterol from the plasma membrane, e.g. methyl- β -cyclodextrin (M β CD) (Mahammad and Parmryd, 2015).

Without doubt, genetic and pharmacological perturbation means are powerful tools. The drawback of both approaches is that their effects are rather global. Genetic manipulations provide only poor temporal control as transfection or induction of protein expression take time. Drugs produce faster responses but subcellular control of individual or a subset of molecules is not amenable. Optogenetics is a relatively new technique to overcome these limitations. These tools are derived from light-sensitive proteins, mostly found in plants. By fusing these photo-responsive proteins to the protein of interest, signaling events can be observed and dimerization, oligomerization or dissociation can be actuated using light, harnessing the power of spatially and temporally precise illumination (Tischer and Weiner, 2014; Rost *et al.*, 2017; Zhang *et al.*, 2017). For example, cell membrane dynamics has been altered by optogenetic targeting of Tiam1 (a guanine exchange factor of the small GTPase Rac) and phosphatidylinositol 3,4,5-trisphosphate (PIP₃) signaling (Ueda and Sato, 2018). Despite the subcellular and temporally tight control that optogenetics afford, it is not possible to manipulate single molecules and particularly not to directly steer molecule movement since optogenetic recruitment relies on diffusion or native transport processes.

3.2. Optical tweezers

Optical tweezers, magnetic tweezers and AFM are the most common techniques for single-molecule manipulation (Neuman and Nagy, 2008). Similar to SPT, these methods have the power to detect transient or rare events that would be concealed by population averaging in ensemble methods (*cf.* 2.3). Magnetic tweezers will be introduced in detail later (4.1.2). Although AFM can be used to map the topography of the plasma membrane with high resolution (Frankel *et al.*, 2006; Heinisch *et al.*, 2010; Liu *et al.*, 2019) and to measure the mechanical properties of membranes (Gumí-Audenis *et al.*, 2016), it is less suitable for the manipulation of single molecules in the plasma membrane of living cells.

Optical tweezers make use of a highly focused laser beam to create a diffraction-limited spot, in which dielectric particles are trapped. Near the focus, the particle experiences a restoring force due to the steep gradient of the optical field. Thus, objects can be non-invasively manipulated in solution. Atoms, nanoparticles to whole living cells can be moved or hold in position (Ashkin and Dziedzic, 1987). Optical tweezers can apply forces between 0.1 and 100 pN with laser powers in excess of 10 W. To reduce phototoxicity to biological specimens, near-infrared lasers (800-1100 nm) are used for optical trapping. However, even in this wavelength range, oxygen-mediated photodamage still

occurs. Although biological objects like single cells and organelles inside cells can be trapped directly (from ~20 nm to several micrometers), it is common for single-molecule studies to attach polystyrene or silica microspheres to the molecule of interest. Different approaches have been developed to measure the position of the trapped object. The most sensitive method, back-focal plane interferometry, which measures the asymmetry in the interference profile upon bead displacement, achieves sub-nanometer spatial resolution at sampling rates of more than 100 kHz (10 μ s time resolution). Usually, only one bead can be manipulated and detected at a time, although instruments with two different detection lasers or polarization filters, which split the laser into two beams, have been realized to enable the tracking of two trapped beads. Another drawback is that optical traps are not specific and will entrap any particle that is dielectric and in the vicinity of the trapping laser focus. Furthermore, the high laser intensities required for stable trapping lead to local heating, which is moderate in terms of the temperature rise (~1 K) but may be sufficient to alter the viscosity in the local environment of the bead. Lastly, optical tweezers that allow tight control of the exerted forces and sensitive detection of the displacements are very expensive and technically demanding instruments.

Developed in the 1980's by Arthur Ashkin and colleagues (Ashkin *et al.*, 1986), for which Ashkin was awarded the Nobel prize in Physics in 2018, optical tweezers have been used to study molecular motors, the viscoelastic properties of the cytoskeleton or enzymatic catalysis (Neuman and Nagy, 2008). For example, it has been used to measure the force and displacement of kinesin on microtubules or the binding kinetics and force of viruses on erythrocytes (Block, Goldstein and Schnapp, 1990; Svoboda *et al.*, 1993; Mammen *et al.*, 1996). For the study of the organization of the plasma membrane, optical tweezers have been used to measure the distance that a membrane molecule linked to an optically trapped bead can be displaced in the plane of the membrane. Thus, the presence of barriers to the lateral diffusion of these membrane molecules can be tested. The first study to apply this approach found that the barrier-free path (BFP) of a GPI-anchored protein was longer than that of a related transmembrane protein (Edidin, Kuo and Sheetz, 1991). A dependence of the BFP from the size of the cytoplasmic domain of transmembrane proteins has been observed later (Edidin, Zúñiga and Sheetz, 1994; Sako *et al.*, 1998). When the transferrin receptor was pulled over the plasma membrane, half of the mobile particles escaped the trap at a trapping force of 0.1 pN, suggesting the energy required to cross the barriers as proposed in the Fence model was only slightly above the thermal energy (Sako and Kusumi, 1995). In another study of the Kusumi laboratory, the optical tweezers were used in erythrocyte ghosts to pull on the sub-membranous cytoskeleton through anchored Band 3 transmembrane proteins and it was observed that diffusing Band 3 followed the deformation of the membrane skeleton (Tomishige, Sako and Kusumi, 1998; Tomishige and Kusumi, 1999). The combination of SPT experiments with optical tweezers is thus a very useful

approach as it obtains information on membrane molecules that are inaccessible by SPT alone, such as the force required to move the molecule through the membrane (Peters *et al.*, 1999). However, applications are scarce in the literature, probably owing to the technical hurdles associated with optical tweezers.

4. Magnetic particles

Magnetic particles can be manipulated by an external magnetic field and can thus be used in a similar way as optical tweezers. The phenomenon of magnetism was first used in the magnetic compass, famously one of the Four Great Inventions from ancient China. Different organisms such as birds, salmon or magneto-tactic bacteria also make use of magnetism for navigation (Blakemore, 1975; Walker *et al.*, 1997; Naisbett-Jones *et al.*, 2020). Application of magnetic material to study biology appeared as early as in the 1920s by Heilbronn and Seifriz (Pankhurst *et al.*, 2009). Later in the 1950s, Crick and Hughes investigated the physical properties of the cytoplasm using magnetic particles (Crick and Hughes, 1950). In the last few decades, the development of nanometer-sized magnetic particles has enabled new magnetic applications in life sciences. Due to their size, magnetic nanoparticles (MNPs) possess properties that differ from the bulk material which allows tuning of magnetic behavior by controlling size, shape and composition (Pankhurst *et al.*, 2003, 2009; Jun, Seo and Cheon, 2008). To understand the MNP-specific properties, general concepts of (bulk) magnetism will be introduced first. Then, magnetic tweezers as the instrument to exert control over the MNPs will be described. Lastly, an overview of the diverse fields of applications for magnetic particles will be given, before discussing the concept of “magnetogenetics” as a means to control cellular activities in time and space using magnetic particles and fields.

4.1. Physical and technical background

4.1.1. Magnetism

All matter responds to magnetic fields but to a varying extent. The external magnetic field either induces magnetic moments in the atoms or molecules of the material, or, if already present, aligns the atomic magnetic moments. A material placed in a magnetic field of strength H , experiences a magnetization M which contributes to the overall magnetic induction B .

$$\vec{B} = \mu_0 (\vec{H} + \vec{M}), \quad (10)$$

where μ_0 is the permeability in vacuum. The macroscopic magnetization M is the sum of the individual atomic dipole moments per unit volume of the material and depends on the material-dependent magnetic susceptibility χ (Demtröder, 2017).

$$\vec{M} = \chi \vec{H}. \quad (11)$$

Materials are classified according to their magnetic susceptibility as diamagnetic or paramagnetic, which show only weak magnetic responses, or as ferro-, ferri-, or antiferromagnetic, which display large magnetizations and are commonly referred to as “magnetic materials”. Most biological

materials such as proteins containing only carbon, hydrogen, nitrogen and oxygen are diamagnetic (Pankhurst *et al.*, 2003), for which χ is negative and small. Paramagnetic materials such as the iron-containing haemoglobin possess permanent magnetic dipole moments but their orientation is randomized by thermal energy and are hence non-magnetic in the absence of a magnetic field (χ is positive but also small, *cf.* also below). Ferro-, ferri-, or antiferromagnets are already magnetic in the absence of an applied field due to ordered magnetic moments in the material and are distinguished by the coupling pattern between neighboring electron spins which give rise to different ranges of χ between 10^5 and zero (Demtröder, 2017). Ferro- and ferrimagnets resist loss of magnetization (coercivity). When placed in a magnetic field, the magnetization M initially follows curve i (Figure 9a) with increasing field strength H until it reaches saturation (Demtröder, 2017). However, if the field strength is now changed in the opposite direction, the material resists demagnetization and hence the magnetization follows a different curve, yielding a so-called hysteresis loop (Figure 9a, curves ii+iii). The reasons for hysteresis lie in the microscopic and atomic structure of the material (grain boundaries, magnetic domains, crystal lattice and impurities). Examples of ferromagnetic materials are iron or cobalt, while iron oxides (ferrites) such as magnetite Fe_3O_4 are ferrimagnetic.

For magnetic micro- to nanoparticles, the shape of the hysteresis loop depends also on the particle size (Leslie-Pelecky and Rieke, 1996). Micrometer-sized particles have multiple magnetic domains (Figure 9b, 1), regions in which the atomic magnetic moments are uniformly oriented, but if the size is further decreased, the particle consists only of a single domain (Figure 9b, 2). The smaller the particle, the more susceptible are the magnetic dipole moments to flipping by thermal fluctuations. Nanometer-sized (tens of nanometers or smaller) particles thus display superparamagnetism and no hysteresis (Figure 9b, 3). Superparamagnetic behavior is only observed above a certain temperature, the blocking temperature T_B (below which the MNPs behave as ferromagnets) (Jun, Seo and Cheon, 2008). Observation of superparamagnetic behavior is not only dependent on the temperature but also on the measurement time. If the thermal relaxation is fast compared to the measurement time, the particle appears (super-)paramagnetic (Pankhurst *et al.*, 2003). The nanoparticle size also affects the saturation magnetization M_s due to surface canting effects but this is only noticeable for particles smaller than ~ 5 nm (Jun, Seo and Cheon, 2008). The phenomenon of superparamagnetism makes MNPs ideally suited for biological applications. Due to the lack of hysteresis, the magnetization is lost immediately upon removal of the external field, allowing tight control of the nanoparticle activity. Ferromagnetic particles may also be used if the relaxation is fast at the relevant physiological temperatures (room to body temperature) relative to the measurement time.

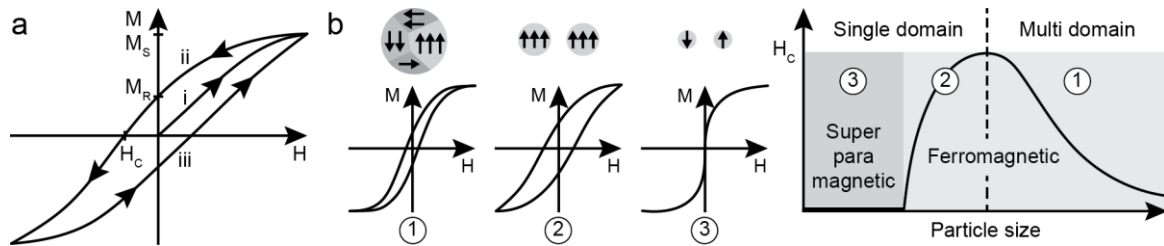


Figure 9: Magnetic properties of (bulk) ferromagnetic materials and magnetic particles

a) The magnetization M of a ferromagnetic material in a magnetic field of varying strength H follows a hysteresis curve. If the magnetic field around an initially demagnetized sample is increased, the magnetization grows linearly until it reaches a saturation plateau (curve i). If H is then reduced, M follows a different curve (ii) until saturation is reached again at $-H$. The residual magnetization M_R at zero magnetic field is the remanence and the reversed field strength H_c required to demagnetize the sample is called coercivity. Repeated change of the field closes the M - H curve (curve iii). This dependence of the previous magnetization state stems from microscopic impurities in the material and intrinsic properties of the crystalline lattice (Pankhurst *et al.*, 2003). Modified from (Demtröder, 2017). **b)** Dependence of magnetic properties on particle size. (1) Large, micron-sized particles reside in a multi-domain ground state. The hysteresis loop is narrow as it requires only relatively little energy to move the magnetic domain walls. (2) Smaller particles consist only of a single domain, in which all magnetic spins are aligned. The magnetic coercivity is increased, leading to broad hysteresis. (3) For particle sizes of tens of nanometers or below, superparamagnetism is observed. The energy barrier for the magnetic moment to change from a spin-up state to a spin-down state is proportional to the particle volume. For nanoparticles, the energy barrier is comparable to the thermal energy $k_B T$, e.g. at room temperature. Therefore, the dipole moment of the whole magnetic particle can fluctuate with the thermal energy and no hysteresis is detected. Modified from (Leslie-Pelecky and Rieke, 1996; Pankhurst *et al.*, 2003; Pekarsky and Spadiut, 2020)

Responses in magnetic materials can be induced by static or time-varying magnetic fields. Using alternating magnetic fields (usually at radiofrequency between ~ 100 kHz and ~ 1 GHz), it is possible to transfer energy to magnetic materials which is then released in form of thermal energy (see 4.2.1 and 4.2.3). The energy transfer is proportional to the area enclosed by the hysteresis curve (Pankhurst *et al.*, 2003). This heating mechanism by hysteresis loss applies to ferromagnetic particles. Superparamagnetic particles can also be heated but the mechanism of heat dissipation is based on relaxational processes (Liu *et al.*, 2020). Additionally, magnetic cooling during demagnetization is also possible due to entropic effects (Duret *et al.*, 2019) (see 4.2.3).

4.1.2. Structure and composition of magnetic particles for biological applications

Apart from the size, the shape and composition of magnetic particles can also modify their magnetic properties. Most magnetic particles are based on iron oxide (ferrite), such as magnetite (Fe_3O_4), maghemite ($\gamma\text{-Fe}_2\text{O}_3$), and metal-doped versions hereof such as cobalt ferrite. The mass magnetization (magnetization per unit mass) can be improved by doping with manganese for example (Lee *et al.*, 2007). MNPs suffer from the same issues as other nanoparticles such as colloidal instability, aggregation, potential cytotoxicity, difficulties in quantitative (bio-)functionalization, formation of protein corona, etc., which may compromise their use in biological applications (Shubayev, Pisanic and Jin, 2009; Clarke *et al.*, 2011; Salvati *et al.*, 2013; Wu *et al.*, 2019). Therefore, MNPs are usually coated with biocompatible polymers to improve colloidal properties and to reduce

cytotoxicity (Figure 10). For many targeted biological applications, protocols to efficiently bio-functionalize MNPs must be established. Bifunctional fluorescent magnetic particles are desirable to allow concomitant magnetic actuation and observation by fluorescence microscopy (Corr, Rakovich and Gun'Ko, 2008). For the synthesis of fluorescent MNPs, it has to be considered that the magnetic component can quench the fluorescent component. The fluorescent entity in those composites can be organic dyes (Figure 10a) as well as semiconductor nanocrystals (QDs) (Figure 10b). Many of these issues have been tackled in the last decades and thus made magnetic particles with tailored magnetic, chemical and biological properties available for a wide range of applications (4.2).

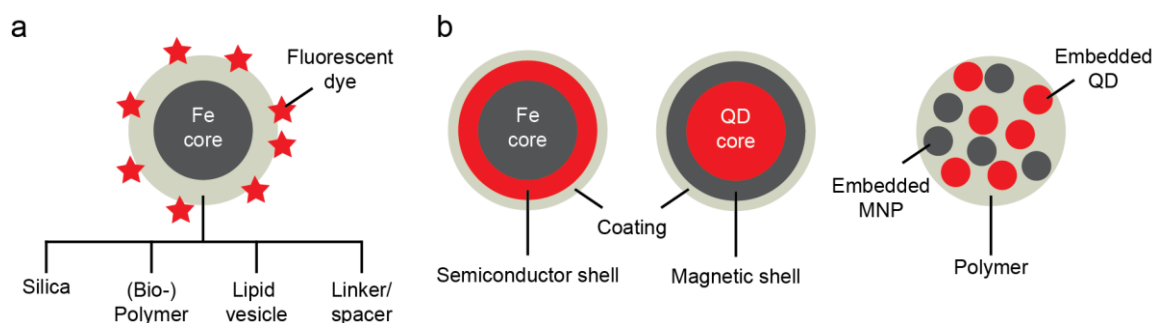


Figure 10: Types of fluorescent magnetic composite particles

a) Fluorescent organic dye composites. Different coatings or surface modifications are possible to improve colloidal properties, biocompatibility and to allow bio-functionalization (not shown). **b)** QD composites. Core-shell particles with either the magnetic or semiconducting entity as the core or shell have been synthesized. Coatings are mandatory to allow biocompatibility and functionalization. Additionally, mesoparticles of polymer-embedded MNPs and QDs are possible. **a, b)** Not drawn to scale.

4.1.3. Magnetic tweezers

Magnetic tweezers are instruments to manipulate magnetic materials at microscopic scales. The principle is straightforward: permanent magnets or electromagnets are brought into proximity of the sample to which a magnetic particle is attached or into which magnetic particles have been introduced. The external magnetic field exerts a force and/or torque on the magnetic particle and thus on the attached molecule. The position of the magnetic particles is measured by video- or laser-based tracking on a suitable microscope (Neuman and Nagy, 2008). If the magnetic field is uniform, the magnetic particle experiences only a torque which aligns the magnetic moment of the particle with the external field (like the needle of a compass through the Earth's magnetic field). To exert a translational force, a magnetic field gradient is necessary (Pankhurst *et al.*, 2003). If we consider the magnetic particle as a point-like magnetic dipole m , the magnetic force F_m is the differentiation of B along the direction of m .

$$\vec{F}_m = (\vec{m} \nabla) \vec{B}. \quad (12)$$

The dipole moment m of the magnetic particle can be expressed as

$$\vec{m} = V_m \vec{M}, \quad (13)$$

where V_m is the particle volume and M the volumetric magnetization. For a magnetic particle in aqueous solution, the effective magnetization M (see Eq. (11)) depends on the difference of the magnetic susceptibilities between the particle and water.

$$\vec{M} = (\chi_m - \chi_w) \vec{H} = \Delta\chi \vec{H}. \quad (14)$$

For a single magnetic particle or a dilute suspension in water, Eq. (10) can be simplified to

$$\vec{B} = \mu_0 \vec{H}. \quad (15)$$

Using Eqs. (12)-(15), the magnetic force can be written as

$$\vec{F}_m = V_m \Delta\chi \nabla(\mu_0 \vec{H}^2). \quad (16)$$

The force is proportional to the particle volume and the gradient of the square of the magnetic field strength. In three-dimensional space, the particle will move along the steepest ascent in the magnetic field (Pankhurst *et al.*, 2003). Therefore, it is counterintuitively not necessary to apply high magnetic field strengths. Instead, small field strengths can generate large forces if the field gradient is steep. To achieve steep gradients, magnet poles with sharp tips and small permanent magnets are used (Figure 11), as larger magnets provide higher field strengths but shallower field gradients (Tanase, Biais and Sheetz, 2007). For a fixed magnetic tweezer geometry, the magnetic field strength and hence the force on the magnetic particle decreases roughly exponentially with the distance from the magnet. Therefore, the stiffness of the force clamp is negligible (in the order of 10^{-6} pN/nm) and magnetic tweezers afford forces as small as 1 fN and up to 10 nN.

Typical magnetic tweezer setups are vertically arranged as they are used for single-molecule force spectroscopy (Lipfert, Hao and Dekker, 2009). Two small permanent magnets are placed over the sample (Figure 11a) to exert a pulling force axially to the light path of the microscope. Usually, neodymium magnets (neodymium iron boron, Nd₂Fe₁₄B) are used which have the highest energy density of available permanent magnets (Neuman and Nagy, 2008). For single-molecule force measurements, the magnetic particles are attached to the molecule of interest which is fixed to the substrate or bound to an interaction partner (e.g. DNA or microtubules) (Smith, Finzi and Bustamante, 1992; Gosse and Croquette, 2002). By rotating the magnets, the magnetic particle follows the movement and introduces a torque to the attached molecule (Gosse and Croquette, 2002). However, as the range of torque that is imposed is far larger than physiologically relevant torques, other configurations have been designed to sense torque and twist (Gore *et al.*, 2006; De Vlaminck and Dekker, 2012). There are also lateral setups which allow the detection of the molecule(s) of interest and the magnetic particle in the focal plane of the microscope (Figure 11b) (Yan, Skoko and Marko,

2004; Graham, Johnson and Marko, 2011; Etoc *et al.*, 2013; Madariaga-Marcos *et al.*, 2018). This type of configuration is particularly suited for the combination with microfluidic systems. On the other hand, magnetic tweezers can also be constructed with electromagnets. A ferromagnetic pole is milled and polished to create a sharp tip and then wrapped with coils to form the solenoid (Figure 11c) (Tanase, Biais and Sheetz, 2007). The advantage of electromagnetic tweezers is that force and torque (with at least two poles) can be controlled by the electric current through the magnetic solenoids and no physical movement of the magnetic poles is necessary, in contrast to permanent magnet setups. With three or more magnetic poles, the three-dimensional position of the magnetic particle, as well as force and rotation can be controlled freely (Figure 11d) (De Vries *et al.*, 2005; Fisher *et al.*, 2006). However, the changes in electric current induce hysteresis and the large currents necessary to generate sufficient field strengths lead to considerable heat generation which may require additional cooling strategies. Therefore, electromagnetic tweezers are substantially more complex instruments in terms of construction, handling and maintenance than permanent magnetic tweezers.

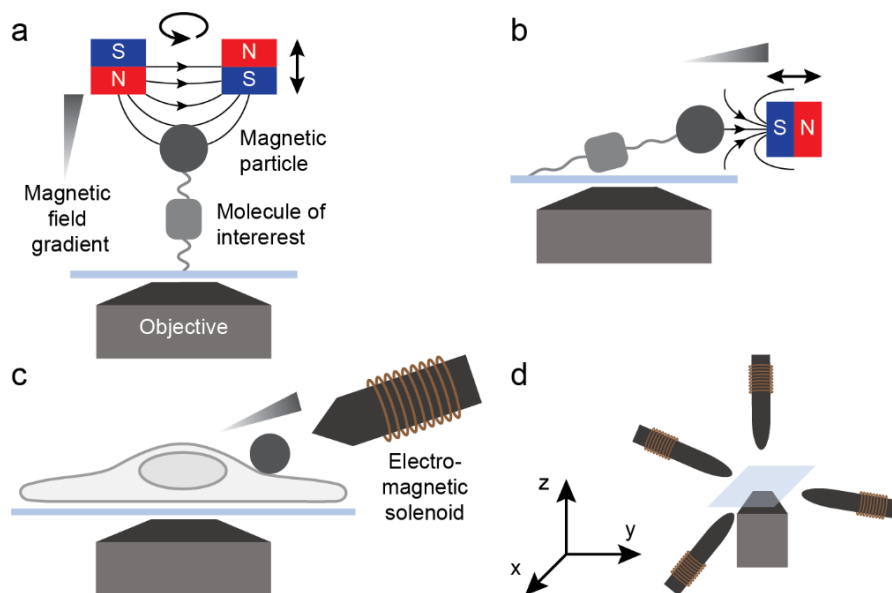


Figure 11: Typical magnetic tweezer configurations

a, b) Permanent magnet and **c, d)** electromagnetic setups. **a)** Axial magnetic tweezer typically used for single-molecule force spectroscopy. A pair of neodymium magnets with edge lengths of a few millimeters and with a small gap between each other is mounted on a motorized micromanipulator or a piezoelectric stage and can be moved up and down (bidirectional arrow) to control the force, and/or rotated to apply a torque (circular arrow). Setups with only a single or cylindrical magnet exist which generate circularly symmetric magnetic fields. Due to the significant difference in dimensions between the magnets and the field of view of the microscope (not drawn to scale), the magnetic field is relatively homogeneous in the focal plane across the field of view. **b)** Lateral or tilted magnetic tweezer configurations are possible with one or a pair of magnets like in **a)** (not shown). A ferromagnetic needle can be attached to the single magnet to create a steeper field gradient and higher forces (Etoc *et al.*, 2013; Bush and Maruthamuthu, 2019). **c)** Electromagnetic tweezers consisting of an iron core with a microfabricated pole tip and wrapped with copper coils to create the electromagnetic solenoid. The solenoid is connected to a computer-controlled power amplifier to provide electric current. Passive or active cooling systems may be installed on the solenoid. Due to the large size of the apparatus, the magnetic pole is usually placed sideways in a tilted angle. **d)** Electromagnetic tweezer with four magnetic poles positioned in a tetrahedral arrangement.

Designs with three to six poles have been realized (De Vries *et al.*, 2005; Fisher *et al.*, 2006; Berndt *et al.*, 2018).

To calibrate the magnetic tweezers, viscous drag experiments are usually carried out with the magnetic particles to be used. The aim of the calibration is to determine the magnetic force as a function of the distance from the magnet or magnetic pole tip (Tanase, Biais and Sheetz, 2007). The magnetic particles are suspended in a highly viscous liquid such as silicone oil or glycerol of known viscosity. The velocity with which the particle moves towards the magnet is measured. Using the Stokes formula

$$F = 6\pi\eta r v, \quad (17)$$

where η is the viscosity of the solution, r the particle radius assuming a spherical particle, and v the velocity, the magnetic forces can be calculated. For magnetic tweezer configurations in which the pulling force is exerted perpendicular to the surface to which the magnetic particle is tethered, another calibration method can be used. Based on the equipartition theorem, the applied pulling force can be calculated from the thermal fluctuations of the transverse particle position and the length of the tether (Gosse and Croquette, 2002; Neuman and Nagy, 2008). Other possibilities to determine the forces are numerical simulation (finite element method) or experimental measurement of the 3D magnetic field (Toraille *et al.*, 2018). Additionally, the force can also be discontinuously probed by pulling on double-stranded DNA with known rupture forces in different unzipping geometries (Seo *et al.*, 2016).

Magnetic tweezers can be used for different types of microscopic manipulations from single molecules to whole specimen (Neuman and Nagy, 2008; Berndt *et al.*, 2018), but is most popular for single-molecule force spectroscopy (see also 4.2.1). The ability to actuate rotational movement and measure torque and twist has been useful in the study of DNA topology and the activity of DNA-binding enzymes such as helicases (De Vlaminck and Dekker, 2012). Although application of torque and twist is more straightforward with magnetic tweezers, specialized optical tweezer setups can also impose torque on birefringent particles. Another advantage of magnetic tweezers over optical tweezers is the possibility of parallel manipulation of multiple magnetic particles (Ribeck and Saleh, 2008; De Vlaminck *et al.*, 2011). This reduces the number of single experiments required to obtain statistically significant amount of data and alleviates the impact of sample variations between experiments. The manipulation is highly selective to the magnetic particle and the attached molecule given specific binding via appropriate surface functionalization. Optical tweezers on the other hand will trap any dielectric particle in the vicinity of the trapping laser focus. Also, magnetic tweezers introduce neither photodamage (not more than the chosen microscopy method) nor heat to the sample (unless intended, see 4.1.1 and 4.2). The effective stiffness of magnetic tweezers is by several

orders of magnitude smaller than for optical tweezers (*cf.* above and 3.2), hence smaller forces can be applied, and weaker interactions can be studied. Nevertheless, optical tweezers remain more popular, mainly because of the more versatile manipulation possibilities and because a similar level of control using magnetic tweezers is only afforded by highly sophisticated electromagnetic setups.

4.2. Applications in life sciences

4.2.1. Overview of applications

Magnetic materials and fields are used in a wide variety of biomedical applications and in fundamental life science research. The most established use of magnetic particles in the biomedical and clinical practices are magnetic separation and contrast enhancement for magnetic resonance imaging. In the former case, biological entities are tagged with magnetic materials and then separated from the bulk solution in a magnetic separation device (Whitesides, Kazlauskas and Josephson, 1983; Pankhurst *et al.*, 2003). For specific targeting, magnetic particles are usually coated with a biocompatible polymer and then labeled with an antibody, hormone or other biomolecule that confers binding specificity. The biological entities to be separated include cells (Miltenyi *et al.*, 1990; Wang *et al.*, 2004; Furlani, 2007; Plouffe, Murthy and Lewis, 2015), proteins (Xu *et al.*, 2004; Franzreb *et al.*, 2006) or DNA (Berensmeier, 2006), and several commercial separation systems specialized for each of these applications compete on the market. A related approach are magnetic biosensing platforms that detect protein analytes or bacteria with high sensitivity (Gu *et al.*, 2003; Nam, Thaxton and Mirkin, 2003; Shubayev, Pisanic and Jin, 2009; Chung *et al.*, 2013; Wu *et al.*, 2019).

MNPs are used for contrast enhancement in Magnetic Resonance Imaging (MRI). MRI is superior to other clinical imaging modalities in terms of spatial resolution, tomography capability and non-invasiveness (Wu and Huang, 2017). However, the technique suffers from inherently low sensitivity as it measures the weak interaction of the protons present in biological tissues with large radio-frequency magnetic fields. Iron oxide nanoparticles are routinely used as MRI contrast agents and new MNPs with higher sensitivity are being developed (Pankhurst *et al.*, 2009; Lee and Hyeon, 2012). Additionally, Magnetic Particle Imaging (MPI) is a relatively new medical imaging method and holds great promises for the imaging of the brain, vascular system and other organs with high resolution and sensitivity (Gleich and Weizenecker, 2005; Knopp, Gdaniec and Möddel, 2017; Wu *et al.*, 2019).

In addition to diagnostics, MNPs can be employed in various therapeutic strategies. The use of MNPs as vehicles for targeted drug and gene delivery (Wu and Huang, 2017; Vangijzegem, Stanicki and Laurent, 2019) is highly desirable since cytotoxic drugs could be localized to the target site such as a specific organ or a tumor using an externally applied magnetic field, thus reducing the systemic and side-effects of the drug and/or the required dosage. Despite of a growing body of encouraging preclinical studies, targeted drug delivery by MNPs has not yet been translated to the clinical practice.

In contrast, MNP-induced hyperthermia (see 4.1.1 for the physical basis) has already demonstrated clinical success in the treatment of cancers such as glioblastoma and prostate cancer (Chang *et al.*, 2018; Liu *et al.*, 2020). For this therapy, which is being developed by Jordan *et al.* in Berlin (Jordan *et al.*, 2001), MNPs are directly injected into the tumor and the patient is subjected to strong alternating magnetic fields. The MNPs heat up the surrounding tissue to $\geq 42^{\circ}\text{C}$ causing localized cell death. Furthermore, MNPs are interesting for regenerative medicine and tissue engineering (Ito *et al.*, 2005; Dobson, 2008), for example to construct artificial vascular tissue (Shimizu *et al.*, 2007) or to direct stem cells into osteogenic differentiation (Kanczler *et al.*, 2010) (see also 4.2.3). Another well-established application is magnetofection, the MNP-assisted transfection of DNA vectors, as an alternative to viral transduction and for the transfection of cell types that are notoriously difficult to transfect (Yang *et al.*, 2008; Sauer *et al.*, 2009).

In terms of fundamental biological research, magnetic tweezers represent an important biophysical tool (see 4.1.3) (Neuman and Nagy, 2008). Different specialized modalities exist to interrogate biophysical properties of various biological systems (e.g. microrheology, biomolecule interaction and (un-)folding), with the commonality that defined magnetic forces are exerted on the specimen. The principles of force generation, different ways to construct magnetic tweezers and the comparison to optical tweezers have been discussed in section 4.1.3. Magnetic tweezers have been used to investigate the viscoelastic properties of the cytoplasm (Zaner and Valberg, 1989; Bausch, Möller and Sackmann, 1999; Wilhelm, 2008), cytoskeleton (Zaner and Valberg, 1989), chromatin (De Vries *et al.*, 2007), cell surface (Bausch *et al.*, 1998; Saphirstein *et al.*, 2013), ECM (Aermes *et al.*, 2020) and mucus (Kirch *et al.*, 2012). Single-molecule force spectroscopy using magnetic tweezers have unraveled the mechanical properties of DNA and RNA, and the action of polymerases, topoisomerases and helicases (Smith, Finzi and Bustamante, 1992; Strick *et al.*, 1996; De Vlaminck and Dekker, 2012) as well as of proteins (Löff *et al.*, 2019).

Magnetic particles have also been used to study diverse cellular processes, e.g. endocytosis or intracellular transport (Mahowald, Arcizet and Heinrich, 2009; Sauer *et al.*, 2009; Steketee *et al.*, 2011; Zablotskii *et al.*, 2011). Also at tissue level, MNPs can be employed to study collective behaviors such as cell migration or morphogenesis (Desprat *et al.*, 2008; Weber, Bjerke and DeSimone, 2012). Neurite growth can be magnetically guided either by endocytosed MNPs or targeted receptor activation (Steketee *et al.*, 2011; Riggio *et al.*, 2012; Jin *et al.*, 2019). Approaches that exploit the interaction of MNPs and magnetic fields to manipulate cellular events and behaviors are a new and promising alternative to optogenetics. The term “magnetogenetics” in analogy to “optogenetics” has been coined in this respect (Bonnemay, Hoffmann and Gueroui, 2015; Monzel *et al.*, 2017; Nimpf and Keays, 2017; Alvarsson and Stanley, 2018). It should be mentioned here that in other contexts,

“magnetogenetics” refers to the production and accumulation of magnetic material *in vivo* by adapting naturally occurring mechanisms in magnetotactic bacteria (Pekarsky and Spadiut, 2020). Examples of magnetogenetic approaches in the former sense will be reviewed in section 4.2.3 with focus on applications at the plasma membrane.

4.2.2. Advantages and limitations

Several unique features of magnetism make magnetic approaches attractive for biological applications (Monzel *et al.*, 2017; Duret *et al.*, 2019). For one, magnetic fields interact only weakly with biological materials as most biomolecules are diamagnetic (4.1.1). Therefore, the interaction is exclusive to the magnetic probe while the specimen itself, whether it is macromolecules, cells, tissues or whole organisms, is unaffected even by strong magnetic fields. However, as magnetic interactions are relatively weak, the physical effects are also relatively small. As a consequence, large magnetic field strengths are required for MRI or hyperthermia treatment, and the force range achieved by magnetic tweezers is lower than by optical tweezers and AFM. The second strength is that magnetic fields penetrate deep into tissue including bone, which allows non-invasive, remote applications such as magnetic resonance imaging (see 4.2.1) (Wu and Huang, 2017) and magnetogenetic manipulations in freely moving animals (see 4.2.3) (Huang *et al.*, 2010; Munshi *et al.*, 2017). The contactless magnetic actuation allows to directly correlate molecular processes with animal behavior. This is an advantage over light-based manipulations – because light transmission in tissue is very limited (depending on the wavelength), a light source needs to be surgically implanted to enable optogenetic manipulations deep in the tissue. Magnetic fields can be generated in different geometries and size scales and affect all magnetic particles within the field simultaneously, therefore highly parallelized applications are possible. While this is relatively straightforward at single-molecule scales (see 4.1.3) (Ribeck and Saleh, 2008; De Vlaminck *et al.*, 2011), already at single-cell level usually only one cell can be investigated at a time. An interesting “double magnetization” approach has been used to overcome this limitation: using micropatterning technology, superparamagnetic micromagnets and cells are deposited in a regular array with controlled distances (Tseng, Judy and Di Carlo, 2012; Toraille *et al.*, 2018). An external magnetic field is applied to magnetize the micromagnets which in turn attract the MNPs inside the cells. A similar strategy of magnetic field enhancement from macroscopic to microscopic scale is known from the commercial MACS cell separation technology (Miltenyi *et al.*, 1990). Depending on the application, magnetic particles must fulfil high demands in terms of colloidal stability, homogeneity, biocompatibility, and functionalization to allow efficient delivery and proper function (see 4.1.2). A general challenge is to introduce the magnetic particles into the specimen. In animals and humans, MNPs are usually injected. Delivery strategies into cells include endocytosis, microinjection, and cell-penetrating peptides. This limitation could be overcome by genetically encoding a magnetically responsive protein. Ferritin, the iron-storage protein, represents

a promising candidate but the nature of its response to external magnetic fields has been questioned (see 4.2.3) (Meister, 2016). Another advantage is that magnetic materials respond relatively quickly to changes of the magnetic field which enables high temporal resolution. Lastly, magnetic fields do not strongly interfere with other stimuli such as light, ultrasound, chemical or thermal signals. Therefore, several means of manipulation and detection can be combined, for instance magnetic actuation and fluorescent detection (see 4.1.2) (Corr, Rakovich and Gun'Ko, 2008; Zhang *et al.*, 2014).

4.2.3. Magnetogenetics

Magnetogenetics makes use of magnetic particles and fields to actuate mechanical, thermal or biochemical stimuli to remotely control cellular behaviors (Monzel *et al.*, 2017). The first study to report magnetic activation of a mechanosensitive ion channel, targeted magnetic particles to the extracellular loop of the potassium channel TREK-1 (K_{2P}2.1) (Hughes *et al.*, 2008). By applying a static or low frequency (1 Hz) magnetic field using a permanent magnet, the channel could be opened with 0.2-20 pN forces, leading to whole-cell currents (Figure 12a, left). Since TREK-1 plays a crucial role in connective tissues, the same mechano-magnetic approach could be used to direct human stem cells towards osteochondral differentiation to form bone and cartilage (Kanczler *et al.*, 2010; Henstock *et al.*, 2014). Such targeted activation of mechanosensitive receptors that orchestrate differentiation and morphogenesis is particularly interesting for tissue engineering efforts and regenerative medicine.

Apart from ion channels, other mechanosensitive membrane proteins such as platelet endothelial cell adhesion molecule-1 (PECAM-1) or the Notch receptor can also be magnetically activated (Collins *et al.*, 2012; Gordon *et al.*, 2015) (Figure 12b, right). Seo *et al.* presented a magnetic toolbox to manipulate both the localization and the mechano-signaling activity of Notch receptors and vascular-endothelial cadherin (VE-cadherin) (Seo *et al.*, 2016). They synthesized plasmonic MNPs by coating a Zn-doped ferrite core with a plasmonic gold shell and conjugated them monovalently with DNA binders to allow modular functionalization (~60 nm diameter including functionalization). By placing the vertical permanent magnetic tweezer 2 μm above the cell surface, the MNP-bound receptors could be aggregated in dense spots of 4-20 μm in a weak-force regime (1 pN force in perpendicular direction to the membrane) (Figure 12b, right). Lowering the magnetic needle to 0.7 μm above the cell surface, they could apply stronger forces of 9 pN to mechanically activate the receptors (Figure 12a, right), leading to nuclear transcription activation in the case of the Notch receptor and sustained actin polymerization and vinculin recruitment in the case of VE-cadherin. This way, the contribution of the spatial arrangement *vs.* the mechanical activation of the receptors to the downstream signaling could be dissected.

The concept of spatial manipulation by magnetic particles can be generalized to study all sorts of signaling processes. At the plasma membrane, magnetic particles have been used to actuate different

biochemical signals through signaling receptors. Magnetically induced oligomerization or clustering of the Fc ϵ RI receptor, the death receptor 4 (DR4) or epidermal growth factor (EGF) receptor to activate downstream responses have been realized (Mannix *et al.*, 2008; Cho *et al.*, 2012; Bharde *et al.*, 2013). In the first case, ligand conjugated MNPs induced Fc ϵ RI receptor clustering in mast cells through magnetic dipole-dipole interactions (Figure 12b, left), which activated intracellular calcium signaling in a reversible and field-strength dependent manner (Mannix *et al.*, 2008). A similar approach was used with anti-DR4 antibody conjugated MNPs to trigger apoptosis in zebrafish embryos (Figure 12b, right) (Cho *et al.*, 2012). Injection of these functionalized MNPs led to defects in tail morphogenesis under magnetic field exposure. Using a ligand-independent targeting strategy such as antibodies, streptavidin-biotin, or Halo-/SNAP-tag, clustering-dependent receptor activation can be demonstrated by magnetically induced aggregation (Cho *et al.*, 2012; Bharde *et al.*, 2013).

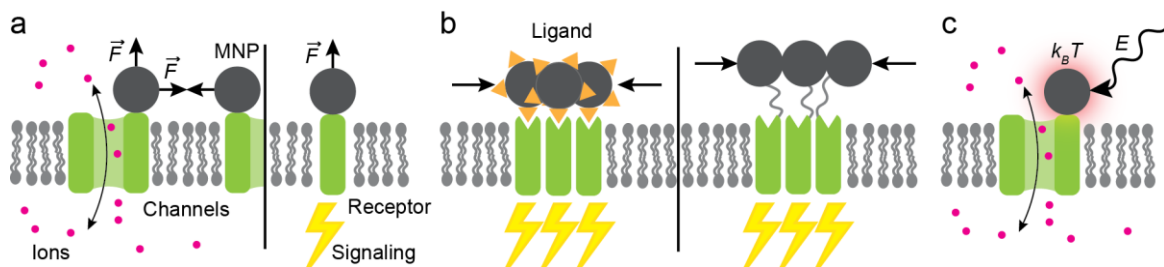


Figure 12: Magnetogenetic control of plasma membrane proteins

a) Activation of mechanosensitive ion channels and membrane receptors. By applying an external magnetic field, transverse or lateral forces can be exerted on MNP-tagged channels and receptors, leading to ion gating and/or downstream signaling pathways. **b)** Activation of ligand- or clustering-sensitive receptors. Receptors can be aggregated by dipole-dipole interaction between MNPs induced by static or alternating magnetic fields. By targeting with either the ligand (left) or an unrelated system (right) one can distinguish between ligand- and clustering-mediated receptor activation. **c)** Activation of thermosensitive ion channels. Exposure to radiofrequency alternating magnetic fields heats the MNPs and thereby opens the channels. **a-c)** Not drawn to scale.

Magnetic particles have also been used intracellularly to manipulate the cytoskeletal architecture and dynamics via signaling activation. By bio-functionalization with the small GTPase Ran (Hoffmann *et al.*, 2013) or the guanine exchange factor TIAM1 (Etoc *et al.*, 2013) it was possible to control the nucleation of microtubules or to initiate actin polymerization in the lamellipodium, respectively. If a high concentration of MNPs can be introduced to the sample, a gradient of the MNPs and thus of the biochemical effector can be generated (Hoffmann *et al.*, 2013; Etoc *et al.*, 2015). This is useful to investigate non-linear behaviors as a function of molecule concentration (switching behavior at a threshold concentration or cooperativity).

Magneto-thermal actuation is based on the same physical principles (see 4.1.1) as magnetic hyperthermia for cancer therapy (see 4.2). By delivering MNPs to temperature-sensitive ion channels, ion gating can be activated by subjecting them to alternating magnetic fields in the radiofrequency

range (Huang *et al.*, 2010; Stanley *et al.*, 2012; Chen *et al.*, 2015). Targeting the cation channel TRPV1 with this approach elicited action potentials in neurons both *in vitro* and *in vivo*, evoking magnetically controlled moto-behavior in *C. elegans* and mice (Huang *et al.*, 2010; Munshi *et al.*, 2017). Additionally, Munshi *et al.* could either excite or silence neurons by targeting TRPV1 or the chloride channel anoctamin 1 (TMEM16A), respectively (Munshi *et al.*, 2017; Munshi, Qadri and Pralle, 2018). Selective targeting is even dispensable provided the concentration of receptors and MNPs is sufficiently high, as demonstrated by transgenic overexpression of TRPV1 and injection of untargeted MNPs which enabled deep brain stimulation in mice (Chen *et al.*, 2015).

While most approaches use exogeneous MNPs, several studies attempted the use of genetically encoded ferritin, a naturally occurring superparamagnetic particle. Ferritin has been fused to the cation channels TRPV1 or TRPV4 to elicit calcium signaling and to thus control brain activity and glucose homeostasis in mice and zebrafish (Stanley *et al.*, 2012, 2015, 2016; Wheeler *et al.*, 2016). This approach avoids difficulties of introducing MNPs into the specimen. However, these studies caused an on-going controversy about the biophysical mechanism (Meister, 2016) and reproducibility (Xu *et al.*, 2020). The original publications claimed an effect by either magnetic heating or mechanical stimulation, whereas later studies propose entirely different mechanisms (Barbic, 2019; Duret *et al.*, 2019; Brier *et al.*, 2020; Christiansen, Hornslien and Schuerle, 2020; Hernández-morales *et al.*, 2020). This highlights the importance of proper quantification of the applied magnetic field and other physical parameters such as the exerted forces and investigation of the mechanism of magnetic actuation.

5. Aims of the study

Diffusion barriers are crucial for the maintenance of functional membrane domains in polarized cells. On a nanoscopic level, models such as the Picket and Fence model have been developed to describe the restricted movement of molecules in the plasma membrane. However, it is unclear how nanoscopic compartmentalization gives rise to diffusion barriers at larger scales. The physical properties of diffusion barriers, their molecular composition and mechanism of action remain poorly understood in many biological contexts.

Major insights into the diffusive behavior of membrane molecules were made with SPT which allows the observation of single-molecule events. The movement patterns could be correlated with cellular structures such as the cortical cytoskeleton. However, to directly test the existence of a physical barrier, it is desirable to drive a probe against the barrier by applying a force (Figure 13, left). Optical tweezers can perform such experiments, but due to the limited throughput and technical demands, this method has only rarely been used for this purpose. Additionally, in these optical tweezer studies the dragged distance was analyzed statistically, but the trajectories have not been mapped to the actual location on the cell or correlated with cellular structures. These studies thus failed to identify the physical position at which the dragged molecule experienced a barrier and the molecular species constituting the barrier.

Similar actuation of force to nanoscale objects is possible by magnetic nanoparticles via magnetic tweezers. Although this approach has been used to manipulate the ensemble distribution of membrane proteins, to our knowledge, it has never been used in conjunction with SPT to observe the movement of single membrane molecules and to direct their movement. This work therefore pursues the development of magnetic tweezers as a tool to move membrane molecules through the plasma membrane in order to detect diffusion barriers in living cells (Figure 13). To do so, high spatiotemporal resolution has to be achieved using fluorescent magnetic nanoparticles for SPT. The following aims are addressed in detail:

- Are fluorescent magnetic nanoparticles (FMNPs) suitable for high-speed, high-resolution SPT? In previous studies where magnetic particles have been tracked, either larger microbeads or clustered particles were used or only a poor resolution has been achieved. Nanometer-sized magnetic particles on the other hand have mostly been used for ensemble measurements.
Can FMNPs be coupled to individual membrane molecules in artificial membranes and in the plasma membrane of living cells to observe their lateral movement?
Do they allow SPT with nanometer-range localization precision at milliseconds time resolution by fluorescence microscopy?
- Is it possible to move membrane molecules through the membrane with magnetic tweezers?

Can we exert the dragging force along the plane of the membrane using a lateral magnetic tweezer setup equipped on a fluorescence microscope? Most magnetic tweezers are vertical but lateral setups have been realized before.

Can we steer the movement of membrane molecules with magnetic tweezers against the viscous drag of the membrane? Less than 1 pN are required to move membrane molecules by optical tweezers, but since the magnetic force scales with the particle volume, are nanometer-sized magnetic particles capable of exerting sufficient force to introduce a directional movement?

What range of forces are exerted on the membrane molecules? Can we quantify the effective force experienced in lateral direction to the membrane?

- Can we actuate the magnetic manipulation reversibly? Do FMNP-coupled membrane probes revert to random diffusion after removal of the magnetic field?
- Can we move different types of membrane molecules through the membrane, such as lipids, lipid-anchored proteins, or transmembrane proteins?
- Can we combine FMNP tracking and manipulation with super-resolution imaging of potential barrier molecules? Diffusion barriers are thought to be built up by nanoscopic assemblies in and in proximity of the plasma membrane, such as the cortical cytoskeleton or anchored transmembrane proteins. To detect these assemblies and to elucidate their supramolecular organization, sub-diffraction resolved microscopy is required.

Can we correlate the trajectories of the FMNPs with cellular structures such as the cortical cytoskeleton?

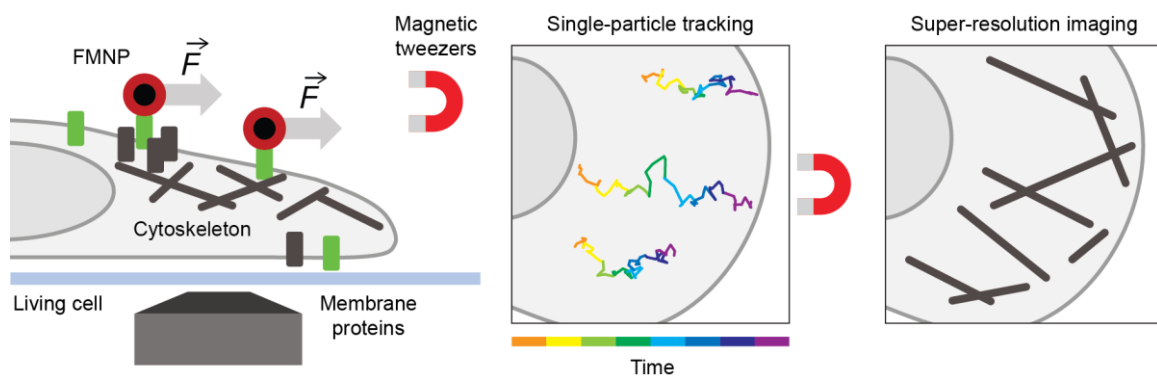


Figure 13: FMNPs and magnetic tweezers as a tool to manipulate membrane molecule motion and to detect diffusion barriers in the plasma membrane

FMNPs are targeted to membrane molecules in artificial (not shown) or cellular membranes for SPT. The movement of the membrane molecule is manipulated into a desired direction by application of an external magnetic field using magnetic tweezers. Simultaneously, the FMNPs are tracked by fluorescence microscopy with high resolution. Cellular structures that potentially act as diffusion barriers (e.g. the cortical cytoskeleton) are visualized by super-resolution microscopy, matching the resolution of SPT, such that the FMNPs trajectories can be correlated with these structures. Not drawn to scale.

Results and Discussion

6. Selection of suitable FMNPs

Magnetic nanoparticles are versatile tools that have been intensively explored for biotechnological and biomedical application in the last decade. A plethora of MNPs with different particle properties are available from commercial vendors while new reagents with ever improved and ever specialized properties are being designed in research laboratories. To perform high-resolution SPT with FMNPs, which has not been done before to our knowledge, we first had to identify suitable particles and, crucially, what characteristics actually make the particles fit for our needs.

6.1. Requirements in particle properties

To achieve the aims of this study as defined in the previous chapter (see 5), the bifunctional nanoparticles must fulfill a set of requirements (Table 1). First, the particles must be magnetic, and the saturation magnetization must be sufficient such that magnetic actuation using a magnetic tweezer setup is feasible within a space and time frame relevant for live-cell imaging, i.e. over micrometers and several minutes. To allow reversible magnetic control, the particles would ideally be superparamagnetic, or, if ferromagnetic, any effective remnant magnetization should be lost quickly. Second, the particles must be fluorescent and bright enough to allow SPT with high localization precision. Third, the particles should be as small as possible, so that they accurately report the position of the tracked molecules and introduce little steric hindrance. To facilitate SPT analysis, they should be sized below the diffraction limit of light, i.e. <200 nm, such that they appear as diffraction-limited spot and can be localized by common SPT algorithms. Large spherical microparticles can be tracked with nanometer spatial precision but are unsuitable for SPT of single diffusing molecules due to their size (Chronopoulos *et al.*, 2020). A related property is the dispersity; the particles should be monodisperse and remain unaggregated throughout the application and in storage. In the case of MNPs, there is a trade-off between the particle size and the amount of magnetizable material per particle, characterized by the saturation magnetization. Lastly, for targeting of the molecules of interest, the particles must be bio-functionalized with a binder with high affinity and specificity. Four types of FMNPs of different sources have been tested here and the “BNF-Starch-redF Streptavidin” particles (Micromod) have emerged as the best compromise in all these terms (Li *et al.*, 2020). Hence, they were used for all experiments presented in the sections 7-8 and will be characterized in detail in the next subsection 6.2. To illustrate the importance of these considerations and for the sake of completeness, other particles which failed in at least one of these aspects are discussed in the following.

Table 1: Criteria for the suitability of FMNPs for SPT and magnetic manipulation

BASIC REQUIREMENT	IDEAL PROPERTIES
Magnetic	Superparamagnetic, high saturation magnetization
Fluorescent	Bright, photostable
Sub-diffraction sized (<200 nm)	As small as possible
Disperse	Stably monodisperse over time and under physiological buffer conditions (pH, ionic strengths, presence of serum etc.)
Biofunctionalized	Binding with high affinity and specificity, no unspecific binding

Particle size and dispersity are properties of colloidal materials that are notoriously difficult to control and to maintain, as nanoparticles tend to aggregate, i.e. to become polydisperse. Aggregation was an issue for all particles tested so far but to a varying extent. The “Nano-screenMAG-Streptavidin” (Chemicell) are superparamagnetic particles with a magnetite core and a fluorescent starch matrix conjugated with streptavidin. These FMNPs were strongly aggregated with a broad distribution in sizes and additionally, when conjugated with biotinylated anti-GFP nanobodies, failed to bind specifically to eGFP-GPI expressing cells (GFP-GPI hereafter, Figure 14a). The “MyQuVigen-Streptavidin” (Nvigen) particles were more promising, as they bound specifically to GFP-GPI cells when conjugated to biotinylated GFP antibodies or nanobodies (Figure 14c). Additionally, they are bright due to the QD core which is surrounded by a shell of superparamagnetic iron oxide. As demonstrated by Paula Santos Otte (Santos Otte, 2017), the particles diffused on the plasma membrane and could also be moved over a few micrometers using an external magnet ((Santos Otte, 2017), Figures 19-22, p. 28-30). However, a large fraction of particles was nevertheless aggregated (Figure 14d-e; (Santos Otte, 2017), Figure 19-22, p. 28) and the aggregation increased over time, which could be alleviated by sonication but not reversed. Therefore, most particles were immobile or diffused only with low mobility on cells. Next, I tested magnetite particles synthesized by Lucas Kuhrts in the laboratory of Damien Faivre (Reichel *et al.*, 2017), which were covalently conjugated with mCherry by EDC/NHS-reaction. These particles form chains of varying sizes from stable single domains, thus, mesoparticles of different sizes are present (Figure 14b). Also, mCherry is very dim compared with organic dyes or QDs. As the concentration of these magnetite particles was lower by several orders of magnitude than that of the commercial products, targeting membrane molecules would have been inefficient. The results with these three types of FMNPs demonstrated and narrowed down our requirements for FMNPs to be applicable for fluorescent SPT (Table 1).

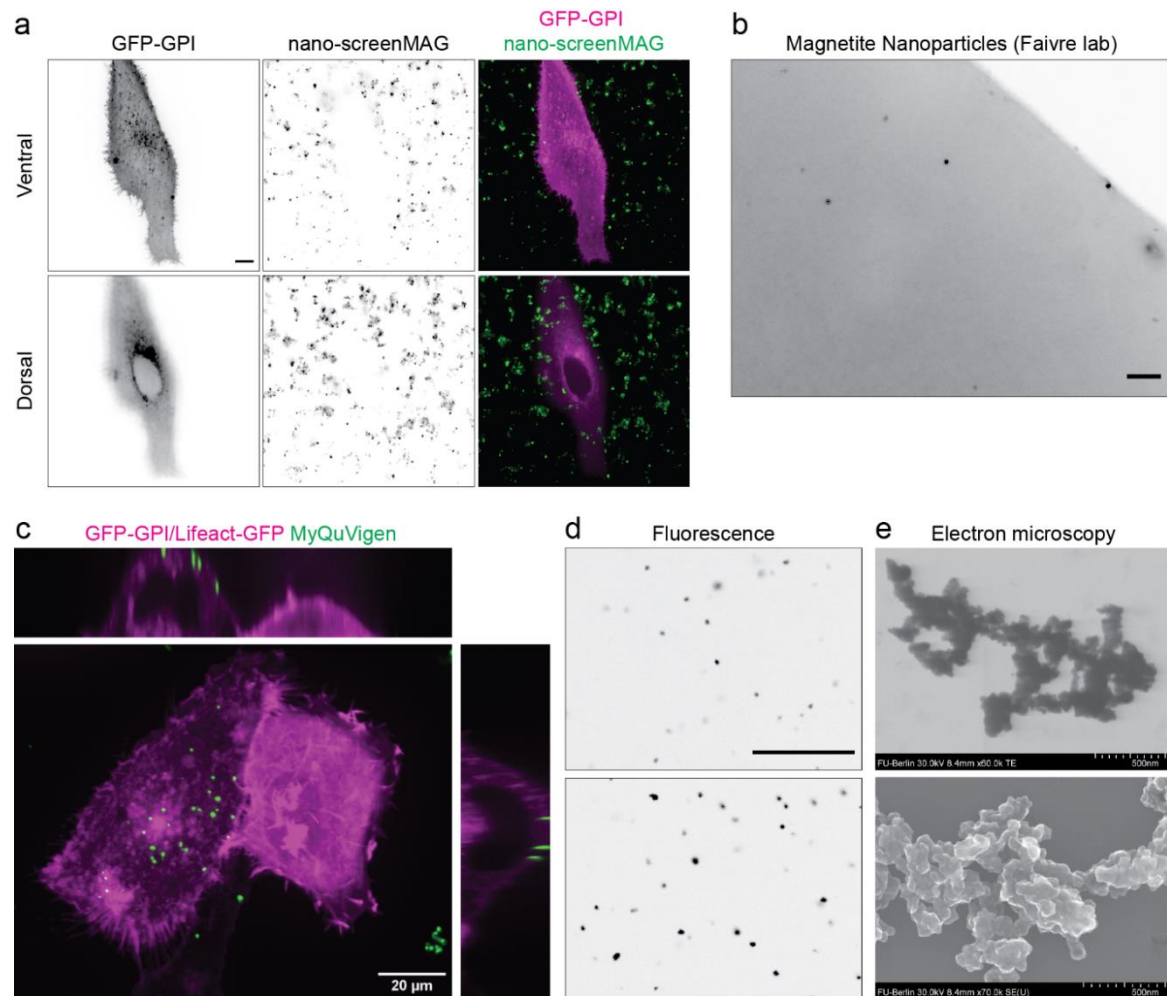


Figure 14: Screening of different FMNPs for desired properties

a) GFP-GPI expressing CV-1 cells incubated with Nano-screenMAG-Streptavidin (547/581 nm ex/em) functionalized with biotinylated GFP antibodies. FMNPs form aggregates and fail to bind specifically to GFP on the cell surface. Confocal fluorescence shown with inverted LUT and pseudo-color merge (right). Scale bar is 10 μm . **b)** A drop of mCherry-conjugated magnetite nanoparticles from the Faivre lab (fluorescence, inverted LUT). The particle concentration is low, and the solution is fluorescent (compare top right corner, which is outside of the drop) probably due to free mCherry. Scale bar is 10 μm . **c-e)** Microscopy of MyQuVigen-Streptavidin (em 615 nm) demonstrate specific binding but also nanoparticle aggregation. **c)** U2OS cells expressing GFP-GPI (left cell) and Lifeact-GFP (right cell) incubated with biotinylated GFP nanobodies and FMNPs. Average projection of a confocal z-stack with xz- (top) and zy-slice (right). **d)** FMNPs in solution (top) and on the surface of the cover glass (confocal, inverted LUT). Scale bar is 20 μm . **e)** Representative particles in transmission and scanning electron microscopy (TEM, top; SEM, bottom). Scale bars are 500 nm.

6.2. Characterization of FMNP properties

The “BNF-Starch-redF Streptavidin” particles (Micromod) consist of a 100 nm iron oxide core and a matrix of nonionic hydroxyethyl starch covalently conjugated with the red dye Dy555 and streptavidin (Figure 15a). They are not spherical (“cluster-shaped”; Figure 15b), but the organic starch shell has too little contrast in EM to judge how rough the surface is. They occasionally formed aggregates (Figure 15b) but were overall highly monodisperse, as confirmed by Dynamic Light Scattering (DLS) measurements (Figure S28). The hydrodynamic diameter of 159 ± 2 nm is below the diffraction limit of light; thus, the particles appear as single spots in fluorescence microscopy (Figure

15c). With a hydrodynamic radius of ~ 80 nm, the diffusion coefficient D would be $2.7 \mu\text{m}^2/\text{s}$ in aqueous solution according to the Stokes-Einstein relation (2). Due a large amount of embedded dyes, the particles are very bright and could be imaged for a long time (Figure 15d). Due to the brightness, the center of the FMNP could be localized with sub-pixel precision below 10 nm (Figure 15e-f). Diffusion of the particles in solution could be tracked with 5 ms time resolution (200 Hz frame rate). 3D SPT of the particles in cell culture medium obtained an average D of $2.5 \mu\text{m}^2/\text{s}$ ($n=80$ tracks; Figure S29), which is in good agreement with the theoretical value. The experimental D might be slightly underestimated due to a bias in SPT towards longer trajectories of slower particles as faster particles are more likely to diffuse out of focus. The particles could be magnetized by an external magnetic field (e.g. in a magnetic separator) and after removal from the field, could be retrieved as a monodisperse suspension. Magnetic separation happened relatively quickly; already after 5-10 min, the particles were quantitatively accumulated on one side of the microfuge tube as visible by eye. This allows the separation of unbound molecules after the functionalization with biotinylated molecules (see 9.5.1 and 7.6.1). The magnetic forces that can be exerted on attached molecules will be quantified and discussed in sections 7.4 and 7.5. The streptavidin-functionalized particles bound specifically to biotin (Figure 15c) and showed only little unspecific binding (*cf.* Figure 21b). Overall, these particles are suitable for high-resolution SPT and simultaneous magnetic manipulation by magnetic tweezers, which will be described in the following sections.

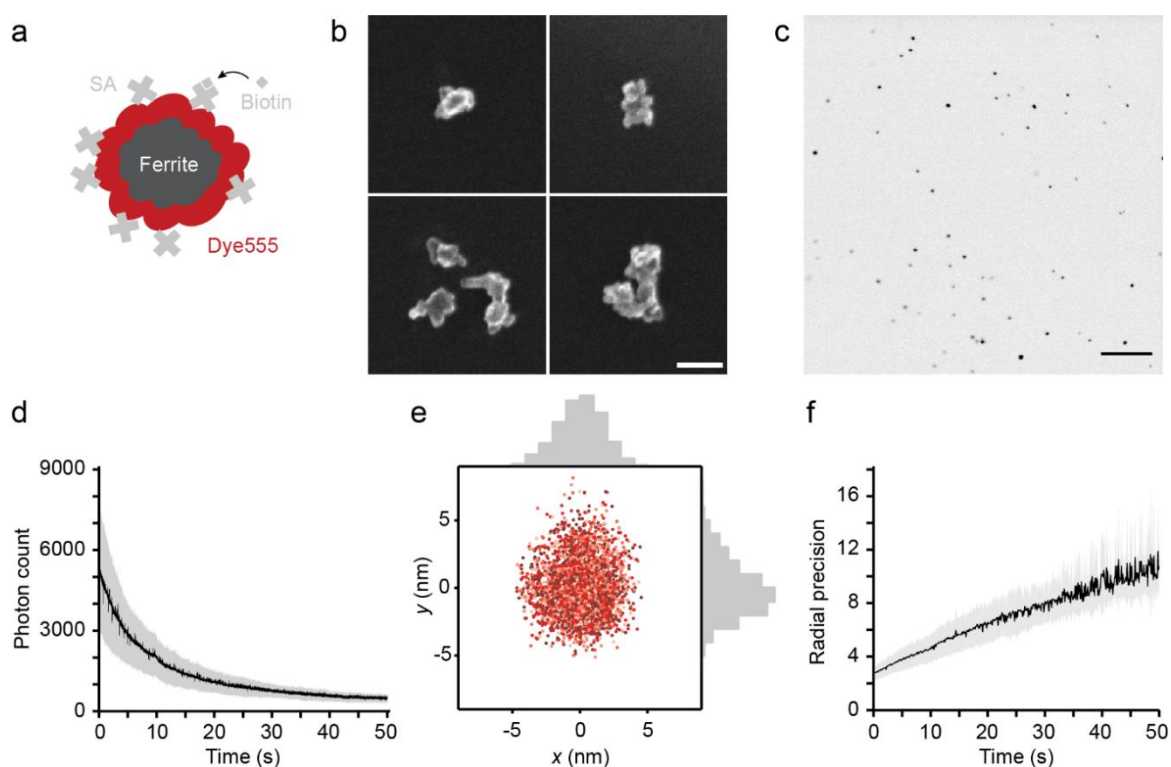


Figure 15: Characterization of "BNF-Starch-redF Streptavidin" particles (Micromod)

a) Schematic representation of particle composition. SA: streptavidin. Not drawn to scale. **b)** SEM images of the particles show that they are cluster-shaped and around 100-200 nm in length. Scale bar is 100 nm. **c-f)** BNF particles are bright and can be imaged for a long time with high localization precision.

Photophysical properties of single immobilized FMNPs measured with 50 Hz and a laser-power density of 400 W/cm² using the 561 nm laser line. **c)** The particles bind specifically to a coverslip coated with BSA-biotin and appear as single, diffraction limited spot. Only few immobilized particles were observed on a control coverslip coated with BSA (not shown). Fluorescence image with inverted LUT. Scale bar is 20 μ m. **d)** Mean photon count over time for 6 particles with standard deviation (s.d.) as grey shaded area. **e)** Sub-pixel localized positions in x and y of one single FMNP over 3000 frames, colored by time (light to dark red) with histograms of the x and y positions. **f)** Mean localization precision in xy over time of 9 particles with s.d. as grey shaded area.

6.3. Discussion

At the beginning of the project, it was clear that the particles had to be magnetic, fluorescent, sub-diffraction sized and functionalized (or ready for functionalization). Most particles we tested failed our expectations, however, the different issues we encountered with each type of particle sharpened our list of criteria (see 6.1). Through these experiences, I have developed a set of qualitative and quantitative controls to evaluate the FMNPs (Table 2; for more details see 9.1). Although some of these controls appear rather trivial, performing these tests upon receipt of a new sample or a new batch and combining them purposefully (e.g. fluorescence microscopy before and after magnetic separation to check for magnetization-induced aggregation), avoids wasting time and resources experimenting with inapt reagents.

Table 2: Experiments to check the suitability of FMNPs for SPT and magnetic manipulation

CONTROL EXPERIMENT	PROPERTIES EVALUATED
Magnetic separation	Magnetization, time to separate, dispersity after resuspension
Fluorescence microscopy	Aggregation/dispersity, estimation of particle density, brightness, localization precision, bleaching
DLS	Hydrodynamic size distribution, dispersity
TEM/EM	Core size distribution, shape, dispersity
Binding tests	Biofunctionalization, unspecific binding, functionalization-induced aggregation

The reason why most particles failed is that they are produced for purposes that do not require a high quality on a single particle basis. Although MNPs have been used for biological applications in many ways (reviewed in 4.2), the majority of applications are in batch mode (Pankhurst *et al.*, 2003), relying on the ensemble properties or measuring ensemble effects (Mannix *et al.*, 2008; Bharde *et al.*, 2013; Seo *et al.*, 2016). Thus, inhomogeneities and shortcomings can be compensated, e.g. a low fluorescence intensity per particle can still lead to a detectable signal if a large concentration of particles is used or enough particles are aggregated. Many commercial magnetic nanoparticles for biological or biomedical applications are intended for the magnetic separation of single cells or purification of nucleic acids and proteins in bulk (Miltenyi *et al.*, 1990; Berensmeier, 2006; Franzreb *et al.*, 2006; Plouffe, Murthy and Lewis, 2015) and not necessarily suited for single-particle applications. This study is the first effort to use FMNPs for high-speed and high-resolution fluorescent SPT. As such, the demands were especially high in terms of monodispersity and fluorescence brightness. Previous studies in which magnetic particles were tracked used either magnetic microbeads or

clusters of magnetic nanoparticles (Etoc *et al.*, 2013). Magnetic microbeads are commonly used in magnetic force spectroscopy and the size is required to actuate pico- to nanonewton range forces (Neuman and Nagy, 2008; Collins *et al.*, 2012; Aermes *et al.*, 2020; Chronopoulos *et al.*, 2020). One study that employed sub-micron sized particles for SPT inside cells achieved only a poor time and spatial resolution (Sauer *et al.*, 2009).

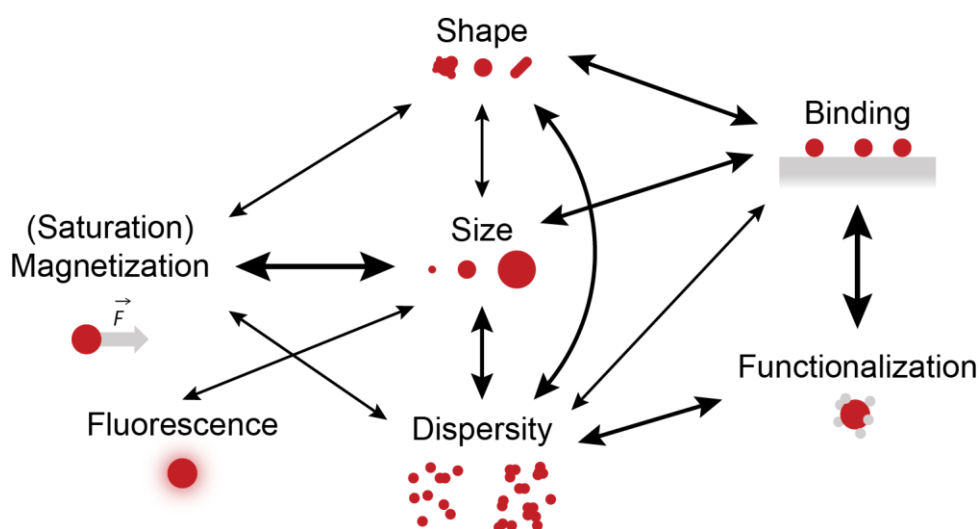


Figure 16: Relationship of desired particle properties for FMNPs

Schematic representation of conflicts or dependencies between colloidal, physical and biochemical properties. Thickness of arrows roughly indicate the extent of which one property affects another. Magnetizable material content and particle size are a central trade-off. Size also entails the size distribution and aggregation changes the effective distribution of particle size (dispersity). Target binding depends on the (bio-)functionalization but also size and shape affect the binding kinetics. The depicted properties and relationships are not exhaustive, and the relevance depends on the specific application. Not drawn to scale.

6.3.1. Limitations of the FMNPs

The “BNF-Starch-redF Streptavidin” particles from Micromod are bright, monodisperse and can be tracked with 10 nm localization precision at 200 Hz (5 ms time resolution) (Figure 15). In fact, SPT of magnetic nanoparticles with such spatial and temporal resolution has not been achieved before to the best of our knowledge. Nanometer localization can be accomplished but using micron-sized magnetic beads (Chronopoulos *et al.*, 2020). SPT of magnetic lipoplexes has been performed with ~4 Hz. The spatiotemporal resolution achieved here is thus unprecedented for FMNPs. Although the particles fulfill the basic requirements in terms of fluorescence, size, binding (Figure 15), and magnetic properties as shown later (see 7.2.2 and 7.4), there are limitations. Ideally, the particles should be spherical to minimize potential steric hindrance (see also 7.3 and 7.7), although we mitigated this issue with a PEG linker (see 7.2.1 and 7.6.1). A major drawback is the large size of ~160 nm in hydrodynamic diameter (Figure 15b). The diffusion coefficient is relatively low with 2.5-2.7 $\mu\text{m}^2/\text{s}$ and any target molecule that is tracked with this probe, would be limited in its diffusion at least to this value (Clausen and Lagerholm, 2011). Despite the ~100-fold difference in the viscosity of

the membrane bilayer to its surrounding aqueous medium (Saffman and Delbrück, 1975), the FMNPs are so large that their diffusion in aqueous medium falls into the range of lipids diffusing laterally in a lipid bilayer. The diffusion coefficient D for different phospholipids diffusing in an artificial supported lipid bilayer (SLB) was measured to be $\sim 3\text{-}10 \mu\text{m}^2/\text{s}$ (Kusumi *et al.*, 2012). Therefore, I would expect a small to moderate effect in SLBs (see 7.2). For membrane molecules in the plasma membrane, this would be less of an issue (see 7.7), as they typically diffuse one order of magnitude slower than in artificial membranes (Kusumi *et al.*, 2012). Additionally, the slow diffusion affects the binding kinetics (see 7.6.1) which should be considered for sparse targets. In such cases, it could take an extensive time or extremely high concentration of particles to achieve a satisfying number of bound particles. Furthermore, due to the size these particles can only bind to the dorsal side of adherent cells (see also Figure 21). A particle diameter of $\sim 30 \text{ nm}$ (size of the larger far-red QDs) would have a D of $\sim 15 \mu\text{m}^2/\text{s}$ and enable diffusion between the cell and the glass substrate to bind the ventral membrane. Smaller MNPs are available but generally come at the cost of less saturation magnetization (a 30 nm diameter particle has ~ 150 times less volume than a 160 nm diameter particle assuming a spherical shape). A smaller saturation magnetization value per particle could be compensated by the strength of the magnetic field, as I discuss in the next section after quantification of the magnetic forces (see 7.4). Another idea is to let the cells adhere on a patterned substrate with micro-/nanopillars such that the FMNPs can diffuse under the cell (Nomura *et al.*, 2006). Furthermore, smaller particles have the advantage that monovalent functionalization is easier and that the valency can be checked by (native) gel electrophoresis (Zhang, Servos and Liu, 2012; Seo *et al.*, 2016; Reina *et al.*, 2018; Liao *et al.*, 2019).

6.3.2. Alternative fluorescent magnetic particles

The “BNF-Starch-redF” particles bleach, and the localization accuracy deteriorates over time (Figure 15d, f). Quantum Dot-MNP composites such as the “MyQuVigen” particles are more desirable in this respect (Gu *et al.*, 2004; Wang *et al.*, 2004; Roullier *et al.*, 2008; Mahajan *et al.*, 2013; Chen *et al.*, 2014). Unfortunately, the QD-based “MyQuVigen” particles fell short in terms of colloidal dispersity and stability (Figure 14c-e). Nevertheless, the initial results obtained with these particles demonstrated that membrane proteins in the plasma membrane of living cells could be moved by FMNPs and an external magnet, and most importantly, that our approach was feasible (Santos Otte, 2017). Alternatively, plasmonic magnetic particles with a gold shell have been synthesized and successfully used on cellular membranes (Seo *et al.*, 2016). They do not bleach, as the mechanism of photon emission is different from fluorescence, and protocols for quantitative functionalization have been developed for these (Zhang, Servos and Liu, 2012). However, due to the different optical properties, plasmonic particles might appear dim under standard fluorescence microscopes. In general, several of the desired properties of FMNPs affect each other (Figure 16). High quality FMNPs

that fulfill special demands have been synthesized in research laboratories (Corr, Rakovich and Gun'Ko, 2008; Mahajan *et al.*, 2013; Chen *et al.*, 2014), but may not be easily available in the desired quantities. Commercial products have the advantage that they are readily available and that the quality is more consistent. In our case, the “BNF-Starch-redF Streptavidin” particles exhibited increased unspecific binding over time probably due to degradation of streptavidin but ordering a new batch solved the problem.

To conclude, we tested different FMNP to find particles that would allow SPT and simultaneous magnetic manipulation. In the process, we defined a comprehensive catalogue of requirements for the particle properties and devised a corresponding set of validation experiments. We did not find particles that fulfilled all criteria perfectly, especially in terms of size and shape, as the trade-off between various properties needs to be considered for the selection of the particle. The evidence collected confirm that the “BNF-Starch-redF Streptavidin” will be suitable for our aims going forward: They are bright, small, monodisperse and, crucially, can be used as probes for high-speed high-resolution SPT. They can be quickly and reversibly magnetized, enabling the non-invasive actuation of magnetic forces.

7. Magnetic manipulation of membrane molecules

After identifying suitable magnetic nanoparticles (section 6.2), I next tested whether it was possible to label and move single membrane molecules with these particles. To do so, I established magnetic tweezers and applied the FMNPs to an artificial lipid bilayer.

7.1. Lateral magnetic tweezer setup

To move membrane molecules with magnetic particles, an external magnetic field must be applied to exert a certain magnetic force. Magnetic tweezers can be built in numerous ways (Matthews *et al.*, 2004; Fisher *et al.*, 2006; Lipfert, Hao and Dekker, 2009; Etoc *et al.*, 2013, 2015; Daldrop *et al.*, 2015; Chronopoulos *et al.*, 2016; Madariaga-Marcos *et al.*, 2018). In classical force spectroscopy, the direction of the magnetic field is oriented such that the force is exerted perpendicular to the surface where the magnetic bead is attached. However, in our case the magnetic field must be applied laterally in order to displace membrane molecules in a planar membrane bilayer (Figure 17a), while imaging the membrane on a standard inverted microscope. To do so, we implemented a simple setup (Etoc *et al.*, 2013, 2015) of a thin steel needle (Figure 17b) attached to a millimeter-sized permanent Neodyn magnet (Figure 17a,c). To conveniently control the position of the magnetic needle, a motorized micromanipulator (Figure 17c) is used. In principle, the magnetic field strength in the field of view can be varied using magnets of different sizes or by placing the magnetic tip at different distances from the field of view. However, in most experiments, a 6×4×2 mm magnet was used (Figure 17c) and the tip of the magnetic needle was placed as shown in Figure 17a.

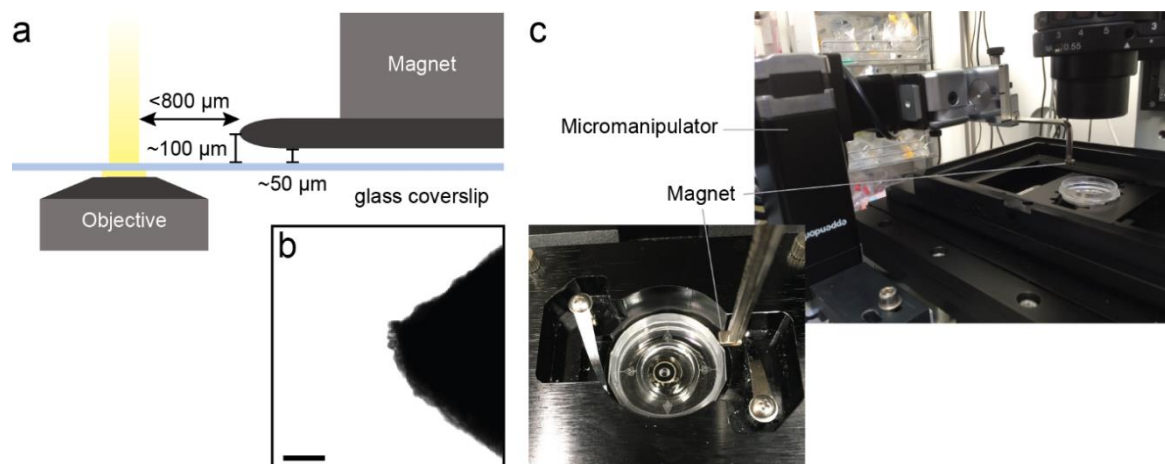


Figure 17: Lateral magnetic tweezer setup

a) Schematic representation of the magnetic tweezer setup. The magnetic needle is adjusted into this position relative to the field of view of the microscope which is set as “home” position on the micromanipulator (PatchMan, Eppendorf). Not drawn to scale. **b)** Transmission light micrograph of the tip of the needle. Scale bar is 10 μm . **c)** Photos of the setup on an IX71 microscope (Olympus; right) and on a Vutara 352 microscope (Bruker; left). The micromanipulator was set to the “off” position. The position moves to the “home” position on the push of a button.

7.2. Manipulation of lipids in an artificial membrane

7.2.1. Tracking of lipids by FMNPs

We first tested the FMNPs for SPT of lipids in an artificial lipid membrane. SLBs were formed on cleaned cover glass from a suspension of small unilamellar vesicles of controlled lipid composition. Biotinylated lipids were incorporated into the SLB such that the streptavidin functionalized FMNPs can bind directly to the membrane. To avoid crosslinking of lipids by binding of several streptavidin molecules on the surface of the particle, only 0.005-0.001 mol% of biotinylated lipid was used in the lipid composition. However, when the biotin was directly attached to the head group of the lipid, only few particles would bind and most particles were immobile. Therefore, we introduced lipids with a short polyethylene glycol (PEG) linker of ~ 10 nm length between the head group and biotin. More FMNPs bound to these SLBs and, importantly, more particles were mobile (Figure 18b, c). However, a fraction of particles was always immobile, and some mobile particles became immobile during observation. They either resumed movement during the period of observation or remained immobile until the end of observation. The mobile particles underwent simple Brownian motion as indicated by MSD analysis of the trajectories (Figure 18c, d) with a mean/median diffusion coefficient D of 0.21/0.18 $\mu\text{m}^2/\text{s}$ (Figure 18e), which is lower than would be expected for a lipid in SLBs (discussed in 7.3.2). Next, I tried to manipulate the lipid movement using the magnetic tweezer setup described in the previous section.

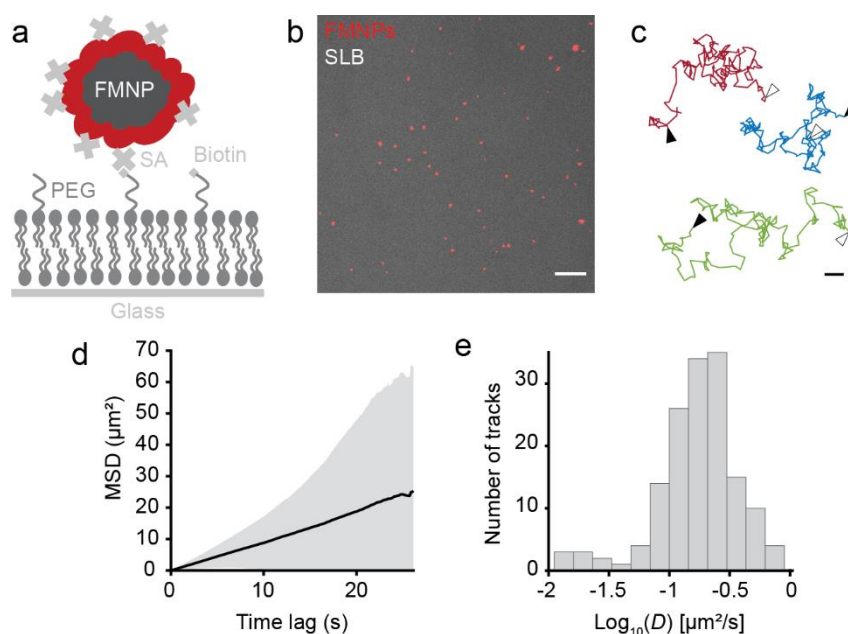


Figure 18: SPT of lipids in an SLB by FMNPs

a) Schematic representation of the targeting strategy. FMNPs bind to lipids with a short PEG linker and biotin (DSPE-PEG(2k)-biotin). Additionally, the SLB contains lipids with only the PEG moiety (without biotin), to “cushion” the SLB. Not drawn to scale. **b)** TIRF imaging of FMNPs (red) bound to an SLB containing 0.001 mol% DSPE-PEG(2k)-biotin and carboxyfluorescein-conjugated lipid (DOPE-CF, grey). Scale bar is 10 μm . **c)** Exemplary trajectories of single FMNPs bound to lipids diffusing in the SLB. Colors are random; start and end are marked with white and black arrowheads, respectively. Scale bar is 1 μm . **d, e)** FMNP-

bound lipids show free diffusion. TIRF imaging with 7.7 Hz for 26 s at room temperature (RT). Trajectories longer than 40 frames and with a diffusion coefficient D over $0.005 \mu\text{m}^2/\text{s}$ were considered ($n = 151$). **d)** Mean MSD plot with s.d. shown as grey shaded area. **e)** Histogram of the logarithmized D calculated per trajectory.

7.2.2. Directional manipulation of lipid movement

Since we could use the FMNPs to observe the free diffusion of lipids in the SLB, we next applied our lateral magnetic tweezer to directionally control the lipid movement. To do so, the tip of the magnetic needle was placed directly at the edge of the field of view on the microscopy (Figure 19a) and $\sim 50 \mu\text{m}$ above the plane of the cover glass to avoid disrupting the SLB (Figure 17a). When the magnetic needle was engaged, the lipids/FMNPs showed a directional movement towards the magnetic tip. When the magnetic needle was removed, the lipids/FMNPs returned to random diffusion. Occasionally, particles became immobile during the magnetic pulling as did the example shown in Figure 19b (the particle was mostly immobilized during the time gap between panel 2 and 3). The particle resumed movement shortly after lifting the magnetic needle. However, both immobilization of particles and regaining of movement were observed with or without the magnetic needle. The particles moved clearly towards the magnet over time, but the displacement was not monotonously increasing. Instead, the movement appeared to be the result of a random walk and with an underlying directional movement with a similar range of displacement per frame (see also 7.4). These results show that we can pull lipid molecules through an SLB by using FMNPs and a lateral magnetic tweezer while tracking the lipid movement with high spatial resolution.

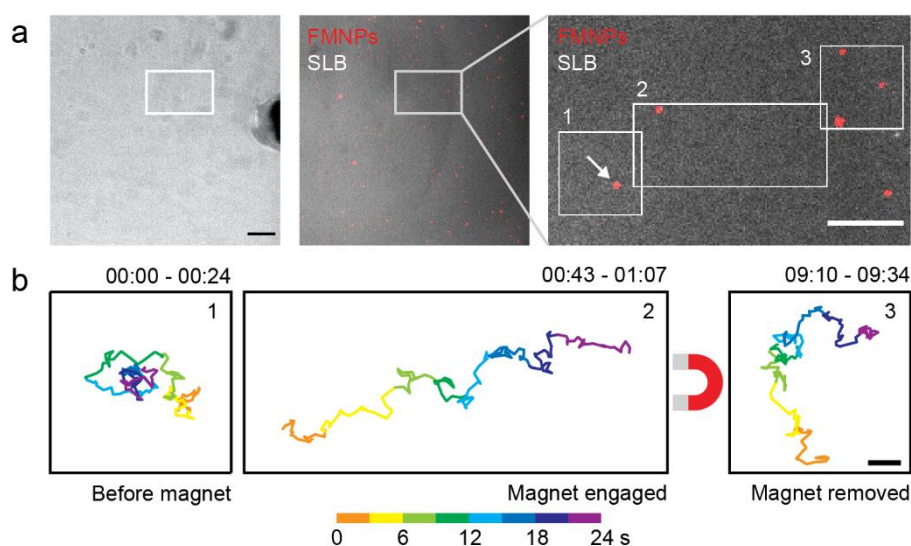


Figure 19: Magnetic manipulation of lipid motion in an SLB by the magnetic needle.

a) Left: Transmission light micrograph of the magnetic needle tip in the “home” position; scale bar is $20 \mu\text{m}$. Middle: Fluorescence pseudo-color merge of FMNPs (red) bound to a DOPE-CF doped SLB (grey; inhomogeneous signal is due to the illumination). Right: Enlarged area relating to b). Scale bar is $10 \mu\text{m}$. **b)** Trajectories of the same FMNP marked with an arrow in a) with the magnetic needle in the “off” position (1, 3) or “home” position (2). Scale bar is $1 \mu\text{m}$.

7.3. Discussion

The “BNF-Starch-redF Streptavidin” particles could indeed be used to simultaneously track and move lipids in an artificial lipid bilayer with a magnetic needle (Figure 19). When the external magnetic field is applied by moving the magnetic needle near to the field of view on the SLB, the particles start to move in a directional pattern, which becomes evident within 10s of seconds. After removal of the magnet, the particles resume random diffusion. This clearly demonstrates the feasibility of our concept to combine high-resolution SPT with magnetic control over the molecule movement.

The lateral magnetic tweezer allows to move the lipids in the plane of the membrane. The magnetic tweezer consisting of a steel needle attached to a permanent magnet and a commercial micromanipulator is a convenient and versatile setup which could be fitted to different microscopes. Compared to optical tweezers, the implementation, handling, and maintenance of such a magnetic tweezer setup is much easier and affordable. Importantly, the magnetic tweezer allows to move many particles over the SLB at the same time (*cf.* Figure 20c), which permits a significantly higher throughput than optical tweezers. Even to simultaneously trap two objects requires a highly sophisticated optical tweezer setup (see 3.2).

7.3.1. Diffusion coefficient of FMNP-tracked lipids

Although accurate measurement of the diffusion coefficient was not within our scope here, it is of note that the FMNP-bound lipids in the SLB moved slower, with $0.21 \mu\text{m}^2/\text{s}$ on average (Figure 18), than what would be expected for phospholipids, which typically move with $\sim 3\text{-}10 \mu\text{m}^2/\text{s}$ in SLBs (Kusumi *et al.*, 2012). As mentioned above (see 6.2 and 6.3.1), the FMNPs diffuse with a D of $2.5\text{-}2.7 \mu\text{m}^2/\text{s}$ in aqueous medium as expected from the Stokes-Einstein formula (2) and determined by SPT experiments. Hence the particle would cap the diffusivity of the coupled lipids (Clausen and Lagerholm, 2011). However, one should mention here, that in practice, determining D is not trivial especially on biological membranes (see 2.3.3) (Martin, Forstner and Käs, 2002; Wieser and Schütz, 2008; Frost *et al.*, 2012; Kerkhoff and Block, 2020), since the accuracy depends on the time and spatial resolution and other technical factors such as background and noise. Thus, comparing values measured with different techniques, samples and spatiotemporal resolution is tricky. Also, different methods have been proposed to calculate the diffusion coefficient (Qian, Sheetz and Elson, 1991; Wieser *et al.*, 2007; Michalet and Berglund, 2012). I have used the classical method by fitting the slope of the MSD curve (Qian, Sheetz and Elson, 1991; Sbalzarini and Koumoutsakos, 2005).

7.3.2. Potential causes of reduced lipid diffusion on SLBs

The diffusivity of the FMNPs alone or the uncertainty in the determination of D cannot explain the more than one order of magnitude difference to literature values measured here. Other possible

reasons for the low mobility include binding of several biotinylated lipids (crosslinking), steric hindrance, and unspecific interactions, which are all inherently connected to the particle size.

Multivalent binding of nanoparticles to SLBs slows down the diffusion of the crosslinked lipids which can even be exploited to determine the valency. Block *et al.* tracked 100-nm diameter lipid vesicles that were tethered with DNA to an SLB and by specifically filtering for fluctuations of D , could distinguish vesicles with distinct numbers of DNA tethers as peaks in the D histogram for up to 9 tethers (Block, Zhdanov and Höök, 2016). Reina *et al.* measured with (STED-)FCS a ~ 40 -fold slow-down of biotin-lipids in SLBs by a multivalent streptavidin-coated 40-nm gold nanoparticle compared to a fluorescent lipid analogue (0.12 vs. $5.3 \mu\text{m}^2/\text{s}$), whereas a smaller probe of 20 nm introduced only a ~ 20 -fold reduction in lipid diffusion ($0.3 \mu\text{m}^2/\text{s}$). The authors regard the difference in D to a higher propensity of the 40-nm probe to crosslink lipids than the 20-nm probe and to a lesser extent to the probe size, highlighting the interdependence of these factors (Reina *et al.*, 2018). In a recent iSCAT study (Liao *et al.*, 2019), a two-fold difference in the diffusion of 20-nm gold nanoparticles mono- and bivalently bound to biotin-lipid was measured in SLBs (1.2 vs. $2.0 \mu\text{m}^2/\text{s}$). Strikingly, by comparing the dependence of the monovalent and bivalent D values on the particle sizes ranging from 10 to 40 nm, the authors claim that the gold probe needs to have a 20-fold faster D in aqueous solution than the target molecule in the membrane in order to avoid probe size-related artifacts, i.e. a nanoparticle ≤ 15 nm to track a lipid species with a D of $1.4 \mu\text{m}^2/\text{s}$. If the factor of 20 between the D of the probe and the target was universal, this would reciprocally mean for our FMNPs that they could only report the diffusion of a membrane molecule below $0.14 \mu\text{m}^2/\text{s}$ accurately. But it remains questionable whether this factor holds up across scales and for different probes. Altogether, these findings in the recent literature point to a combined effect of probe size and binding valency on the detected lipid diffusivity. In our case, the particle size has already been or will be discussed later (see 6.3 and 7.5). Regarding binding valency, the FMNPs contain ~ 30 streptavidin molecules on average according to the supplier. To alleviate the effect of crosslinking, the amount of biotinylated lipid was reduced to 0.001 mol%. At higher concentrations, the particles moved markedly slower on the SLB. However, roughly estimating the average distance $\langle d \rangle$ of biotin-lipids in the SLB by

$$\langle d \rangle = \sqrt{A/f} \quad (18)$$

where A is the surface area of one lipid and f is the fraction of the biotin-lipid, yields ~ 220 nm. Therefore, it is still likely that one FMNP binds several biotinylated lipids and hence the concentration of biotinylated lipid in the SLB could be reduced even further. Another question is whether more biotin-lipid bonds could be acquired by the particle while it is dragged over the membrane. Exemplarily going through individual long tracks, we found that they indeed occasionally showed changes in diffusivity in both directions, which could be interpreted as binding and unbinding events.

Due to the high affinity of the streptavidin-biotin bond it is likely that most sterically possible interactions are already formed upon incubation of the SLB with the FMNPs and dissociation of a formed interaction is unlikely, which are therefore only rare events during our observation period.

Another factor that could contribute to the low mobility are unspecific interactions (van der Waals force, electrostatic and double layer interactions). Liao *et al.* found a small but consistent difference in the D between tetrameric streptavidin and dimeric rhizavidin (both monovalently bound to the membrane lipid), which they attribute to non-specific interactions of the empty biotin-pocket in the streptavidin with the nearby membrane. In our case, possible unspecific interactions and steric hindrance is mitigated by a PEG linker of ~10 nm length between the biotin and phospholipid head group. The linker noticeably improved the efficiency of binding and particle mobility. I will mention that non-specific interactions likely cause completely immobile particles, as the fraction of immobile particles was strongly increased when an old aliquot of FMNPs was used, and aggregation of long-term stored streptavidin is a well-known issue. In control experiments without incorporated biotin-lipid, there was no significant number of particles that would bind the SLB and diffuse over it.

Apart from particle-related phenomena, it is possible that nanoscopic defects in the SLB limited the mobility. The particles seemed to stochastically become immobilized for varying periods of time. Although immobilization and resuming of diffusion was observed both with and without the magnetic influence, it is striking that many immobile particles regained mobility upon release of the magnetic pull, either immediately or after a short time lag. Although FRAP control experiments confirm fluidity of the SLB with the expected kinetics (D of DOPE-CF was $8.6 \mu\text{m}^2/\text{s}$ on average), it is possible that nanoscopic impurities exist in the SLB that immobilize the lipids when they encounter them but do not significantly affect the fluorescence recovery in ensemble. The particle-coupled lipid could become trapped in these defects when a directional magnetic force is exerted but without it, it can escape by Brownian motion. Indeed, in some experiments, small black holes in the SLB were found at the end of the experiment which were not present at the beginning. To test whether the biotin-lipid would also randomly immobilize without the FMNP, one could add fluorescently labeled streptavidin (ideally monomeric) and simultaneously track both probes.

Taken together, the FMNP size, crosslinking, unspecific and steric interactions, and the SLB quality could all contribute to the slow lipid diffusion, but more control experiments would be required to disentangle the influence of each factor. The slow mobility itself does not invalidate our approach; valuable information can be obtained by comparing the motion with and without magnetic influence or over the course of the magnetic pulling (see 8.2). However, the dynamic range in which differences in mobility can be detected and the maximum displacement under magnetic pull within a time period, i.e. the velocity, are limited. This means a smaller surface coverage and thus a lower

information throughput (see also 7.7). However, it is important to stress here, that the movement mode was determined to be Brownian diffusion as shown with the MSD plot (Figure 18), therefore, changes in the motion mode will still be detectable.

7.3.3. Alternative applications of magnetic SPT

The magnetic tweezer setup allows us to apply the magnetic force laterally in the focal plane of conventionally used inverted microscopes which makes it compatible with many optical imaging techniques including super-resolution imaging (see 2.4 and 8.2). We employ fluorescence-based SPT here, but the approach could easily be used with non-fluorescent SPT methods as well, such as iSCAT for even higher temporal resolution. In that case, the requirement for bright and stable fluorescence would not apply and more commercial products with excellent particle properties would be available.

Beyond the scope of this work here, the method might be interesting for studies of the general biophysical properties of lipid bilayers. For example, lipids could be pulled through the SLB at different temperatures or through liquid-ordered and disordered domains. If the force is constant, the diffusion coefficient and velocity could be compared to theoretical predictions.

To summarize, the proof-of-concept that FMNPs can be applied for simultaneous tracking and magnetic manipulation was successful. The FMNPs are useful as SPT probes to observe the diffusion mode of membrane lipids although alternative methods should be chosen to accurately measure their diffusion coefficient. The application of an external magnetic field in plane of the membrane by approaching a magnetic needle with a motorized micromanipulator effectively induces a directional movement within seconds, which is reversible on the push of a button.

7.4. Magnetic forces

After demonstrating that my magnetic tweezer setup was indeed capable of moving diffusing lipids in the plane of the supported lipid bilayer, I asked how much magnetic force was exerted on the lipids by subjecting the FMNPs to the magnetic field of the needle. The standard procedure to calibrate magnetic tweezers is to measure the velocity with which the magnetic particles are attracted to the tweezer tip in a viscous solution. The Stokes formula (17) is then used to calculate the magnetic forces, using the known viscosity of the solution, the particle radius assuming a spherical particle, and the measured velocity. With this approach, Areeya Wedchasan (Wedchasan, 2019) could determine forces in the range of 0.1 pN, which as expected decreased with increasing distance from the magnetic tip ((Wedchasan, 2019), Figure 4.4, p. 34). However, we made the strange observation that when the particles came closer to the magnetic tip than 100 μm , they slowed down and hence the calculated magnetic forces decreased markedly in an almost linear fashion. At the peak around 100 μm from the tip, the magnetic force was 0.1 pN. Another approach to estimate the magnetic forces

is to simulate the magnetic field of the magnetic needle with FEMM (Finite Element Method Magnetics), a software to visualize magnetic field lines of electromagnetic objects and to simulate the magnetic field strength. With the help of Isaac Wong, we generated 2D models of the permanent magnet and the needle tip from the top and side view (Figure S30; (Wedchasan, 2019), Figure 4.1, p. 30). The simulation showed that the magnetic field exhibited a steeper gradient around the tip of the needle than having only the magnet without a needle and thus supporting this setup. Using the equation

$$\vec{F} = V_m \sigma \rho \nabla \vec{B}, \quad (19)$$

derived from Eqs. (12) and (13), where σ is the particle mass magnetization, and ρ the particle density, the magnetic force along the axis of the needle could be calculated ((Wedchasan, 2019), Figure 4.3, p. 32). The magnetic force at 100 μm distance from the tip was 0.3 pN, although this value is likely overestimated as FEMM only allowed the simulation of air as the medium and the magnetic susceptibility of water is lower than air. Importantly, the visualization of the magnetic field lines of the magnet and needle in side view showed that the field lines coming from the tip of the needle were strongly curved ((Figure S30; (Wedchasan, 2019), Figure 4.1, p. 30). Since the magnetic needle can only be placed above the plane of the lipid bilayer, depending on the height of the needle above the plane of the membrane and the lateral distance of the particle to the tip, the force vector could be oriented largely in z . The magnetic nanoparticle would then be pulled more in perpendicular direction to the membrane and experience only less force in lateral direction. In consequence, I tried to always place the needle as low as possible over the sample and the tip in ~ 0.5 mm lateral distance from the field of view instead of directly next to it (see Figure 16a). The visualization made also clear that both methods are not well suited to estimate the magnetic forces for MNPs that are restricted to move in a 2D plane which is placed underneath the magnetic needle.

To estimate the magnetic forces more realistically, we had to perform the force calibration in a planar membrane. When a membrane bound MNP is attracted by the magnetic needle, the movement results from a directed component in direction of the magnetic field and a random component due to the inherent Brownian motion (Figure 20a). By separately extracting these two movement components from the trajectory (Block *et al.*, 2016), the force can be calculated according to the equation

$$F = k_B T \frac{v_x}{D}, \quad (20)$$

where k_B is the Boltzmann constant and T the temperature. The average velocity v_x is given by the linear movement in the direction of the magnetic field (defined as x direction, Figure 20b). The diffusion coefficient D can be extracted from the fluctuations in the direction perpendicular to the

magnetic field (in y). In practice, the average D is calculated from the short-term displacements in both x and y . We performed the calculation for hundreds of particles bound to lipids in an SLB (Figure 20c). If the magnetic needle tip is placed at the side of the field of view, the apparent forces in x -direction are 4.26 ± 6.87 fN (mean \pm s.d., 2161 tracks; Figure 20d) and are undetectable without the magnet (-0.03 ± 4.35 fN, 670 tracks). Also, the apparent force decreases with increasing distance from the tip (Figure 20f). Above $100 \mu\text{m}$ the distance-dependency is obscured by noise. The noise is due to the splitting of trajectories into shorter fragments to calculate the forces for a certain distance to the tip within the field of view of $\sim 200 \mu\text{m}$. The apparent magnetic forces vary slightly with inherent variability of the needle positioning (Figure S31). If the magnet is moved millimeters away (Figure 20f), it is still able to attract the FMNPs and smaller force values are determined (Figure 20g).

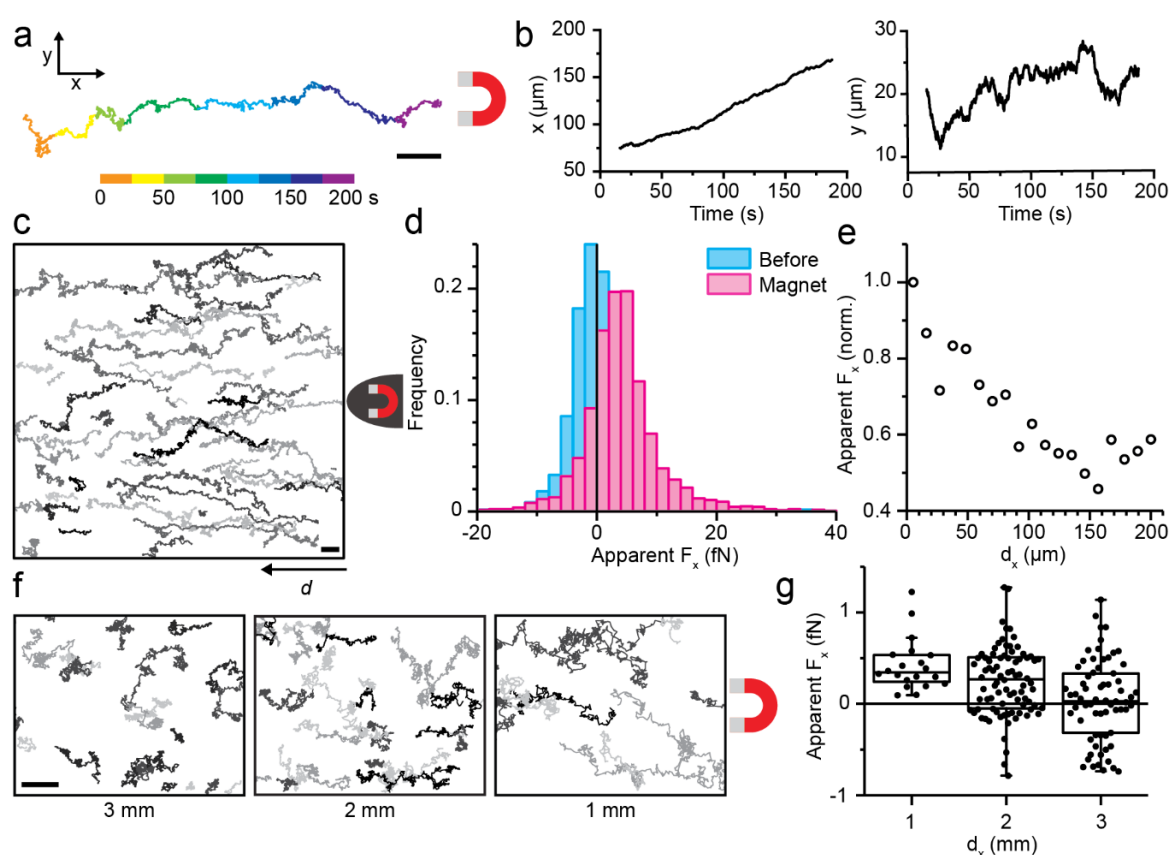


Figure 20: Magnetic force calibration on SLBs

a-b) The trajectory of a magnetically pulled FMNP on an SLB can be split up in a directional component along x and a random component along y . **a)** Time-color coded track. **b)** Plot of the x (left) and y (right) positions over time of the track in a. **c)** Trajectories of FMNPs tracked with the very tip of the magnetic needle placed to the right. A subset of all tracks is shown in random grey levels for clarity. **d)** Histogram of apparent forces F_x per trajectory exerted on FMNPs in presence (magenta, 2161 tracks) and absence (blue, 670 tracks) of the magnetic needle. **e)** Distance dependency of the apparent force. Forces were calculated for sliding windows of each trajectory in the dataset in d) and mapped to the average distance d_x from the tip in direction of x . **f)** Trajectories of FMNPs tracked with the magnet in millimeter distance. **g)** Boxplots of the apparent force for data shown in f. **a-f)** All scale bars are $10 \mu\text{m}$

7.5. Discussion

Calibrating the magnetic forces on SLBs employing Eq. (20) (Block *et al.*, 2016) has two advantages over the approaches using the Stokes law (17) and calculation from the magnetic field simulation with FEMM using Eq. (19). First, the specific geometry of the lateral magnetic tweezer and the confinement of the diffusing particle in 2D space are already considered since the calibration experiments are performed in a similar configuration as the later experiments on living cells (see 7.6). Second, Eq. (20) is independent of the particle properties. Both Eqs. (17) and (19) assume a spherical particle with a radius r . As the particle core appears irregularly shaped (Figure 15), it remains unclear how the particles are shaped overall and how the shape would affect the calculated magnetic forces. In consequence, the forces calculated with Eqs. (17) and (19) likely overestimate the relevant magnetic forces in our system by one to two orders of magnitude ($\sim 100\text{-}300$ fN *vs.* $\sim 1\text{-}10$ fN). The simulation was very useful, nonetheless, as it drew attention to the positioning of the magnetic needle in respect to the bilayer (Figure S30). Other methods to calibrate the magnetic forces are imaginable. For example, Seo *et al.* measured the rupture force of DNA zippers although the force range here would be too small to dissociate the hybridized DNA used in that study and weaker DNA zippers would be required (Seo *et al.*, 2016). The variance-based equipartition method commonly used to calibrate axial magnetic tweezers could possibly be adapted for lateral tweezers (Neuman and Nagy, 2008).

Using the method developed by Block *et al.*, we could determine the magnetic forces to be in the lower femtonewton range, i.e. 1-10 fN, depending on the distance from the magnetic tip. Usual forces in single-molecule force spectroscopy are in the piconewton range (Neuman and Nagy, 2008). For optical tweezers, the force range is 0.1–100 pN. For magnetic tweezers, much larger forces than achieved here are possible with magnetic microbeads, up to 100 pN, and even up to 10 nN using electromagnets. Our force range is thus on the lower spectrum of magnetic tweezers, which is unattainable for optical tweezers.

7.5.1. Physiological relevance of exerted magnetic forces

Femtonewton forces are relatively small forces even at cellular and molecular scales (Monzel *et al.*, 2017). Notably, the displacements per frame in-direction-of and perpendicular-to the magnetic field are comparable, as both the directed and the Brownian motion are directly evident from the trajectories (Figure 20a). Therefore, the energy which is spent to drag the molecule through the lipid bilayer against friction must be on the order of the thermal energy $k_B T$. On the nanoscopic level, the molecules do not experience a “notable” force; it only manifests over the long term (minutes, micrometer scale). The larger the force, the more the resulting movement shifts away from a stochastic towards a deterministic behavior and hence physical barriers would also be detected more reliably. In theory, larger forces could be achieved either by using particles with larger saturation

magnetization or by applying a stronger magnetic field. The former could be achieved by spherical particles (filling the volume with magnetizable content at the same effective particle size), a different chemical composition with higher saturation magnetization and larger particles, although a larger particle size would be undesirable (see 6.1). The magnetic field could be increased by using a larger permanent magnet provided that it can still be accommodated on the microscope setup and the sample holder. Another option that also allows much more control would be to install an electromagnet (Fisher *et al.*, 2006; Weber, Bjerke and DeSimone, 2012; Chronopoulos *et al.*, 2016, 2020). Not only could a stronger magnetic field be applied, it could also be switched on and off without time lag. This would be a significant improvement compared to the delay of ~10 seconds for the mechanic displacement of the magnetic needle using the current micromanipulator setup. Additionally, by placing several magnetic coils laterally (Fisher *et al.*, 2006), the field gradient could be approximately homogeneous within the field of view.

Increasing the magnetic forces would be possible with some modifications to our current setup, but it is not necessarily desirable for our purposes. It is unclear how larger lateral forces applied to membrane proteins on living cells would affect their native behavior and the interactions with other molecules. It has been shown that forces of ~5 pN can dissociate the streptavidin-biotin bond at effective rates (Evans, 2001). Around 50 pN are required to extract a single lipid from a membrane bilayer. The largest force we detected in our assay (~100 fN for singular particles) is still more than an order of magnitude smaller than the disrupting force range. Interestingly, in an early study that used a similar approach with optical tweezers, Sako and Kusumi assumed the energy for the Transferrin receptor to cross between compartments in the Fence model to be ~0.1 pN (Edidin, Kuo and Sheetz, 1991; Sako and Kusumi, 1995). Under such forces, the membrane molecule would be pulled through potential membrane barriers, thus prohibiting the detection of these obstacles by SPT. Instead, our forces (~1-10 fN) will likely permit delicate interactions with the membrane environment while the membrane molecule is moved through the membrane. Therefore, in order to make the detection of barriers more stringent, the forces can be increased by one order of magnitude but likely not more. Of course, as we target the (dorsal) plasma membrane of living cells, the surface topography, and the composition of the membrane and of its apposed structures will be much more complex than on the SLB.

Our current FMNP/magnetic tweezer setup thus enables us to remotely control the movement of membrane molecules by exerting a minimally invasive magnetic force under which the target molecule can still interact naturally with other molecules.

7.6. Manipulation of membrane proteins in living cells

After demonstrating the feasibility of using FMNPs to track and pull membrane molecules in an artificial membrane bilayer and quantifying the involved magnetic forces, we aimed to apply this approach to membrane proteins in the plasma membrane of living cells.

7.6.1. Targeting and tracking of membrane proteins by FMNPs

Since the FMNPs are coated with streptavidin, we can employ biotin for targeting membrane molecules. However, instead of tagging the target proteins directly with biotin, we use an intermediary binder, namely a biotinylated nanobody (Figure 21a). This strategy has the advantage that the stoichiometry of nanobody to FMNP can be tuned. Unlike the composition of an SLB, the concentration of a membrane protein cannot be controlled precisely. Because each particle contains a calculated average of ~30 streptavidin molecules, the target proteins can be crosslinked by binding multiple streptavidin molecules on one nanoparticle. Especially when overexpressing the target protein by transfection, the surface concentration is high and thus crosslinking is likely. Instead, the FMNPs are functionalized with a minimal number of nanobodies per particle. The nanobodies are covalently labeled with biotin, with a short PEG linker for the same reasoning as on the SLBs (see 7.2.1). The FMNPs can be pre-incubated with the nanobodies and unbound nanobody can be separated from the FMNPs using a magnetic separator. The magnetic separation is crucial here. When we directly added the FMNPs together with these mixed nanobodies to cells expressing the target protein on their surface, the FMNPs would bind, but very inconsistently between experiments and also within one sample, e.g. more particles would bind a cell with a low expression of the target protein than a neighboring high-expressing cell (data not shown). I hypothesize that the free nanobodies compete with the FMNP-nanobody conjugates for binding sites and due to the significant difference in diffusion coefficient because of the $>10^5$ -fold difference in volume, the free nanobodies bind much faster and thus block potential binding sites for the nanobody-bound FMNPs. The concentration of unlabeled nanobodies, i.e. without biotin, was high because a low biotin labeling ratio was chosen to avoid aggregation of FMNPs by nanobodies with multiple biotins. By magnetically separating the free nanobody it was possible to achieve consistent binding of FMNPs to membrane proteins via nanobodies. The functionalized FMNPs bind specifically to GFP presented on living cells (Figure 21b), however only on the dorsal plasma membrane due to the particle size.

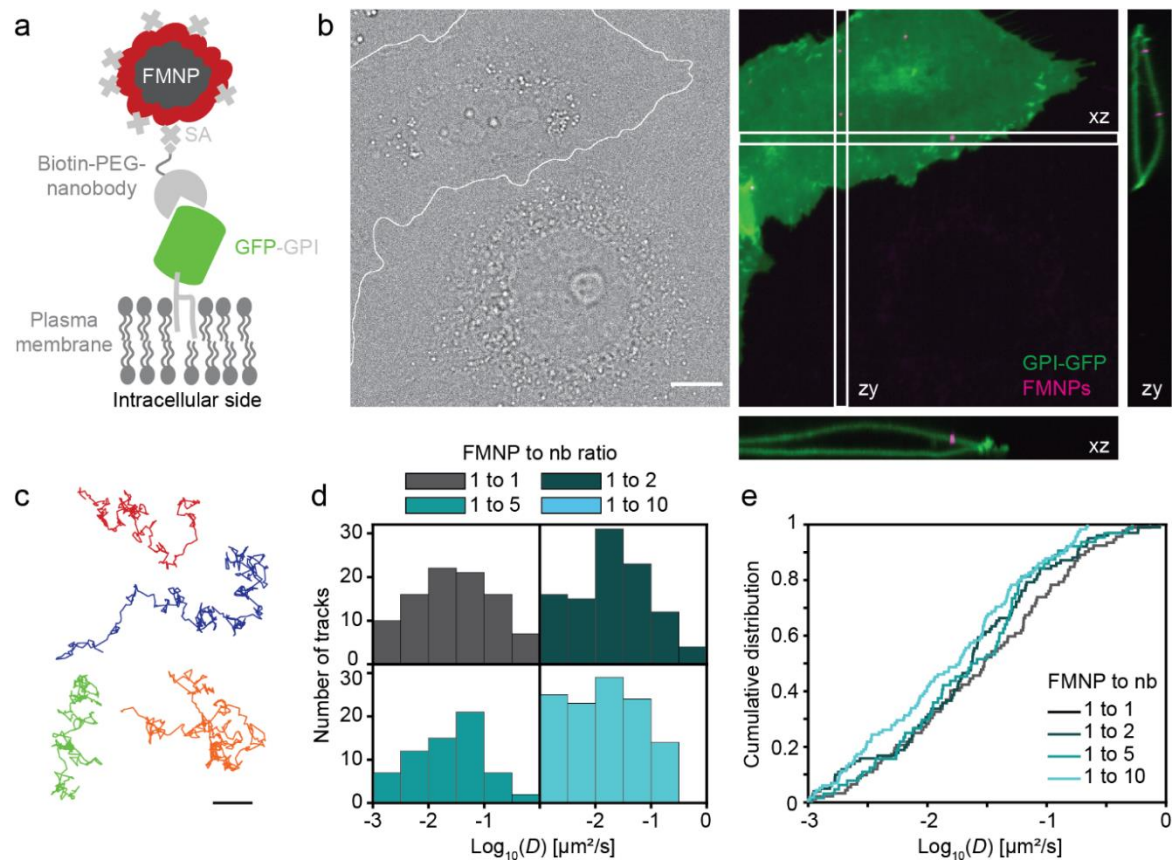


Figure 21: SPT of GFP-GPI via GFP nanobody-coated FMNPs

a) Targeting strategy for extracellularly GFP-tagged membrane proteins, in this case lipid-anchored GFP. **b)** The FMNPs bind specifically to GFP on the dorsal cell membrane via biotinylated GFP nanobodies. GFP-GPI expressing (white outlined) and wild-type CV-1 cells incubated with functionalized FMNPs. Bright field and average projection of a confocal fluorescence z-stack with pseudo-color merge and xz- and zy-slices. Scale bar is 10 μm . **c)** Example trajectories of SPT with 20 Hz for 25 s at RT. Scale bar is 1 μm . **d, e)** Diffusion coefficients D for different FMNP to nanobodies (nb) ratios calculated from the MSD for each trajectory. Trajectories longer than 30 frames and with a diffusion coefficient D over $0.001 \mu\text{m}^2/\text{s}$ were considered ($n = 64-115$). **d)** Histograms of $\log_{10}(D)$. **e)** Cumulative distribution function of $\log_{10}(D)$.

Although in principle, the nanobody-to-FMNP ratio can be precisely tuned, the absolute molar ratio is difficult to determine. This is because both the concentration of biotinylated nanobody and FMNPs can only be determined or assumed with uncertainty. The ratio of biotinylated nanobody *vs.* unlabeled nanobody was estimated from the labeling efficiency (see 9.5.1) and for the FMNPs the concentration given by the supplier was assumed. Additionally, many factors influence the binding, e.g. incubation time and temperature, concentration of target proteins on the plasma membrane, the position where the nanobody is attached to the non-spherical FMNP or the Poissonian distribution of nanobodies to FMNPs (which carry ~ 30 molecules of streptavidin on average according to the supplier). Therefore, I took an empirical approach to determine a practical ratio, using the diffusion coefficient as measure. To this end, I prepared anti-GFP nanobody-FMNP conjugates with different ratios and used them to track GFP-GPI on stably expressing CV-1 cells (Figure 21c). In a previous study from our laboratory (Albrecht, Winterflood and Ewers, 2015), the diffusion coefficient for GFP-GPI tracked with organic dye-labeled GFP nanobodies (SMT) was measured to be $0.46/0.29 \mu\text{m}^2/\text{s}$

(mean/median). Of the ratios tested, the 1:1 FMNP-to-nanobody ratio yielded the closest D to the dye-nanobody labeled reference, albeit lower by one order of magnitude with a mean/median D of 0.051/0.038 $\mu\text{m}^2/\text{s}$ (Figure 21d). However, there was only a significant difference in D between the 1:1 and 1:10 FMNP-to-nanobody ratio (two tailed t -test, $p < 0.005$; Figure 21e). Therefore, a 2-1:1 ratio of FMNP to nanobody was used for all following experiments.

7.6.2. Directional manipulation of membrane proteins

Using anti-GFP nanobodies in a defined ratio to the FMNPs (see 7.6.1), I could track mobile GFP-GPI molecules on living cells. Next, I combined this with the magnetic tweezer to pull the membrane probe through the plasma membrane (Figure 22). When the magnetic needle was 'on', the particles moved towards the magnetic tip (Figure 22a, ii), thus dragging the GFP-GPI through the plasma membrane, like the lipids on the SLBs (see 7.2.2). The particles moved unambiguously over the plasma membrane and not in solution, as they followed the shape of the dorsal cell surface which becomes visible in 3D SPT (Figure 22b). Very rarely, particles detached completely during magnetization, which then moved faster and in and out of focus. When the magnetic needle was 'off' again, the particles resumed random movement (Figure 21 and Figure 22a, iii), like before the magnetic manipulation (Figure 22a, i). Apart from this expected "ideal" behavior, a variety of movement patterns were observed. For some particles, the path appeared very indirect, i.e. there was a net displacement in the direction of the magnetic tip only after a long time and they revisited certain areas (Figure 22c). Other particles continued to move non-directionally despite the presence of the needle. A small subset of almost immobile particles exhibited slow directional movement in alignment with the magnetic field, which could be particles undergoing endocytosis. Moreover, some particles stopped moving, either transiently or permanently (at least until the end of the observation time), both with and without the magnetic needle. In many cases, the particles seemed to become immobile or less mobile upon magnetization. They could then resume random movement immediately or shortly after removal of the magnetic needle (Figure 22d) or stay immobilized (Figure 22e). Rarely, when under magnetic drag, particles "jumped" after being stalled for a short time by making a big step in the first frame of regaining mobility (Figure 22f). Taking all these behaviors together, the diffusion coefficient appears lower during the magnetic manipulation than without the magnet ($p < 0.001$, paired t -test; Figure 22f). Of note, Figure 22g includes all types of trajectories shown in Figure 22a-f, but for trajectories with fast directional movement (Figure 22a, f), the calculated D from the MSD could be biased due to the directional component. Nevertheless, Figure 22g shows that while most particles retained a similar mobility, for a fraction of particles, the diffusion coefficient decreased dramatically upon magnetization (D of around 16% of particles dropped by one order of magnitude). On the other hand, many particles gain in mobility but less dramatically. Of the particles that resumed mobility after removal of the magnetic field, the diffusion coefficient is not significantly

different to the one before magnetic manipulation (not significant (n.s.), two-tailed paired *t*-test; Figure 22g). The velocity of the directional movement measured for stretches of steady, linear movement towards the magnetic tip is $0.23 \pm 0.18 \mu\text{m/s}$ (s.d.; 3 cells of 3 experiments, 9 particles total).

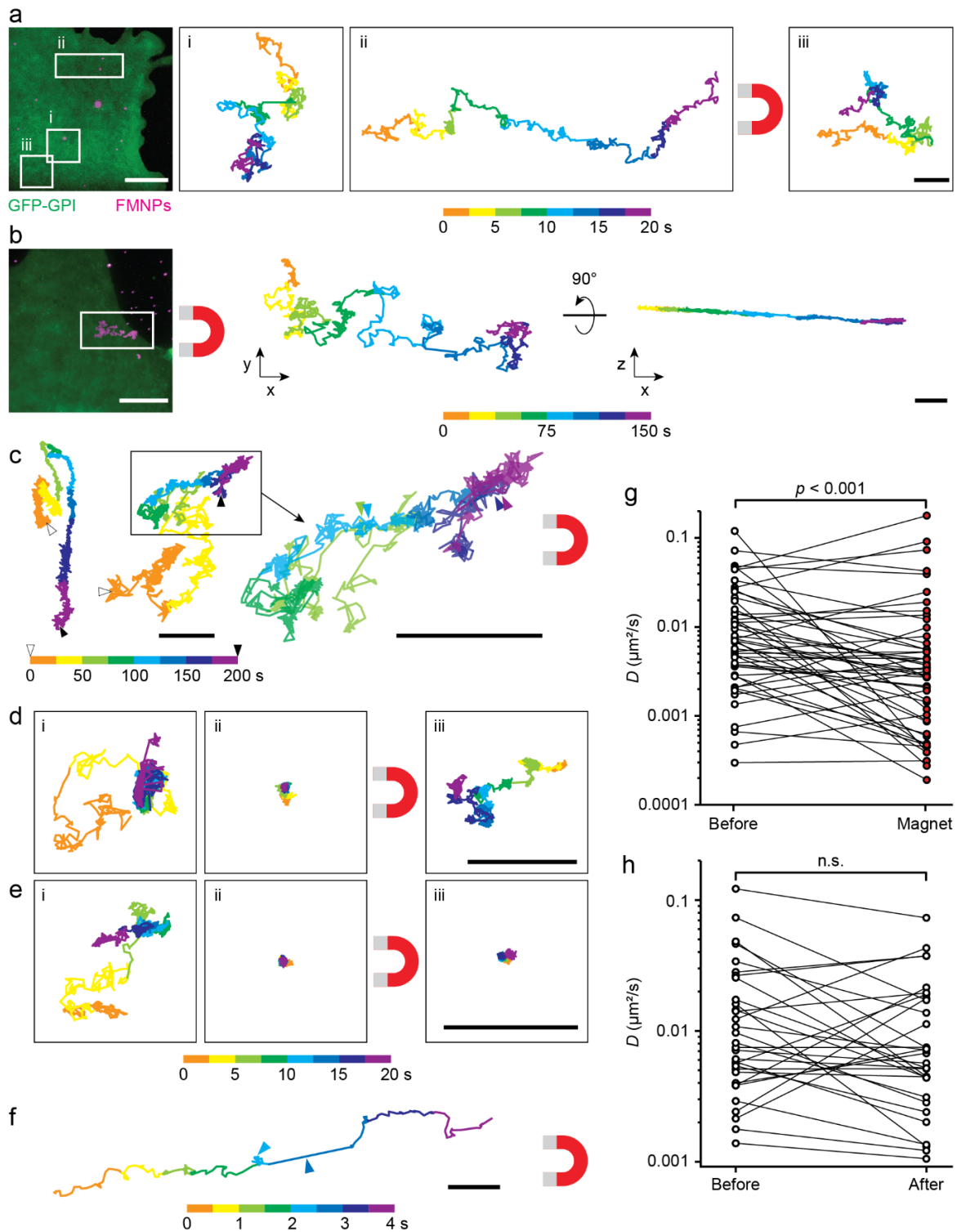


Figure 22: SPT and magnetic manipulation of GFP-GPI via GFP nanobody-coated FMNPs

a) GFP-GPI can be dragged over several micrometers by approaching the magnetic tip. Fluorescence image of GFP-GPI (green) and bound FMNPs (magenta) on the plasma membrane of a living CV-1 cell. Trajectories of FMNPs which moved in the white-framed areas on the cell before (i), during (ii) and after (iii) magnet

engagement. **b)** The FMNPs stay attached to the GFP-GPI during pulling and follow the slope of the plasma membrane in z . Maximum projection of the FMNP video (magenta) merged with GFP-GPI image (green); xy and xz views of the trajectory. **a, b)** White scale bars are $10\ \mu\text{m}$ and black bars $1\ \mu\text{m}$. **c)** Trajectory that shows a net displacement towards the magnet but in an indirect way. Start and end are marked with white and black arrowheads, respectively. In the enlarged part, colored double arrowheads mark areas that are revisited. Scale bars are $10\ \mu\text{m}$. **d)** Example of a particle that became immobile during magnetization but regains mobility after removal of the needle. **e)** Example of a particle that immobilizes upon magnetization and remains so until the end of observation. **f)** Example of a particle under magnetic pulling that stops transiently and then makes a larger step. **d-f)** Scale bars are $1\ \mu\text{m}$. **g, h)** Paired diffusion coefficients D of the same GFP-GPI bound FMNP under different conditions. Note the logarithmic scale. Data from 11 cells of 5 independent experiments, 50 particles in total. The data in **g)** and **h)** are only partially identical because particles can move in and out of focus or the field of view or it is unclear whether it is the same particle under the three conditions. Two-tailed paired t -tests were performed for $\log(D)$. **g)** D values as low as $1 \times 10^{-4}\ \mu\text{m}^2/\text{s}$ were considered to include particles that became immobile upon magnetization. **h)** Particles with low mobility ($< 1 \times 10^{-3}\ \mu\text{m}^2/\text{s}$) were excluded. **a-f)** Note that the scale bars and time color codes differ between panels. Frame rates are 50 Hz, except for 10 Hz in **b)**.

GFP-GPI is only anchored in the outer leaflet of the membrane. To demonstrate the applicability of our approach to generic membrane proteins, I performed experiments with two representative transmembrane (TM) probes (Figure 1a). These membrane probes are L-YFP-GT46, consisting of eYFP, a single-spanning TM domain of the LDL receptor, and the cytoplasmic tail of CD46; and TfR-GFP, which is the eGFP-tagged transferrin receptor (also single-spanning TM domain). Like for GFP-GPI, the diffusion coefficients from FMNP tracking are lower than what has been reported previously (Albrecht, Winterflood and Ewers, 2015) (also see the discussion 7.7). Surprisingly, L-YFP-GT46 appears to diffuse significantly slower than TfR-GFP although both contain a single membrane-spanning TM domain (Figure 1b). All three probes can be dragged over the membrane using FMNPs and the magnetic needle (Figure 1c). Corresponding to the lower mobility, L-YFP-GT46 can only be displaced over a shorter distance than the other two probes within the same period of time.

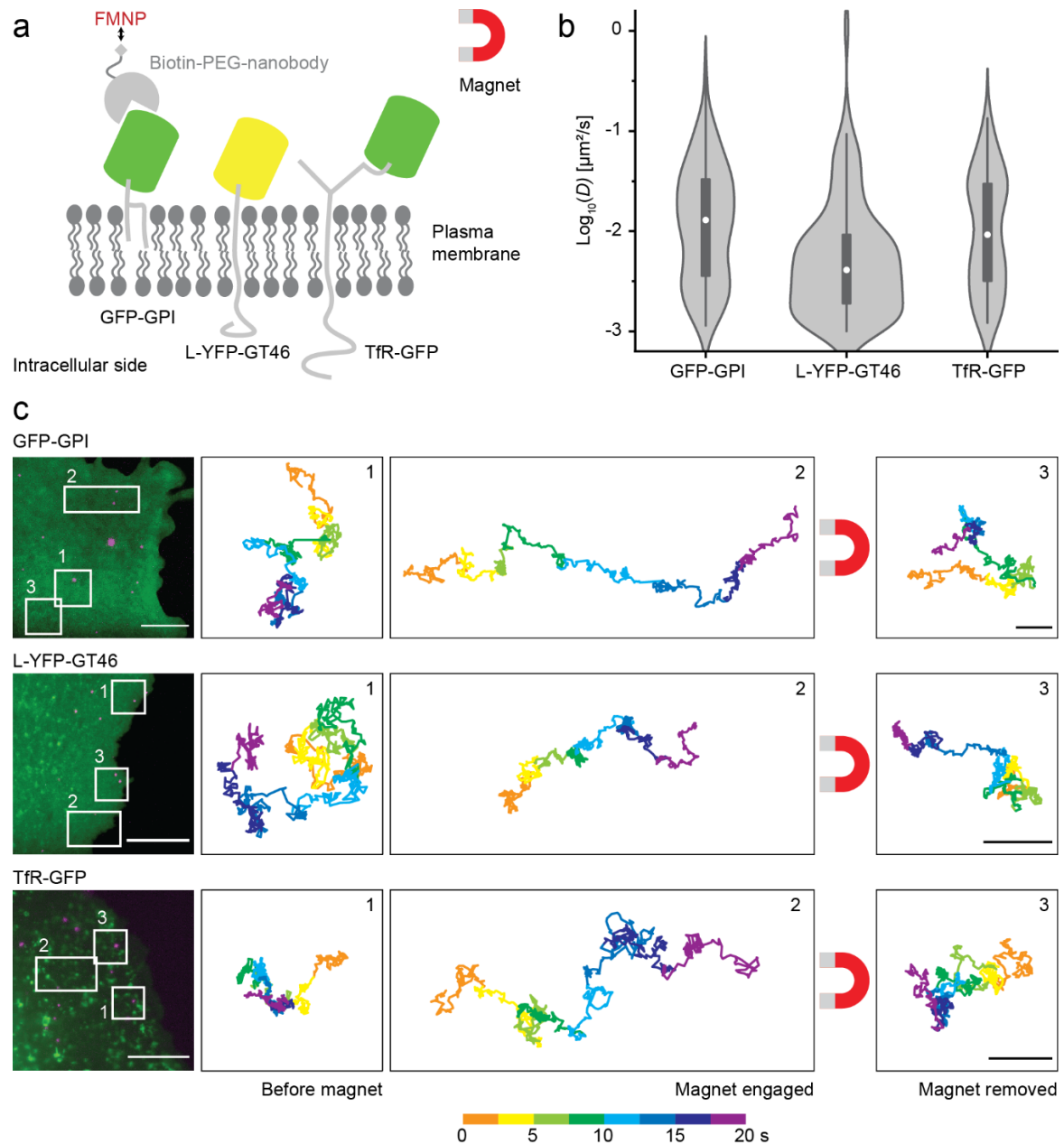


Figure 23: SPT and magnetic pulling of different membrane probes via GFP nanobody-coated FMNPs
a) Schematic representation of the membrane proteins. Not drawn to scale. **b)** Diffusion coefficients of the respective membrane probes tracked with FMNPs in the absence of the magnetic needle. Violin plots of $\log_{10}(D)$ with box; white dot: median, box: interquartile range 25-75% (IQR), whiskers: $1.5 \times \text{IQR}$. Imaging with 50 Hz for 20 s at RT. Tracks over 30 frames and with D over $0.001 \mu\text{m}^2/\text{s}$ were considered ($n = 73\text{-}205$, from 2 independent experiments, 2-6 cells per experiment). **c)** From top to bottom: Experiments of the membrane protein probes GFP-GPI, L-YFP-GT46, and TfR-GFP pulled across the plasma membrane of living CV-1 cells. Left: Fluorescence micrographs of single cells expressing the respective constructs (green) with bound FMNPs (magenta). Scale bars are $10 \mu\text{m}$. Right: Trajectories of exemplary FMNPs which moved in the white-framed areas on the cell before (1), during (2) and after (3) magnet engagement. Trajectories are color coded for time. Scale bars are $1 \mu\text{m}$.

7.7. Discussion

Our FMNP approach can be transferred to living cells by targeting GFP-tagged membrane proteins with anti-GFP nanobodies (Figure 22). The use of an intermittent binder is necessary to tune the stoichiometry. Other binders that could be used are antibodies or fragments hereof (F_{ab}) and the

cognate ligands when targeting receptors (see 2.3.2) (Clausen and Lagerholm, 2011). In these cases, the functionality of the target protein needs to be verified e.g. in downstream signaling. The advantage of using an anti-GFP nanobodies is that many validated GFP-tagged fusion constructs are available for which it has been shown that their function is unimpaired by the tag. This applies also to other commonly used protein tags (e.g. Halo-, SNAP-, His-tag). Moreover, addition of the nanobody may as well change the activity or dynamics of the protein of interest which needs to be considered depending on the question at hand (Küey *et al.*, 2019; Schneider *et al.*, 2021).

7.7.1. Diffusion coefficient of membrane probes tracked with FMNPs

All tracked membrane probes exhibited lower mobility with FMNPs (average D of $0.051 \mu\text{m}^2/\text{s}$ for GFP-GPI) than previously observed in the literature and in our laboratory using fluorescent nanobodies or QDs as labels for SPT (Umemura *et al.*, 2008; Albrecht, Winterflood and Ewers, 2015). Additionally, the mobility of the membrane probes decreases over time and is considerably lower ~ 1 h after incubation with the FMNPs. This time dependence might be due to unspecific interactions acquired over time or by becoming trapped in a smaller area e.g. by endocytic activities.

Like on SLBs (see 7.2.1), the diffusion coefficient is lower by about one order of magnitude than expected. This finding argues for a systematic origin of the lowered mobility either due to the particle properties or my experimental setup. At a more detailed comparison, the factor of difference between expected and measured D on the SLBs was $\sim 15\text{-}50$, whereas on cells the factor is $\sim 6\text{-}9$ (for GFP-GFP, compared to (Umemura *et al.*, 2008; Albrecht, Winterflood and Ewers, 2015). This relative difference agrees with the theoretical considerations made in section 6.3 about the relative influence of the particle size on molecules in an artificial membrane *vs.* in cellular membranes. All the potential probe-related causes of the reduced diffusion have been discussed in detail for SLBs (see 7.3.2) and apply also on the live plasma membrane. Sheets *et al.* compared the diffusion properties of pauci- and multivalent 40-nm gold particles by SPT of Thy-1, a GPI-Anchored protein, in C3H 10T1/2 cells (Sheets *et al.*, 1997). There, they found good agreement between pauci- and multivalent probes for both D and confinement size. On the other hand, Umemura *et al.* found in CHO cells that a MHC Class II-based GPI-anchored probe would exhibit a median D of $0.23 \mu\text{m}^2/\text{s}$ when tracked with fluorescently labeled F_{ab} fragments but only a median D of $0.032 \mu\text{m}^2/\text{s}$ when tracked with a 40-nm gold nanoparticle coupled to the same F_{ab} fragment, matching the D distribution of my experiments. The authors also attributed this difference in mobility to steric hindrance and/or crosslinking (Umemura *et al.*, 2008). Depending on the targeted protein, crosslinking could activate unwanted signaling processes. While titrating the nanobody *vs.* the FMNP concentration clearly improved binding efficiency and crucially the mobility (Figure 21), paucivalent binding cannot be excluded and particles with two or more accessible nanobodies might bind preferentially within the incubation

time of 15 min compared to particles with only one accessible binding site. Analogous to the biotin-PEG-lipid (see 7.2.1), a PEG linker was introduced between the nanobody and the biotin to evade potential steric obstruction. The length of the linker should allow the FMNP to move above the extracellular moieties of membrane glycoproteins and -lipids and components of the ECM. However, depending on the shape of the particle, steric interactions with the local membrane topography and the organization of the pericellular space, might still affect the particle movement. To avoid or alleviate these issues, smaller or spherically shaped FMNPs could be used (see also 6.3). The lowered mobility does not affect the general ability to detect different motion modes (see 7.3). However, an inherent problem of the slow mobility is that the surface coverage and the range to detect differences in mobility is diminished. Therefore, finer differences in diffusivity might be obscured by statistical and technical noise.

The markedly slower diffusion of the L-YFP-GT46 probe is enigmatic. Its diffusion is ~35-fold lower than previously measured (Albrecht, Winterflood and Ewers, 2015) and clearly lower than the other two probes. GFP-GPI and TfR-GFP show a similar diffusion with the distribution of TfR-GFP slightly shifted towards smaller values, which agrees with the larger membrane-immersed TM domain *vs.* the single lipid-anchor. An evident difference between L-YFP-GT46 expressing cells and the other membrane probes was that the cells appeared much brighter (the reference images in Figure 1 are adjusted for contrast and do not represent the original brightness level). The brightness of eYFP is slightly higher than eGFP (45 *vs.* 34, ratio of extinction coefficient and quantum yield) (Lambert, 2019), but both have been imaged with the same microscopy settings in the channel optimized for GFP in terms of excitation and emission filter. Therefore, I assume that the considerably brighter L-YFP-GT46 plasma membrane signal reflects a higher protein concentration. Indeed, the L-YFP-GT46 construct contains a sequence that prevents endocytosis (see 9.7) and the secreted protein accumulates in the plasma membrane. This might have led to more molecular crowding and/or crosslinking in comparison to the other two membrane probes.

7.7.1. FMNP tracking on other cells

An interesting notion is that using the same experimental setup to track GFP-GPI in neurons and neuron- or astrocyte-like cells (derived from neural stem cells), visibly faster diffusion was observed (preliminary data). Two-dimensional calculation of the diffusion coefficient yields a median D of $0.063 \mu\text{m}^2/\text{s}$ which is only slightly higher than on the CV-1 cells but likely underestimating the real mobility since the GFP-GPI can also move over the sides of the neural processes (Wieser and Schütz, 2008). This cell-type dependent difference in mobility when tracking with FMNP could be explained in different ways: CV-1 cells could have a denser ECM or a different matrix composition which promotes more steric hindrance or unspecific binding, or a different lipid composition in the plasma

membrane than neural cells. The rounded shape of the neural processes with mostly positive membrane curvature could facilitate the movement of the large, irregularly shaped FMNPs. The CV-1 cell membrane on the other hand has more variation in membrane curvature in the mesoscale (see also 8.2), probably also in the nanoscale, and thus might impose more steric obstruction. The influence of the cytoskeleton underneath the plasma membrane will also be discussed in section 8.3, but it is worthwhile to shortly compare the cortical cytoskeleton between CV-1 and neural cells here. The restriction of the diffusion of phospholipids and membrane proteins by the cortical cytoskeleton depends on the effective mesh size, which has been found to differ between cells lines (Andrade *et al.*, 2015; Fujiwara *et al.*, 2016). In platinum-replica electron microscopy of unroofed cells, the subplasmalemmal cytoskeleton of COS-7 cells (which are derived from CV-1 cells) appears denser and more multilayered than in neurons (Vassilopoulos *et al.*, 2019; Yang and Svitkina, 2019). This difference in density would support the notion of slower diffusion in the CV-1 versus the neural plasma membrane. However, due to the multiple layers of the COS-7 cortex, it is not clear how dense the membrane-associated layer is. Additionally, it can be assumed that the CV-1 cytoskeleton is more dynamic since the submembrane neuronal cytoskeleton is considered to be rather stable (Xu, Zhong and Zhuang, 2013; Zhong *et al.*, 2014; Ganguly *et al.*, 2015). To clarify these questions, one would need to measure the membrane molecule diffusion in those cell types thoroughly in 3D and acquire more information on the composition and organization of the plasma membrane including submembrane cortex, ECM, and their connections to the membrane.

7.7.1. Movement behavior under magnetic drag

When subjected to the external magnetic field of the magnetic needle, the FMNPs can drag lipid-anchored and transmembrane proteins over micrometers on the plasma membrane within seconds to tens of seconds (Figure 1). However, a significant portion of particles deviate from the expected behavior of random movement before magnetic manipulation and directional movement during magnetic manipulation (Figure 22). Independent of the initial mobility, some particles do not move directionally under magnetic drag. This could be due to a low iron oxide content in the particle core and hence a low magnetization under the permanent magnetic field. Also, it is not uncommon that particles under magnetic pull revisit the same areas and move back and forth in one area. This type of movement suggests that they are restricted in their movement to a certain area when the directional force is applied. Also, the particle occasionally moved backwards after release of the magnetic tweezer and revisited the same areas as before under magnetic drag. This could potentially support the notion that the barriers are elastic and were deformed under magnetic pull, which was released when the magnetic field was removed. Optical tweezer studies found the compartment boundaries to be elastic with a spring constant of 3 pN/ μm (Sako and Kusumi, 1995). Therefore, it would be interesting to perform experiments with two magnetic needles mounted at opposite sides of the field

of view such that one can pull first to one side and then revert the direction of magnetic force (Lipfert, Hao and Dekker, 2009).

The immobilization events, which were partially random and partially correlated with approaching or removal of the magnet (Figure 22d, e), could be caused by (reversible) trapping or by irreversible specific interactions (e.g. endocytosis). Consistent with these qualitative observations is that a significant portion of particles have a slower D when the magnet needle is 'on' than before (Figure 22g). Some particles also moved very fast under the magnetic drag (Figure 22f) and these particles seemed often brighter. This observation suggests that these particles had a larger core and thus exerted more magnetic force which may have pushed them over potential barriers in the membrane. Especially when the particle stopped transiently and then made a clear "jump" in their directional path, one might imagine that the membrane probe passed an elastic barrier there. However, these jumps cannot be thought of as propelled movement through release of energy stored by elastic deformation of the barrier. Because of the high viscosity of the membrane bilayer, the molecule would be immediately stopped (Sako and Kusumi, 1995). Instead, it is more likely in these cases that the molecule passed into an area with less dense or weaker barriers. The principle of the magnetic tweezer approach here is very different to optical tweezer experiments. If the optical trapping force is insufficient to overcome the barrier, the particle is released from the optical trap, while with magnetic tweezers, the force is constant and the particle will stop in front of the boundary or move around it (see 8.1).

The current magnetic tweezer setup only allows measurements at room temperature. It could be argued that the lower temperature induces stress signaling in cells and possibly altered cellular behaviors. Regarding diffusion, only a little effect would be expected for a difference of 15 K between room temperature and 37°C, which makes for a 5% difference in D for Brownian diffusion. On the other hand, the kinetics of endocytosis and the turnover of the cytoskeleton (see 1.3.1) is also slowed. To enable magnetic manipulation at 37°C, a large incubation chamber would have to be installed or the magnetic tweezer setup would have to be miniaturized.

At this point, these observations remain anecdotal, as the current dataset is too little for a thorough statistical analysis. With more data, the frequency of certain behaviors could be determined and correlations with certain sites of the cell (e.g. lamellipodium *vs.* perinuclear area) could be made. In principle, one could increase the particle density to retrieve more information per cell. But already under the current conditions of maximum a few 10s of particles per cell, I have occasionally observed that two particles fused under magnetization. In previous work, large scale aggregation of magnetic particles was intentionally utilized to elicit receptor signaling (Mannix *et al.*, 2008; Bharde *et al.*, 2013; Seo *et al.*, 2016). For our single-particle approach, the particle density must be chosen with care. The

density must be lower than for standard SPT which limits the throughput. On the other hand, the throughput is still much higher than using optical tweezers.

Furthermore, it would be interesting to perform a sub-track analysis as different behaviors were exhibited in one trajectory, and to map these changes spatially to the cell surface (see also 8.2) (Beheiry, Dahan and Masson, 2015; Vega *et al.*, 2018). In this context, it could be interesting to calculate the instantaneous velocity or acceleration, or the apparent force (see 7.4) for trajectories on living cells. I have refrained from calculating the apparent force on cells like on SLBs, because the presence of physical obstacles in the plasma membrane is expected to affect both the diffusion coefficient and the velocity of the dragged membrane molecules (Eq. (20); see 1.3.1). However, as seen for the force calibration, more information can be extracted by splitting the trajectories into the directional component in direction of the magnetic gradient and the random component perpendicular to the force vector (Block *et al.*, 2016). By calculating the velocity, acceleration, or apparent force (or simply the ratio of velocity in x and D in y) over appropriate rolling windows, one could map them to the cell surface. For such analyses, an even higher frame rate would be desirable such as it is possible by iSCAT (Taylor *et al.*, 2019). Changes in these parameters might inform of local heterogeneities and could be correlated with cellular structures (see also 8.2). Such sub-track analysis would also be helpful to detect subtle differences in the movement behavior for example between control conditions and drug treatment (see also 8.3.1). The potential to analyze the random and directional movement component individually and to relate them to each other and to the cellular location is an advantage of using magnetic tweezers *vs.* optical tweezers. Due to the centering force exerted by optical tweezers, the natural diffusive behavior cannot be observed under optical trapping.

In this section, I have demonstrated that FMNPs can be used for high-resolution SPT of membrane lipids and proteins on living cells, although other methods should be complementarily used to measure the diffusion coefficient accurately. Using the magnetic tweezers, the movement of the target membrane molecules can be steered into one direction, exposing behaviors that cannot not be observed otherwise. This method provides a versatile tool to manipulate the motion of molecules in the plasma membrane and to observe the movement with high spatiotemporal resolution. Thus, various dynamic and site-specific activities of membrane molecules can be studied with this approach. Signaling processes often require oligomerization or clustering of membrane receptors and recruitment of co-factors in a concerted manner. Magnetic manipulation could be used to perturb individual components dynamically and to thus test the response of the signaling network to these perturbations (see also 8.3.2). On the other hand, the different movement patterns of the membrane probes observed under magnetic pull raise the question what caused them. In line with the theories of restricted movement in the plasma membrane of living cells (see 1.3), these patterns could be

caused by physical obstacles in the plane of the membrane, i.e. nanoscopic diffusion barriers, or by specific interactions with certain molecular species. In the next section, I will investigate whether diffusion barriers can be identified with magnetic manipulation by FMNPs and magnetic tweezers.

8. Detection of barriers to the diffusion of membrane molecules

As we have now seen, magnetically dragging membrane proteins via magnetic forces through the plasma membrane of living cells revealed a wide range of intriguing behaviors, which implies that the tracked proteins have possibly encountered a range of structural heterogeneities in the plasma membrane. These structures include specific membrane topologies, the ECM, endocytic assemblies, transmembrane complexes, and the cortical cytoskeleton (1.3), some of which will be addressed in this section. To relate the path of the magnetically controlled membrane probes with the membrane and surrounding cellular structures, the trajectories were overlaid onto reference images in other fluorescence channels recorded during the SPT session or onto post-hoc recorded images after fixation and staining.

8.1. Correlation with absolute barriers

To demonstrate the capability of the FMNPs to detect diffusion barriers to membrane molecules, we first investigated naturally occurring, obvious barriers. Such a barrier exists for example at the edge of an SLB, either at the border of the glass substrate or at defects within the bilayer (Figure 24a). If lipids in an SLB are pulled against such a defect using FMNPs and magnetic tweezers (see 7.2.2), they cannot move across the edge of the defect and instead move along the border of the continuous bilayer (Figure 24a). Doing so, the particles delineate the shape of the bilayer edge with subpixel precision surpassing the diffraction-limited TIRF image of the fluorescently labeled SLB (Figure 24b). In another experiment, a semipermeable barrier was observed (Figure 24c, d). The SLB exhibits a defect at which some of the particles are stalled (Figure 24c) while other particles cross this barrier quickly or after some random movement (Figure 24d) in front of what appears as a thin, slightly darker line in the fluorescence image of the SLB (Figure 24c, inset). Therefore, the membrane seems to be continuous, at least in part, over this defect. There could possibly be a cut or scratch in the cover glass over which the bilayer could partially form, creating a discontinuous physical barrier.

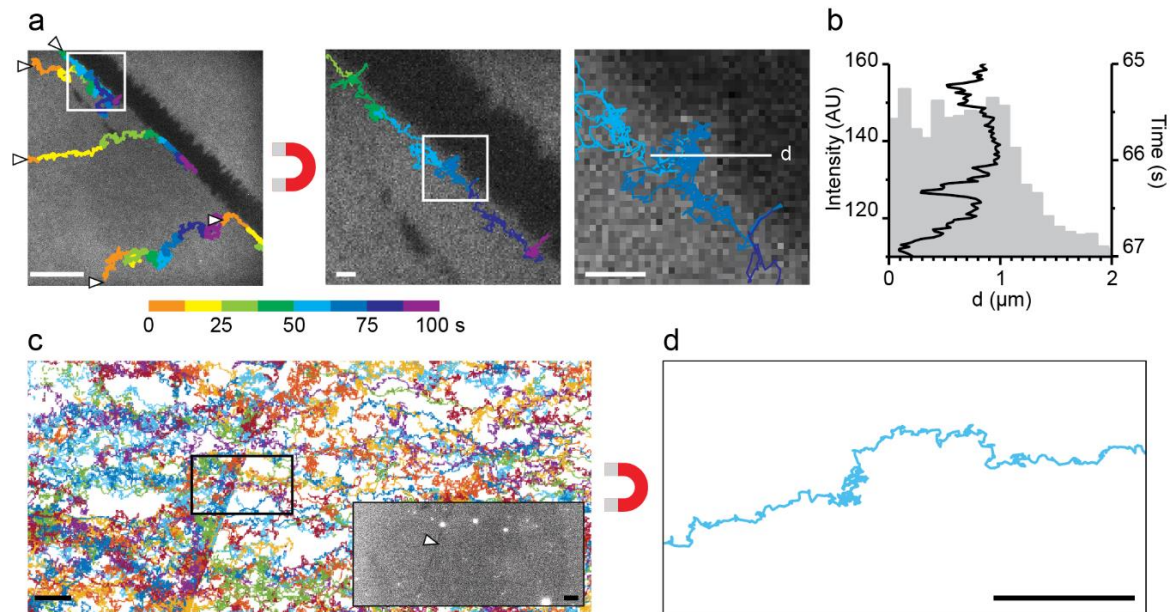


Figure 24: Correlation of FMNP-pulled lipid trajectories with the SLB topography

a, b) FMNP-coupled lipids in an SLB are pulled against the edge of the continuous lipid bilayer at a defect in the SLB. Trajectories are color coded by time and overlaid onto the TIRF image of the SLB (doped with DOPE-CF). Arrows mark the beginning of each trajectory. Scale bar is $10\ \mu\text{m}$. Middle: Enlarged views of the boxed areas. Scale bars are $1\ \mu\text{m}$. **b)** Plot of the FMNP localization in direction of the white line (d) shown in a) over time above the plot of the SLB fluorescence intensity in the TIRF image along (d). **c, d)** Semi-permeable defect in an SLB. Scale bars are $10\ \mu\text{m}$. **c)** All trajectories recorded on the SLB in random colors per track. Inset: TIRF image of the DOPE-CF doped SLB after SPT imaging; the brightness was set very high to make the fracture visible (marked with an arrowhead). **d)** Enlarged view of a single track of a particle that was hold off for a while before crossing the defect in the SLB.

To test whether our method can detect physical obstacles when they are peripherally attached to an otherwise continuous membrane, I turned to membrane sheets. Membrane sheets are generated by unroofing adherent cells, i.e. removing the dorsal membrane, cytosol and in this case also the nucleus and other internal organelles, and hence the inner face of the ventral plasma membrane is exposed (Figure 25a, b). Although most of the cytoskeleton is removed, a dense meshwork of cortical components such as membrane bound actin remains on the ventral membrane. The inner leaflet probe MyrPalm-YFP (myristoylated and palmitoylated eYFP; MP-YFP) allows binding by the nanobody-FMNPs in the same manner as GFP-GPI for the outer leaflet (Figure 25a). The cortical actin can be visualized live by staining with phalloidin-AF647 during the incubation with nanobody-FMNPs (Figure 25c). Most particles moved clearly between the membrane-bound actin filaments. In areas of relatively sparse actin, the particles can drag the MyrPalm-YFP through the membrane sheet when the magnet is applied (Figure 25d). In areas of intermediate actin density, the particles can “go around” actin filaments (Figure 25e). In densely occupied areas, the particles appeared to be more confined or even immobilized by the surrounding actin upon magnet engagement (Figure 25f). This is reflected also by the diffusion coefficient and the slope of the moment scaling spectrum for trajectories without external magnetic field and under the magnetic needle (Figure 25g, h). The MSS

slope is a measure of different diffusion modes exhibited by the diffusing molecule (see also 2.3.3) (Ferrari, Manfroi and Young, 2001; Ewers *et al.*, 2005). Free diffusion is characterized by an MSS slope of 0.5, while <0.5 indicates the subdiffusive (i.e. confined diffusion) motion regime. During magnetization, the population of low mobility tracks ($0.01 > D > 0.001 \mu\text{m}^2/\text{s}$) increased while the mobile fraction ($D > 0.01 \mu\text{m}^2/\text{s}$) became slower compared to before the magnetic manipulation (peaks at $0.16 \mu\text{m}^2/\text{s}$ before and $0.05 \mu\text{m}^2/\text{s}$ during magnetization; Figure 25g). The MSS slope shows initially two populations of trajectories, a smaller fraction of strongly confined particles with an MSS slope close to zero, and a broad fraction of moderately confined particles with a peak at 0.3 (Figure 25h). Under the magnetic field, the population of freely diffusing particles practically vanished leaving a strongly skewed distribution towards low MSS slope values. Although the movement of the FMNP-tagged MyrPalm-YFP appears to be overall affected by the remaining actin meshwork on the membrane sheet, there are also cases of particles that moved in flat areas devoid of actin and became confined or immobilized when the magnetic needle was approached. As I have only stained for actin in these experiments, it is up to speculation whether other cortical components, transmembrane or integral proteins or even remaining membrane-bound internal organelles such as mitochondria or the endoplasmic reticulum (ER) may have caused the confinement (Yang and Svitkina, 2019). Additionally, the sensitivity and diffraction-limited resolution of the confocal spinning disk microscopy used in these experiments was probably insufficient to resolve smaller single actin filaments.

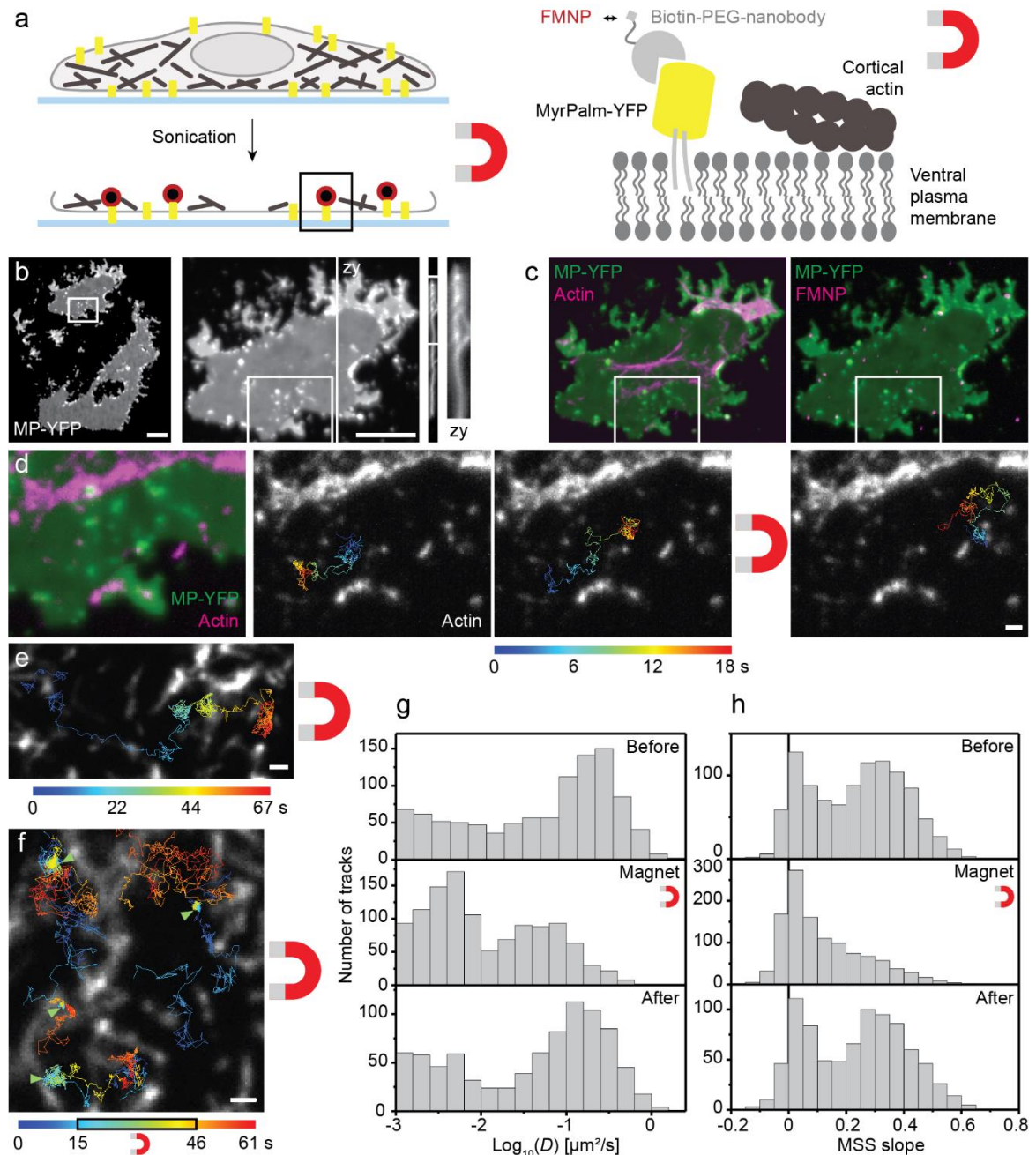


Figure 25: Correlation of FMNP-pulled MP-YFP trajectories with the cortical actin on membrane sheets
a) Schematic representation of membrane sheet generation and targeting of the inner-leaflet probe MP-YFP. Not drawn to scale. **b)** Membrane sheets represent the single ventral plasma membrane. Average projection of a confocal z-stack of a MP-YFP sheet. Views of the zy-plane show dorsal membrane preserved at the cell edge. Scale bars are 10 μm . **c)** Membrane-bound actin stained with phalloidin-AF647 (magenta, left) and FMNPs (magenta, right) bound to MP-YFP (green). Maximum and average projection of a z-stack of actin and MP-YFP, respectively. **d)** MP-YFP can be dragged by FMNPs in areas where little actin has remained on the membrane sheet. Overlay of time-color coded trajectories (20 Hz) on the maximum projection of actin in the region marked in b, c). **e)** FMNPs move around “free-standing” actin filaments when being dragged by the magnetic needle. **f)** In actin-dense areas, the particles become virtually immobile during magnetization (marked with arrowheads) while before and afterwards, they can move in the gaps of the cortical actin mesh. The magnetization period is indicated in the time-encoding color bar below d-f) Scale bars are 1 μm . **g, h)** Diffusion coefficient and MSS slope calculated for trajectories of FMNP-coupled MP-YFP before, during and after magnetic needle engagement. Data from tracks shorter than 30 frames and with $D < 0.001 \mu\text{m}^2/\text{s}$ were disregarded. **g)** Histograms of $\log_{10}(D)$. **h)** Histograms of the MSS slope.

8.2. Correlation with cellular structures

In living cells, another trivial “barrier” exists at the cell edge. The “barrier” here results from the membrane curvature at the cell edge placing the magnetic field in a perpendicular orientation to the plane of the membrane while the forces are too weak to rip off the FMNPs from the bound membrane protein. When membrane proteins are magnetically pulled (see 7.6.2) until the cell periphery, they demarcate the boundaries of the cell membrane (Figure 26a) with high precision including prominent structures such as filopodia (Figure 26b). The local membrane topography could generally explain some of the restricted movement patterns that a significant portion of the FMNP-labeled membrane probes show under influence of the magnetic field (see 7.6.2). Mesoscale and nanoscale membrane deformations such as protrusions, e.g. ruffles or spikes, as well as cavities e.g. created by endocytic activities, could limit the range of movement considerably (Adler *et al.*, 2010). Due to the lateral orientation of the magnetic needle and the inhomogeneity of its magnetic field (see 4.1.3), the effective magnetic force in-plane with the plasma membrane experienced by the FMNP will depend on the location on the cell and the local inclination of the membrane. Membrane ruffles are dynamic membrane protrusions commonly found in the lamellipodium of adherent cells (Figure 26c). Biplane mode imaging provides a rough picture of the membrane topography by reproducing two focal planes simultaneously (Figure 26d). Areas of higher GFP signal intensity can be identified as membrane ruffles which extend from the plane of the surrounding membrane. Indeed, particles moved strikingly around these areas and even seemed to partially follow the membrane topography in z (Figure 26d, e).

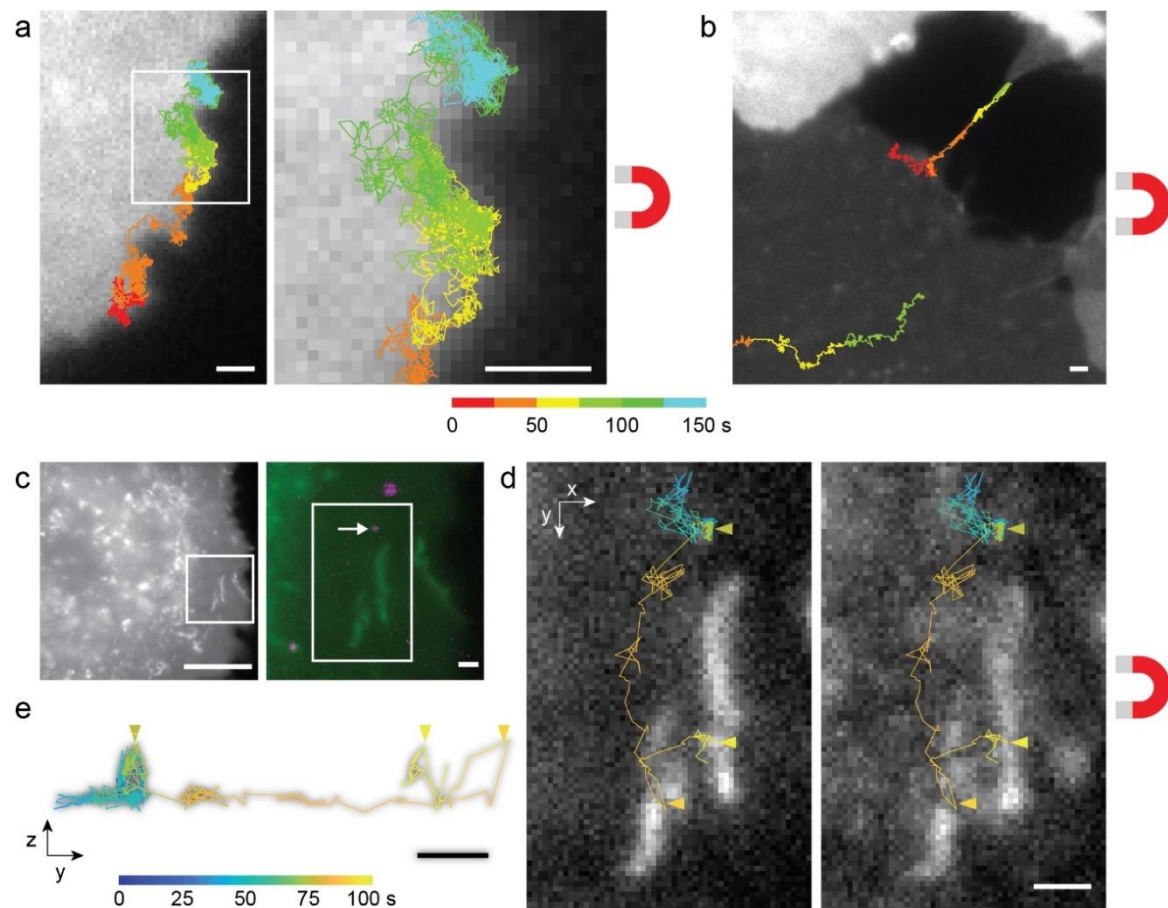


Figure 26: Correlation of FMNP-pulled GFP-GPI trajectories with membrane ruffles

a, b) FMNP-coupled L-YFP-GT46 on CV-1 cells are pulled to the cell edge. Scale bars are 1 μm . **a)** The track maps the cell edge. **b)** L-YFP-GT46 is dragged into a thin filopodium contacting another cell. **c)** CV-1 cells have membrane ruffles in the lamellipodium. Overview of the GFP-GPI CV-1 cell and enlarged area of the lamellipodium as merged image of GFP-GPI (green) and FMNPs (magenta). Scale bars are 10 and 1 μm . **d, e)** The path of the magnetically dragged GFP-GPI appears to be blocked by the membrane ruffles and it seems to move up in z (marked with colored arrowheads) when encountering these membrane structures. Trajectory of the particle marked by an arrow in **c)**, color-coded by time. Scale bars are 1 μm . **d)** Overlay on the upper plane (left) and lower plane (right) of the biplane GFP-GPI micrograph. **e)** View of the same trajectory in yz , shaded for better visibility.

As seen on the membrane sheets, the membrane-attached actin meshwork can restrict the movement of magnetically dragged membrane probes when both actin and FMNP are attached to the same face of the membrane. To ask whether the cytoskeletal cortex underneath the plasma membrane could also act as a physical barrier to the movement of membrane probes on the outer leaflet of the membrane, I performed correlative SPT and 3D super resolution imaging. First, I tracked and magnetically manipulated the movement of GFP-GPI on the surface of CV-1 cells (Figure 27a). Then, I fixed the cells immediately after live-cell imaging and stained the filamentous actin (F-actin) with phalloidin-AF647 (Figure 27b). Finally, I used biplane *d*STORM super-resolution microscopy to visualize the 3D volume of the actin cytoskeleton (Figure 27c). To overlay the diffraction-limited and super-resolved image of the F-actin with the trajectory, we aligned them with fiducial markers which were present in both the live-cell SPT and fixed-cell *d*STORM experiments (registration software in

Matlab, written by Braedyn Au). Figure 27 shows a striking example of such an experiment (more examples see Figure S32). The GFP-GPI molecule first moved over the cell membrane in a meandering path for $> 2 \mu\text{m}$ towards the magnetic needle, but then it slowed down and came to a halt (Figure 27a). The dorsal plasma membrane, as indicated by the GFP-GPI signal, was relatively flat at this site. In the actin overlays, it appears that the particle avoided sites of dense F-actin on the way (Figure 27b, e), which was observed also in other examples (Figure S32). It then slowed down exactly where a thick, bundled actin filament was located, and seemed to slide along this filament in direction of the magnetic field. It stopped moving completely between the long filament and a bright actin cluster and remained immobile until the end of the imaging session. To rule out that this filament is located in the cytosol or on the ventral side of the cell, I cut the 3D volume into a dorsal and ventral slice (Figure 27d). Where the actin filament in question is located, there is a clear gap between the dorsal and ventral actin cortex (yz-view in Figure 27d). This result strongly suggests that the FMNP-steered GFP-GPI experienced a physical hindrance imposed by the actin filament at this site. Which molecules and what mechanism exactly stopped the GFP-GPI in its path remains open to speculation.

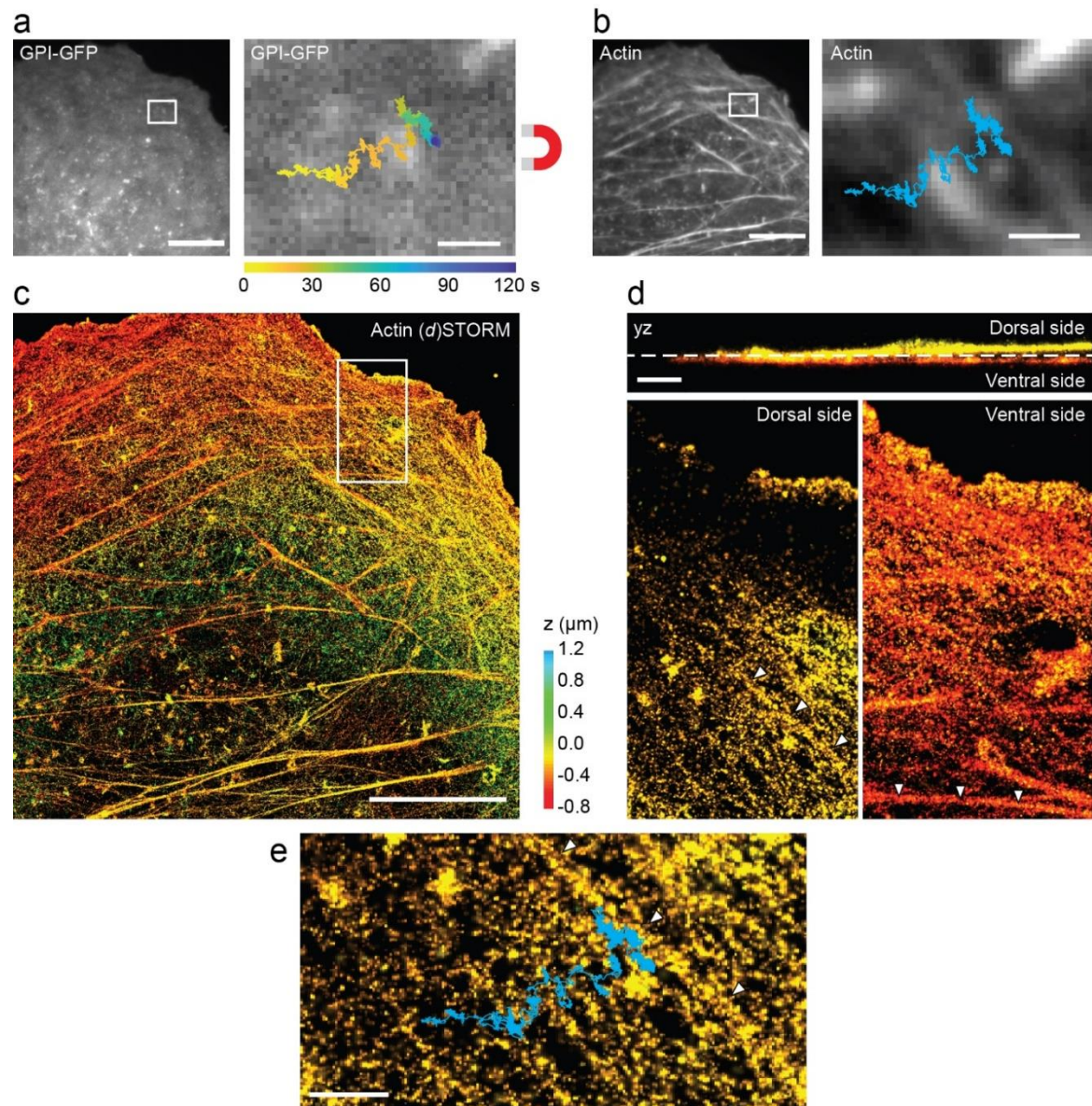


Figure 27: Correlation of FMNP-pulled GFP-GPI trajectories with the subplasmalemmal actin cytoskeleton
a) Live fluorescence image of the membranous GFP-GPI signal in a CV-1 cell. Time color-coded trajectory of a FMNP bound to GFP-GPI and pulled by the magnetic needle overlaid onto the GFP-GPI signal (right). **b)** Conventional epifluorescence microscopy of F-actin stained with phalloidin-AF647 in the same cell as in a) after fixation and the same trajectory (cyan) overlaid onto the epifluorescence image after image registration via fiducials (right). **a, b)** Scale bars are 10 and 1 μm. **c)** 3D dSTORM super-resolution microscopy, color scale by the depth z. Scale bar is 10 μm. **d)** Slicing of the 3D dSTORM volume to remove the ventral cytoskeleton. Top: yz view of the selected z-slices, the dotted line at -0.6 μm in z is where the dorsal and ventral part was separated. Actin filaments only on the dorsal (left) or ventral side (right) are highlighted with arrowheads. Scale bar is 1 μm. **e)** Trajectory of FMNP overlaid onto the dSTORM dorsal z-slice of F-actin. Scale bar is 1 μm.

8.3. Discussion

In this section, I correlated the movements of the FMNP-steered membrane molecules with membrane structures or surrounding cellular components. As simple positive controls, I observed how magnetically moved lipids delineate the edges of the continuous SLB (Figure 24), and on living cells how magnetically pulled membrane probes trace the cell edge and membrane ruffles (Figure 26). Experiments on membrane sheets demonstrate that the inner-leaflet probe MyrPalm-YFP becomes corralled between the remaining cortical actin under the magnetic influence (Figure 25). In living CV-1 cells, I correlated the movement of GFP-GPI under magnetic drag with the membrane topography and the cortical F-actin and could indeed observe that the movement was influenced by these cellular structures.

A common finding of these experiments is that the magnetically pulled membrane probes delineated the physical structures they encounter. They trace the boundaries of the SLB (Figure 24), the edge of the cell membrane (Figure 26) and even the orientation of the actin filament underneath the plasma membrane (Figure 27; discussed also below). These experiments demonstrate a fundamental difference of using magnetic tweezers to pull membrane components than with optical tweezers. If the trapping of the force optical tweezers is insufficient to cross the barrier, the molecule would be stopped by these barriers and the particle lost from the trapping focus when it is scanned beyond the boundary (Edidin, Kuo and Sheetz, 1991; Sako and Kusumi, 1994). With magnetic tweezers, the force is constantly applied towards one direction and one direction only, which allows the particle to still diffuse in perpendicular direction. This allows the probe molecule to explore the shape of the boundary as seen in the different examples presented in this section.

The correlation of the trajectory under magnetic pull with the F-actin cytoskeleton (Figure 27) demonstrates an important advantage of our approach over standard SPT. By introducing a directional movement component through magnetic forces, the site of impedance can be detected directly and dynamically. Classical SPT also allows the visualization of compartmented diffusion and correlation with local structures (Andrews *et al.*, 2008; Albrecht *et al.*, 2016; Sungkaworn *et al.*, 2017). However, due to the random nature by which the membrane probe explores the cellular environment, large statistical sampling is required to draw conclusions from the movement patterns. Instead, with our method, each individual particle can already be highly informative as demonstrated by the trajectory shown in Figure 27.

The results of the membrane sheets experiments could be understood as the “maximum effect” that potential barriers may have on the diffusion of membrane molecules: the membrane-associated actin, the adaptor proteins and the transmembrane proteins are on the same side of the membrane as the probe and they all together can act as physical barriers to the movement of both the membrane

probe and the bound FMNP. Consequently, when the magnetic field was activated, the mobility of MyrPalm-YFP dropped clearly as they became confined by the surrounding actin mesh (Figure 25). On living cells, where the cytoskeleton is on the inner face of the membrane, the membrane probe has to “sense” the cytoskeleton through the membrane and a less pronounced effect would be expected. Some particles seemed to become immobilized or confined in areas without actin or a special membrane structure. It would be interesting to see with super-resolution imaging whether single actin filaments are present at these sites which could not be resolved by confocal imaging, or whether these stops are mediated by other molecular species or even membrane-associated organelles that remained on the membrane sheet.

8.3.1. Relevance of membrane topography for magnetic pulling

As seen in Figure 26, the laterally dragged membrane probes could follow the shape of the membrane to a certain degree, until the angle of the membrane was such that the net magnetic force in the plane of the membrane was zero which is the case at cell edges or membrane ruffles. Consistently, in preliminary experiments, I failed to move GFP-GPI on the surface of HeLa cells which are more rounded and had many spikes and protrusions. The particles were virtually immobile and could also not be moved by the magnetic needle. Therefore, the morphology of the cell type has to be considered in general, as the cell surface topography strongly influences motion (Adler *et al.*, 2010). The CV-1 cells, which have been used throughout this study, are exceptionally flat apart from the nuclear region, and have a large surface area. Flat adherent cells such as fibroblasts and epithelial cells are best suited for this technique. Small round cells (e.g. stem cells) or generally cells with varying mesoscale membrane curvature or with special morphologies (neurons) can be used as long as the surface is rather smooth and static, but the area in which the magnetic field can effectively displace the target molecules would be limited. Cells with a very rugged surface or cells that quickly remodel their plasma membrane, e.g. immune cells, are probably less suited. These observations demonstrate that before any efforts to correlate the trajectories of magnetically pulled membrane probes with certain molecular species or membrane-associated assemblies, one must take the membrane topography into account. Three-dimensional information of the membrane or the trajectory are invaluable in this respect.

8.3.1. Effect of actin on magnetically dragged GFP-GPI

Lastly, we aimed to correlate the FMNP:GFP-GPI trajectories with the cortical actin cytoskeleton. A rich body of literature exists which shows that the dense actin meshwork underneath the plasma membrane restricts the movement of membrane proteins and lipids (see 1.3.1) (Andrews *et al.*, 2008; Goswami *et al.*, 2008; Mueller *et al.*, 2011; Weigel *et al.*, 2011; Albrecht *et al.*, 2016; Fujiwara *et al.*, 2016; Sungkaworn *et al.*, 2017; Freeman *et al.*, 2018). To visualize the actin cytoskeleton, I fixed the cells

immediately after live-cell SPT and magnetic pulling and performed 3D super-resolution microscopy of F-actin. In the example in Figure 27, it seems that a bundled actin filament stopped the magnetically moved GFP-GPI on its way. Since I can only *correlate* the trajectory and the actin cytoskeleton here, I cannot directly claim causation. However, what makes this interpretation very plausible is that first, the particle slows down as it reaches the site of the actin filament, second, it moves in the same angle as the filament is positioned and third, it still moves in the direction of the magnet. These features of the track make it seem highly unlikely that the particle randomly moved that way without being influenced by this actin filament. Because the actin bundle is located on the intracellular side while the GFP-GPI is anchored in the outer leaflet of the plasma membrane, the obstruction cannot be directly imposed by the actin filament *per se*. In line with the picket-fence model, the actin could be crosslinked with transmembrane proteins by adaptor proteins, e.g. ezrin, radixin and moesin (Fehon, McClatchey and Bretscher, 2010). The accumulation of these cytoskeleton-anchored transmembrane pickets at the actin bundle could have blocked the GFP-GPI directly. Additionally, it is possible that the GFP-GPI sensed the actin filament through the plasma membrane via interleaflet coupling (Spillane *et al.*, 2014; Raghupathy *et al.*, 2015). Furthermore, it might be possible that the bundled filament bent the membrane at a nanoscopic scale which is invisible in the epifluorescence image of the GFP-GPI. But to do so, the actin filament would have to be strongly attached to the membrane. Septins, another type of cytoskeletal proteins, could be involved as they bind both curved membranes and F-actin, and play a crucial role in many large-scale diffusion barriers in polarized cells (see also 1.3.1) (Kinoshita *et al.*, 2002; Caudron and Barral, 2009; Mostowy and Cossart, 2012; Bridges *et al.*, 2016; Beber *et al.*, 2019). On the other hand, ECM components could be aligned with the actin filament, possibly through interaction with transmembrane proteins which in turn associate with actin (Freeman *et al.*, 2018; Sil *et al.*, 2020). When the tracked GFP-GPI finally became completely immobile, it could be that it was trapped in a spot of very dense transmembrane pickets or ECM, from which it could not escape anymore, or it could be due to specific interactions for example with a clathrin-coated pit.

Before the particle in Figure 27 reached the site of the prominent actin filament, it moved in a meandering and indirect path as observed before (see 7.6.2 and Figure S32). The time and spatial resolution achieved here (>5 ms and ~10 nm) may not permit the observation of hop diffusion between 20-250 nm sized compartments (Kusumi, Sako and Yamamoto, 1993; Fujiwara *et al.*, 2002, 2016). A temporal resolution of 20 μ s was required to detect the compartmentalization of a GPI-anchored protein with an average dwell time of only 1-3 ms in one compartment (Umemura *et al.*, 2008). But the path of the GFP-GPI under magnetic drag shows a notable anti-correlation with areas of high actin signal (Figure 27 and Figure S32) but no obvious “hop diffusion” was observed. The anticorrelation of trajectories with the cytoskeleton has also been observed for different membrane

receptors and GFP-GPI in neurons (Andrews *et al.*, 2008; Albrecht *et al.*, 2016; Sungkaworn *et al.*, 2017; Freeman *et al.*, 2018). The membrane cytoskeleton compartments as proposed in the picket-fence theory may have caused this complex path but random diffusion together with the directional force could have produced a similar trajectory (see 7.2.2). Therefore, more experimental evidence or possibly a sophisticated statistical analysis would be needed to support this interpretation. As mentioned earlier, a sub-track analysis to detect changes in the diffusive behavior or the apparent force within single trajectories could possibly reveal interesting correlations with the underlying actin (see 7.7.1) (Beheiry, Dahan and Masson, 2015; Vega *et al.*, 2018).

It is in this context also not surprising that the strong correlation of the GFP-GPI trajectory and the actin cortex occurred at a long, bundled filament. No matter what mechanism, it can be assumed that the barrier must have been relatively stable, strong and/or dense such that it could be identified so clearly by our method. We would not detect the barrier if it was remodeled quickly or if it was unable to withstand tens of femtonewton of force. Furthermore, it is likely that the *d*STORM reconstruction of the cortical actin in Figure 27 visualizes only a portion of the actually present F-actin in the CV-1 cell. In previous *d*STORM and recent platinum replica electron microscopy of the cytoskeleton in the related COS-7 cell line, the cortical actin appears even denser than here (Xu, Babcock and Zhuang, 2012; Yang and Svitkina, 2019). With the pointillistic image reconstruction of *d*STORM, bundled actin filaments are easier to identify than single filaments. Another objection that could be raised here, is that the actin might have been still too far away from the membrane to have acted as a barrier. Indeed, the 3D reconstruction allows only to locate the actin filament in question to the dorsal cortex, but the actual distance to the membrane remains unknown. Even additional super-resolution imaging of the membrane could not prove that they are close enough because of the worse *z* resolution (the axial localization precision of actin was ~60 nm in this case). Other methods that measure distances in *z* with nanometer precision, e.g. FRET, would be required to verify the distance between the plasma membrane and the cortical actin. To finally prove the causal relationship, one would have to first detect the actin filament as a barrier and then remove said actin filament to demonstrate the free path for the membrane probe. Following along this line, I attempted at destroying the actin cytoskeleton with CytoD, a drug that prevents actin (de)polymerization (see 3.1). But I could not find facilitated magnetic pulling after CytoD treatment. Fujiwara *et al.* found a only small effect of CytoD on the diffusion coefficient of TfR and only within the first 10 min of treatment (Fujiwara *et al.*, 2016). The cell possibly compensates the effects of altered actin dynamics quickly and therefore other direct means are needed to locally eliminate the actin, e.g. laser ablation or optogenetic tools.

8.3.2. Further correlative approaches with magnetic SPT

Instead of using the magnetic tweezers to pull on single membrane molecules, the cytoskeleton itself could be pulled to demonstrate the compartmentalization of the plasma membrane and the restriction of lateral diffusion herein (Tomishige, Sako and Kusumi, 1998). By attaching magnetic microparticles to picket molecules such as CD44 (Freeman *et al.*, 2018; Sil *et al.*, 2020), one could displace the whole picket-cytoskeleton assembly while observing the movement of nearby membrane probes by SPT to test the Picket model.

The correlation of the trajectories under magnetic pull with super-resolution imaging of actin could be extended to other membrane structures or peripheral cellular assemblies that potentially restrict the movement of membrane molecules (see 3.1). These include other membrane-interacting cytoskeletal proteins such as septins (Kaplan *et al.*, 2015; Vissa *et al.*, 2019), clathrin-coated pits or caveolae (Khater *et al.*, 2018; Mund *et al.*, 2018), the ECM (Letschert *et al.*, 2014; Möckl *et al.*, 2019), or contract sites of ER or mitochondria with the plasma membrane (Lebiedzinska *et al.*, 2009; Poteser *et al.*, 2016; Hsieh *et al.*, 2017; Szymański *et al.*, 2017). These studies could provide further evidence on how the movement of membrane molecules is regulated at nanoscopic scales. Finally, the method can be applied to study the mechanism of macroscopic diffusion barriers such as in the AIS in neurons (Albrecht *et al.*, 2016). The diffusion barrier in the AIS was also investigated with optical tweezers but the trajectories of the optically dragged nanoparticle was not correlated to structures present in the AIS in these studies (Winckler, Forscher and Mellman, 1999; Nakada *et al.*, 2003).

The combination of FMNP tracking and *d*STORM demonstrates the general usefulness of this approach to study different membrane activities. The principle can be applied to investigate mechanisms that segregate membrane molecules as attempted here, or processes in which components come together to function, for example receptor signaling at the plasma membrane. One could use the FMNPs to drag one component out of a signaling hub to interrogate possible changes in signaling output by correlative imaging of downstream effectors. Another idea is to use the magnetic displacement to test for true receptor dimerization as opposed to coincidental colocalization. Here for, one could pull on one receptor subunit and observe the concomitant movement of the other subunit and thus determine the dimerized fraction of each subunit. The method could also be interesting to study polarized cells that have distinct membrane domains which fulfill specific functions. A resident molecule in one domain could be moved to the other domain and both the response of the target molecules to the new environment and the response of the environment to the ectopic molecules could be examined. To correlate the magnetically directed movement with cellular structures, I overlaid the trajectories from magnetic pulling either on the images of the membrane (Figure 24 to Figure 27) or post-hoc recorded images of the actin cytoskeleton (Figure 27). Other

imaging methods, e.g. PALM or live-cell STED could also be combined with magnetic tracking. These techniques have the advantage that they could monitor the environment, through which the target molecules move, simultaneously with the magnetic manipulation. The correlative approach therefore provides new avenues for exciting studies of all kinds of dynamic processes in the plasma membrane.

Conclusion

The purpose of this work was to develop a tool to remotely control the movement of membrane molecules and to track their movement with high resolution. The aim was to detect diffusion barriers in the plasma membrane of living cells by dragging membrane probes against the barrier. To do so, we aimed to use FMNPs for SPT and magnetic tweezers to simultaneously apply magnetic force on the nanoparticles. With the development of this novel method, we intended to identify obstacles in the path of membrane molecules by correlation of particle trajectories with super-resolution images of potential barrier molecules. Lateral diffusion barriers are prevalent in many biological contexts and ensure the proper segregation of membrane molecules into functional membrane domains. Nanoscopic compartmentalization of lateral diffusion is thought to give rise to macroscopic diffusion barriers but the mechanism of barrier establishment and the molecular composition is in many cases poorly understood. Previous work to study diffusion barriers relied on the observation of random movements of membrane probes and correlated the resulting patterns of movement with observations of the underlying cytoskeleton. In contrast, our work, by using force to actively drag a probe against such barriers reveals the nanoscopic localization of the barrier and renders the direct investigation of diffusion barriers tractable. The few examples in the literature that employed optical tweezers for this purpose failed to relate the trajectories to actual structures present at the plasma membrane. Magnetic tweezers have mostly been used to manipulate the ensemble distribution of membrane molecules but have not been combined with SPT before to observe diffusion at the single-molecule level. We closed this technological gap here by establishing FMNPs as bifunctional probes to directionally steer membrane molecule motion and to simultaneously track the real-time location of the molecule with high-resolution SPT.

We first identified suitable FMNPs that would allow fluorescence-based SPT, specific targeting of the molecule of interest, and the application of magnetic forces sufficient to move molecules through the membrane. We find that our FMNPs achieve SPT with 10 nm localization precision at 5 ms temporal resolution (200 Hz). Then, we demonstrated the feasibility of the approach on SLBs, by pulling lipids through the bilayer with a lateral magnetic tweezer setup. To measure the magnetic forces, we made use of a novel method that is better suited for the two-dimensional nature of membrane bilayers than classical calibration methods and find that magnetic forces in the low femtonewton range (1-10 fN) are sufficient to drag the molecules through the membrane. Next, we applied the FMNPs on the plasma membrane of living cells and generalize our method to different types of membrane proteins. Finally, we demonstrate that we can indeed detect physical obstacles to the diffusion of membrane molecules by correlating the trajectories under magnetic pull with 3D *d*STORM super-resolution images of cortical

actin filaments underneath the plasma membrane. The power of this correlative approach is that the presence of barriers, their nanoscopic location and molecular identity can be tested. In principle, the magnetic tracking can be performed in combination with most optical microscopy techniques, either concomitantly or post-hoc as demonstrated with *d*STORM here. The ability to directly detect diffusion barriers combined with the determination of the nanoscopic location is unprecedented and opens the doors to a mechanistic understanding of the nanoscale organization of the plasma membrane.

The use of brightly fluorescent, nanometer-sized magnetic particles achieved SPT with high spatiotemporal resolution. The particle properties, however, could be further optimized to better control valency, to avoid potential particle-related artifacts, and to exert larger forces. The forces that we applied here are relatively small, which allows the membrane probe to explore the cellular environment and to undergo natural interactions with the molecules it encounters. However, increasing the applied force is desirable as it would make the detection of barriers more stringent. The magnetic force could be increased by one order of magnitude without reaching the disruptive force range (>500 fN). To exert larger forces, the magnetic properties of the FMNPs or the magnetic tweezer setup could be improved. Compared to optical tweezers, the magnetic tweezer approach is straightforward and inexpensive, and affords manipulation of many targets at the same time. On the other hand, compared to state-of-the-art SPT, the throughput is limited as the density has to be kept low such that the FMNPs do not attract each other.

The unique features of the method presented here make it an ideal approach to study diffusion barriers, but the usefulness goes beyond this question. Other dynamic processes in the plasma membrane such as receptor signaling could be interrogated by targeted magnetic manipulation and real-time observation of the involved molecules. This work introduces a generic experimental framework to probe and to perturb molecule motion in biological membranes using FMNPs and magnetic tweezers. Our method thus expands the current toolbox to study the complex and dynamic activities occurring in and around the plasma membrane.

Materials and Methods

9. Procedures

If not specified, experiments were carried out at room temperature (RT).

9.1. Nanoparticle characterization

The initial experiences using FMNPs which failed to meet our expectations led to the development of a comprehensive set of tests (Table 3) to qualify those FMNPs that are suitable probes for SPT and magnetic manipulation.

Table 3: Quality assessment of FMNPs

TEST	INFORMATION GAINED	DESCRIBED IN
Magnetic separation	Efficient magnetization, time of separation	See below
Light/fluorescence microscopy	Fluorescence brightness/ bleaching, size, monodispersity	See below
Dynamic light scattering	Size, monodispersity/ aggregation	9.1.1
Electron microscopy	Size, shape, aggregation	9.1.2
Binding tests	Functionalization	See below

To test the magnetization of the FMNPs, I diluted the stock so that the FMNPs were still clearly visible by eye and placed the suspension into a commercial magnetic separator. Then the accumulation of the FMNPs to the side of the magnet in the magnetic separator was observed over time. If the particles were not efficiently concentrated within about half an hour, the particle magnetization was considered too low to allow displacement by the magnetic needle over a reasonable time and distance. The different methods and experiments to check particle size and dispersity, fluorescence and functionalization are detailed in the following sections.

For quick visualization of the particles, a 10-fold serial dilution of the FMNP stock was prepared in PBS. A drop of 2 μ l was placed on an uncleaned glass coverslip for imaging. To immobilize particles or to test the specific binding via streptavidin, coverslips were plasma cleaned for 5 min, incubated with either 0.1 mg/ml BSA-biotin or BSA in PBS for 30 min and washed 3 times with PBS. The 1:1000 diluted FMNPs were added to the BSA-coated coverslips for 10 min and then washed again 3 times.

9.1.1. Dynamic light scattering

The particles were diluted 1:500 in PBS and filled into a cuvette. DLS was measured with a 633 nm laser and the results analyzed by the Zetasizer software. The BNF-Starch-redF Streptavidin particles were confirmed to be monodisperse with a Polydispersity index of 0.11 (<0.2 is considered monodisperse) and a hydrodynamic radius of 159 ± 2 nm (Z-Average size). In comparison, the

MyQuVigen-Streptavidin particles showed a Polydispersity index between 0.25 – 0.81 and a Z-Average size between 620 – 1900 nm.

9.1.2. Electron microscopy

For EM of the BNF-Starch-redF Streptavidin particles, the particles were diluted 1:100 in MilliQ water. A small drop of ~5 μ l of the suspension was placed on an EM grid and allowed to air-dry. The sample was then imaged with a scanning/transmission electron microscope at 20 kV and 40,000 \times magnification. The remaining PBS from the stock solution crystallized on the grid but areas without salt crystals that contained single FMNPs could be found.

9.2. Magnetic tweezer setup

For the magnetic needle, a spring steel wire of 0.1 mm diameter was pulled in a Bunsen flame to create a tip. The needle was then glued to a 6 \times 4 \times 2 mm Neodyn magnet such that it extended from the magnet by ~0.5 mm. The magnet is then attached to a motorized micromanipulator with a hexagonal socket wrench. The micromanipulator was fitted to the microscopes using custom-build aluminum adaptors. To position the magnetic needle, the needle was lowered until it touched the bottom of a dummy sample dish and raised again so that it was placed above the bottom of the sample. By moving the z-position of the microscope stage until the very tip of the needle came into focus, I estimated that the center of the tip was placed around 100 μ m above the focus of the glass surface. The bottom of the ~100 nm thick needle was hence around 50 μ m above the glass surface. When placed as wished, the magnetic needle can be moved to the farthest position in xyz in the range of the micromanipulator using the “home” button and return to the set position using the button again. To avoid collision of the magnetic needle with the dish or other parts of the setup, the micromanipulator is fitted such that the displacement upon pressing the “home” button is mainly in z.

9.3. Supported lipid bilayer experiments

Suspensions of small unilamellar vesicles (SUV) were prepared by ultrasonication and used to form SLBs by the vesicle drop method. Fluidity of the resulting SLB was tested by FRAP on the spinning disk confocal microscope. The vesicle suspensions were then stored at 4 $^{\circ}$ C for up to 3 weeks until use.

9.3.1. SUV preparation and SLB formation

DOPC, 0.2-2 mol% PE-CF and 1-2 mol% of either DSPE-PEG(2k) or DSPE-PEG(2k)-biotin were dissolved in 1:1 chloroform:methanol and dried under vacuum overnight. The lipids films were then hydrated in SLB buffer, tip sonicated for 50 s in an ice bath and centrifuged for 45 min at top speed on a table-top centrifuge. The supernatants containing the SUVs were retrieved for SLB formation.

(When stored at 4°C, the SUV suspensions were warmed up in a 37°C water bath prior to SLB formation at RT.) Coverslips or glass-bottom dishes were plasma cleaned for 5 min. Suspensions of DSPE-PEG(2k)- or DSPE-PEG(2k)-biotin-containing vesicles were mixed in appropriate ratios to achieve a final concentration of 0.001-0.005 mol% DSPE-PEG(2k)-biotin in the solution and dropped directly onto the glass. After 10 min incubation, the bilayer was washed ten times with SLB buffer. To check fluidity, FRAP experiments were performed on the spinning disk confocal microscope equipped with an iLas2 FRAP system. Intensity of the bleached area and a reference region (next to the bleached area) were measured over the time-lapse sequence. The ratio of the intensity of the bleached area to the reference was normalized and the curves fitted from the bleach time point on with the formula

$$y(t) = a(1 - e^{-\tau_D t}), \quad (21)$$

where y is the normalized intensity, and t the time. Fitting was performed in OriginPro (OriginLab) (Nonlinear curve fit, exponential, 'BoxLucas1'). The diffusion coefficient was calculated with

$$\tau_D = \frac{A}{4\pi D}, \quad (22)$$

where A is the area of the bleached spot.

9.3.2. Force calibration experiments

The magnetic needle/micromanipulator setup was fitted on the Nikon TIRF microscope. Using a dummy dish, the tip of the magnetic needle was placed at the edge of the field of view as low as possible over the cover glass without touching, and then sent to the "off-home" position. SLBs were formed, placed on the microscope and incubated with 1×10^9 /ml FMNPs in SLB buffer with 1% BSA. In TIRF mode, binding of FMNPs was observed until tens to hundreds of particles per field of view had bound to the SLB, and then the SLB was washed 5-10 times with SLB buffer before recording. Data was acquired under continuous illumination with 100 ms camera exposure time with 1-7 Hz frame rate for 4,000-17,000 frames at 2×2 binning and 217 nm pixel size. During acquisition, the "home" button was pressed to bring the magnetic needle to the pre-set position or to remove the needle again.

9.3.3. Force calibration data analysis

For the force calibration, the data was analyzed using home written Matlab scripts from the Block laboratory. First, trajectories of the individual particles were generated from the movies. Then the velocity and diffusion coefficient of each trajectory was extracted to calculate the apparent force. For the calculation of forces, trajectories with a D below $0.02 \mu\text{m}^2/\text{s}$ were discarded. For the x-resolved

force analysis, trajectories slower than $0.01 \mu\text{m}^2/\text{s}$, shorter than 200 frames and with a displacement smaller than $10 \mu\text{m}$ were discarded to reduce noise.

9.4. Cell culture and transfection

Cells were cultured in a humidified incubator at 37°C and 5% CO_2 until use. Wildtype *Cercopithecus aethiops* kidney fibroblasts (CV-1) were grown in culture medium until 90-100% confluency before splitting 1:5 or 1:10. Stably transfected GFP-GPI CV-1 cells were maintained with $50 \mu\text{g}/\text{ml}$ Geneticin in the culture medium. For transient transfection, the Neon Transfection System was used according to the supplier's protocol for COS-7 cells. In brief, a 10-cm dish of CV-1 cells at 70-100% confluency (sufficient for 4 glass-bottom dishes or 4 wells in a 12- or 6-well plate) was harvested and washed with PBS by centrifugation. The cell pellet is resuspended in $20\text{-}40 \mu\text{l}$ R buffer (Neon kit) and $12 \mu\text{l}$ of the concentrated cell suspension is mixed with 0.5 mg of DNA ($\sim 1 \mu\text{g}/\mu\text{l}$). The cells are then electroporated and dispensed into culture medium at RT. After 15-20 min recovery time, the cells are gently resuspended and plated on glass-bottom dishes or well plates. Transfected cells were imaged or fixed 16-48 h after transfection

9.5. Live cell experiments

9.5.1. Particle functionalization

The nanobodies must be labeled with one biotin moiety only because they would otherwise crosslink and aggregate the FMNPs. The nanobodies were therefore reacted with a low concentration of biotin, yielding a mix of biotinylated and non-biotinylated nanobodies. LaG-16 anti-GFP nanobodies were recombinantly produced in house (Fridy *et al.*, 2014; Fabricius *et al.*, 2018). For the labeling reaction (Platonova, Winterflood and Ewers, 2015), α -Biotin- ω -(succinimidyl pro- pionate)-24(ethylene glycol) was added to the nanobody at only 2x molar excess and reacted for 1 h under shaking (300 rpm). After the labeling reaction, the nanobodies were purified from the free biotin by sequential passaging through three 7 kDa MWCO desalting columns. To determine the labeling efficiency, the same amounts were reacted with Alexa Fluor 647 (AF647) carboxylic acid, succinimidyl ester and purified in parallel, and the efficiency calculated from absorbance measurements of the AF647-labeled nanobodies. The efficiency was thus estimated to be 0.06 dye per protein.

For live-cell experiments targeting GFP or YFP, the FMNPs were mixed with the biotin-PEG-labeled GFP nanobodies in a 10:1 to 1:2 molar ratio and magnetically separated for 1 h. In the meantime, a cup of tea was prepared by steeping loose black tea leaves in $\sim 100^\circ\text{C}$ hot water for 3-5 min and enjoyed with an optional side of pastry. The supernatant containing a majority of unlabeled nanobodies was gently removed and discarded, and the pellet resuspended in imaging medium or PBS.

9.5.2. Membrane sheet generation

Membrane sheets were generated from adherent cells by tip sonication (Hümpfer, 2016). To avoid detachment of cells during sonication, the cells were seeded on poly-L-lysine. Glass-bottom dishes were plasma cleaned for 5-10 min and incubated with 300 μ l of 0.1 mg/ml solution of poly-L-lysine in borate buffer for 1 h in the cell culture incubator at 37°C. The poly-L-lysine was then aspirated, and the dishes dried under the cell culture hood. The dry dishes were washed three times with PBS and used for seeding cells after transfection (see 9.4). To generate membrane sheets, the medium was exchanged with 2 ml ice cold sonication buffer (Saka *et al.*, 2014) and the dish placed on ice with the cells ~2 mm underneath the sonotrode tip immersed in the sonication buffer. The sample was sonicated for 1 s and 3 cycles of 10%. Immediately afterwards, the sample was washed 2x with sonication buffer and checked under the spinning disk microscope for successful unroofing.

9.5.3. Live imaging

Living cells or membrane sheets were incubated with a suspension of FMNP:nanobody at a final concentration of 10^{10} – 10^{11} particles per ml in medium for 15 min. On living cells, the suspension was mixed twice during the incubation time by gently pipetting up and down. Afterwards, the samples were washed three to five times with PBS or medium. Cells were imaged in imaging medium or in the conditioned medium supplemented with 10-30 mM HEPES. Membrane sheets were washed and imaged in RT sonication buffer. Cells were imaged on the Vutara super-resolution microscope in epifluorescence illumination because the FMNPs bind to the dorsal cell membrane. Membrane sheets were imaged on the spinning disk confocal microscope. Typically for SPT, a single image series of 1,000-10,000 frames was collected with a 5-50 ms acquisition time (20-200 Hz, in total 20 s to 200 s) at a laser-power density of 8-200 W/cm² using the 561 nm laser line. For correlative imaging of the cytoskeleton, 100 nm red fluorescent beads were added as fiduciary markers and cells were fixed immediately after live-cell imaging (9.6.1).

9.5.4. Data analysis

All images were analyzed with Fiji (Schindelin *et al.*, 2012). SPT analysis was performed with the MOSAIC Particle Tracker (Sbalzarini and Koumoutsakos, 2005), Trackmate (Tinevez *et al.*, 2017) or the built-in particle tracker in the SRX software (Bruker) and the Matlab package MSD analyzer (Tarantino *et al.*, 2014). Immobile particles ($D < 0.005 \mu\text{m}^2/\text{s}$) and trajectories shorter than 30-50 frames were discarded. Trajectories and other data were analyzed and plotted with OriginPro (OriginLab). Statistics of the diffusion coefficient were calculated for $\log_{10}(D)$ due to the log-normal distribution of D and differences between before and after magnetic dragging were tested using a two-tailed paired Student's t -test (t -statistic = 0.63, degrees of freedom = 9, P -value = 0.54).

9.6. Super-resolution imaging

9.6.1. Fixation and staining

For fixation and permeabilization (Xu, Babcock and Zhuang, 2012), the medium was aspirated, the cells washed with PBS pre-warmed to 37°C and incubated with 0.3% glutaraldehyde and 0.25% Triton X-100 in cytoskeletal buffer (CB) for 1-2 min. The sample was then fixed in a second step with 2% glutaraldehyde in CB for 10 min. The fixation reaction was then quenched with freshly prepared 0.1% NaBH₄ in PBS for 7 min. The sample is then washed for 3x with PBS. For the staining, phalloidin-Alexa Fluor 647 is diluted in PBS with 1% BSA to ~0.5 μM. The sample is incubated in a humidity chamber in the dark at 4°C overnight. The phalloidin solution is best freshly prepared and used but can be re-used up to three times within 2 weeks. Wash the sample only once with PBS before imaging.

9.6.2. dSTORM imaging

dSTORM imaging was carried out in blinking buffer on a Vutara super-resolution microscope. Imaging was performed in biplane mode in epifluorescence illumination at a laser-power density of 4.4 kW/cm² using the 640 nm laser. Typically, 20,000–40,000 frames were acquired with 20 ms acquisition time at 99 nm pixel size (Ries *et al.*, 2012).

9.6.3. Data analysis

Analysis of dSTORM imaging was done in the SRX software (Bruker). Localization was performed with maximum likelihood fitting to a 3D measured calibration point spread function (PSF). The localizations were rendered with a Gaussian distribution by radial precision (Euclidean norm of the precision of the x and y axes calculated as the Cramér-Rao lower bound from the Fisher information of the PSF). To overlay the trajectories onto the dSTORM images, registration via fiducials was performed by nonreflective similarity transformation in Matlab (MathWorks) using the built-in function *fitgeotrans* with a home written script by Braedyn Au.

9.7. Materials

Table 4: FMNPs tested in this study

FMNP	SPECIFICATION	SOURCE
BNF-Starch-redF Streptavidin	100 nm magnetite core, starch shell crosslinked with Dy555 and streptavidin, thermally blocked at RT	Micromod
Nano-screenMAG/P Streptavidin	100 and 200 nm, superparamagnetic magnetite core, fluorescent starch matrix (ex 547 nm, em 581 nm), streptavidin	Chemicell
MyQuVigen-Streptavidin	Quantum dot core, superparamagnetic iron oxide shell, streptavidin, em 615 nm	Nvigen
Magnetite particles	Chains of single domain magnetic nanoparticles of different length, covalently conjugated with mCherry	Lucas Kuhrts, Faivre Laboratory (Reichel <i>et al.</i> , 2017)

Table 5: Reagents used in this work

REAGENTS	SOURCE
100 nm red fluorescent (580/605) beads	ThermoFisher Scientific
2-(N-morpholino)ethanesulfonic acid (MES)	PanReac AppliChem
Adenosine triphosphate (ATP)	Carl Roth
Boric acid	Carl Roth
Bovine serum albumin (BSA)	Carl Roth
BSA-biotin	Thermo Fisher Scientific
CaCl ₂	Sigma Aldrich
Catalase	Sigma Aldrich
Chloroform	Carl Roth
Dithiothreitol (DTT)	Carl Roth
DMEM without phenol red	Thermo Fisher Scientific
DOPC (1,2-dioleoyl-sn-glycero-3-phosphocholine)	Avanti Polar Lipids
DOPE-CF (1,2-dioleoyl-sn-glycero-3-phosphoethanolamine-N-carboxyfluorescein)	Avanti Polar Lipids
DSPE-PEG(2k) (1,2-distearoyl-sn-glycero-3-phosphoethanolamine-N-[carboxy(polyethylene glycol)-2000])	Avanti Polar Lipids
DSPE-PEG(2k)biotin (1,2-distearoyl-sn-glycero-3-phosphoethanolamine-N-[biotinyl(polyethylene glycol)-2000])	Avanti Polar Lipids
ethylene glycol-bis(β-aminoethyl ether)-N,N,N',N'-tetraacetic acid (EGTA)	Carl Roth
Fetal bovine serum (FBS)	Thermo Fisher Scientific
Fluorobrite DMEM	Thermo Fisher Scientific
Geneticin	Thermo Fisher Scientific
Glucose	Sigma Aldrich
Glucose oxidase	Sigma Aldrich
GlutaMAX	Thermo Fisher Scientific
HEPES (N-2-hydroxyethylpiperazine-N-2-ethane sulfonic acid), powdered	Sigma Aldrich
HEPES, 1 M sterile solution	Thermo Fisher Scientific
Methanol	Carl Roth
MgCl ₂	Thermo Fisher Scientific
NaCl	Sigma Aldrich
Potassium acetate	Carl Roth
Potassium glutamate	Sigma Aldrich
Sodium tetraborate	Carl Roth
Tris-HCl	Sigma Aldrich
α-Biotin-ω-(succinimidyl pro- pionate)-24(ethylene glycol)	Iris Biotech
β-mercaptoethanol	Sigma Aldrich

Table 6: Other materials and equipment used in this work

Material/device	Specification	Source/Manufacturer
DLS	Zetasizer Nano	Malvern
Glass coverslips	Round 25 mm #1.5 coverslips	VWR
Glass-bottom dishes	35 mm diameter imaging dish with 18 mm cover glass bottom	Zell-Kontakt
Magnetic separator	Dynal, 6 tubes	Invitrogen
Micromanipulator	PatchMan	Eppendorf
Micromanipulator adaptor	Custom-made aluminum blocks with holes for M6 screws	Engineering workshop, Institute of Chemistry, Freie Universität Berlin
Nikon TIRF microscope	Inverted Ti-E, high-pressure mercury lamp, Apo TIRF 60×/NA 1.49 oil objective, Andor Zyla 4.2 sCMOS camera (Andor Technology)	Nikon
Permanent magnet	6 × 4 × 2 mm Neodyn magnet (QM-06x04x02-N)	Magnets4you
Plasma cleaner	Zepto	Diener Electronic
SEM/TEM	SU8030	Hitachi
Sonicator	Sonopuls sonicator HD 2070	Bandelin
Sonotrode tip	MS 73 (3 mm diameter)	

Spinning disk confocal microscope	Inverted IX71, 60×/NA 1.42 oil objective, CSU-X1 spinning disk (Yokogawa), iLas2 FRAP system (Gataca Systems), ORCA Flash 4.0LT CMOS camera (Hamamatsu)	Olympus
Spring steel wire	100 nm diameter	Fohrmann-Werkzeuge
Vutara super-resolution microscope	Vutara 352, 60×/NA 1.49 oil immersion TIRF objective (Olympus), ORCA Flash 4.0 V2 CMOS (Hamamatsu)	Bruker
Zeba Spin Desalting Columns	7 kDa MWCO	ThermoFisher Scientific

Table 7: Buffer compositions

BUFFER	COMPOSITION
PBS	137 mM NaCl, 2.7 mM KCl, 10 mM Na ₂ HPO ₄ , 1.8 mM KH ₂ PO ₄ , pH 7.4
SLB buffer	2 mM CaCl ₂ , 200 mM NaCl and 10 mM HEPES, pH 6.8
Cell culture medium	DMEM without phenol red, 10% FBS, 1% GlutaMAX
Imaging medium	Fluorobrite DMEM, 10% FBS, GlutaMAX, 10-30 mM HEPES
Borate buffer	50 mM boric acid, 12.5 mM sodium tetraborate, pH 8.5
Sonication buffer	120 mM potassium glutamate, 20 mM potassium acetate, 10 mM EGTA, 4 mM MgCl ₂ , 20 mM HEPES-KOH, pH 7.2 DTT and ATP were added freshly <i>ad</i> 2 mM and 0.5 mM, respectively, before sonication
Cytoskeletal buffer (CB)	10 mM MES pH 6.1, 150 mM NaCl, 5 mM EGTA, 5 mM glucose, and 5 mM MgCl ₂
Blinking buffer	150 mM Tris-HCl, 1.5% β-mercaptoethanol, 0.5% (v/w) glucose, 0.25 mg/ml glucose oxidase and 20 μg/ml catalase, pH 8.8

Table 8: Plasmid constructs used for transfection

CONSTRUCT	COMPONENT	DESCRIPTION	SOURCE
GFP-GPI	Signal sequence of rabbit lactase phlorizin hydrolase	Membrane translocation and entrance to the secretory pathway	Helenius Laboratory
	eGFP	Consensus N-glycosylation site	
	GL GPI-anchor signal		
L-YFP-GT46	Signal sequence of rabbit lactase phlorizin hydrolase	See above	Patrick Keller
	eYFP	Single membrane-spanning helix	
	Consensus N-glycosylation site		
	Human low-density lipoprotein (LDL) receptor transmembrane domain CD46 cytoplasmic tail		
MyrPalm-YFP	Myristoylation and palmitoylation sequence eYFP	From Lyn kinase	Helenius Laboratory
TfR-GFP	Transferrin receptor eGFP	Full length	Helenius Laboratory

References

- Abraham, L. *et al.* (2017) 'Limitations of Qdot labelling compared to directly-conjugated probes for single particle tracking of B cell receptor mobility', *Scientific Reports*. Nature Publishing Group, 7(1). doi: 10.1038/s41598-017-11563-9.
- Adler, J. *et al.* (2010) 'Plasma membrane topography and interpretation of single-particle tracks', *Nature Methods*. Nature Publishing Group, 7(3), pp. 170–171. doi: 10.1038/nmeth0310-170.
- Aermes, C. *et al.* (2020) 'Environmentally controlled magnetic nano-tweezer for living cells and extracellular matrices', *Scientific Reports*. Nature Research, 10(1), pp. 1–16. doi: 10.1038/s41598-020-70428-w.
- Aitken, C. E., Marshall, R. A. and Puglisi, J. D. (2008) 'An oxygen scavenging system for improvement of dye stability in single-molecule fluorescence experiments', *Biophysical Journal*, 94(5), pp. 1826–1835. doi: 10.1529/biophysj.107.117689.
- Albrecht, D. *et al.* (2016) 'Nanoscopic compartmentalization of membrane protein motion at the axon initial segment', *Journal of Cell Biology*. Rockefeller University Press, 215(1). doi: 10.1083/jcb.201603108.
- Albrecht, D. (2016) *The axon initial segment diffusion barrier at the nanoscopic level*. ETH Zurich. doi: 10.3929/ethz-a-010717612.
- Albrecht, D., Winterflood, C. M. and Ewers, H. (2015) 'Dual color single particle tracking via nanobodies', *Methods and Applications in Fluorescence*. IOP Publishing, 3(2), p. 024001. doi: 10.1088/2050-6120/3/2/024001.
- Alcor, D., Gouzer, G. and Triller, A. (2009) 'Single-particle tracking methods for the study of membrane receptors dynamics', *European Journal of Neuroscience*, pp. 987–997. doi: 10.1111/j.1460-9568.2009.06927.x.
- Alvarsson, A. and Stanley, S. A. (2018) 'Remote control of glucose-sensing neurons to analyze glucose metabolism', *American Journal of Physiology - Endocrinology and Metabolism*, 315(3), pp. E327–E339. doi: 10.1152/ajpendo.00469.2017.
- Ambrose, E. J. (1956) 'A Surface Contact Microscope for the study of Cell Movements', *Nature*, 178(4543), pp. 1194–1194. doi: 10.1038/1781194a0.
- Andrade, D. M. *et al.* (2015) 'Cortical actin networks induce spatio-temporal confinement of phospholipids in the plasma membrane -A minimally invasive investigation by STED-FCS', *Scientific Reports*. Nature Publishing Group, 5. doi: 10.1038/srep11454.
- Andrews, N. L. *et al.* (2008) 'Actin restricts FcεRI diffusion and facilitates antigen-induced receptor immobilization', *Nature Cell Biology*, 10(8), pp. 955–963. doi: 10.1038/ncb1755.
- Ashby, M. C. *et al.* (2006) 'Lateral diffusion drives constitutive exchange of AMPA receptors at dendritic spines and is regulated by spine morphology', *Journal of Neuroscience*. J Neurosci, 26(26), pp. 7046–7055. doi: 10.1523/JNEUROSCI.1235-06.2006.
- Ashkin, A. *et al.* (1986) 'Observation of a single-beam gradient force optical trap for dielectric particles', *Optics Letters*, 11(5), p. 288. doi: 10.1364/OL.11.000288.
- Ashkin, A. and Dziedzic, J. M. (1987) 'Optical trapping and manipulation of viruses and bacteria', *Science*, 235(4795), pp. 1517–1520. doi: 10.1126/science.3547653.
- Axelrod, D. *et al.* (1976) 'Lateral motion of fluorescently labeled acetylcholine receptors in membranes of developing muscle fibers', *Proceedings of the National Academy of Sciences of the United States of America*, 73(12), pp. 4594–4598. doi: 10.1073/pnas.73.12.4594.
- Axelrod, D. (1981) 'Cell-substrate contacts illuminated by total internal reflection fluorescence', *Journal of Cell Biology*, 89(1), pp. 141–145. doi: 10.1083/jcb.89.1.141.
- Barbic, M. (2019) 'Possible magneto-mechanical and magneto-thermal mechanisms of ion channel activation in magnetogenetics', *eLife*, 8, pp. 1–18. doi: 10.7554/eLife.45807.
- Bates, M., Huang, B. and Zhuang, X. (2008) 'Super-resolution microscopy by nanoscale localization of photo-switchable fluorescent probes', *Current Opinion in Chemical Biology*, 12(5), pp. 505–514. doi: 10.1016/j.cbpa.2008.08.008.
- Bausch, A. R. *et al.* (1998) 'Local measurements of viscoelastic parameters of adherent cell surfaces by magnetic bead microrheometry', *Biophysical Journal*. Biophysical Society, 75(4), pp. 2038–2049. doi: 10.1016/S0006-3495(98)77646-5.
- Bausch, A. R., Möller, W. and Sackmann, E. (1999) 'Measurement of local viscoelasticity and forces in living cells by magnetic tweezers', *Biophysical Journal*, 76(1 I), pp. 573–579. doi: 10.1016/S0006-3495(99)77225-5.
- Bayer, M. E. (1991) 'Zones of membrane adhesion in the cryofixed envelope of Escherichia coli', *Journal of*

- Structural Biology*, 107(3), pp. 268–280. doi: 10.1016/1047-8477(91)90052-X.
- Beber, A. *et al.* (2019) ‘Membrane reshaping by micrometric curvature sensitive septin filaments’, *Nature Communications*. Springer US, 10(1). doi: 10.1038/s41467-019-08344-5.
- Beheiry, M. El, Dahan, M. and Masson, J. B. (2015) ‘InferenceMAP: Mapping of single-molecule dynamics with Bayesian inference’, *Nature Methods*. Nature Publishing Group, 12(7), pp. 594–595. doi: 10.1038/nmeth.3441.
- Bekku, Y. *et al.* (2010) ‘Bral1: Its role in diffusion barrier formation and conduction velocity in the CNS’, *Journal of Neuroscience*. Society for Neuroscience, 30(8), pp. 3113–3123. doi: 10.1523/JNEUROSCI.5598-09.2010.
- Berensmeier, S. (2006) ‘Magnetic particles for the separation and purification of nucleic acids’, *Applied Microbiology and Biotechnology*, 73(3), pp. 495–504. doi: 10.1007/s00253-006-0675-0.
- Berglund, A. J. (2010) ‘Statistics of camera-based single-particle tracking’, *Physical Review E - Statistical, Nonlinear, and Soft Matter Physics*, 82(1). doi: 10.1103/PhysRevE.82.011917.
- Berndt, F. *et al.* (2018) ‘Dynamic and non-contact 3D sample rotation for microscopy’, *Nature Communications*. Springer US, 9(1), pp. 1–7. doi: 10.1038/s41467-018-07504-3.
- Bethani, I. *et al.* (2010) ‘Spatial organization of transmembrane receptor signalling’, *The EMBO Journal*. Nature Publishing Group, 29(16), pp. 2677–2688. doi: 10.1038/emboj.2010.175.
- Betzig, E. *et al.* (2006) ‘Imaging intracellular fluorescent proteins at nanometer resolution’, *Science*. American Association for the Advancement of Science, 313(5793), pp. 1642–1645. doi: 10.1126/science.1127344.
- Bharde, A. A. *et al.* (2013) ‘Magnetic Nanoparticles as Mediators of Ligand-Free Activation of EGFR Signaling’, *PLoS ONE*, 8(7). doi: 10.1371/journal.pone.0068879.
- Blakemore, R. (1975) ‘Magnetotactic bacteria’, *Science*, 190(4212), pp. 377–379. doi: 10.1126/science.170679.
- Blasie, J. K. and Worthington, C. R. (1969) ‘Planar liquid-like arrangement of photopigment molecules in frog retinal receptor disk membranes’, *Journal of Molecular Biology*, 39(3). doi: 10.1016/0022-2836(69)90136-3.
- Block, S. *et al.* (2016) ‘Two-dimensional flow nanometry of biological nanoparticles for accurate determination of their size and emission intensity’, *Nature Communications*. Nature Publishing Group, pp. 1–18. doi: 10.1038/ncomms12956.
- Block, S. M., Goldstein, L. S. B. and Schnapp, B. J. (1990) ‘Bead movement by single kinesin molecules studied with optical tweezers’, *Nature*, 348(6299), pp. 348–352. doi: 10.1038/348348a0.
- Block, S., Zhdanov, V. P. and Höök, F. (2016) ‘Quantification of multivalent interactions by tracking single biological nanoparticle mobility on a lipid membrane’, *Nano Letters*, 16(7), pp. 4382–4390. doi: 10.1021/acs.nanolett.6b01511.
- Bonnemay, L., Hoffmann, C. and Gueroui, Z. (2015) ‘Remote control of signaling pathways using magnetic nanoparticles’, *Wiley Interdisciplinary Reviews: Nanomedicine and Nanobiotechnology*, 7(3), pp. 342–354. doi: 10.1002/wnan.1313.
- De Brabander, M. *et al.* (1988) ‘Dynamic behavior of the transferrin receptor followed in living epidermoid carcinoma (A431) cells with nanovid microscopy.’, *Cell motility and the cytoskeleton*, 9(1), pp. 30–47. doi: 10.1002/cm.970090105.
- Bridges, A. A. *et al.* (2016) ‘Micron-scale plasma membrane curvature is recognized by the septin cytoskeleton’, *Journal of Cell Biology*. Rockefeller University Press, 213(1), pp. 23–32. doi: 10.1083/jcb.201512029.
- Brier, M. I. *et al.* (2020) ‘Uncovering a possible role of reactive oxygen species in magnetogenetics’, *Scientific Reports*. Nature Publishing Group UK, 10(1), pp. 1–13. doi: 10.1038/s41598-020-70067-1.
- Bush, J. and Maruthamuthu, V. (2019) ‘In situ determination of exerted forces in magnetic pulling cytometry’, *AIP Advances*, 9(3). doi: 10.1063/1.5084261.
- Bussell, S. J., Koch, D. L. and Hammer, D. A. (1995) ‘Effect of hydrodynamic interactions on the diffusion of integral membrane proteins: diffusion in plasma membranes’, *Biophysical Journal*. Elsevier, 68(5), pp. 1836–1849. doi: 10.1016/S0006-3495(95)80360-7.
- Caudron, F. and Barral, Y. (2009) ‘Septins and the Lateral Compartmentalization of Eukaryotic Membranes’, *Developmental Cell*. Elsevier Inc., 16(4), pp. 493–506. doi: 10.1016/j.devcel.2009.04.003.
- Chang, D. *et al.* (2018) ‘Biologically Targeted Magnetic Hyperthermia: Potential and Limitations’, *Frontiers in Pharmacology*. Frontiers Media S.A., 9(AUG). doi: 10.3389/fphar.2018.00831.
- Chen, O. *et al.* (2014) ‘Magneto-fluorescent core-shell supernanoparticles’, *Nature Communications*. Nature Publishing Group, 5, pp. 1–8. doi: 10.1038/ncomms6093.
- Chen, R. *et al.* (2015) ‘Wireless magnetothermal deep brain stimulation’, *Science*. American Association for the Advancement of Science, 347(6229), pp. 1477–1480. doi: 10.1126/science.1261821.
- Cho, M. H. *et al.* (2012) ‘A magnetic switch for the control of cell death signalling in in vitro and in vivo systems’, *Nature Materials*. Nature Publishing Group, 11(12), pp. 1038–1043. doi: 10.1038/nmat3430.
- Choquet, D. and Triller, A. (2003) ‘The role of receptor diffusion in the organization of the postsynaptic membrane’, *Nature Reviews Neuroscience*, 4(4), pp. 251–265. doi: 10.1038/nrn1077.

References

- Christiansen, M., Hornslien, W. and Schuerle, S. (2020) 'A Possible Inductive Mechanism for Magnetogenetics', *bioRxiv*, pp. 1–10. doi: 10.1101/2020.07.16.207126.
- Chronopoulos, A. *et al.* (2016) 'ATRA mechanically reprograms pancreatic stellate cells to suppress matrix remodelling and inhibit cancer cell invasion', *Nature Communications*, 7(c). doi: 10.1038/ncomms12630.
- Chronopoulos, A. *et al.* (2020) 'Syndecan-4 tunes cell mechanics by activating the kindlin-integrin-RhoA pathway', *Nature Materials*, 19(6), pp. 669–678. doi: 10.1038/s41563-019-0567-1.
- Chung, H. J. *et al.* (2013) 'A magneto-DNA nanoparticle system for rapid detection and phenotyping of bacteria', *Nature Nanotechnology*. Nature Publishing Group, 8(5), pp. 369–375. doi: 10.1038/nnano.2013.70.
- Clarke, S. *et al.* (2011) 'A simple and general route for monofunctionalization of fluorescent and magnetic nanoparticles using peptides', *Nanotechnology*, 22(17), p. 175103. doi: 10.1088/0957-4484/22/17/175103.
- Clausen, M. P. and Lagerholm, B. C. (2011) 'The Probe Rules in Single Particle Tracking', *Current Protein & Peptide Science*, 12(8), pp. 699–713. doi: 10.2174/138920311798841672.
- Clausen, M. P. and Lagerholm, B. C. (2013) 'Visualization of plasma membrane compartmentalization by high-speed quantum dot tracking', *Nano Letters*, 13(6), pp. 2332–2337. doi: 10.1021/nl303151f.
- Cognet, L., Leduc, C. and Lounis, B. (2014) 'Advances in live-cell single-particle tracking and dynamic super-resolution imaging', *Current Opinion in Chemical Biology*. Elsevier Ltd, pp. 78–85. doi: 10.1016/j.cbpa.2014.04.015.
- Cohen, A. E. and Shi, Z. (2020) 'Do Cell Membranes Flow Like Honey or Jiggle Like Jello?', *BioEssays*, 42(1), pp. 1–13. doi: 10.1002/bies.201900142.
- Collins, C. *et al.* (2012) 'Localized tensional forces on PECAM-1 elicit a global mechanotransduction response via the integrin-RhoA pathway', *Current Biology*. Cell Press, 22(22), pp. 2087–2094. doi: 10.1016/j.cub.2012.08.051.
- Corr, S. A., Rakovich, Y. P. and Gun'Ko, Y. K. (2008) 'Multifunctional magnetic-fluorescent nanocomposites for biomedical applications', *Nanoscale Research Letters*, 3(3), pp. 87–104. doi: 10.1007/s11671-008-9122-8.
- Cox, M. and Nelson, D. L. (2008) *Lehninger Principles of Biochemistry*. 4th Ed. New York: W.H. Freeman and Company. Available at: <http://www.amazon.co.uk/Lehninger-Principles-Biochemistry-Michael-Cox/dp/0716743396>.
- Crick, F. H. C. and Hughes, A. F. W. (1950) 'The physical properties of cytoplasm. A study by means of the magnetic particle method Part I. Experimental', *Experimental Cell Research*, 1(1), pp. 37–80. doi: 10.1016/0014-4827(50)90048-6.
- Dahan, M. *et al.* (2003) *Diffusion Dynamics of Glycine Receptors Revealed by Single-Quantum Dot Tracking, Science*. doi: 10.1126/science.1088525.
- Daldrop, P. *et al.* (2015) 'Extending the range for force calibration in magnetic tweezers', *Biophysical Journal*. Biophysical Society, 108(10), pp. 2550–2561. doi: 10.1016/j.bpj.2015.04.011.
- Day, C. A. and Kenworthy, A. K. (2012) 'Mechanisms Underlying the Confined Diffusion of Cholera Toxin B-Subunit in Intact Cell Membranes', *PLoS ONE*. Edited by L. Johannes. Public Library of Science, 7(4), p. e34923. doi: 10.1371/journal.pone.0034923.
- Demtröder, W. (2017) *Experimentalphysik 2, Kapitel 3, Statische Magnetfelder*. Springer Verlag. doi: 10.1007/978-3-662-55790-7_3_79.
- Desprat, N. *et al.* (2008) 'Tissue Deformation Modulates Twist Expression to Determine Anterior Midgut Differentiation in Drosophila Embryos', *Developmental Cell*, 15(3), pp. 470–477. doi: 10.1016/j.devcel.2008.07.009.
- Destainville, N. and Salomé, L. (2006) 'Quantification and correction of systematic errors due to detector time-averaging in single-molecule tracking experiments', *Biophysical Journal*, 90(2), pp. 17–19. doi: 10.1529/biophysj.105.075176.
- Diaspro, A. *et al.* (2001) 'Two-photon microscopy and spectroscopy based on a compact confocal scanning head', *Journal of Biomedical Optics*, 6(3), p. 300. doi: 10.1117/1.1382809.
- Dobbelaere, J. and Barral, Y. (2004) 'Spatial coordination of cytokinetic events by compartmentalization of the cell cortex', *Science*. American Association for the Advancement of Science, 305(5682), pp. 393–396. doi: 10.1126/science.1099892.
- Dobson, J. (2008) 'Remote control of cellular behaviour with magnetic nanoparticles', *Nature Nanotechnology*, 3(3), pp. 139–143. doi: 10.1038/nnano.2008.39.
- Duret, G. *et al.* (2019) 'Magnetic Entropy as a Proposed Gating Mechanism for Magnetogenetic Ion Channels', *Biophysical Journal*. Biophysical Society, 116(3), pp. 454–468. doi: 10.1016/j.bpj.2019.01.003.
- Dustin, M. L. and Choudhuri, K. (2016) 'Signaling and Polarized Communication Across the T Cell Immunological Synapse', *Annual Review of Cell and Developmental Biology*, 32, pp. 303–325. doi: 10.1146/annurev-cellbio-100814-125330.
- Eddin, M., Kuo, S. and Sheetz, M. (1991) 'Lateral movements of membrane glycoproteins restricted by

- dynamic cytoplasmic barriers', *Science*. American Association for the Advancement of Science, 254(5036), pp. 1379–1382. doi: 10.1126/science.1835798.
- Eididin, M., Zagzansky, Y. and Lardner, T. J. (1976) 'Measurement of membrane protein lateral diffusion in single cells', *Science*, 191(4226), pp. 466–468. doi: 10.1126/science.1246629.
- Eididin, M., Zúñiga, M. C. and Sheetz, M. P. (1994) 'Truncation mutants define and locate cytoplasmic barriers to lateral mobility of membrane glycoproteins', *Proceedings of the National Academy of Sciences of the United States of America*. National Academy of Sciences, 91(8), pp. 3378–3382. doi: 10.1073/pnas.91.8.3378.
- Eggeling, C. *et al.* (2009) 'Direct observation of the nanoscale dynamics of membrane lipids in a living cell', *Nature*. Nature Publishing Group, 457(7233), pp. 1159–1162. doi: 10.1038/nature07596.
- Etoc, F. *et al.* (2013) 'Subcellular control of Rac-GTPase signalling by magnetogenetic manipulation inside living cells', *Nature Nanotechnology*. Nature Publishing Group, 8(3), pp. 193–198. doi: 10.1038/nnano.2013.23.
- Etoc, F. *et al.* (2015) 'Magnetogenetic control of protein gradients inside living cells with high spatial and temporal resolution', *Nano Letters*. American Chemical Society, 15(5), pp. 3487–3494. doi: 10.1021/acs.nanolett.5b00851.
- Evans, E. (2001) 'Probing the Relation Between Force—Lifetime—and Chemistry in Single Molecular Bonds', *Annual Review of Biophysics and Biomolecular Structure*, 30, pp. 105–128. doi: 10.1146/annurev.biophys.30.1.105.
- Ewers, H. *et al.* (2005) 'Single-particle tracking of murine polyoma virus-like particles on live cells and artificial membranes', *Proceedings of the National Academy of Sciences*, 102(42), pp. 15110–15115. doi: 10.1073/pnas.0504407102.
- Fabricius, V. *et al.* (2018) 'Rapid and efficient C-terminal labeling of nanobodies for DNA-PAINT', *Journal of Physics D: Applied Physics*. Institute of Physics Publishing, 51(47). doi: 10.1088/1361-6463/aae0e2.
- Fahey, P. F. *et al.* (1977) 'Lateral diffusion in planar lipid bilayers', *Science*, 195(4275), pp. 305–306. doi: 10.1126/science.831279.
- Feder, T. J. *et al.* (1996) 'Constrained diffusion or immobile fraction on cell surfaces: a new interpretation', *Biophysical Journal*, 70(6), pp. 2767–2773. doi: 10.1016/S0006-3495(96)79846-6.
- Fehon, R. G., McClatchey, A. I. and Bretscher, A. (2010) 'Organizing the cell cortex: The role of ERM proteins', *Nature Reviews Molecular Cell Biology*. Nature Publishing Group, 11(4), pp. 276–287. doi: 10.1038/nrm2866.
- Ferrari, R., Manfroï, A. J. and Young, W. R. (2001) 'Strongly and weakly self-similar diffusion', *Physica D: Nonlinear Phenomena*, 154(1–2), pp. 111–137. doi: 10.1016/S0167-2789(01)00234-2.
- Fisher, J. K. *et al.* (2006) 'Thin-foil magnetic force system for high-numerical-aperture microscopy', *Review of Scientific Instruments*. American Institute of Physics, 77(2), p. 23702. doi: 10.1063/1.2166509.
- Frankel, D. J. *et al.* (2006) 'Revealing the topography of cellular membrane domains by combined atomic force microscopy/fluorescence imaging', *Biophysical Journal*. Elsevier, 90(7), pp. 2404–2413. doi: 10.1529/biophysj.105.073692.
- Franzreb, M. *et al.* (2006) 'Protein purification using magnetic adsorbent particles', *Applied Microbiology and Biotechnology*, 70(5), pp. 505–516. doi: 10.1007/s00253-006-0344-3.
- Freeman, S. A. *et al.* (2018) 'Transmembrane Pickets Connect Cyto- and Pericellular Skeletons Forming Barriers to Receptor Engagement', *Cell*. Elsevier Inc., 172(1–2), pp. 305–317.e10. doi: 10.1016/j.cell.2017.12.023.
- Fridy, P. C. *et al.* (2014) 'A robust pipeline for rapid production of versatile nanobody repertoires', *Nature Methods*. Nature Publishing Group, 11(12), pp. 1253–1260. doi: 10.1038/nmeth.3170.
- Frost, N. A. *et al.* (2012) 'Optimization of cell morphology measurement via single-molecule tracking PALM', *PLoS one*. Edited by Y. Yang. Public Library of Science, 7(5), p. e36751. doi: 10.1371/journal.pone.0036751.
- Frye, L. D. and Eididin, M. (1970) 'The rapid intermixing of cell surface antigens after formation of mouse-human heterokaryons.', *Journal of cell science*. The Company of Biologists Ltd, 7(2), pp. 319–35. Available at: <https://jcs.biologists.org/content/7/2/319>.
- Fujiwara, T. *et al.* (2002) 'Phospholipids undergo hop diffusion in compartmentalized cell membrane', *Journal of Cell Biology*, 157(6), pp. 1071–1081. doi: 10.1083/jcb.200202050.
- Fujiwara, T. K. *et al.* (2016) 'Confined diffusion of transmembrane proteins and lipids induced by the same actin meshwork lining the plasma membrane', *Molecular Biology of the Cell*. American Society for Cell Biology, 27(7), pp. 1101–1119. doi: 10.1091/mbc.E15-04-0186.
- Furlani, E. P. (2007) 'Magnetophoretic separation of blood cells at the microscale', *Journal of Physics D: Applied Physics*, 40(5), pp. 1313–1319. doi: 10.1088/0022-3727/40/5/001.
- Gambin, Y. *et al.* (2006) 'Lateral mobility of proteins in liquid membranes revisited', *Proceedings of the National Academy of Sciences of the United States of America*, 103(7), pp. 2098–2102. doi: 10.1073/pnas.0511026103.
- Ganguly, A. *et al.* (2015) 'A dynamic formin-dependent deep F-actin network in axons', *Journal of Cell Biology*, 210(3), pp. 401–417. doi: 10.1083/jcb.201506110.

References

- Garcia-Parajo, M. F. *et al.* (2000) 'Real-time light-driven dynamics of the fluorescence emission in single green fluorescent protein molecules', *Proceedings of the National Academy of Sciences of the United States of America*. National Academy of Sciences, 97(13), pp. 7237–7242. doi: 10.1073/pnas.97.13.7237.
- Garcia-Parajo, M. F. *et al.* (2014) 'Nanoclustering as a dominant feature of plasma membrane organization', *Journal of Cell Science*. Company of Biologists Ltd, 127(23), pp. 4995–5005. doi: 10.1242/jcs.146340.
- Gautreau, A., Louvard, D. and Arpin, M. (2000) 'Morphogenic effects of ezrin require a phosphorylation-induced transition from oligomers to monomers at the plasma membrane', *Journal of Cell Biology*, 150(1), pp. 193–203. doi: 10.1083/jcb.150.1.193.
- Geerts, H. *et al.* (1987) 'Nanovid tracking: a new automatic method for the study of mobility in living cells based on colloidal gold and video microscopy', *Biophysical Journal*. Elsevier, 52(5), pp. 775–782. doi: 10.1016/S0006-3495(87)83271-X.
- Giannone, G. *et al.* (2010) 'Dynamic super-resolution imaging of endogenous proteins on living cells at ultra-high density _ Supplementary information', *Biophysical journal*. Biophysical Society, 99(4), pp. 1303–1310. doi: 10.1016/j.bpj.2010.06.005.
- Gleich, B. and Weizenecker, J. (2005) 'Tomographic imaging using the nonlinear response of magnetic particles', *Nature*, 435(7046), pp. 1214–1217. doi: 10.1038/nature03808.
- Goiko, M., de Bruyn, J. R. and Heit, B. (2018) 'Membrane Diffusion Occurs by Continuous-Time Random Walk Sustained by Vesicular Trafficking', *Biophysical Journal*. Biophysical Society, 114(12), pp. 2887–2899. doi: 10.1016/j.bpj.2018.04.024.
- Gordon, W. R. *et al.* (2015) 'Mechanical Allostery: Evidence for a Force Requirement in the Proteolytic Activation of Notch', *Developmental Cell*. Cell Press, 33(6), pp. 729–736. doi: 10.1016/j.devcel.2015.05.004.
- Gore, J. *et al.* (2006) 'DNA overwinds when stretched', *Nature*, 442(7104), pp. 836–839. doi: 10.1038/nature04974.
- Gosse, C. and Croquette, V. (2002) 'Magnetic tweezers: Micromanipulation and force measurement at the molecular level', *Biophysical Journal*. Elsevier, 82(6), pp. 3314–3329. doi: 10.1016/S0006-3495(02)75672-5.
- Goswami, D. *et al.* (2008) 'Nanoclusters of GPI-Anchored Proteins Are Formed by Cortical Actin-Driven Activity', *Cell*, 135(6), pp. 1085–1097. doi: 10.1016/j.cell.2008.11.032.
- Gowrishankar, K. *et al.* (2012) 'Active Remodeling of Cortical Actin Regulates Spatiotemporal Organization of Cell Surface Molecules', *Cell*. Elsevier Inc., 149(6), pp. 1353–1367. doi: 10.1016/j.cell.2012.05.008.
- Graham, J. S., Johnson, R. C. and Marko, J. F. (2011) 'Counting proteins bound to a single DNA molecule', *Biochemical and Biophysical Research Communications*. Elsevier Inc., 415(1), pp. 131–134. doi: 10.1016/j.bbrc.2011.10.029.
- Gu, H. *et al.* (2003) 'Using Biofunctional Magnetic Nanoparticles to Capture Vancomycin-Resistant Enterococci and Other Gram-Positive Bacteria at Ultralow Concentration', *Journal of the American Chemical Society*, 125(51), pp. 15702–15703. doi: 10.1021/ja0359310.
- Gu, H. *et al.* (2004) 'Facile One-Pot Synthesis of Bifunctional Heterodimers of Nanoparticles: A Conjugate of Quantum Dot and Magnetic Nanoparticles', *Journal of the American Chemical Society*, 126(18), pp. 5664–5665. doi: 10.1021/ja0496423.
- Gumi-Audenis, B. *et al.* (2016) 'Structure and nanomechanics of model membranes by atomic force microscopy and spectroscopy: Insights into the role of cholesterol and sphingolipids', *Membranes*, 6(4). doi: 10.3390/membranes6040058.
- Gustafsson, M. G. L. (2000) 'Surpassing the lateral resolution limit by a factor of two using structured illumination microscopy. SHORT COMMUNICATION', *Journal of Microscopy*, 198(2), pp. 82–87. doi: 10.1046/j.1365-2818.2000.00710.x.
- Hansen, A. S. *et al.* (2018) 'Robust model-based analysis of single-particle tracking experiments with Spot-On', *eLife*, 7, pp. 1–33. doi: 10.7554/eLife.33125.
- Hauser, M. *et al.* (2018) 'The Spectrin-Actin-Based Periodic Cytoskeleton as a Conserved Nanoscale Scaffold and Ruler of the Neural Stem Cell Lineage', *Cell Reports*. Elsevier B.V., 24(6), pp. 1512–1522. doi: 10.1016/j.celrep.2018.07.005.
- Hebert, B., Costantino, S. and Wiseman, P. W. (2005) 'Spatiotemporal image correlation spectroscopy (STICS) theory, verification, and application to protein velocity mapping in living CHO cells', *Biophysical Journal*. Biophysical Society, 88(5), pp. 3601–3614. doi: 10.1529/biophysj.104.054874.
- Heilemann, M. *et al.* (2008) 'Subdiffraction-resolution fluorescence imaging with conventional fluorescent probes', *Angewandte Chemie - International Edition*, 47(33), pp. 6172–6176. doi: 10.1002/anie.200802376.
- Heilemann, M. *et al.* (2009) 'Super-resolution imaging with small organic fluorophores', *Angewandte Chemie - International Edition*, 48(37), pp. 6903–6908. doi: 10.1002/anie.200902073.
- Heinisch, J. J. *et al.* (2010) 'Single-molecule atomic force microscopy reveals clustering of the yeast plasma-membrane sensor Wsc1', *PLoS ONE*, 5(6). doi: 10.1371/journal.pone.0011104.

- Helppolainen, S. H. *et al.* (2007) 'Rhizavidin from *Rhizobium etli*: The first natural dimer in the avidin protein family', *Biochemical Journal*. Biochem J, 405(3), pp. 397–405. doi: 10.1042/BJ20070076.
- Henstock, J. R. *et al.* (2014) 'Remotely Activated Mechanotransduction via Magnetic Nanoparticles Promotes Mineralization Synergistically With Bone Morphogenetic Protein 2: Applications for Injectable Cell Therapy', *STEM CELLS Translational Medicine*, 3(11), pp. 1363–1374. doi: 10.5966/sctm.2014-0017.
- Hernández-morales, M. *et al.* (2020) 'FeRIC-based magnetogenetics : evaluation of methods and protocols in in vitro models', *bioRxiv*, (510), pp. 1–30. doi: 10.1101/2020.12.10.419911.
- Hess, S. T., Girirajan, T. P. K. and Mason, M. D. (2006) 'Ultra-high resolution imaging by fluorescence photoactivation localization microscopy', *Biophysical Journal*. Biophysical Journal, 91(11), pp. 4258–4272. doi: 10.1529/biophysj.106.091116.
- Hiramoto-Yamaki, N. *et al.* (2014) 'Ultrafast Diffusion of a Fluorescent Cholesterol Analog in Compartmentalized Plasma Membranes', *Traffic*, 15(6), pp. 583–612. doi: 10.1111/tra.12163.
- Hoffmann, C. *et al.* (2013) 'Spatiotemporal control of microtubule nucleation and assembly using magnetic nanoparticles', *Nature Nanotechnology*. Nature Publishing Group, 8(3), pp. 199–205. doi: 10.1038/nnano.2012.246.
- Holtzer, L., Meckel, T. and Schmidt, T. (2007) 'Nanometric three-dimensional tracking of individual quantum dots in cells', *Applied Physics Letters*, 90(5), pp. 10–13. doi: 10.1063/1.2437066.
- Honigsmann, A. *et al.* (2014) 'Scanning STED-FcS reveals spatiotemporal heterogeneity of lipid interaction in the plasma membrane of living cells', *Nature Communications*. Nature Publishing Group, 5. doi: 10.1038/ncomms6412.
- Howarth, M. *et al.* (2006) 'A monovalent streptavidin with a single femtomolar biotin binding site', *Nature Methods*. Nature Publishing Group, 3(4), pp. 267–273. doi: 10.1038/nmeth861.
- Howarth, M. *et al.* (2008) 'Monovalent, reduced-size quantum dots for imaging receptors on living cells', *Nature Methods*. Nat Methods, 5(5), pp. 397–399. doi: 10.1038/nmeth.1206.
- Hsieh, T. S. *et al.* (2017) 'Cortical actin contributes to spatial organization of ER-PM junctions', *Molecular Biology of the Cell*, 28(23), pp. 3171–3180. doi: 10.1091/mbc.E17-06-0377.
- Hu, Q. *et al.* (2010) 'A Septin Diffusion Barrier at the Base of the Primary Cilium Maintains Ciliary Membrane Protein Distribution', *Science*, 329(5990), pp. 436–439. doi: 10.1126/science.1191054.
- Huang, H. *et al.* (2010) 'Remote control of ion channels and neurons through magnetic-field heating of nanoparticles', *Nature Nanotechnology*. Nature Publishing Group, 5(8), pp. 602–606. doi: 10.1038/nnano.2010.125.
- Hughes, S. *et al.* (2008) 'Selective activation of mechanosensitive ion channels using magnetic particles', *Journal of The Royal Society Interface*. Royal Society, 5(25), pp. 855–863. doi: 10.1098/rsif.2007.1274.
- Hümpfer, N. (2016) *Generation of plasma membrane sheets for super-resolution microscopy of the membrane cytoskeleton*. Freie Universität Berlin.
- Ihara, M. *et al.* (2005) 'Cortical organization by the septin cytoskeleton is essential for structural and mechanical integrity of mammalian spermatozoa', *Developmental Cell*. Cell Press, 8(3), pp. 343–352. doi: 10.1016/j.devcel.2004.12.005.
- Iino, R., Koyama, I. and Kusumi, A. (2001) 'Single molecule imaging of green fluorescent proteins in living cells: E-cadherin forms oligomers on the free cell surface', *Biophysical Journal*. Elsevier, 80(6), pp. 2667–2677. doi: 10.1016/S0006-3495(01)76236-4.
- Ito, A. *et al.* (2005) 'The effect of RGD peptide-conjugated magnetite cationic liposomes on cell growth and cell sheet harvesting', *Biomaterials*, 26(31), pp. 6185–6193. doi: 10.1016/j.biomaterials.2005.03.039.
- Izeddin, I. *et al.* (2014) 'Single-molecule tracking in live cells reveals distinct target-search strategies of transcription factors in the nucleus', *eLife*, 2014(3), pp. 1–27. doi: 10.7554/eLife.02230.
- Jacobson, K., Liu, P. and Lagerholm, B. C. (2019) 'The Lateral Organization and Mobility of Plasma Membrane Components', *Cell*. Cell Press, 177(4), pp. 806–819. doi: 10.1016/j.cell.2019.04.018.
- Jaqaman, K. *et al.* (2011) 'Cytoskeletal control of CD36 diffusion promotes its receptor and signaling function', *Cell*. Elsevier Inc., 146(4), pp. 593–606. doi: 10.1016/j.cell.2011.06.049.
- Jin, Y. *et al.* (2019) 'Magnetic Control of Axon Navigation in Reprogrammed Neurons', *Nano Letters*, 19(9), pp. 6517–6523. doi: 10.1021/acs.nanolett.9b02756.
- Jordan, A. *et al.* (2001) 'Presentation of a new magnetic field therapy system for the treatment of human solid tumors with magnetic fluid hyperthermia', *Journal of Magnetism and Magnetic Materials*, 225(1–2), pp. 118–126. doi: 10.1016/S0304-8853(00)01239-7.
- Juette, M. F. *et al.* (2008) 'Three-dimensional sub-100 nm resolution fluorescence microscopy of thick samples', *Nature Methods*, 5(6), pp. 527–529. doi: 10.1038/nmeth.1211.
- Jun, Y. W., Seo, J. W. and Cheon, J. (2008) 'Nanoscaling laws of magnetic nanoparticles and their applicabilities in biomedical sciences', *Accounts of Chemical Research*, 41(2), pp. 179–189. doi: 10.1021/ar700121f.

References

- Jungmann, R. *et al.* (2010) 'Single-molecule kinetics and super-resolution microscopy by fluorescence imaging of transient binding on DNA origami', *Nano Letters*, 10(11), pp. 4756–4761. doi: 10.1021/nl103427w.
- Jungmann, R. *et al.* (2014) 'Multiplexed 3D cellular super-resolution imaging with DNA-PAINT and Exchange-PAINT', *Nature Methods*. Nature Publishing Group, 11(3), pp. 313–318. doi: 10.1038/nmeth.2835.
- Kalay, Z., Fujiwara, T. K. and Kusumi, A. (2012) 'Confining Domains Lead to Reaction Bursts: Reaction Kinetics in the Plasma Membrane', *PLoS ONE*. Edited by R. M. H. Merks, 7(3), p. e32948. doi: 10.1371/journal.pone.0032948.
- Kamboj, S. and Haganir, R. L. (1998) 'Receptor clustering: Activate to accumulate?', *Current Biology*, 8(20). doi: 10.1016/s0960-9822(98)70457-9.
- Kanczler, J. M. *et al.* (2010) 'Controlled differentiation of human bone marrow stromal cells using magnetic nanoparticle technology', *Tissue Engineering - Part A*, 16(10), pp. 3241–3250. doi: 10.1089/ten.tea.2009.0638.
- Kao, H. P. and Verkman, A. S. (1994) 'Tracking of single fluorescent particles in three dimensions: use of cylindrical optics to encode particle position', *Biophysical Journal*. Elsevier, 67(3), pp. 1291–1300. doi: 10.1016/S0006-3495(94)80601-0.
- Kaplan, C. *et al.* (2015) 'Absolute Arrangement of Subunits in Cytoskeletal Septin Filaments in Cells Measured by Fluorescence Microscopy', *Nano Letters*. American Chemical Society, 15(6), pp. 3859–3864. doi: 10.1021/acs.nanolett.5b00693.
- Karslake, J. D. *et al.* (2020) 'SMAUG: Analyzing single-molecule tracks with nonparametric Bayesian statistics', *Methods*. doi: 10.1016/j.ymeth.2020.03.008.
- Keller, P. *et al.* (2001) 'Multicolour imaging of post-Golgi sorting and trafficking in live cells', *Nature Cell Biology*. Nature Publishing Group, 3(2), pp. 140–149. doi: 10.1038/35055042.
- Kerkhoff, Y. and Block, S. (2020) 'Analysis and refinement of 2D single-particle tracking experiments', *Biointerphases*. American Vacuum Society, 15(2), p. 021201. doi: 10.1116/1.5140087.
- Khater, I. M. *et al.* (2018) 'Super Resolution Network Analysis Defines the Molecular Architecture of Caveolae and Caveolin-1 Scaffolds', *Scientific Reports*, 8(1), p. 9009. doi: 10.1038/s41598-018-27216-4.
- Kinoshita, M. *et al.* (2002) 'Self- and actin-templated assembly of mammalian septins', *Developmental Cell*, 3(6), pp. 791–802. doi: 10.1016/S1534-5807(02)00366-0.
- Kirch, J. *et al.* (2012) 'Optical tweezers reveal relationship between microstructure and nanoparticle penetration of pulmonary mucus', *Proceedings of the National Academy of Sciences of the United States of America*, 109(45), pp. 18355–18360. doi: 10.1073/pnas.1214066109.
- Kiuchi, T. *et al.* (2015) 'Multitarget super-resolution microscopy with high-density labeling by exchangeable probes', *Nature Methods*. Nature Publishing Group, 12(8), pp. 743–746. doi: 10.1038/nmeth.3466.
- Klar, T. A. and Hell, S. W. (1999) 'Subdiffraction resolution in far-field fluorescence microscopy', *Optics Letters*, 24(14), p. 954. doi: 10.1364/ol.24.000954.
- Knopp, T., Gdaniec, N. and Möddel, M. (2017) 'Magnetic particle imaging: From proof of principle to preclinical applications', *Physics in Medicine and Biology*. Institute of Physics Publishing, pp. R124–R178. doi: 10.1088/1361-6560/aa6c99.
- Kobayashi, T. *et al.* (1992) 'A functional barrier to movement of lipids in polarized neurons', *Nature*, 359(6396), pp. 647–650. doi: 10.1038/359647a0.
- Korn, E. D. (1969) 'Cell Membranes: Structure and Synthesis', *Annual Review of Biochemistry*, 38(1), pp. 263–288. doi: 10.1146/annurev.bi.38.070169.001403.
- Küey, C. *et al.* (2019) 'Unintended perturbation of protein function using GFP nanobodies in human cells', *Journal of Cell Science*. Company of Biologists Ltd, 132(21), p. jcs234955. doi: 10.1242/jcs.234955.
- Kuno, M. *et al.* (2000) 'Nonexponential "blinking" kinetics of single CdSe quantum dots: A universal power law behavior', *The Journal of Chemical Physics*, 112(7), pp. 3117–3120. doi: 10.1063/1.480896.
- Kusumi, A. *et al.* (2005) 'Paradigm shift of the plasma membrane concept from the two-dimensional continuum fluid to the partitioned fluid: High-speed single-molecule tracking of membrane molecules', *Annual Review of Biophysics and Biomolecular Structure*, 34, pp. 351–378. doi: 10.1146/annurev.biophys.34.040204.144637.
- Kusumi, A. *et al.* (2012) 'Dynamic Organizing Principles of the Plasma Membrane that Regulate Signal Transduction: Commemorating the Fortieth Anniversary of Singer and Nicolson's Fluid-Mosaic Model', *Annual Review of Cell and Developmental Biology*. Annual Reviews, 28(1), pp. 215–250. doi: 10.1146/annurev-cellbio-100809-151736.
- Kusumi, A., Sako, Y. and Yamamoto, M. (1993) 'Confined Lateral Diffusion of Membrane Receptors', *Biophysical Journal*. Biophysical Journal, 65(5), pp. 2021–2040. doi: 10.1016/S0006-3495(93)81253-0.
- Kwitny, S., Klaus, A. V. and Hunnicutt, G. R. (2010) 'The annulus of the mouse sperm tail is required to establish a membrane diffusion barrier that is engaged during the late steps of spermiogenesis', *Biology of*

- Reproduction*. Biol Reprod, 82(4), pp. 669–678. doi: 10.1095/biolreprod.109.079566.
- Lambert, T. J. (2019) 'FPbase: a community-editable fluorescent protein database', *Nature Methods*, 16(4), pp. 277–278. doi: 10.1038/s41592-019-0352-8.
- Lebiedzinska, M. *et al.* (2009) 'Interactions between the endoplasmic reticulum, mitochondria, plasma membrane and other subcellular organelles', *International Journal of Biochemistry and Cell Biology*, 41(10), pp. 1805–1816. doi: 10.1016/j.biocel.2009.02.017.
- Lee, G. M. *et al.* (1993) 'Unconfined lateral diffusion and an estimate of pericellular matrix viscosity revealed by measuring the mobility of gold-tagged lipids', *Journal of Cell Biology*. J Cell Biol, 120(1), pp. 25–36. doi: 10.1083/jcb.120.1.25.
- Lee, J. H. *et al.* (2007) 'Artificially engineered magnetic nanoparticles for ultra-sensitive molecular imaging', *Nature Medicine*, 13(1), pp. 95–99. doi: 10.1038/nm1467.
- Lee, N. and Hyeon, T. (2012) 'Designed synthesis of uniformly sized iron oxide nanoparticles for efficient magnetic resonance imaging contrast agents', *Chem. Soc. Rev.* The Royal Society of Chemistry, 41(7), pp. 2575–2589. doi: 10.1039/C1CS15248C.
- Lee, S. *et al.* (2018) 'Actin filaments partition primary cilia membranes into distinct fluid corrals', *Journal of Cell Biology*. Rockefeller University Press, 217(8), pp. 2831–2849. doi: 10.1083/jcb.201711104.
- Lenne, P. F. *et al.* (2006) 'Dynamic molecular confinement in the plasma membrane by microdomains and the cytoskeleton meshwork', *EMBO Journal*, 25(14), pp. 3245–3256. doi: 10.1038/sj.emboj.7601214.
- Leslie-Pelecky, D. L. and Rieke, R. D. (1996) 'Magnetic Properties of Nanostructured Materials', *Chemistry of Materials*. American Chemical Society, 8(8), pp. 1770–1783. doi: 10.1021/cm960077f.
- Letschert, S. *et al.* (2014) 'Super-Resolution Imaging of Plasma Membrane Glycans', *Angewandte Chemie International Edition*. Wiley-VCH Verlag, 53(41), pp. 10921–10924. doi: 10.1002/anie.201406045.
- Li, J. H. *et al.* (2020) 'Directed manipulation of membrane proteins by fluorescent magnetic nanoparticles', *Nature Communications*. Springer US, 11(1), pp. 1–7. doi: 10.1038/s41467-020-18087-3.
- Liao, Y. H. *et al.* (2019) 'Monovalent and Oriented Labeling of Gold Nanoprobes for the High-Resolution Tracking of a Single-Membrane Molecule', *ACS Nano*, 13(10), pp. 10918–10928. doi: 10.1021/acsnano.9b01176.
- Lingwood, D. and Simons, K. (2010) 'Lipid Rafts As a Membrane-Organizing Principle', *Science*. American Association for the Advancement of Science, 327(5961), pp. 46–50. doi: 10.1126/science.1174621.
- Lipfert, J., Hao, X. and Dekker, N. H. (2009) 'Quantitative modeling and optimization of magnetic tweezers', *Biophysical Journal*. Biophysical Society, 96(12), pp. 5040–5049. doi: 10.1016/j.bpj.2009.03.055.
- Liu, P. *et al.* (2012) 'The Formation and Stability of DC-SIGN Microdomains Require its Extracellular Moiety', *Traffic*, 13(5), pp. 715–726. doi: 10.1111/j.1600-0854.2012.01337.x.
- Liu, P. *et al.* (2017) 'Rapid, directed transport of DC-SIGN clusters in the plasma membrane', *Science Advances*, 3(11). doi: 10.1126/sciadv.aao1616.
- Liu, X. *et al.* (2020) 'Comprehensive understanding of magnetic hyperthermia for improving antitumor therapeutic efficacy', *Theranostics*, 10(8), pp. 3793–3815. doi: 10.7150/thno.40805.
- Liu, Y. *et al.* (2019) 'Visualization of perforin/gasdermin/complement-formed pores in real cell membranes using atomic force microscopy', *Cellular and Molecular Immunology*. Springer US, 16(6), pp. 611–620. doi: 10.1038/s41423-018-0165-1.
- Löf, A. *et al.* (2019) 'Multiplexed protein force spectroscopy reveals equilibrium protein folding dynamics and the low-force response of von Willebrand factor', *Proceedings of the National Academy of Sciences of the United States of America*, 116(38), pp. 18798–18807. doi: 10.1073/pnas.1901794116.
- Lorent, J. H. *et al.* (2020) 'Plasma membranes are asymmetric in lipid unsaturation, packing and protein shape', *Nature Chemical Biology*. Springer US, 16(6), pp. 644–652. doi: 10.1038/s41589-020-0529-6.
- Ma, X. *et al.* (2007) 'Lateral diffusion of TGF- β type I receptor studied by single-molecule imaging', *Biochemical and Biophysical Research Communications*, 356(1), pp. 67–71. doi: 10.1016/j.bbrc.2007.02.080.
- Madariaga-Marcos, J. *et al.* (2018) 'Force determination in lateral magnetic tweezers combined with TIRF microscopy', *Nanoscale*. Royal Society of Chemistry, 10(9), pp. 4579–4590. doi: 10.1039/c7nr07344e.
- Magenau, A. *et al.* (2015) 'Discreet and distinct clustering of five model membrane proteins revealed by single molecule localization microscopy', *Molecular Membrane Biology*, 32(1), pp. 11–18. doi: 10.3109/09687688.2014.990997.
- Mahajan, K. D. *et al.* (2013) 'Magnetic quantum dots in biotechnology - synthesis and applications', *Biotechnology Journal*, 8(12), pp. 1424–1434. doi: 10.1002/biot.201300038.
- Mahammad, S. and Parmryd, I. (2015) 'Cholesterol Depletion Using Methyl- β -cyclodextrin', in Owen, D. M. (ed.) *Methods in Membrane Lipids: Second Edition*. New York, NY: Springer New York (Methods in Molecular Biology), pp. 91–102. doi: 10.1007/978-1-4939-1752-5_8.
- Mahowald, J., Arcizet, D. and Heinrich, D. (2009) 'Impact of external stimuli and cell micro-architecture on

References

- intracellular transport states', *ChemPhysChem*, 10(9–10), pp. 1559–1566. doi: 10.1002/cphc.200900226.
- Mammen, M. *et al.* (1996) 'Optically controlled collisions of biological objects to evaluate potent polyvalent inhibitors of virus-cell adhesion', *Chemistry and Biology*. Elsevier Ltd, 3(9), pp. 757–763. doi: 10.1016/S1074-5521(96)90252-5.
- Manley, S. *et al.* (2008) 'High-density mapping of single-molecule trajectories with photoactivated localization microscopy', *Nature Methods*, 5(2), pp. 155–157. doi: 10.1038/nmeth.1176.
- Mannix, R. J. *et al.* (2008) 'Nanomagnetic actuation of receptor-mediated signal transduction', *Nature Nanotechnology*, 3(1), pp. 36–40. doi: 10.1038/nnano.2007.418.
- Manzo, C. and Garcia-Parajo, M. F. (2015) 'A review of progress in single particle tracking: From methods to biophysical insights', *Reports on Progress in Physics*. IOP Publishing, 78(12). doi: 10.1088/0034-4885/78/12/124601.
- Martin, D. S., Forstner, M. B. and Käs, J. A. (2002) 'Apparent subdiffusion inherent to single particle tracking', *Biophysical Journal*. doi: 10.1016/S0006-3495(02)73971-4.
- Matter, K. and Balda, M. S. (2003) 'Functional analysis of tight junctions', *Methods*. Academic Press Inc., 30(3), pp. 228–234. doi: 10.1016/S1046-2023(03)00029-X.
- Matthews, B. D. *et al.* (2004) 'Electromagnetic needles with submicron pole tip radii for nanomanipulation of biomolecules and living cells', *Applied Physics Letters*, 85(14), pp. 2968–2970. doi: 10.1063/1.1802383.
- Meister, M. (2016) 'Physical limits to magnetogenetics', *eLife*, 5(AUGUST), pp. 1–14. doi: 10.7554/eLife.17210.
- Metzler, R. *et al.* (2014) 'Anomalous diffusion models and their properties: Non-stationarity, non-ergodicity, and ageing at the centenary of single particle tracking', *Physical Chemistry Chemical Physics*. The Royal Society of Chemistry, 16(44), pp. 24128–24164. doi: 10.1039/c4cp03465a.
- Michalet, X. (2010) 'Mean square displacement analysis of single-particle trajectories with localization error: Brownian motion in an isotropic medium', *Physical Review E - Statistical, Nonlinear, and Soft Matter Physics*, 82(4). doi: 10.1103/PhysRevE.82.041914.
- Michalet, X. and Berglund, A. J. (2012) 'Optimal diffusion coefficient estimation in single-particle tracking', *Physical Review E - Statistical, Nonlinear, and Soft Matter Physics*, 85(6), pp. 1–14. doi: 10.1103/PhysRevE.85.061916.
- Milo, R. *et al.* (2009) 'BioNumbers The database of key numbers in molecular and cell biology', *Nucleic Acids Research*, 38(SUPPL.1), pp. 750–753. doi: 10.1093/nar/gkp889.
- Miltenyi, S. *et al.* (1990) 'High gradient magnetic cell separation with MACS', *Cytometry*, 11(2), pp. 231–238. doi: 10.1002/cyto.990110203.
- Minsky, M. (1957) 'Microscopy Apparatus', *US Patent 3013467*. USA. Available at: <https://worldwide.espacenet.com/patent/search/family/024791595/publication/US3013467A?q=pn%3DU53013467>.
- Mitra, K. *et al.* (2004) 'Modulation of the bilayer thickness of exocytic pathway membranes by membrane proteins rather than cholesterol', *Proceedings of the National Academy of Sciences of the United States of America*, 101(12), pp. 4083–4088. doi: 10.1073/pnas.0307332101.
- Möckl, L. *et al.* (2019) 'Quantitative Super-Resolution Microscopy of the Mammalian Glycocalyx', *Developmental Cell*, 50(1), pp. 57–72.e6. doi: 10.1016/j.devcel.2019.04.035.
- Monzel, C. *et al.* (2017) 'Magnetic control of cellular processes using biofunctional nanoparticles', *Chemical Science*. Royal Society of Chemistry, 8(11), pp. 7330–7338. doi: 10.1039/c7sc01462g.
- Morone, N. *et al.* (2006) 'Three-dimensional reconstruction of the membrane skeleton at the plasma membrane interface by electron tomography', *Journal of Cell Biology*, 174(6), pp. 851–862. doi: 10.1083/jcb.200606007.
- Mostowy, S. and Cossart, P. (2012) 'Septins: The fourth component of the cytoskeleton', *Nature Reviews Molecular Cell Biology*. Nature Publishing Group, 13(3), pp. 183–194. doi: 10.1038/nrm3284.
- Mueller, V. *et al.* (2011) 'STED nanoscopy reveals molecular details of cholesterol- and cytoskeleton-modulated lipid interactions in living cells', *Biophysical Journal*, 101(7), pp. 1651–1660. doi: 10.1016/j.bpj.2011.09.006.
- Mund, M. *et al.* (2018) 'Systematic Nanoscale Analysis of Endocytosis Links Efficient Vesicle Formation to Patterned Actin Nucleation', *Cell*, 174(4), pp. 884–896.e17. doi: 10.1016/j.cell.2018.06.032.
- Munshi, R. *et al.* (2017) 'Magnetothermal genetic deep brain stimulation of motor behaviors in awake, freely moving mice', *eLife*, 6, pp. 1–26. doi: 10.7554/eLife.27069.
- Munshi, R., Qadri, S. M. and Pralle, A. (2018) 'Transient magnetothermal neuronal silencing using the chloride channel anoctamin 1 (TMEM16A)', *Frontiers in Neuroscience*, 12(AUG), pp. 1–13. doi: 10.3389/fnins.2018.00560.
- Murase, K. *et al.* (2004) 'Ultrafine membrane compartments for molecular diffusion as revealed by single molecule techniques', *Biophysical Journal*. doi: 10.1529/biophysj.103.035717.

- Naisbett-Jones, L. C. *et al.* (2020) 'Magnetoreception in fishes: the effect of magnetic pulses on orientation of juvenile Pacific salmon', *The Journal of Experimental Biology*. Company of Biologists Ltd, 223(10), p. jeb222091. doi: 10.1242/jeb.222091.
- Nakada, C. *et al.* (2003) 'Accumulation of anchored proteins forms membrane diffusion barriers during neuronal polarization', *Nature Cell Biology*, 5(7), pp. 626–632. doi: 10.1038/ncb1009.
- Nam, J., Thaxton, C. S. and Mirkin, C. A. (2003) 'Nanoparticle-Based Bio – Bar Codes for the Ultrasensitive', *Science*, 301(September), pp. 1884–1887.
- Neuman, K. C. and Nagy, A. (2008) 'Single-molecule force spectroscopy: Optical tweezers, magnetic tweezers and atomic force microscopy', *Nature Methods*, 5(6), pp. 491–505. doi: 10.1038/nmeth.1218.
- Nicolson, G. L. (1976) 'Transmembrane control of the receptors on normal and tumor cells. I. Cytoplasmic influence over cell surface components', *BBA - Reviews on Biomembranes*, 457(1), pp. 57–108. doi: 10.1016/0304-4157(76)90014-9.
- Nimpf, S. and Keays, D. A. (2017) 'Is magnetogenetics the new optogenetics?', *The EMBO Journal*, 36(12), pp. 1643–1646. doi: 10.15252/embj.201797177.
- Nirmal, M. *et al.* (1996) 'Fluorescence intermittency in single cadmium selenide nanocrystals', *Nature*. MIT Press, 383(6603), pp. 802–804. doi: 10.1038/383802a0.
- Nishimura, S. Y. *et al.* (2006) 'Cholesterol depletion induces solid-like regions in the plasma membrane', *Biophysical Journal*. Biophysical Society, 90(3), pp. 927–938. doi: 10.1529/biophysj.105.070524.
- Nomura, S. *et al.* (2006) 'Nanopillar sheets as a new type of cell culture dish : detailed study of HeLa cells cultured on nanopillar sheets', *J Artif Organs*, 9, pp. 90–96. doi: 10.1007/s10047-006-0329-0.
- Ober, R. J., Ram, S. and Ward, E. S. (2004) 'Localization Accuracy in Single-Molecule Microscopy', *Biophysical Journal*. doi: 10.1016/S0006-3495(04)74193-4.
- Ortega-Arroyo, J. and Kukura, P. (2012) 'Interferometric scattering microscopy (iSCAT): New frontiers in ultrafast and ultrasensitive optical microscopy', *Physical Chemistry Chemical Physics*, 14(45), pp. 15625–15636. doi: 10.1039/c2cp41013c.
- Pankhurst, Q. A. *et al.* (2003) 'Applications of magnetic nanoparticles in biomedicine', *Journal of Physics D: Applied Physics*, 36(13), pp. 167–181. doi: 10.1088/0022-3727/36/13/201.
- Pankhurst, Q. A. *et al.* (2009) 'Progress in applications of magnetic nanoparticles in biomedicine', *Journal of Physics D: Applied Physics*, 42(22), p. 224001. doi: 10.1088/0022-3727/42/22/224001.
- Paparelli, L. *et al.* (2016) 'Inhomogeneity Based Characterization of Distribution Patterns on the Plasma Membrane', *PLoS Computational Biology*, 12(9), pp. 1–23. doi: 10.1371/journal.pcbi.1005095.
- Pavani, S. R. P. *et al.* (2009) 'Three-dimensional, single-molecule fluorescence imaging beyond the diffraction limit by using a double-helix point spread function', *Proceedings of the National Academy of Sciences of the United States of America*. Proc Natl Acad Sci U S A, 106(9), pp. 2995–2999. doi: 10.1073/pnas.0900245106.
- Pekarsky, A. and Spadiut, O. (2020) 'Intrinsically Magnetic Cells: A Review on Their Natural Occurrence and Synthetic Generation', *Frontiers in Bioengineering and Biotechnology*, 8(October), pp. 1–19. doi: 10.3389/fbioe.2020.573183.
- Peters, I. M. *et al.* (1999) '3D single-particle tracking and optical trap measurements on adhesion proteins', *Cytometry*, 36(3), pp. 189–194. doi: 10.1002/(SICI)1097-0320(19990701)36:3<189::AID-CYTO7>3.0.CO;2-3.
- Petersen, N. O. *et al.* (1993) 'Quantitation of membrane receptor distributions by image correlation spectroscopy: concept and application', *Biophysical Journal*, 65(3), pp. 1135–1146. doi: 10.1016/S0006-3495(93)81173-1.
- Petrov, E. P. and Schwill, P. (2008) 'Translational diffusion in lipid membranes beyond the Saffman-Delbrück approximation', *Biophysical Journal*. doi: 10.1529/biophysj.107.126565.
- Pike, L. J. (2006) 'Rafts defined: A report on the Keystone symposium on lipid rafts and cell function', *Journal of Lipid Research*. Elsevier, 47(7), pp. 1597–1598. doi: 10.1194/jlr.E600002-JLR200.
- Pinaud, F. *et al.* (2010) 'Probing cellular events, one quantum dot at a time', *Nature Methods*. Nature Publishing Group, 7(4), pp. 275–285. doi: 10.1038/nmeth.1444.
- Platonova, E., Winterflood, C. M. and Ewers, H. (2015) 'A Simple Method for GFP- and RFP-based Dual Color Single-Molecule Localization Microscopy', *ACS Chemical Biology*. American Chemical Society, 10(6), pp. 1411–1416. doi: 10.1021/acscchembio.5b00046.
- Plouffe, B. D., Murthy, S. K. and Lewis, L. H. (2015) 'Fundamentals and application of magnetic particles in cell isolation and enrichment: A review', *Reports on Progress in Physics*. IOP Publishing, 78(1). doi: 10.1088/0034-4885/78/1/016601.
- Poteser, M. *et al.* (2016) 'Live-cell imaging of ER-PM contact architecture by a novel TIRFM approach reveals extension of junctions in response to store-operated Ca²⁺-entry', *Scientific Reports*. Nature Publishing Group, 6(July), pp. 1–13. doi: 10.1038/srep35656.
- Pratt, A. J. and MacRae, I. J. (2009) 'The RNA-induced silencing complex: A versatile gene-silencing machine',

References

- Journal of Biological Chemistry*. Elsevier, pp. 17897–17901. doi: 10.1074/jbc.R900012200.
- Qian, H., Sheetz, M. P. and Elson, E. L. (1991) 'Analysis of diffusion and flow in two-dimensional systems', *Biophysical Journal*. Biophysical Journal, 60(October), pp. 910–921. doi: 10.1016/S0006-3495(91)82125-7.
- Raghupathy, R. *et al.* (2015) 'Transbilayer Lipid Interactions Mediate Nanoclustering of Lipid-Anchored Proteins', *Cell*. Cell Press, 161(3), pp. 581–594. doi: 10.1016/j.cell.2015.03.048.
- Rao, M. and Mayor, S. (2014) 'Active organization of membrane constituents in living cells', *Current Opinion in Cell Biology*. Elsevier Ltd, 29(1), pp. 126–132. doi: 10.1016/j.ceb.2014.05.007.
- Rawicz, W. *et al.* (2000) 'Effect of chain length and unsaturation on elasticity of lipid bilayers', *Biophysical Journal*. Elsevier, 79(1), pp. 328–339. doi: 10.1016/S0006-3495(00)76295-3.
- Reichel, V. *et al.* (2017) 'Single crystalline superstructured stable single domain magnetite nanoparticles', *Scientific Reports*. Nature Publishing Group, 7(March), pp. 1–8. doi: 10.1038/srep45484.
- Reina, F. *et al.* (2018) 'Complementary studies of lipid membrane dynamics using iSCAT and super-resolved fluorescence correlation spectroscopy', *Journal of Physics D: Applied Physics*. IOP Publishing, 51(235401). doi: 10.1088/1361-6463/aac04f.
- Reits, E. A. J. and Neefjes, J. J. (2001) 'From fixed to FRAP: measuring protein mobility and activity in living cells', *Nature Cell Biology*, 3(6), pp. E145–E147. doi: 10.1038/35078615.
- Ribeck, N. and Saleh, O. A. (2008) 'Multiplexed single-molecule measurements with magnetic tweezers', *Review of Scientific Instruments*, 79(9), pp. 0–6. doi: 10.1063/1.2981687.
- Richter, D. *et al.* (2017) 'Ligand-induced type II interleukin-4 receptor dimers are sustained by rapid re-association within plasma membrane microcompartments', *Nature Communications*. Nature Publishing Group, 8(1), pp. 1–15. doi: 10.1038/ncomms15976.
- Di Rienzo, C. *et al.* (2013) 'Fast spatiotemporal correlation spectroscopy to determine protein lateral diffusion laws in live cell membranes', *Proceedings of the National Academy of Sciences of the United States of America*, 110(30), pp. 12307–12312. doi: 10.1073/pnas.1222097110.
- Ries, J. *et al.* (2012) 'A simple, versatile method for GFP-based super-resolution microscopy via nanobodies', *Nature Methods*. Nature Publishing Group, 9(6), pp. 582–584. doi: 10.1038/nmeth.1991.
- Riggio, C. *et al.* (2012) 'Poly-L-lysine-coated magnetic nanoparticles as intracellular actuators for neural guidance', *International Journal of Nanomedicine*, 7, pp. 3155–3166. doi: 10.2147/ijn.s28460.
- Rios, J. C. *et al.* (2003) 'Paranodal interactions regulate expression of sodium channel subtypes and provide a diffusion barrier for the node of ranvier', *Journal of Neuroscience*. Society for Neuroscience, 23(18), pp. 7001–7011. doi: 10.1523/jneurosci.23-18-07001.2003.
- Rossier, O. *et al.* (2012) 'Integrins $\beta 1$ and $\beta 3$ exhibit distinct dynamic nanoscale organizations inside focal adhesions', *Nature Cell Biology*. Nature Research, 14(10), pp. 1057–1067. doi: 10.1038/ncb2588.
- Rost, B. R. *et al.* (2017) 'Optogenetic Tools for Subcellular Applications in Neuroscience', *Neuron*. Elsevier Inc., 96(3), pp. 572–603. doi: 10.1016/j.neuron.2017.09.047.
- Roullier, V. *et al.* (2008) 'Small bioactivated magnetic quantum dot micelles', *Chemistry of Materials*, 20(21), pp. 6657–6665. doi: 10.1021/cm801423r.
- Rust, M. J., Bates, M. and Zhuang, X. (2006) 'Sub-diffraction-limit imaging by stochastic optical reconstruction microscopy (STORM)', *Nature Methods*, 3(10), pp. 793–795. doi: 10.1038/nmeth929.
- Saffman, P. G. and Delbrück, M. (1975) 'Brownian motion in biological membranes', *Proceedings of the National Academy of Sciences of the United States of America*. National Academy of Sciences, 72(8), pp. 3111–3113. doi: 10.1073/pnas.72.8.3111.
- Saka, S. K. *et al.* (2014) 'Multi-protein assemblies underlie the mesoscale organization of the plasma membrane', *Nature Communications*. Nature Publishing Group. doi: 10.1038/ncomms5509.
- Sako, Y. *et al.* (1998) 'Cytoplasmic regulation of the movement of E-cadherin on the free cell surface as studied by optical tweezers and single particle tracking: Corraling and tethering by the membrane skeleton', *Journal of Cell Biology*, 140(5), pp. 1227–1240. doi: 10.1083/jcb.140.5.1227.
- Sako, Y. and Kusumi, A. (1994) 'Compartmentalized structure of the plasma membrane for receptor movements as revealed by a nanometer-level motion analysis', *Journal of Cell Biology*, 125(6), pp. 1251–1264. doi: 10.1083/jcb.125.6.1251.
- Sako, Y. and Kusumi, A. (1995) 'Barriers for lateral diffusion of transferrin receptor in the plasma membrane as characterized by receptor dragging by laser tweezers: Fence versus tether', *Journal of Cell Biology*. Rockefeller Univ Press, 129(6), pp. 1559–1574. doi: 10.1083/jcb.129.6.1559.
- Salvati, A. *et al.* (2013) 'Transferrin-functionalized nanoparticles lose their targeting capabilities when a biomolecule corona adsorbs on the surface', *Nature Nanotechnology*. Nature Publishing Group, 8(2), pp. 137–143. doi: 10.1038/nnano.2012.237.
- Santos Otte, P. (2017) *Magnetische Manipulation und Analyse der Diffusionseigenschaften von Membranproteinen*. Humboldt Universität zu Berlin.

- Saphirstein, R. J. *et al.* (2013) 'The Focal Adhesion: A Regulated Component of Aortic Stiffness', *PLoS ONE*, 8(4). doi: 10.1371/journal.pone.0062461.
- Sauer, A. M. *et al.* (2009) 'Dynamics of magnetic lipoplexes studied by single particle tracking in living cells', *Journal of Controlled Release*. Elsevier B.V., 137(2), pp. 136–145. doi: 10.1016/j.jconrel.2009.04.003.
- Saxton, M. J. and Jacobson, K. (1997) 'SINGLE-PARTICLE TRACKING: Applications to Membrane Dynamics', *Annual Review of Biophysics and Biomolecular Structure*, 26(1), pp. 373–399. doi: 10.1146/annurev.biophys.26.1.373.
- Sbalzarini, I. F. and Koumoutsakos, P. (2005) 'Feature point tracking and trajectory analysis for videoimaging in cell biology', *Journal of Structural Biology*, 151(2), pp. 182–195. Available at: <http://linkinghub.elsevier.com/retrieve/pii/S1047847705001267>.
- Schindelin, J. *et al.* (2012) 'Fiji: An open-source platform for biological-image analysis', *Nature Methods*, pp. 676–682. doi: 10.1038/nmeth.2019.
- Schmidt, K. and Nichols, B. J. (2004) 'A barrier to lateral diffusion in the cleavage furrow of dividing mammalian cells', *Current Biology*. Cell Press, 14(11), pp. 1002–1006. doi: 10.1016/j.cub.2004.05.044.
- Schneider, F. *et al.* (2017) 'Diffusion of lipids and GPI-anchored proteins in actin-free plasma membrane vesicles measured by STED-FCS', *Molecular Biology of the Cell*, 28(11), pp. 1507–1518. doi: 10.1091/mbc.E16-07-0536.
- Schneider, F. *et al.* (2021) 'Influence of nanobody binding on fluorescence emission, mobility, and organization of GFP-tagged proteins', *iScience*. Elsevier Inc., 24(1), p. 101891. doi: 10.1016/j.isci.2020.101891.
- Schneiter, R. *et al.* (1999) 'Electrospray ionization tandem mass spectrometry (ESI-MS/MS) analysis of the lipid molecular species composition of yeast subcellular membranes reveals acyl chain-based sorting/remodeling of distinct molecular species en route to the plasma membrane', *Journal of Cell Biology*, 146(4), pp. 741–754. doi: 10.1083/jcb.146.4.741.
- Schoen, I. *et al.* (2011) 'Binding-activated localization microscopy of DNA I', *Nano Letters*, 11(9), pp. 4008–4011. doi: 10.1021/nl2025954.
- Schueder, F. *et al.* (2017) 'Multiplexed 3D super-resolution imaging of whole cells using spinning disk confocal microscopy and DNA-PAINT', *Nature Communications*. Nature Publishing Group, 8(1). doi: 10.1038/s41467-017-02028-8.
- Schuhmacher, M. *et al.* (2020) 'Live-cell lipid biochemistry reveals a role of diacylglycerol side-chain composition for cellular lipid dynamics and protein affinities', *Proceedings of the National Academy of Sciences*. National Academy of Sciences, p. 201912684. doi: 10.1073/pnas.1912684117.
- Schütz, G. J., Schindler, H. and Schmidt, T. (1997) 'Single-molecule microscopy on model membranes reveals anomalous diffusion', *Biophysical Journal*, 73(2), pp. 1073–1080. doi: 10.1016/S0006-3495(97)78139-6.
- Schwille, P., Koriach, J. and Webb, W. W. (1999) 'Fluorescence correlation spectroscopy with single-molecule sensitivity on cell and model membranes', *Cytometry*, 36(3), pp. 176–182. doi: 10.1002/(SICI)1097-0320(19990701)36:3<176::AID-CYTO5>3.0.CO;2-F.
- Seo, D. *et al.* (2016) 'A Mechanogenetic Toolkit for Interrogating Cell Signaling in Space and Time', *Cell*. Elsevier, 165(6), pp. 1507–1518. doi: 10.1016/j.cell.2016.04.045.
- Sezgin, E. *et al.* (2017) 'The mystery of membrane organization: Composition, regulation and roles of lipid rafts', *Nature Reviews Molecular Cell Biology*. Nature Publishing Group, 18(6), pp. 361–374. doi: 10.1038/nrm.2017.16.
- Sharonov, A. and Hochstrasser, R. M. (2006) 'Wide-field subdiffraction imaging by accumulated binding of diffusing probes', *Proceedings of the National Academy of Sciences of the United States of America*. National Acad Sciences, 103(50), pp. 18911–18916. doi: 10.1073/pnas.0609643104.
- Sheets, E. D. *et al.* (1997) 'Transient confinement of a glycosylphosphatidylinositol-anchored protein in the plasma membrane', *Biochemistry*, 36(41), pp. 12449–12458. doi: 10.1021/bi9710939.
- Sheetz, M. P., Schindler, M. and Koppel, D. E. (1980) 'Lateral mobility of integral membrane proteins is increased in spherocytic erythrocytes', *Nature*, 285(5765), pp. 510–512. doi: 10.1038/285510a0.
- Shi, Z. *et al.* (2018) 'Cell Membranes Resist Flow', *Cell*. Elsevier Inc., 175(7), pp. 1769–1779.e13. doi: 10.1016/j.cell.2018.09.054.
- Shimizu, K. *et al.* (2007) 'Effective cell-seeding technique using magnetite nanoparticles and magnetic force onto decellularized blood vessels for vascular tissue engineering', *Journal of Bioscience and Bioengineering*, 103(5), pp. 472–478. doi: 10.1263/jbb.103.472.
- Shoji, K. *et al.* (2012) 'Cytochalasin D acts as an inhibitor of the actin-cofilin interaction', *Biochemical and Biophysical Research Communications*. Elsevier Inc., 424(1), pp. 52–57. doi: 10.1016/j.bbrc.2012.06.063.
- Shubayev, V. I., Pisanic, T. R. and Jin, S. (2009) 'Magnetic nanoparticles for theragnostics', *Advanced Drug Delivery Reviews*, 61(6), pp. 467–477. doi: 10.1016/j.addr.2009.03.007.
- Sil, P. *et al.* (2020) 'Dynamic actin-mediated nano-scale clustering of CD44 regulates its meso-scale

References

- organization at the plasma membrane', *Molecular Biology of the Cell*, 31(7), pp. 561–579. doi: 10.1091/MBC.E18-11-0715.
- Singer, S. J. and Nicolson, G. L. (1972) 'The fluid mosaic model of the structure of cell membranes', *Science*, 175(4023), pp. 720–731. doi: 10.1126/science.175.4023.720.
- Slator, P. J., Cairo, C. W. and Burroughs, N. J. (2015) 'Detection of diffusion heterogeneity in single particle tracking trajectories using a hidden markov model with measurement noise propagation', *PLoS ONE*. Public Library of Science, 10(10). doi: 10.1371/journal.pone.0140759.
- Smith, S. B., Finzi, L. and Bustamante, C. (1992) 'Direct mechanical measurements of the elasticity of single DNA molecules by using magnetic beads', *Science*, 258(5085), pp. 1122–1126. doi: 10.1126/science.1439819.
- Son, S. *et al.* (2020) 'Molecular height measurement by cell surface optical profilometry (CSOP)', *Proceedings of the National Academy of Sciences of the United States of America*, 117(25), pp. 14209–14219. doi: 10.1073/pnas.1922626117.
- Spillane, K. M. *et al.* (2014) 'High-speed single-particle tracking of GM1 in model membranes reveals anomalous diffusion due to interleaflet coupling and molecular pinning', *Nano Letters*. American Chemical Society, 14(9), pp. 5390–5397. doi: 10.1021/nl502536u.
- Stanley, S. A. *et al.* (2012) 'Radio-Wave Heating of Iron Oxide Nanoparticles Can Regulate Plasma Glucose in Mice', *Science*. American Association for the Advancement of Science, 336(May), pp. 604–608. doi: 10.1126/science.1216753.
- Stanley, S. A. *et al.* (2015) 'Remote regulation of glucose homeostasis in mice using genetically encoded nanoparticles', *Nature Medicine*, 21(1), pp. 92–98. doi: 10.1038/nm.3730.
- Stanley, S. A. *et al.* (2016) 'Bidirectional electromagnetic control of the hypothalamus regulates feeding and metabolism', *Nature*. Nature Publishing Group, 531(7596), pp. 647–650. doi: 10.1038/nature17183.
- Steketee, M. B. *et al.* (2011) 'Nanoparticle-mediated signaling endosome localization regulates growth cone motility and neurite growth', *Proceedings of the National Academy of Sciences of the United States of America*. Edited by R. Langer, 108(47), pp. 19042–19047. doi: 10.1073/pnas.1019624108.
- Strauss, S. and Jungmann, R. (2020) 'Up to 100-fold speed-up and multiplexing in optimized DNA-PAINT', *Nature Methods*. Nature Research, 17(8), pp. 789–791. doi: 10.1038/s41592-020-0869-x.
- Strick, T. R. *et al.* (1996) 'The elasticity of a single supercoiled DNA molecule', *Science*, 271(5257), pp. 1835–1837. doi: 10.1126/science.271.5257.1835.
- Sungkaworn, T. *et al.* (2017) 'Single-molecule imaging reveals receptor-G protein interactions at cell surface hot spots', *Nature*. Nature Publishing Group, 550(7677), pp. 543–547. doi: 10.1038/nature24264.
- Suzuki, K. G. N. *et al.* (2012) 'Transient GPI-anchored protein homodimers are units for raft organization and function', *Nature Chemical Biology*. Nature Publishing Group, 8(9), pp. 774–783. doi: 10.1038/nchembio.1028.
- Svoboda, K. *et al.* (1993) 'Direct observation of kinesin stepping by optical trapping interferometry', *Nature*, 365(6448), pp. 721–727. doi: 10.1038/365721a0.
- Szymański, J. *et al.* (2017) 'Interaction of mitochondria with the endoplasmic reticulum and plasma membrane in calcium homeostasis, lipid trafficking and mitochondrial structure', *International Journal of Molecular Sciences*, 18(7), pp. 1–24. doi: 10.3390/ijms18071576.
- Tanase, M., Biais, N. and Sheetz, M. (2007) 'Magnetic Tweezers in Cell Biology', *Methods in Cell Biology*, 83(07), pp. 473–493. doi: 10.1016/S0091-679X(07)83020-2.
- Tarantino, N. *et al.* (2014) 'Tnf and il-1 exhibit distinct ubiquitin requirements for inducing NEMO-IKK supramolecular structures', *Journal of Cell Biology*, 204(2), pp. 231–245. doi: 10.1083/jcb.201307172.
- Taylor, R. W. *et al.* (2019) 'Interferometric scattering microscopy reveals microsecond nanoscopic protein motion on a live cell membrane', *Nature Photonics*. Springer US, 13(7), pp. 480–487. doi: 10.1038/s41566-019-0414-6.
- Thompson, R. E., Larson, D. R. and Webb, W. W. (2002) 'Precise nanometer localization analysis for individual fluorescent probes', *Biophysical Journal*. doi: 10.1016/S0006-3495(02)75618-X.
- Tinevez, J. Y. *et al.* (2017) 'TrackMate: An open and extensible platform for single-particle tracking', *Methods*, 115, pp. 80–90. doi: 10.1016/j.ymeth.2016.09.016.
- Tischer, D. and Weiner, O. D. (2014) 'Illuminating cell signalling with optogenetic tools', *Nature Reviews Molecular Cell Biology*. Nature Publishing Group, 15(8), pp. 551–558. doi: 10.1038/nrm3837.
- Tokunaga, M., Imamoto, N. and Sakata-Sogawa, K. (2008) 'Highly inclined thin illumination enables clear single-molecule imaging in cells', *Nature Methods*, 5(2), pp. 159–161. doi: 10.1038/nmeth1171.
- Tomishige, M. and Kusumi, A. (1999) 'Compartmentalization of the erythrocyte membrane by the membrane skeleton: Intercompartmental hop diffusion of band 3', *Molecular Biology of the Cell*, 10(8), pp. 2475–2479. doi: 10.1091/mbc.10.8.2475.
- Tomishige, M., Sako, Y. and Kusumi, A. (1998) 'Regulation mechanism of the lateral diffusion of band 3 in

- erythrocyte membranes by the membrane skeleton', *Journal of Cell Biology*, 142(4), pp. 989–1000. doi: 10.1083/jcb.142.4.989.
- Toraille, L. *et al.* (2018) 'Optical Magnetometry of Single Biocompatible Micromagnets for Quantitative Magnetogenetic and Magnetomechanical Assays', *Nano Letters*, 18(12), pp. 7635–7641. doi: 10.1021/acs.nanolett.8b03222.
- Treanor, B. *et al.* (2010) 'The Membrane Skeleton Controls Diffusion Dynamics and Signaling through the B Cell Receptor', *Immunity*. Cell Press, 32(2), pp. 187–199. doi: 10.1016/j.immuni.2009.12.005.
- Trimble, W. S. and Grinstein, S. (2015) 'Barriers to the free diffusion of proteins and lipids in the plasma membrane', *Journal of Cell Biology*. Rockefeller Univ Press, 208(3), pp. 259–271. doi: 10.1083/jcb.201410071.
- Tseng, P., Judy, J. W. and Di Carlo, D. (2012) 'Magnetic nanoparticle-mediated massively parallel mechanical modulation of single-cell behavior', *Nature Methods*, 9(11), pp. 1113–1119. doi: 10.1038/nmeth.2210.
- Tsuji, A. *et al.* (1988) *Regulation of band 3 mobilities in erythrocyte ghost membranes by protein association and cytoskeletal meshwork*, *Biochemistry*. UTC. Available at: <https://pubs.acs.org/sharingguidelines>.
- Tsunoyama, T. A. *et al.* (2018) 'Super-long single-molecule tracking reveals dynamic-anchorage-induced integrin function', *Nature Chemical Biology*. Springer US, 14(5), pp. 497–506. doi: 10.1038/s41589-018-0032-5.
- Ueda, Y. and Sato, M. (2018) 'Cell membrane dynamics induction using optogenetic tools', *Biochemical and Biophysical Research Communications*. Elsevier Inc., 506(2), pp. 387–393. doi: 10.1016/j.bbrc.2017.11.091.
- Umemura, Y. M. *et al.* (2008) 'Both MHC class II and its GPI-anchored form undergo hop diffusion as observed by single-molecule tracking', *Biophysical Journal*, 95(1), pp. 435–450. doi: 10.1529/biophysj.107.123018.
- Vangijzegem, T., Stanicki, D. and Laurent, S. (2019) 'Magnetic iron oxide nanoparticles for drug delivery: applications and characteristics', *Expert Opinion on Drug Delivery*. Taylor & Francis, 16(1), pp. 69–78. doi: 10.1080/17425247.2019.1554647.
- Vassilopoulos, S. *et al.* (2019) 'Ultrastructure of the axonal periodic scaffold reveals a braid-like organization of actin rings', *Nature Communications*. Springer US, 10(1), pp. 1–13. doi: 10.1038/s41467-019-13835-6.
- Vega, A. R. *et al.* (2018) 'Multistep Track Segmentation and Motion Classification for Transient Mobility Analysis', *Biophysical Journal*. Biophysical Society, 114(5), pp. 1018–1025. doi: 10.1016/j.bpj.2018.01.012.
- Vieira, O. V. *et al.* (2006) 'FAPP2, cilium formation, and compartmentalization of the apical membrane in polarized Madin-Darby canine kidney (MDCK) cells', *Proceedings of the National Academy of Sciences*, 103(49), pp. 18556–18561. doi: 10.1073/pnas.0608291103.
- Vissa, A. *et al.* (2019) 'Single-molecule localization microscopy of septin bundles in mammalian cells', *Cytoskeleton*, 76(1), pp. 63–72. doi: 10.1002/cm.21481.
- De Vlaminck, I. *et al.* (2011) 'Highly parallel magnetic tweezers by targeted DNA tethering', *Nano Letters*, 11(12), pp. 5489–5493. doi: 10.1021/nl203299e.
- De Vlaminck, I. and Dekker, C. (2012) 'Recent advances in magnetic tweezers', *Annual Review of Biophysics*, 41(1), pp. 453–472. doi: 10.1146/annurev-biophys-122311-100544.
- De Vries, A. H. B. *et al.* (2005) 'Micro magnetic tweezers for nanomanipulation inside live cells', *Biophysical Journal*. Elsevier, 88(3), pp. 2137–2144. doi: 10.1529/biophysj.104.052035.
- De Vries, A. H. B. *et al.* (2007) 'Direct observation of nanomechanical properties of chromatin in living cells', *Nano Letters*, 7(5), pp. 1424–1427. doi: 10.1021/nl070603+.
- Walker, M. M. *et al.* (1997) 'Structure and function of the vertebrate magnetic sense', *Nature*, 390(6658), pp. 371–376. doi: 10.1038/37057.
- Wang, D. *et al.* (2004) 'Superparamagnetic Fe₂O₃ beads-CdSe/ZnS quantum dots core-shell nanocomposite particles for cell separation', *Nano Letters*, 4(3), pp. 409–413. doi: 10.1021/nl035010n.
- Weber, G. F., Bjerke, M. A. and DeSimone, D. W. (2012) 'A Mechanoresponsive Cadherin-Keratin Complex Directs Polarized Protrusive Behavior and Collective Cell Migration', *Developmental Cell*. Elsevier Inc., 22(1), pp. 104–115. doi: 10.1016/j.devcel.2011.10.013.
- Wedchasan, A. (2019) *Charakterisierung magnetischer Nanopartikel zur Manipulation von Membrankomponenten*. Freie Universität Berlin.
- Weigel, A. V. *et al.* (2011) 'Ergodic and nonergodic processes coexist in the plasma membrane as observed by single-molecule tracking', *Proceedings of the National Academy of Sciences of the United States of America*, 108(16), pp. 6438–6443. doi: 10.1073/pnas.1016325108.
- Weinberg, Z. Y. and Puthenveedu, M. A. (2019) 'Regulation of G protein-coupled receptor signaling by plasma membrane organization and endocytosis', *Traffic*. Blackwell Munksgaard, pp. 121–129. doi: 10.1111/tra.12628.
- Weiß, K. *et al.* (2013) 'Quantifying the Diffusion of Membrane Proteins and Peptides in Black Lipid Membranes with 2-Focus Fluorescence Correlation Spectroscopy', *Biophysical Journal*. Biophys J, 105(2), pp. 455–462. doi: 10.1016/j.bpj.2013.06.004.

References

- Wheeler, M. A. *et al.* (2016) 'Genetically targeted magnetic control of the nervous system', *Nature Neuroscience*, 19(5), pp. 756–761. doi: 10.1038/nn.4265.
- White, M. K. *et al.* (2017) 'CRISPR Editing Technology in Biological and Biomedical Investigation', *Journal of Cellular Biochemistry*, 118(11), pp. 3586–3594. doi: 10.1002/jcb.26099.
- Whitesides, G. M., Kazlauskas, R. J. and Josephson, L. (1983) 'Magnetic separations in biotechnology', *Trends in Biotechnology*, 1(5), pp. 144–148. doi: 10.1016/0167-7799(83)90005-7.
- Wieser, S. *et al.* (2007) '(Un)confined diffusion of CD59 in the plasma membrane determined by high-resolution single molecule microscopy', *Biophysical Journal*. Biophysical Society, 92(10), pp. 3719–3728. doi: 10.1529/biophysj.106.095398.
- Wieser, S. and Schütz, G. J. (2008) 'Tracking single molecules in the live cell plasma membrane—Do's and Don't's', *Methods*. Elsevier Inc., 46(2), pp. 131–140. doi: 10.1016/j.ymeth.2008.06.010.
- Wilhelm, C. (2008) 'Out-of-equilibrium microrheology inside living cells', *Physical Review Letters*, 101(2), pp. 1–4. doi: 10.1103/PhysRevLett.101.028101.
- Wilmes, S. *et al.* (2020) 'Mechanism of homodimeric cytokine receptor activation and dysregulation by oncogenic mutations', *Science*. American Association for the Advancement of Science, 367(6478), pp. 643–652. doi: 10.1126/science.aaw3242.
- Winckler, B., Forscher, P. and Mellman, I. (1999) 'A diffusion barrier maintains distribution of membrane proteins in polarized neurons', *Nature*, 397(6721), pp. 698–701. doi: 10.1038/17806.
- Winkler, P. M. *et al.* (2018) 'Optical Antenna-Based Fluorescence Correlation Spectroscopy to Probe the Nanoscale Dynamics of Biological Membranes', *Journal of Physical Chemistry Letters*, 9(1), pp. 110–119. doi: 10.1021/acs.jpcclett.7b02818.
- Wu, K. *et al.* (2019) 'Magnetic nanoparticles in nanomedicine: A review of recent advances', *Nanotechnology*. IOP Publishing, 30(50). doi: 10.1088/1361-6528/ab4241.
- Wu, M. and Huang, S. (2017) 'Magnetic nanoparticles in cancer diagnosis, drug delivery and treatment (Review)', *Molecular and Clinical Oncology*. Spandidos Publications, 7(5), pp. 738–746. doi: 10.3892/mco.2017.1399.
- Xu, C. *et al.* (2004) 'Nitrilotriacetic Acid-Modified Magnetic Nanoparticles as a General Agent to Bind Histidine-Tagged Proteins', *Journal of the American Chemical Society*, 126(11), pp. 3392–3393. doi: 10.1021/ja031776d.
- Xu, F. X. *et al.* (2020) 'Magneto is ineffective in controlling electrical properties of cerebellar Purkinje cells', *Nature Neuroscience*. Springer US, 23(9), pp. 1041–1043. doi: 10.1038/s41593-019-0475-3.
- Xu, K., Babcock, H. P. and Zhuang, X. (2012) 'Dual-objective STORM reveals three-dimensional filament organization in the actin cytoskeleton', *Nature Methods*. Nature Publishing Group, 9(2), pp. 185–188. doi: 10.1038/nmeth.1841.
- Xu, K., Zhong, G. and Zhuang, X. (2013) 'Actin, Spectrin, and Associated Proteins Form a Periodic Cytoskeletal Structure in Axons', *Science*. American Association for the Advancement of Science, 339(6118), pp. 452–456. doi: 10.1126/science.1232251.
- Yamaguchi, M. *et al.* (2011) 'Structome of *Saccharomyces cerevisiae* determined by freeze-substitution and serial ultrathin-sectioning electron microscopy', *Journal of Electron Microscopy*, 60(5), pp. 321–335. doi: 10.1093/jmicro/dfr052.
- Yan, J., Skoko, D. and Marko, J. F. (2004) 'Near-field-magnetic-tweezer manipulation of single DNA molecules', *Physical Review E - Statistical Physics, Plasmas, Fluids, and Related Interdisciplinary Topics*, 70(1), p. 5. doi: 10.1103/PhysRevE.70.011905.
- Yan, R., Chen, K. and Xu, K. (2020) 'Probing Nanoscale Diffusional Heterogeneities in Cellular Membranes through Multidimensional Single-Molecule and Super-Resolution Microscopy', *Journal of the American Chemical Society*, 142(44), pp. 18866–18873. doi: 10.1021/jacs.0c08426.
- Yang, C. and Svitkina, T. M. (2019) 'Ultrastructure and dynamics of the actin – myosin II cytoskeleton during mitochondrial fission', *Nature Cell Biology*. Springer US, 21(May). doi: 10.1038/s41556-019-0313-6.
- Yang, S.-Y. *et al.* (2008) 'Ex Vivo Magnetofection With Magnetic Nanoparticles: A Novel Platform for Nonviral Tissue Engineering', *Artificial Organs*, 32(3), pp. 195–204. doi: 10.1111/j.1525-1594.2007.00526.x.
- Yin, S., Song, N. and Yang, H. (2018) 'Detection of Velocity and Diffusion Coefficient Change Points in Single-Particle Trajectories', *Biophysical Journal*. Biophysical Society, 115(2), pp. 217–229. doi: 10.1016/j.bpj.2017.11.008.
- Zablotskii, V. *et al.* (2011) 'Nanomechanics of magnetically driven cellular endocytosis', *Applied Physics Letters*, 99(18), pp. 1–4. doi: 10.1063/1.3656020.
- Zahid, M. U. *et al.* (2018) 'Single quantum dot tracking reveals the impact of nanoparticle surface on intracellular state', *Nature Communications*. Nature Publishing Group, 9(1). doi: 10.1038/s41467-018-04185-w.

- Zaner, K. S. and Valberg, P. A. (1989) 'Viscoelasticity of F-actin measured with magnetic microparticles', *Journal of Cell Biology*. The Rockefeller University Press, 109(5), pp. 2233–2243. doi: 10.1083/jcb.109.5.2233.
- Zanetti-Domingues, L. C. *et al.* (2013) 'Hydrophobic Fluorescent Probes Introduce Artifacts into Single Molecule Tracking Experiments Due to Non-Specific Binding', *PLoS ONE*, 8(9). doi: 10.1371/journal.pone.0074200.
- Zhang, H. *et al.* (2014) 'Monodisperse magnetofluorescent nanoplatforms for local heating and temperature sensing', *Nanoscale*. Royal Society of Chemistry, 6(22), pp. 13463–13469. doi: 10.1039/c4nr04884a.
- Zhang, W. *et al.* (2017) 'Optogenetic control with a photocleavable protein, PhocI', *Nature Methods*. Nature Publishing Group, 14(4), pp. 391–394. doi: 10.1038/nmeth.4222.
- Zhang, X., Servos, M. R. and Liu, J. (2012) 'Instantaneous and quantitative functionalization of gold nanoparticles with thiolated DNA using a pH-assisted and surfactant-free route', *Journal of the American Chemical Society*, 134(17), pp. 7266–7269. doi: 10.1021/ja3014055.
- Zhong, G. *et al.* (2014) 'Developmental mechanism of the periodic membrane skeleton in axons', *eLife*, 3, pp. 1–21. doi: 10.7554/eLife.04581.
- Zhou, Y. and Hancock, J. F. (2015) 'Ras nanoclusters: Versatile lipid-based signaling platforms', *Biochimica et Biophysica Acta (BBA) - Molecular Cell Research*. Elsevier B.V., 1853(4), pp. 841–849. doi: 10.1016/j.bbamcr.2014.09.008.
- Zihni, C. *et al.* (2016) 'Desmosomes Tight junctions: from simple barriers to multifunctional molecular gates', *Nature Publishing Group*. doi: 10.1038/nrm.2016.80.

Curriculum Vitae

Biochemist/Biophysicist eager to study dynamic cellular systems across scales using light microscopy. Experienced in live-cell imaging, super-resolution microscopy, and image analysis. Enthusiastic to work in an interdisciplinary team.

Research Experience

- Apr 2017 – present *Controlled manipulation of membrane proteins by fluorescent magnetic nanoparticles*, doctoral thesis, Prof. Dr. Helge Ewers; Freie Universität Berlin
- Oct 2015 – Apr 2018 *Super-resolving BMP signaling pathways and their compartmentalization by septin scaffolds*, research project, Prof. Dr. Helge Ewers; Freie Universität Berlin
- Nov 2014 – Jul 2015 *Investigation of the ABC Transporter HisQMP₂-HisJ-LAO by Fluorescence Correlation Spectroscopy*, Master thesis, Prof. Dr. Salvatore Chiantia and Prof. Dr. Andreas Herrmann; Humboldt-Universität zu Berlin
- 10/2013 – 01/2014 *Optimization of Solubility and Stability of C-type Lectins*, research project, Dr. Christopher Rademacher; Max Planck Institute of Colloids and Interfaces, Berlin
- 06/2013 – 08/2013 *Analysis of Developmental Defects in Fendrr Mutants*, research project, Dr. Phillip Grote and Prof. Dr. Bernhard Herrmann; Max Planck Institute of Molecular Genetics, Berlin
- 11/2012 – 03/2013 *Structural Basis for the Interaction of the Spliceosomal Proteins Brr2 and Prp8*, Bachelor thesis in the group of Prof. Dr. Markus Wahl; Freie Universität Berlin

Publication

- 2020 Li, J.H., Santos-Otte, P., Au, B. *et al.* Directed manipulation of membrane proteins by fluorescent magnetic nanoparticles. *Nature Communications* **11**, 4259 (2020). doi.org/10.1038/s41467-020-18087-3

Personal info

Jia Hui Li

For data protection reasons, personal information is not published in the electronic version.

Skills

Optical microscopy

- Live-cell microscopy
- Single-molecule tracking
- Super-resolution (d STORM, STED)

Wet lab

- Mammalian cell culture
- Immunofluorescence
- Protein biochemistry

Software:

ImageJ/Fiji	Advanced
Matlab, R, Python	Basic
OriginPro, MS Office	Advanced
Adobe Illustrator	Advanced

Languages

German	Native
English (spoken/written)	Fluent
Chinese	Good knowledge
Spanish	Basic

Conferences & trainings

- 2020 Biophysical Society Annual Meeting, San Diego, Biological Fluorescence Subgroup selected flash talk and poster prize awardee
- 2019 Live Cell Single Molecule Tracking Symposium, Ulm, selected talk
 Joint EBSA and ICBP-IUPAP Biophysics Congress, Madrid, poster presentation
 Image processing and analysis workshop by BioVoxel
- 2018 Single Molecule Localisation Microscopy Symposium, Berlin, poster presentation
 3rd International Symposium Membranes and Modules, Berlin, poster presentation
- 2017 EMBO workshop Molecular and cellular biology of septins, Berlin, poster presentation
- 2016 International training course France Biolmaging Advanced Training, Montpellier

Education

- Oct 2015 – present Doctoral student at the Institute of Biochemistry of the Freie Universität Berlin
- Apr 2013 – Jul 2015 Master of Science in Biochemistry, Freie Universität Berlin, final mark: 1,1
- Feb – Jul 2014 Erasmus exchange study at the Katholieke Universiteit Leuven, Belgium, Master program “Biophysics, Biochemistry and Biotechnology”
- Oct 2009 – Jun 2013 Bachelor of Science in Biochemistry, Freie Universität Berlin, final mark: 1,5
- 2009 Abitur (high school degree), final mark: 1,3

Teaching experience

- 2018 / 2019 Supervision of internship students over the competitive DAAD RISE Germany program from Canada and USA (Physics; Computational biology)
- 2017 / 2018 Supervision of Bachelor theses (Biophysics; Physics)
- 2016 – 2018 Teaching assistant in laboratory course for Biochemistry Bachelor students
- 2012 – 2014 Student teaching assistant for Biochemistry I lecture

Extracurricular activities

- 2018 – present DREAM Mentoring, career development program of the Dahlem Research School for female doctoral candidates
- 2017 – present Volunteer at the Long Night of Sciences in Berlin
- 2017 – 2019 Co-student speaker of the Collaborative Research Centre SFB 958
- 2015 – 2018 Mentor for “CyberMentor”, Germany’s largest online-mentoring program for girls in STEM
- 2012 – 2015 Member of the Biochemistry student union, Freie Universität Berlin

Appendix

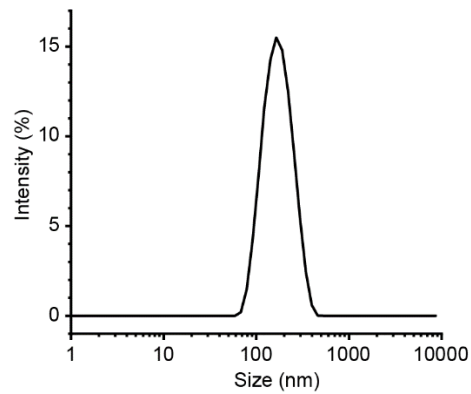


Figure S28: DLS measurement of FMNPs

Intensity based particle size distribution of FMNPs in PBS. Intensity averaged over four measurements against the hydrodynamic diameter (159 ± 2 nm, mean \pm s.d.).

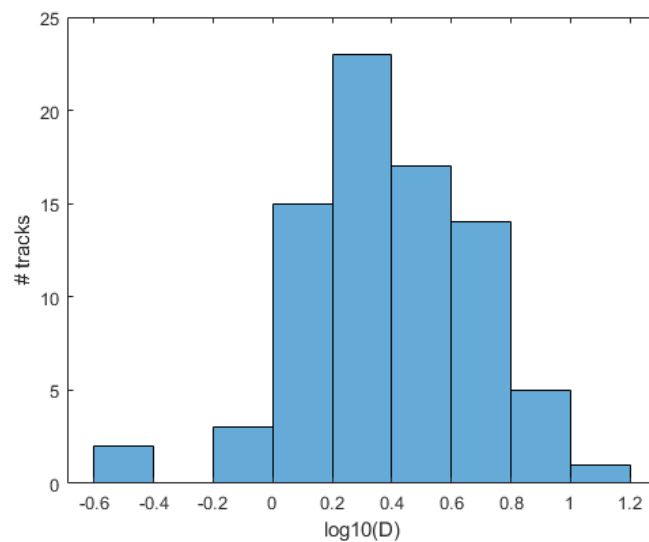


Figure S29: Histogram of diffusion coefficients for FMNPs in solution

Biplane 3D SPT of FMNPs diluted 1:1000 in cell culture medium at 5 ms exposure time (200 Hz). The 3D tracks were filtered by track length (>29 frames) and D (>0.005) and the diffusion coefficients determined with MSD analyzer (mean/median $2.46/2.49 \mu\text{m}^2/\text{s}$, $n=80$ tracks).

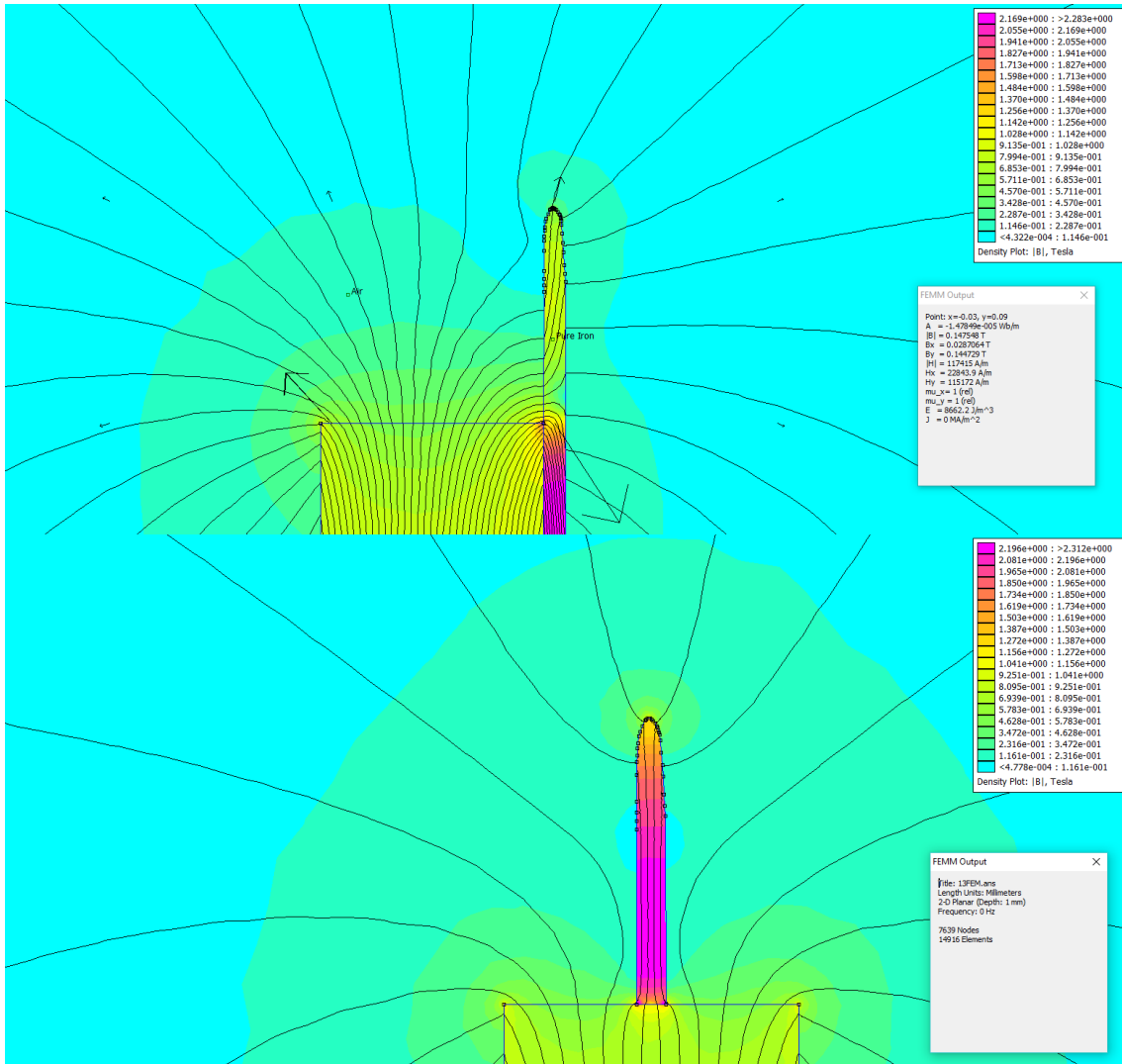


Figure S30: FEMM simulation of the magnetic needle setup

2D magnetic field simulated for a tip extending 1 mm from a 1x1x3 mm permanent magnet. The shape of the tip was traced from a brightfield image. (Areeya Wedchasan and Isaac Wong under my supervision.)

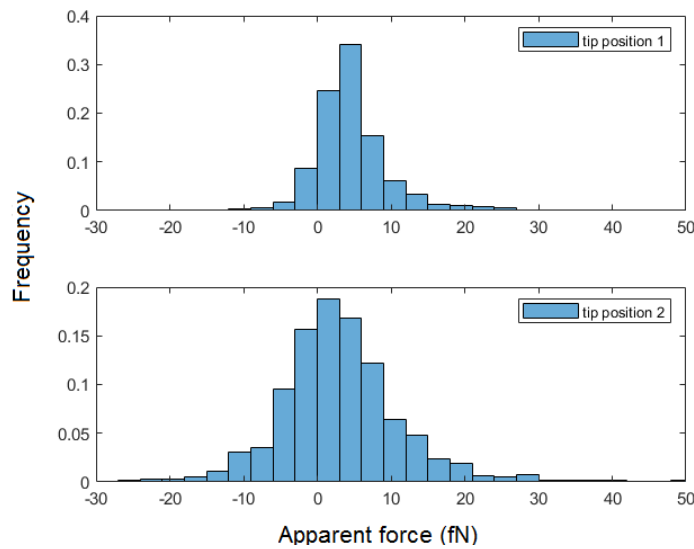


Figure S31: Variability of apparent magnetic forces with tip position

Histograms of apparent forces at two different tip positions set according to the procedure described in 7.4. The mean values differ only slightly (4.9 vs. 3.2 fN) but note the larger spread for position 2 (s.d. 6.0 vs. 8.2 fN).

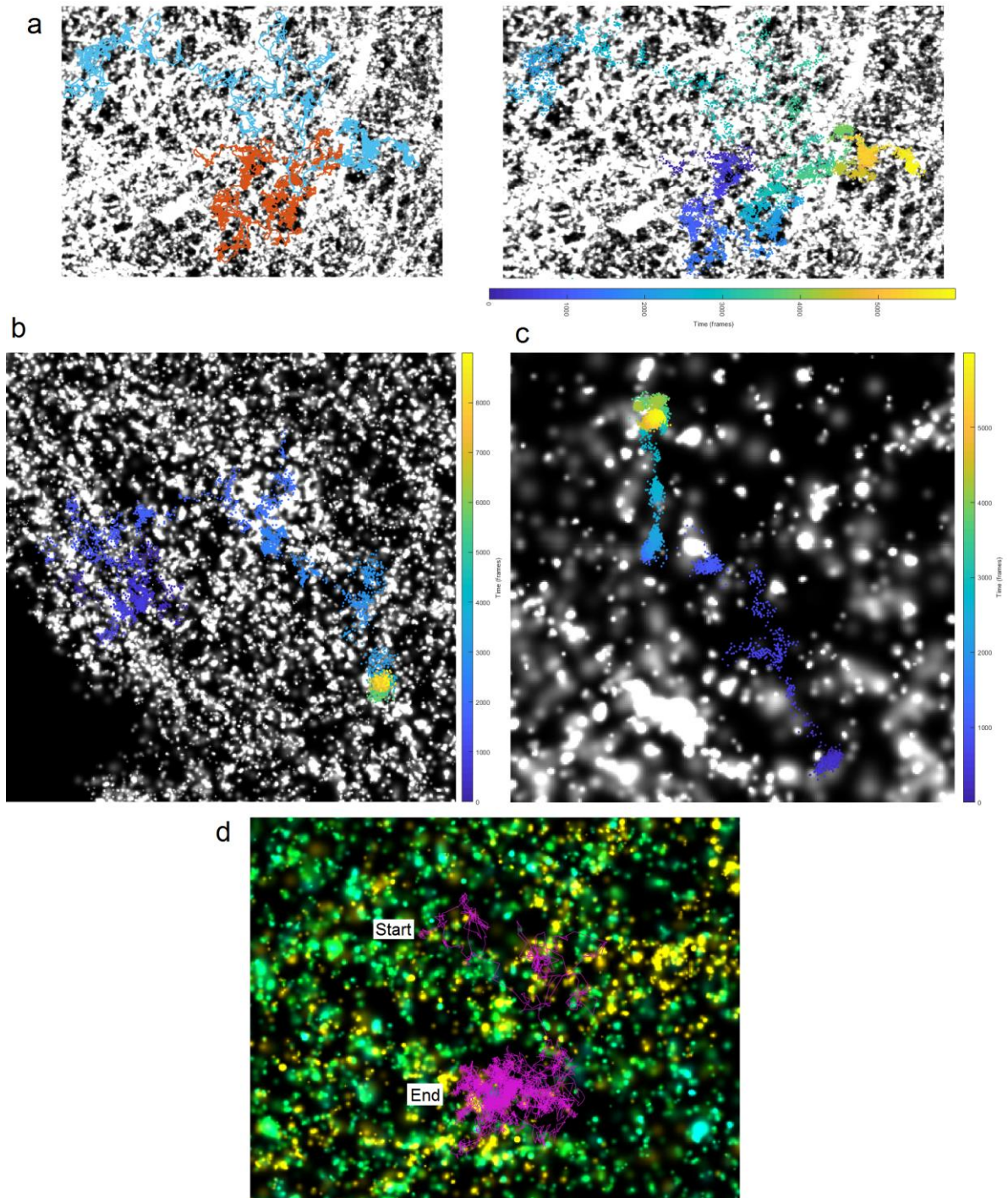


Figure S32: Examples of FMNP-pulled GFP-GPI trajectories correlated with the cortical actin cytoskeleton
a, b) Magnet was placed on the right side. **c)** Magnet was placed on the top. **d)** Magnet was placed below. *d*STORM images of actin color-coded by *z*. (Color scale not shown.) **a-c)** *d*STORM images of actin in grey scale. **a)** Left: Trajectories of two particles colored by track. Right: Localizations of the same two tracks color-coded by time. **b, c)** Localizations colored by time. **a-d)** SPT with 20 ms exposure time (50 Hz). Images have been exported for the purpose of visual inspection (pixel size/scale unknown).

Acknowledgments

I would like to thank my supervisor Prof. Dr. Helge Ewers who had the initial idea and gave me the opportunity to work on this project. I am most grateful that you are always keeping a growth mindset.

I thank Stephan Block for our fruitful collaboration for the force calibration and being my second reviewer.

Paula, you fearlessly demonstrated the feasibility of this project and it was a pleasure working with you. I thank Jakob for help with analysis and discussions. Alex and Saskia for the company. Ando and Purba for giving me a break. I thank all present and former members of the Ewers laboratory for scientific discussions, technical support, and giving me a home away from home. I thank all students I have taught and who taught me *vice versa*. I am indebted to everyone who inspired and challenged me, who supported and encouraged me along the way. Thanks to all proofreaders of this dissertation.

Thanks to my dear Capoeira trainers and friends. She has transformed my body and soul. Axé!

I thank my parents Xu Yaxin and Li Liangping for teaching me to believe in something greater than myself. 你们辛苦了。 Tina, deine große Schwester zu sein ist mir Freude und Stolz.

Dennis, ich danke dir für das Vertrauen, das du mir schenkst. Ich wachse jeden Tag mit dir und blicke voller Vorfreude in unsere Zukunft. In medias res!

„Ich habe mir auch das vorgehalten, was ich mir öfters gesagt habe, daß ich lieber ein bedeutender Naturforscher als ein bedeutender Ingenieur, aber lieber ein unbedeutender Ingenieur als ein unbedeutender Naturforscher sein möchte; jetzt, wo ich an der Grenze stehe, denke ich aber, daß doch auch wahr ist, was Schiller sagt: ‚Und setzet ihr nicht das Leben ein, nie wird euch das Leben gewonnen sein‘, und daß allzuviel Vorsicht Torheit wäre.“

Heinrich Hertz in a letter to his parents

Biography by Josef Kuczera